The Dissertation Committee for Astrid Makowitz Certifies that this is the approved version of the following dissertation:

THE GENETIC ASSOCIATION BETWEEN BRITTLE DEFORMATION AND QUARTZ CEMENTATION: EXAMPLES FROM BURIAL COMPACTION AND CATACLASIS

Committee:

Earle F. McBride, Supervisor

Kitty L. Milliken, Co-Supervisor

Randall Marrett

Rob Lander

Jack Sharp

THE GENETIC ASSOCIATION BETWEEN BRITTLE DEFORMATION AND QUARTZ CEMENTATION: EXAMPLES FROM BURIAL COMPACTION AND CATACLASIS

by

Astrid Makowitz, B.S., M.S.

Dissertation

Presented to the Faculty of the Graduate School of
The University of Texas at Austin
in Partial Fulfillment
of the Requirements
for the Degree of

Doctor of Philosophy

The University of Texas at Austin
May, 2004

Dedication

Für Inge und Erich

Seff Bleib Dou!

Acknowledgements

Much of my work has been dependent on the critique and encouragement of my advisor, Kitty Milliken, who has taught me much about “micro” scale issues in clastic diagenesis. Our discussions have always led to more questions, generally ones I did not think of myself. I hope some of her wisdom has rubbed off on me over the last 5 years. I am also fortunate to have an entire committee who, in one way or another, care about my work. Earle McBride deserves much appreciation for reviewing papers, providing insightful comments, and adding so much to my knowledge of sandstone petrology/petrography. Earle McBride’s financial support helped brighten the November 2003 JSR issue. Rob Lander is truly awesome when it comes to integrating data into models and synthesizing results. He has been a strong advocate of my work and provided much needed support with diagenetic modeling. I feel enlightened now that I see the utility of Touchstone™. Randy Marrett and Jack Sharp have provided intermittent support, by answering questions and clarifying issues in structural geology and hydrogeology, respectively. Steve Laubach is my unofficial committee member who has shown enthusiasm and support through many stages of my dissertation.

Funding for this dissertation was pieced together by numerous small student grants provided by GCAGS, GCSSEPM, GSA, SEPM, and the Geology Foundation in the Jackson School of Geosciences, during my appointments as a

teaching assistant in the Department of Geological Sciences, a research assistant in the FRAC Group at the Bureau of Economic Geology, and a research assistant at the Institute for Geophysics.

A complete sample set of the Mount Simon Formation would not have been possible without the kind help of Dave Morse, Bob Mumm and Rod Norbey, at the Illinois State Geological Survey. Field assistant Tim Flood helped gather Mount Simon outcrop samples during the middle of a hot Midwest summer. Jason and Gordon Gumble deserve much appreciation for braving the ticks and other nasties while sampling in Kentucky, Tennessee, and Virginia.

Many others have helped me in the last years by way of moral support, guidance, editing papers, and laughter. They have also been there to console and/or celebrate: Duncan Sibley, Laura Net, Jason Gumble, Linda Bonnell, Annette Summers Engel, Scott Engel, Aysen Ozkan, Claudia Rassi, Diego Van Berkel, Imtiaz Ahmed, Julymar Morantes, and Alison Mote just to name a few.

And finally, thanks to my family, which has grown substantially in the last year, for providing the unconditional love that has helped me succeed in what I've accomplished.

"Everything flows and nothing abides; everything gives way and nothing stays fixed."

Heraclitus of Ephesus, Greek Philosopher, (536-470 BCE)

THE GENETIC ASSOCIATION BETWEEN BRITTLE DEFORMATION AND QUARTZ CEMENTATION: EXAMPLES FROM BURIAL COMPACTION AND CATACLASIS

Publication No._____________

Astrid Makowitz, Ph.D.
The University of Texas at Austin, 2004

Supervisors: Earle F. McBride and Kitty L. Milliken

Brittle deformation of quartz grains accompanied by quartz cementation is a porosity-reducing mechanism in sandstones. Brittle deformation has historically been overlooked as a mechanism of compaction because it has been poorly understood and techniques for observing it are not commonly used. I have used scanned cathodoluminescence (CL) to quantify brittle deformation of quartz grains, in sandstones undergoing burial and cataclasis.

Sandstone samples of different ages and compositions, taken from two basins with contrasting burial histories, are used to examine the interaction

between brittle deformation and quartz cementation in burial compaction. Trends of increasing deformation by microfracturing with maximum burial depth are observed in both the lithic-rich Frio Formation from the Gulf of Mexico basin and in the quartz-rich Mount Simon Formation of the Illinois basin. Combining information on the degree of brittle deformation and the amount of quartz cement localized within microfractures allows for the calculation of the amount that brittle deformation influences compaction (i.e. porosity loss). For the Frio, 0.12 to 8.37% of initial porosity is lost due to cementation related to brittle deformation, whereas the values for the Mount Simon lie between 0.25 and 2.16%.

Diagenetic forward models are constructed for each formation using petrographic modal analysis and burial history information to determine the depth of quartz cement commencement as an influential factor affecting brittle grain deformation. Most fracturing probably occurred prior to the precipitation of > 2% quartz cement. Commencement of quartz cementation at shallow depths combined with slower burial rates resulted in less brittle deformation in the Mount Simon compared with the Frio, where sandstones underwent rapid burial and quartz cementation began at greater depths.

Cataclastic sandstones within the Pine Mountain Overthrust, eastern Kentucky, show more extreme porosity reduction by fracturing and cementation than normally compacted sandstones. In contrast to normal burial compaction, cataclasis and cementation within the cataclasites occurred over *several* discrete episodes as evidenced by cross-cutting relationships of fractures and cement. Quantitative data on the distribution of *inter*- and *intra*granular quartz cement within cataclasized sandstones combined with CL observations show that the timing of deformation is in agreement with published dates of fault movement.

Table of Contents

List of Tables

List of Figures

Chapter 1: Introduction

Mechanical (physical) and chemical processes, although conventionally viewed as separate processes, actually work in concert to influence rock porosity evolution in compacted and severely deformed sandstones. Although it is has been noted in passing that mechanical and chemical processes work together in the form of grain breakage and cementation (e.g. Hathon and Houseknecht, 1991; Hippler, 1993), previous studies lack *quantification* of combined physical and chemical influences on porosity and other important rock properties.

Brittle deformation in sandstones occurs across a continuum that begins with burial and extends across a wide spectrum of deformation scenarios. This study demonstrates, by observation, quantification, and modeling, the link of physical breaking and crushing of grains to quartz cementation in two deformation scenarios: 1) sandstones undergone burial compaction (Makowitz and Milliken, 2002; Makowitz and Milliken, 2003) and; 2) cataclasized sandstones (Makowitz et al., in prep).

The first goal was to examine and quantify porosity loss due to cementation caused by grain breakage in the simple case of compaction using the Cambrian Mount Simon Formation and the Oligocene Frio Formation.

The second goal was to apply petrographic observations from this simple case to the forward modeling software Touchstone™ to gain an understanding of the relative timing of quartz cementation and overpressuring (Chapter 3). Cement is reported to inhibit grain breakage by stabilizing the packing arrangement of grains (e.g., Bruno and Nelson, 1991; Dvorkin et al., 1994), however, petrographic observations in this study show that fractures occur primarily before and during quartz cementation. Results from this study allow a refinement of the Touchstone™ model to accommodate the history of microscale deformation.

The third goal is to examine microscopically identical processes of grain breakage and cementation that occur within a fault zone (Chapter 4). Microscale information on true particle size distribution, cement distribution, and texture of cataclasized pieces in a quartz-rich cataclasite is vital for understanding the deformation and cementation history, and thus the porosity evolution of severely deformed rocks. Results in Chapter Four also show that intergranular volume (minus cement porosity) is not necessarily lower in cataclasized sandstones compared to nearby undeformed sandstones. This demonstrates that in cataclasis porosity is not destroyed by grains moving together, but rather by the interaction of grains undergoing crushing and cementation. Grains within cataclasite are inflated (expanded) by intragranular fractures, and concomitant quartz cementation reduces the porosity, demonstrating that this is a universal porosity-reducing mechanism occurring across a wide range of deformation scenarios.

BRITTLE DEFORMATION: FROM INTRAGRANULAR MICROFRACTURING TO COMMINUTION

In mechanical compaction, during either burial or tectonic deformation, grains (depositional particles) deform through brittle processes. Brittle deformation encompasses a range of deformation severity from (1) grains with one or several fractures and localized cataclasis (Fig. 1A), to (2) more intense deformation, where a grain is extensively fractured but the outline of the original grain is still recognizable (Fig. 1B), to (3) extreme deformation where a grain is virtually pulverized by extensive fracturing and cataclasis and the original grain outline is not recognizable (Fig. 1C). This evolution is dependent not only on effective stress, but on localization of the stress on a micro-scale and time.

During the initial stages of burial, the effective stress (lithostatic pressure minus pore fluid pressure) is relatively low, and grain-scale frictional slip and rotation are the dominant compaction mechanisms (Füchtbauer, 1967). As the effective stress increases with burial, grain breakage and ductile deformation occurs, but if pore–fluid overpressures develop the effective stress will decrease, thus inhibiting grain breakage and ductile deformation at greater depths. However, compaction experiments show that the effective stress required for grain fracturing can be as low as several kilopascals, which translates to a few

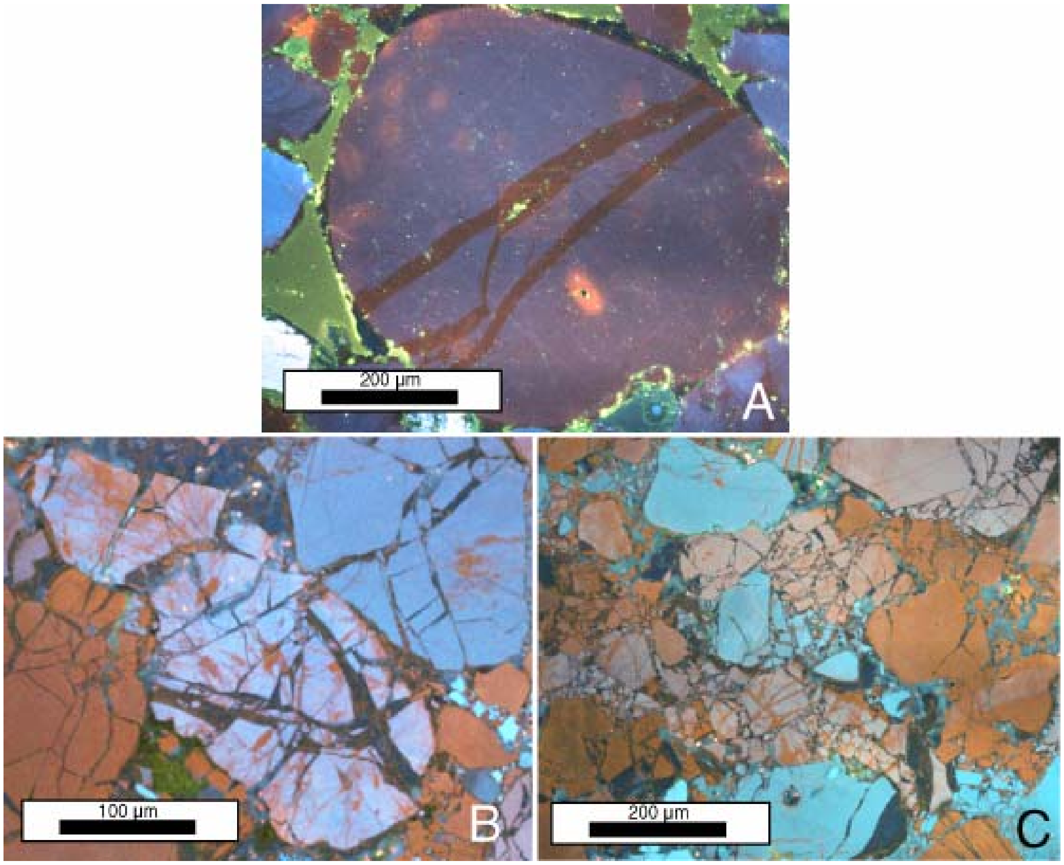

Figure 1. RGB filter CL images. A) Image of a fractured grain. The fractures are filled with quartz cement exhibiting a dark reddish luminescence. The quartz cement luminescence color is continuous from the microfracture to the overgrowth suggesting that it is a compactional fracture and was subsequently filled with quartz cement during the time of overgrowth precipitation. It also suggests that fracturing occurred before the quartz cementation window was reached during burial. B) Image of grains exhibiting extensive microfracturing. Microfractures commonly commence at grain-grain contacts, as depicted in the photomicrograph, where stress on the grains is greatest. The dark areas between the broken pieces are quartz cement, which fills the microfractures. This is a deformed sample from the Pine Mountain region. C) RGB filter CL image of severely crushed, or comminuted grains. This type of deformation is common in sandstones deformed within faults such as this sample from the Pine Mountain overthrust. Interestingly, some grains are completely crushed, whereas other grains in the same vicinity show little brittle deformation.

10’s of meters in depth (Wong 1990). This suggests that the brittle grain breakage can occur at shallow depths and low effective stress and that highly localized breakage at particular stressed grain contacts may continue, even under conditions of reduced effective stress in the bulk material.

Severely deformed rocks undergo cataclasis, a process that is defined by brittle fragmentation of mineral grains with rotation of grain fragments, accompanied by frictional grain boundary sliding and intra-grain dilatancy. Fragmentation is achieved by repeated fracturing of grains. Comminution is a typical process active in the generation of fault gouge (Engelder, 1974; Blenkinsop, 1991). Experimental generation of gouge shows that cataclasis and comminution are active mechanisms in fault generation, reducing both grain size and sorting (Engelder, 1974). Experimental and natural cataclasized porous sandstones demonstrate that a reduction in porosity and permeability occurs because of the decrease in grain size and grain-sorting of the cataclasized region (Pittman, 1981; Antonellini, 1994; Fisher, 2000).

PHYSICAL AND CHEMICAL PARAMETERS AFFECTING GRAIN BREAKAGE

Numerous biaxial compression experiments have been carried out to investigate the influential physical and chemical parameters controlling brittle failure in sandstone and other granular material. The common parameters cited in the literature include particle size, particle shape, presence of cement, cement amount and distribution, porosity of granular material, time, pore fluid presence, and pore fluid composition (Table 1). The results of these experiments are primarily documented in rock mechanics literature. Although experiments provide useful insight by controlling single or sometimes multiple parameters affecting brittle behavior, they do not adequately represent inherent complexities of sandstones (such as sandstone composition, mineralogy, cements, and burial history) in natural settings.

BRITTLE DEFORMATION AND QUARTZ CEMENTATION

No matter what the brittle deformation scenario, it is clear that the combined processes of brittle deformation and concomitant quartz cementation are active porosity-reducing mechanisms for both simple deformation by compaction to more extreme deformation by sandstone cataclasis (Antonellini and Aydin. 1994; Makowitz and Milliken, 2001; Makowitz and Milliken, 2002; Milliken and Reed, 2002; Makowitz and Milliken, 2003; Milliken et al., 2004; Lander et al., 2004; Makowitz and Milliken, 2004; Makowitz and Milliken, in prep; Net and Makowitz, 2004). Deformation of quartz grains, manifested as opening-mode fractures, essentially expand into the pore space, effectively exchanging primary intergranular pore space for secondary intragranular fracture porosity. Newly-created fracture surfaces, in turn, provide fresh nucleation sites,

Table 1. Parameters cited in literature that influence particle breakage.

Particle Size	**Cement**
Borg et al., 1960	Dunn et al, 1973
Gallagher et al., 1974	Bruno and Nelson, 1991
Gallagher et al., 1987	Bernabe and Hayes, 1992
Zhang, 1990	Dvorkin et al., 1994
Brzesowsy, 1995	Yin and Dvorkin, 1994
Lade et al., 1996	Wong and Wu, 1995
Chuhan et al., 2002	Menendez et al., 1996
Makowitz and Milliken, 2002	David et al., 1998
Particle Shape	**Porosity**
Pittman, 1981	Dunn, 1973
Michibayashi, 1996	Wong, 1990
Cladouhos, 1999	Zhang et al., 1990
Tang et al., 2001	Bernabe and Hayes, 1992
Milliken and Reed, 2002	
Pore Fluids	**Time (Duration)**
Park, 1984	Lade et al., 1996
Brezesowsky, 1995	

favorable for quartz cementation, thus, quartz cement precipitates on these surfaces relatively quickly compared to the detrital grains surface. The rate of healing in experimentally fractured quartz grains has been observed to vary with aperture thickness of the fracture, with small aperture fractures (< 10 µm) healing in hours (Brantley et al. 1990). Therefore, deformation of quartz grains, inherently promotes quartz cementation and the occlusion of porosity, not by compaction alone but by the integrated process (aided by compaction) of brittle deformation and subsequent quartz cementation.

MICROFRACTURES

Microfracture Formation

Fractures initiate and propagate from points of critical pressure, such as grain-grain contact (Zhang et al. 1990). Empirical observations of the resulting 'cone-crack' patterns have been observed using glass beads and rock discs (Gallagher et al. 1974), conglomerate pebbles (Gallagher, 1987; McEwen, 1981), and sand grains (Chuhan et al., 2002; Gallagher et al., 1974).

Fracture Classification and Morphology

In structural terms, observed intragranular fractures are classified as opening- mode I fractures (Atkinson, 1987). Laubach (1997) has distinguished three types of fractures based on CL imaging, Categories I, II, and III. Category I fractures have straight traces that cut numerous grains and associated cement and do not radiate from grain contacts. These are common in highly cemented sandstones. Category II includes intragranular fractures. Category III fractures are inherited.

For the most part, fractures observed in the quartz grains of the Frio and Mount Simon sandstones are classified as Category II. These fractures are typically associated with grain-grain contacts and many of them are wedge-shaped with the widest fracture aperture at grain contacts (Fig. 2A). Expansion, or inflation, of individual grains by numerous fractures may create an exploded appearance in CL images (Fig. 2C). Extreme crushing may also occur along grain/grain contacts, where a large number of very small, comminuted particles occur along the contact and lesser degrees of comminution occur at greater distance from the contact (e.g., Milliken, 1994; Dickinson and Milliken, 1995; Figure 7 of Land and Milliken, 2000; Milliken and Laubach, 2000). In some instances, particles are spalled and rotated. These fracture characteristics are detectable in samples from all the depths examined in this study.

MICROSCALE IMAGING OF DEFORMATION FEATURES

Scanned cathodoluminescence (CL) imaging combined with secondary electron imaging (SEI) provides an unambiguous method for distinguishing detrital quartz, authigenic quartz, and voids (e.g., Houseknecht 1991; Sipple 1968; Walker and Burley 1991) (Fig. 3). Until the advent of scanned CL imagining

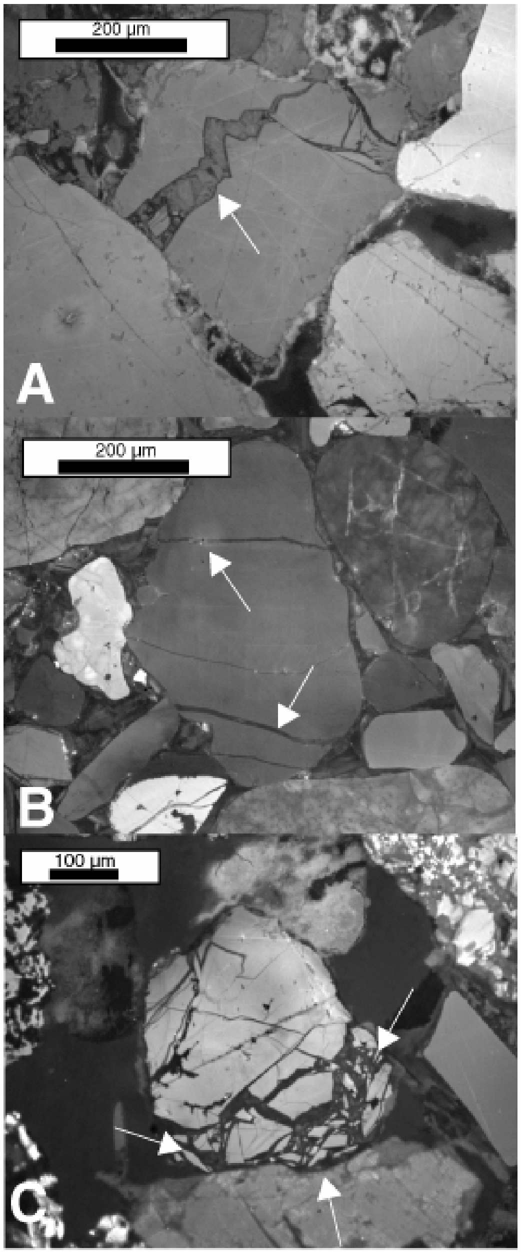

Figure 2. Different fracture morphologies caused by mechanical compaction. A) wedge-shape features are common, with maximum aperture at the boundary between two grains. The aperture decreases in width away from contact (sample 15167, Frio Formation). B) Straight fractures propagating from contacts between two grains, propagating through the whole grain (sample 8466 from Mount Simon). C) Extensive grain crushing (sample 17154 from Frio).

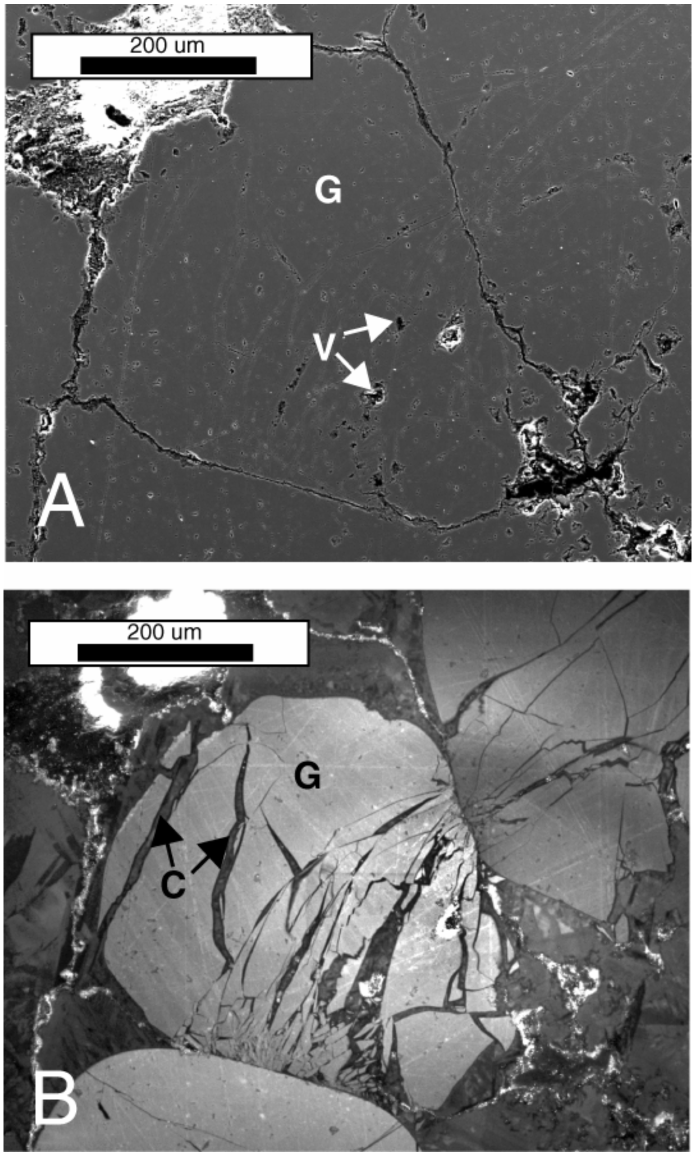

Figure 3. Comparison of two images of identical location and magnification. A) SEI image showing void distribution (arrows). B) Quartz filled-microfractures revealed by cathodoluminescence (arrow). Without CL imaging, fractures would not be observed. G = detrital quartz, C = quartz cement and V = void or pore space.

quartz-healed microfractures were often overlooked because authigenic quartz grows in optical continuity with the detrital quartz grain precluding observation by transmitted light microscopy. In some cases, intragranular microfractures correspond to planes of fluid inclusions that are visible in transmitted plane light (Boiron et al. 1992; Groshong 1988; Laubach 1988a; Laubach 1988b). But, even in optimal cases, fluid inclusion planes provide only limited information about the fractures. Conventional light microscope CL has a too-low magnification range for ready observations of microfractures. Data on fracture presence, fracture morphology, and inter- and intragranular quartz cement distribution is more fully available from CL images. SEI imaging is used to discern voids (inter- and intragranular porosity).

CL imaging performed on a scanning electron microscope (SEM) also has greater utility than conventional light microscope-mounted CL because greater vacuum stability allows longer observing times, images are more readily captured, higher magnifications are possible, digital image acquisition can be done with greater speed, and the automated SEM system facilitates other functions such as sample rotation, measurement tools, and acquisition of other image types (e.g., backscattered electron and secondary electron images). In contrast to panchromatic CL images, scanned CL RGB color images provide even greater detail and information about the internal structure of the inherently less-luminescent authigenic quartz, including crosscutting relations between fractures and the relative timing of grain fracturing with respect to quartz overgrowth formation (Laubach et al., 2003). Approximately a quarter of the images examined in this study were acquired in color.

INTRODUCTION TO COMPACTION

Sediment compaction is a process by which bulk rock volume is reduced under a load. The conventional notion is that mechanical compaction predominates at shallow to intermediate depths (< 3 km) and involves the rearrangement (reorientation and repacking) of grains, localized brittle fracturing of rigid grains, and ductile deformation of soft grains (Füchtbauer, 1957; Berner, 1980; Wilson and Stanton, 1994; Bloch and Helmold, 1995; Paxton et al., 2002). This scheme generally dismisses the contribution of deeper mechanical compaction. Mechanical compaction by brittle deformation is a process often underestimated or ignored because many resulting fractures are sealed with quartz cement and therefore are undetectable unless observed with CL imaging (Houseknecht, 1991; Milliken, 1994; Wilson and Stanton, 1994; Dickinson and Milliken, 1995). Experimental work (e.g., Lade et al., 1996; Chuhan et al., 2002) and empirical data presented here show that brittle deformation plays an important role in burial compaction of sandstones across a wide range of depths in the subsurface (< 1000 m to > 5000 m).

Compaction and cementation are the two causes of porosity reduction of sandstones (e.g., Lundegard, 1992). From a reservoir quality point of view, compaction is a largely irreversible process that decreases intergranular space through increased packing of the solid grain volume, whereas cementation can be a reversible process because some cement phases may, dissolve during burial. Assessing the relative importance of compaction versus cementation as porosity reducing mechanisms has been a focus of many studies (e.g., Lundegard, 1992; Wilson and Stanton, 1994; Ehrenberg, 1995; Dutton, 1997; Stone and Siever, 1997; Paxton et al., 2002). Chapter 2 reviews the methods used to quantify brittle deformation and presents data on the increase in grain fracturing during progressive burial in two sandstone units of contrasting composition that have experienced different burial histories. The ultimate goal is to estimate, through a quantitative technique, the role of brittle grain deformation in mechanical compaction and to assess its implications for porosity and permeability prediction in clastic reservoirs

COMPACTION REVIEW

To evaluate the total effect of sediment compaction, porosity is commonly plotted against maximum burial depth. Porosity-depth trends from empirical observations of natural sandstone generally indicate an exponential porosity decrease with increasing burial (Pryor, 1973; McBride et al., 1991), which is largely in agreement with experimental models (Baldwin and Butler, 1985; Ramm, 1992). Although anomalously high porosities do exist at great depths, their possible causes will not be discussed here (see Aase et al., 1996; Bloch et al., 2002). The varying rates of porosity decrease in sandstones have been modeled and show a dependence on thermal maturity (Schmoker and Gautier, 1988) and first-order dependence on the age of the sandstone, detrital quartz content, maximum burial depth and sorting (Scherer, 1987).

Porosity-depth trends are, of course, strongly influenced by both cementation and compaction. Houseknecht (1987) was the first to propose equations to describe the relative effects of compaction versus cementation in modifying intergranular volume (IGV), where the percentage of original porosity destroyed by compaction:

$$= \frac{40 - IGV}{40} \times 100 \qquad (1)$$

and the percentage of original porosity destroyed by cementation:

$$= \frac{cement}{40} \times 100 \qquad (2)$$

Values in the equations are given in rock volume percentage and 40 represents the percentage of depositional porosity assumed.

The data (cement volume and IGV volume) entered into the equations are collected by thin section modal analysis. Ehrenberg (1989; 1995), Pate (1989), and Lundegard (1992) subsequently refined the equations, incorporating calculations that consider the progressive bulk volume loss during burial. Obtained values suggest that mechanical compaction and chemical compaction, rather than cementation, are the dominant processes in porosity reduction in most sandstones (Lundegard 1992) and even more influential than predicted by Houseknecht (1987). However, in most deeply buried rigid grain sandstones fluid flow properties are more strongly influenced by cementation than by compaction. Errors associated with petrographic modal analysis of thin sections are discussed by Ehrenberg (1995); accuracy can be improved by choosing clear petrographic categories for IGV calculation, a consistent and accurate method for distinguishing authigenic from detrital quartz (e.g., cathodoluminescence if dust rims are not well-developed) and a realistic value for the initial porosity (40 – 45% volume). Also, my results indicate that ignoring sealed quartz grain fractures results in an overestimate of the effect of compaction and an underestimate of quartz cementation.

The amount of mechanical compaction is greatly influenced by the percentage and types of ductile versus rigid grains. Brittle grains, such as feldspar and quartz, fracture whereas ductile lithics deform plastically. In general, sedimentary lithics are more ductile than metamorphic lithics, and volcanic lithics can become very ductile when altered to phyllosilicates (Pittman and Larese, 1991). The presence of ductile grains results in greater pore volume reduction during compaction, as demonstrated both experimentally (Pittman and Larese, 1991; Rittenhouse 1971) and empirically (Bloch, 1991; Lundegard, 1992). Worden at al. (2000) discusses how the porosity decline with depth in Oligocene and Miocene sandstones of the South China Sea is mainly governed by the presence of ductile-rich lithics. Milliken (2001) reports similar findings for porous sandstones in the southern Appalachians.

The relative timing of compaction versus cementation is also important. Compaction experiments using glass beads show that under the same load, cemented beads stay intact whereas uncemented grains undergo intensive crushing (e.g., Gallagher et al., 1974; Henzu and Dvorkin, 1994; Wong, 1990; Zhang et al., 1990). Compaction experiments by Pittman and Larese (1991) show that an early episode of cementation could significantly retard compaction, as observed in the Green River basin by Stone and Siever (1997). Sandstones with little or no cement content may undergo extensive mechanical compaction (Fisher et al., 1999; Wilson and McBride, 1988).

Theoretical models that describe micro-scale grain boundary geometries illustrate how mechanical and chemical processes may be genetically linked during compaction. Microfracturing and subsequent cementation of microfractures result in apparent grain volume expansion, whereas pressure solution results in actual grain volume reduction. The Gratz-grain-boundary model (Gratz, 1991), supported by empirical experiments (den Brok and Spiers, 1991) and CL observations (Milliken and Laubach, 2000), suggests that grain microfractures located closest to dissolving grain boundaries enhance the plumbing system in the grain boundary region, resulting in an increase in the pressure solution strain rate. Compaction experiments performed on sand exhibit indented contacts and fractures with associated dissolution features and sealed microfractures in indented quartz grains (Elias and Hajash, 1992). Onasch (1994) also found microfracturing associated with pressure solution in the Tuscarora Sandstone. These findings point to an intriguing association between microfracturing and pressure solution that may develop in deeper reservoirs that has previously gone unrecognized.

Chapter 2: Quantifying Brittle Deformation With Respect to Burial Compaction

Brittle deformation, together with grain rearrangement and ductile grain deformation, is a key mechanism of compaction in sandstones. Quartz cementation, by virtue of its impact on sandstone mechanical properties, is expected to affect the compaction progress by these various mechanisms. Sandstone samples of different ages and compositions, taken from two basins with contrasting burial histories, are used to quantify the relationship between brittle deformation and quartz cementation in the context of burial compaction. Depth trends of increasing deformation by microfracturing are observed in both the lithic-rich Frio Formation from the Gulf of Mexico basin and in the quartz-rich Mount Simon Formation from the Illinois Basin. The two formations contrast in terms of the observed rate of grain fracture increase with depth. A larger number of quartz grains in the Mount Simon Formation (using calculated maximum burial depths) undergo fracturing at shallow burial (< 2 km) compared to the Frio Formation, whereas at intermediate to deep depths of burial (> 3 km) a larger number of quartz grains are fractured in the Frio sandstones.

Cathodoluminescence (CL) imaging conducted on an SEM shows that grain fracturing and subsequent cementation of fractures by quartz can occur primarily before and sometimes during normal quartz overgrowth precipitation, although fracturing is generally concurrent with cementation. The intensity of brittle deformation for a single fractured grain is independent of depth, as illustrated by plotting the ratio of the number of particles in fractured grains versus depth (r^2= 0.21 for Frio and 0.03 for Mount Simon), suggesting that, once fractured, grains do not tend to become the locus of subsequent fracturing.

Apparent fracture apertures in the Frio grains are slightly wider (average 5 µm) than in Mount Simon grains (average measurable aperture width ~ 4 µm). Quartz grains in the Frio have a variety of fracture morphologies, including wedge-shaped apertures, intense comminution at grain contacts, and grains with exploded fabrics. Apparent fracture apertures in Mount Simon grains are thinner and transect grains as straight, uniform traces. Differences in fracture intensity and pattern are partially attributed to the fact that cementation in the Frio began at greater depth than cementation in the Mount Simon. Other controls could include sorting and IGV, where IGV's are lower for the Mount Simon compared to the Frio (mainly by the influence of pressure solution in the Mount Simon which is perhaps controlled by the temporal differenced between the two sandstones).

Combining information on the degree of brittle deformation and the amount of quartz cement localized within microfractures (here referred to as C_f or volume of intragranular cement) allows calculation of the amount that brittle deformation influences cementation. In the Frio Formation, 0.12 to 8.37% of porosity loss due to intragranular cementaiton can be attributed to brittle deformation, whereas the values for the Mount Simon Formation lie between 0.25 to 2.16%. The larger values within both formations are affiliated with deeper samples in which a majority of grains manifest fracturing.

CASE STUDIES

The Oligocene Frio Formation in the Gulf of Mexico basin and the Cambrian Mount Simon Formation in the Illinois basin are used as contrasting case studies. The purpose of studying two sandstones units that have undergone extensive burial compaction is two fold: (1) to identify fracture intensity in sandstones from different basins and that therefore are influenced by different burial histories (passive margin versus intracratonic basin) (Fig. 4) and (2) to compare the fracture depth trends in sandstones of different framework compositions (Fig. 5) (feldspathic litharenites versus quartzarenites) across a broad depth range. This information will be valuable in identifying the primary controls and influences in fracture development with depth. By virtue of the tectonic settings, neither sandstone has been subjected to significant horizontal compressive stresses. An additional factor is that samples of the Frio and Mount Simon Formations are readily available over a wide range of depths.

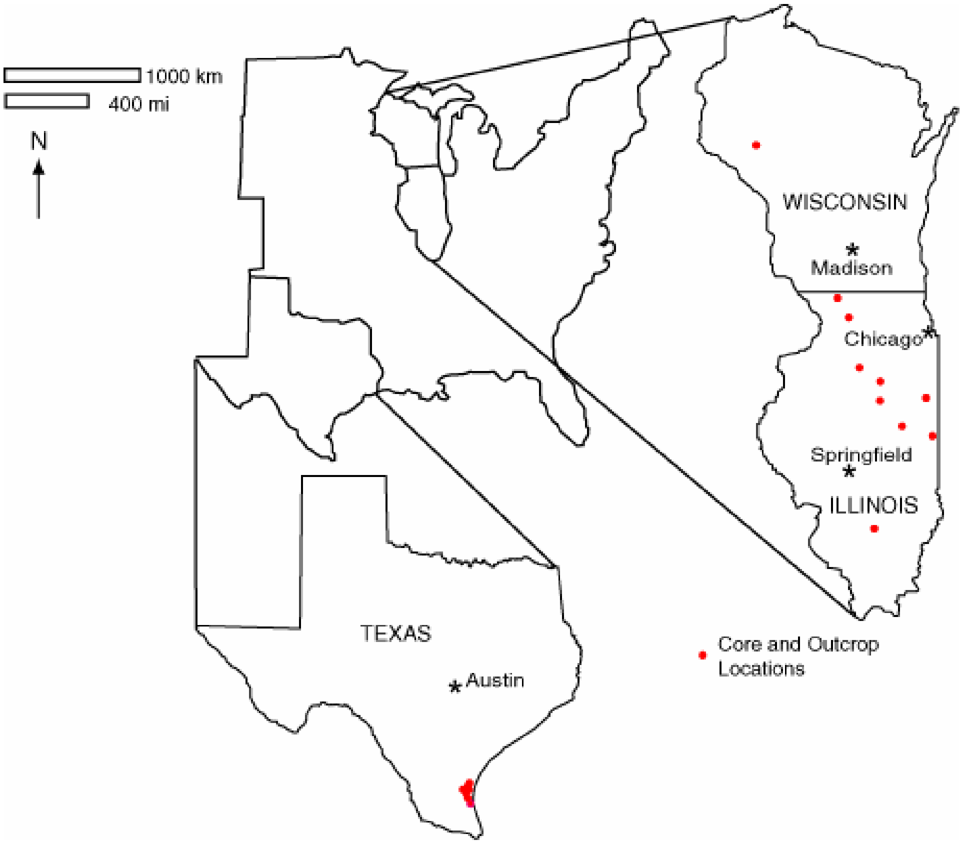

Figure 4. Map showing sample locations. The Frio Formation was sampled in core from various depths in the South Texas Gulf coast, whereas samples from the Mount Simon Formation are from core and outcrop localities within the Illinois basin.

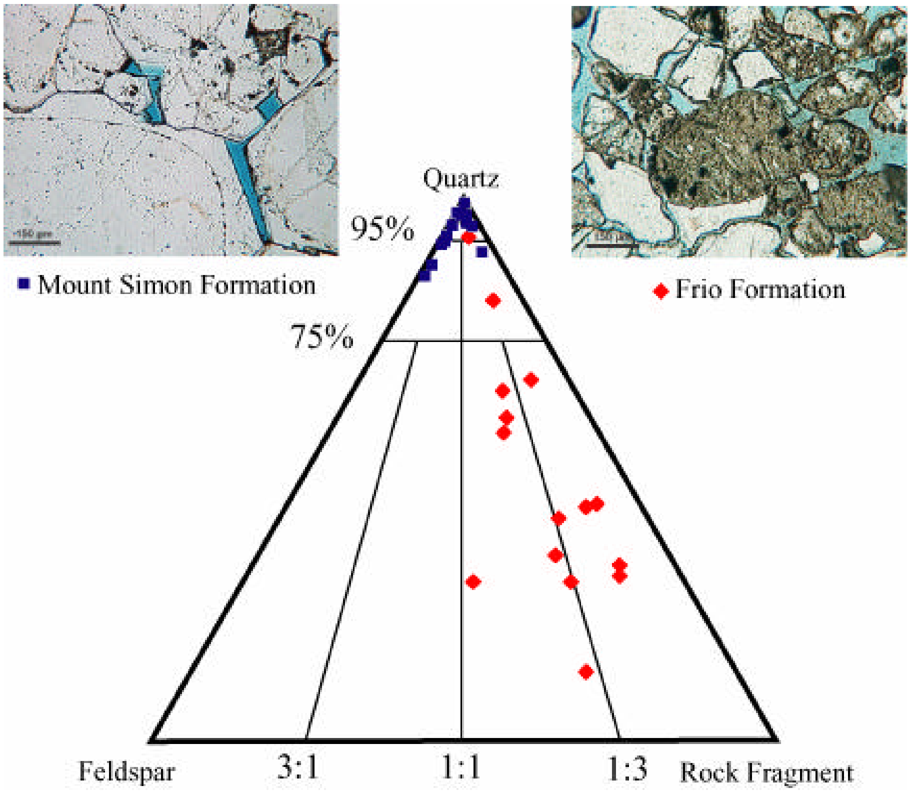

Figure 5. Ternary plot of sandstone sample compositions according to Folk's (1980) classification scheme. Plot shows the variation of sandstone composition between the Mount Simon and Frio Formations. Average compositions of Frio and Mount Simon Formations are feldspathic litharenite and quartzarenite, respectively.

Frio Formation

The Frio Formation was deposited as a regional progradational wedge along the northern margin of the Gulf Coast during the Tertiary. The Frio is characterized by rapid subsidence in areas of sediment loading. In the Rio Grande Embayment, it is composed of undercompacted prodelta and slope muds (Galloway et al., 1982). The Frio Formation is underlain by the Oligocene Vicksburg Formation and downdip it is regionally overlain by the Anahuac Shale, a transgressive marine shale wedge (Galloway et al., 1982). Up-dip, the Frio Formation is a low sinuosity bed-load fluvial system and down-dip it grades into fluvial to deltaic, barrier and strand-plain deposits (Galloway, 1977).

The Oligocene Frio Formation sandstone is ideal for studying brittle deformation during burial compaction because over 3500 m of sediment was rapidly deposited via subsidence and growth faulting during the Middle to Late Oligocene and Early Miocene (Galloway et al., 1982). Moreover, a tectonic overprint is absent, current depths are maximum depths, and growth faults impose a wide range of burial depths and temperatures on materials of relatively uniform initial composition. The predominantly lithic-rich sands of the Frio of the lower Gulf Coast were supplied by the ancient Rio Grande draining the volcanic areas of west Texas and northern Mexico (Loucks et al., 1984). Frio sandstones are moderately sorted, fine- to coarse-grained and range from feldspathic litharenites to sublitharenites (Fig. 5). Cement types and amounts vary with depth. The dominant cement type for all depths is calcite. Zeolite cement is abundant at shallow depths (maximum = 10%), associated with volcanic-derived lithics, whereas quartz cement generally increases with increasing depth (Land, 1984). Kaolinite, iron oxide, chalcedony, and K-feldspar cement are present in minor amounts over a wide depth range. For point counts refer to Appendix A for Frio Formation and Appendix B for Mount Simon Formation.

Mount Simon Formation

The Upper Cambrian Mt. Simon Formation Sandstone lies unconformably over Precambrian basement in the Illinois Basin and crops out in west-central Wisconsin. The siliciclastic sediments of the Mount Simon were derived from subaerially exposed Precambrian shield areas in the northeast, in particular the Wisconsin Arch (Runkel et al., 1998). The Mount Simon sandstone was deposited in nearshore tidal flat and tidal channel environments (Runkel et al., 1998). It is medium-grained, moderately-well to well-sorted, quartz cemented sandstone, that contains minor amounts of pyrite, calcite, iron oxide, and K-feldspar cements. Quartz cement ranges from 0.5 to 17 %.

The Mount Simon Formation has a more complex burial history than the Frio Formation and its depositional history is the subject of ongoing research. The Illinois Basin is an intracratonic basin in which 6000 m of sediments accumulated during the Paleozoic. During the Late Cambrian, the time of Mt. Simon deposition, the tectonic setting of the proto-Illinois Basin was governed by thermal subsidence lasting until Early Mississippian time (Rowan et al., 2002). A second subsidence episode (Middle Mississippian through Early Permian) was caused by flexure in response to the Alleghanian-Hercynian orogeny (Klein and Hsui, 1987), which led to pronounced downwarping in the more southerly parts of the basin leading to thicker sediment accumulation (Sargant, 1991).

Other tectonic events that effected Mount Simon deposition included periodic uplift on bounding arches (e.g., Wisconsin, Kankawee, and Pascola Arches) that separate the Michigan Basin from the Illinois Basin. Coal rank and 2D numerical modeling of burial history using coal vitrinite reflectance and biomarkers suggest that maximum burial was attained during the Permian, approximately 1000–1500 m deeper than present (Damberger et al., 1999; Rowan et al., 2002). During the Quaternary, glacial outwash was deposited over most of the Illinois Basin. Amounts of uplift and erosion in the Illinois Basin vary, with up to 2000 m in the south and approximately 300 m in the north (Hoholick et al., 1984). Other estimates of burial depth provided by Wilson and Sibley (1978) indicate nearly 900 m of erosion in the northerly area. Maximum burial depths of samples for this study were calculated from burial curves modeled by Rowan and others (2002) using fluid inclusion and vitrinite reflectance data throughout the basin. This hybrid model combines burial (considered the most influential factor for temperature in past models) and advective heat transport from a short period of magmatism, allowing both vitrinite reflectance and fluid inclusion data to match model results. Figure 6 shows the burial depth versus time plot by Rowan et al. (2002).

SAMPLE ACQUISITION

Core samples of the Mount Simon Formation were collected from nine locations in Illinois (Fig. 4). Core depths range from 355 to 2581 m. Outcrop samples were collected in Eau Claire, Wisconsin, the type section of the Mount Simon Formation (Ostrom, 1987).

Samples of the Frio Formation used in this report are a subset of a collection of Frio samples that has been extensively used for diagenesis studies at The University of Texas at Austin (e.g., Milliken et al. 1989). Samples were taken from wells located in South Texas (Fig. 4) at depths varying from 982 to 5229 m.

Data Acquisition

Thirty samples of the Mount Simon Formation and 17 samples from the Frio Formation were used in this study. Photomicrographs and measurements were collected on two SEM's with cathodoluminescence detectors: 1) a Phillips SEM XL30 with a Gatan Mono CL2 detector located at the Bureau of Economic

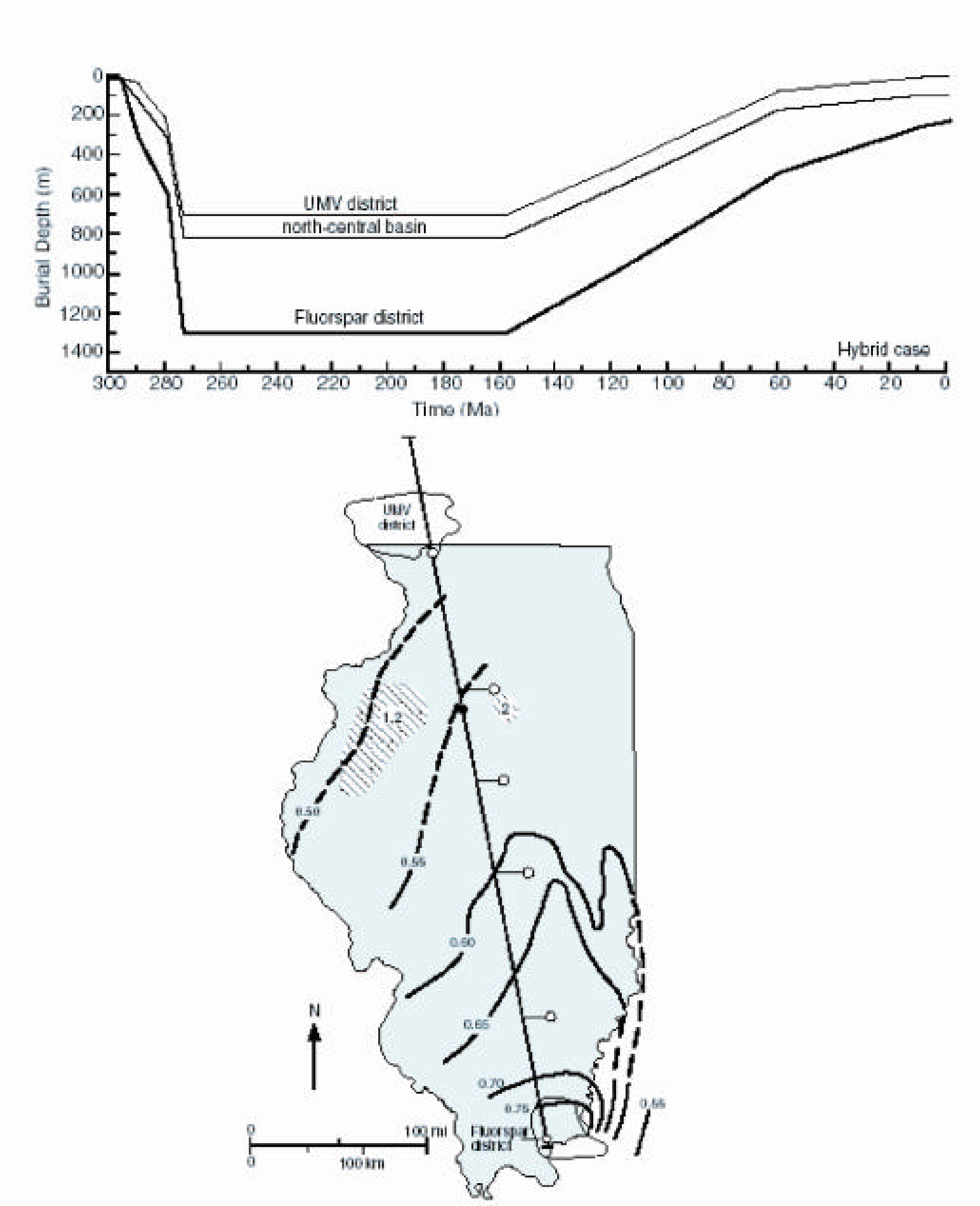

Figure 6. Burial history curves for the Fluorspar district at the Illinois basin's southern margin, the Upper Mississippi Valley zinc district at the basin's northern margin, and a north central location calculated by Rowan et al. (2002). The map shows the location of these sites. Vitrinite reflectance contours are shown for the Pennsylvanian Herrin (No. 6) Coal. Modified from Rowan et al. (2002).

Geology and 2) a Phillips ESEM XL30 with a PanaCL detector with RGB color filters located at the Department of Geological Sciences at the University of Texas at Austin.

One hundred randomly selected quartz grains (regardless of fracture status) were point counted for each sample, collecting the following parameters. Grain size was determined by measuring the long axis of each detrital grain (excluding quartz overgrowth thickness). The arithmetic mean of the size measurements was used to determine average quartz grain size in each thin section. The frequency of fractured grains (the number per 100 grains), the number of pieces of cemented broken grains (fragments per fractured grain), and their reduced particles sizes were also quantified. A maximum of up to 25 fractures were counted per grain because above this number, fracture detection becomes ambiguous. When a large number of fractures are present, they intersect and are closely spaced, making discrimination of individual fractures difficult, and therefore, an arbitrary cut off of 25 fractures was used. The arithmetic mean was used to determine the average number of pieces from individual fractured grains. Refer to Appendix C for comprehensive fracture data collected for Frio and Mount Simon Formations.

RESULTS

Overall, quartz grains in the Frio Formation are more fractured than grains in the Mount Simon Formation (Table 2). Differences in the geometries and apertures of the fractures are also observed between the two formations (Figure 7; Student's t-test shows that average apparent apertures of fractures in the two formations are different at the 99% confidence level). This may be an artifact of having studied shallower samples from the Mount Simon than from the Frio (7E). Fractures in the Frio grains are wider (Fig. 7A and C). Fractures in grains from the Mount Simon Formation have smaller apertures, exhibit fewer wedge-like features, and have straighter traces across grains (Fig. 7B and D). The average number of fractures per grain (1 x 3 cm thin section) in the Frio Formation ranges from 2 to 7 (with an overall average equal to 4.4) whereas, fractured grains in the Mount Simon samples range from 3 to 5 fractures per grain (with an overall average of 3.5). The reason for Frio grains exhibiting larger number of fractures is that more grains in the Frio Formation become crushed at grain-grain contacts and some whole grains appear exploded such that the whole grain is effectively inflated as seen in light microscopy (Fig. 7C). Wedge-shaped fractures with maximum aperture at grain-grain contacts and spalled fractures, radiating at grain-grain contacts, are common in the Frio Formation. These fracture morphologies are also present in fractured Mount Simon samples, however, the majority of

Table 2. Frio and Mount Simon Formation fracture characteristics[1].

Sample #	**Sample Depth**	**Max. # of Fractures Per Grain**	**Avg. # of Fractures Per Grain**	**Max. Aperture[2] Per Grain**	**Avg. Aperture[2] Per Grain**	
Frio Formation						
3223	982	6	2.3	12.7	5	
4908	1496	7	2.7	9.2	4	
6105	1861	>25	4.1	19.9	4	
8901	2716	>25	4.3	25.2	5	
9001	2744	>25	4.2	15.4	5	
9120	2963	>25	6.9	17.9	6	
9547	2910	>25	3.9	28.7	6	
9710	2960	>25	3.5	16.1	4	
9743	2970	>25	5.5	25.8	5	
10169	3100	15	4.1	31.7	6	
13833	4216	17	3.5	17.5	5	
15617	4760	>25	6.3	23.2	6	
15620	4761	>25	4.3	22.8	5	
15640	4767	>25	5.3	21.4	5	
17154	5229	>25	5.6	26.5	5	
			4.4	**20.9**	**5**	**Avgs**
Mount Simon Formation						
71901-1	1016	9	4.0	13.8	5	
71901-2	1016	6	2.9	9.2	3	
1164	1162	10	3.7	16.0	5	
1277	1196	10	3.2	8.8	3	
1288	1200	9	3.2	5.9	2	
2019	1381	8	3.1	14.0	4	
2166	1426	13	3.8	16.7	5	
2384	1586	12	3.5	10.3	4	
2480	1615	7	2.9	15.0	4	
2562	1640	7	3.1	40.8	7	
3134.5	1814	12	3.5	15.7	4	
3177	1734	14	3.4	20.1	3	
3224	1842	7	3.1	10.4	3	
3581.5	1992	10	3.6	14.3	3	
3619	2003	14	3.9	15.7	3	
3793	1922	10	3.1	7.2	2	
4038	2152	14	3.5	4.3	2	
4119	2176	10	3.0	11.2	4	

Table 2 Continued.

Mt Simon Formation Continued

Sample #	Sample Depth	Max. # of Fractures Per Grain	Avg. # of Fractures Per Grain	Max. Aperture[2] Per Grain	Avg. Aperture[2] Per Grain	
4226	2209	21	4.0	13.3	3	
4469	2201	11	3.3	8.1	2	
4477	2203	10	4.1	13.9	6	
4720	2277	6	2.9	26.3	3	
5404	2589	10	4.1	10.3	2	
6154	2817	16	4.5	30.8	7	
6235	2842	15	4.0	20.4	6	
6241	2844	9	3.3	11.3	4	
6497	2922	12	3.3	14.3	5	
6500	2923	11	3.4	11.9	4	
8466	3646	10	3.5	21.7	5	
8468	3647	15	3.2	15.3	4	
			3.5	**14.9**	**4**	**Avgs**
			3.6	**2.7**	**2.7**	**t values**

[1] Data only for fractured grains, among 100 counted, with at least one fracture.

[2] Apparent apertures. Minimum detectable aperture is approximately 1 micron.

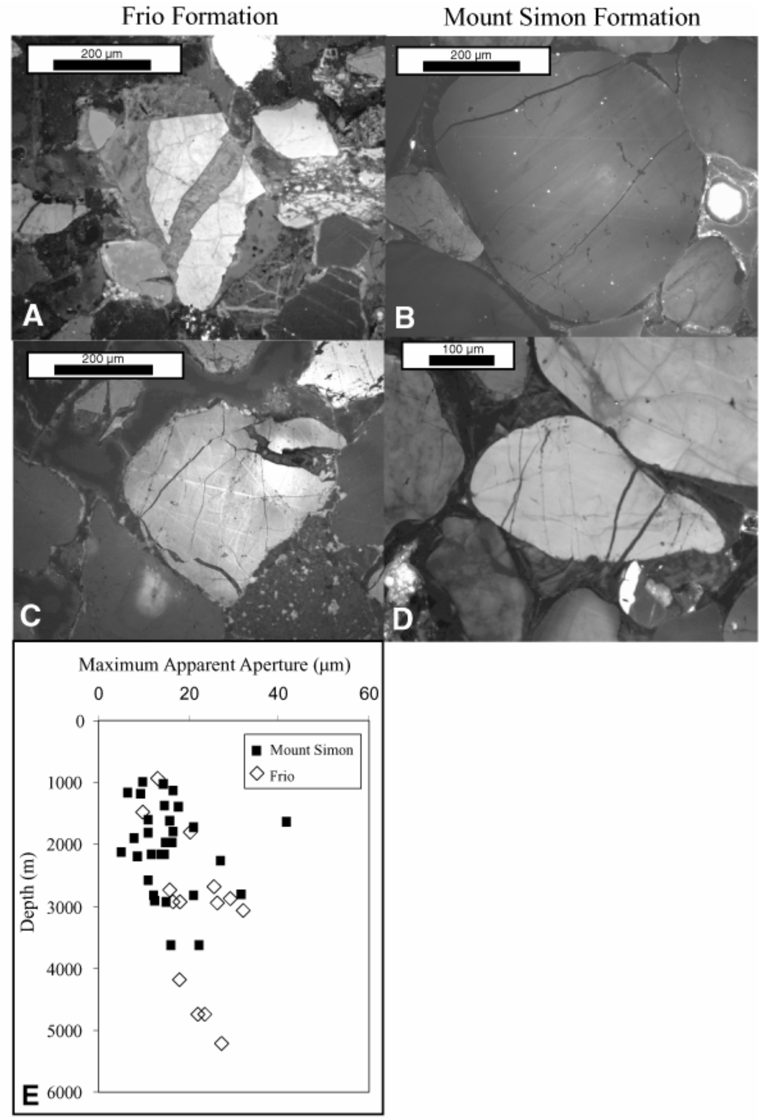

Figure 7. Comparison of fracture apertures between Frio Formation and Mount Simon Formation. Generally, fracture apertures are much wider in the Frio Formation (A and C) than in the Mount Simon Formation (B and D). Also, fractures in the Frio samples show a greater abundance of wedge-like morphologies (C), with wide apertures closest to grain contacts. Fractures in the Mount Simon samples have less-wedge-like morphologies and have straight, thin traces across grains (D). E) Maximum apparent apertures are overall wider in the Frio quartz grains than in the Mount Simon quartz grains.

fractures in the Mount Simon have thin apertures and transect the grain as straight traces of apparent uniform aperture.

Generally, the average apparent fracture aperture for fractured quartz grains in the Frio Formation is larger than in the Mount Simon Formation. The average apertures range from 3.6 µm to 6.5 µm and 1.8 µm to 6.9 µm in Frio and Mount Simon Formation respectively. The overall average for apertures are 5.2 µm for the Frio and 3.9 µm for the Mount Simon. Average apparent aperture in the Mount Simon is a maximum value as a result of numerous fractures below the detection size for measurable fractures. One micron is the limit of apparent fracture aperture detection, due to the resolution capability of the SEM in CL mode.

Degree of Fracturing With Maximum Burial Depth

A trend in the percentage of fractured quartz grains with increasing depth is observed in both the Frio and Mount Simon Formations (Fig. 8A). Although the trends are similar, T-test demonstrates that they significantly different. Above 2 km (depth corrected as previously described), a larger percentage of quartz grains in the Mount Simon sandstones are fractured, whereas below 2 km, quartz grains in the Frio sandstone are more fractured. The trend shows lower increase in percentage of fractured quartz grains for data from the Mount Simon Formation than the Frio Formation. Single fractured grains produce numerous fragments,

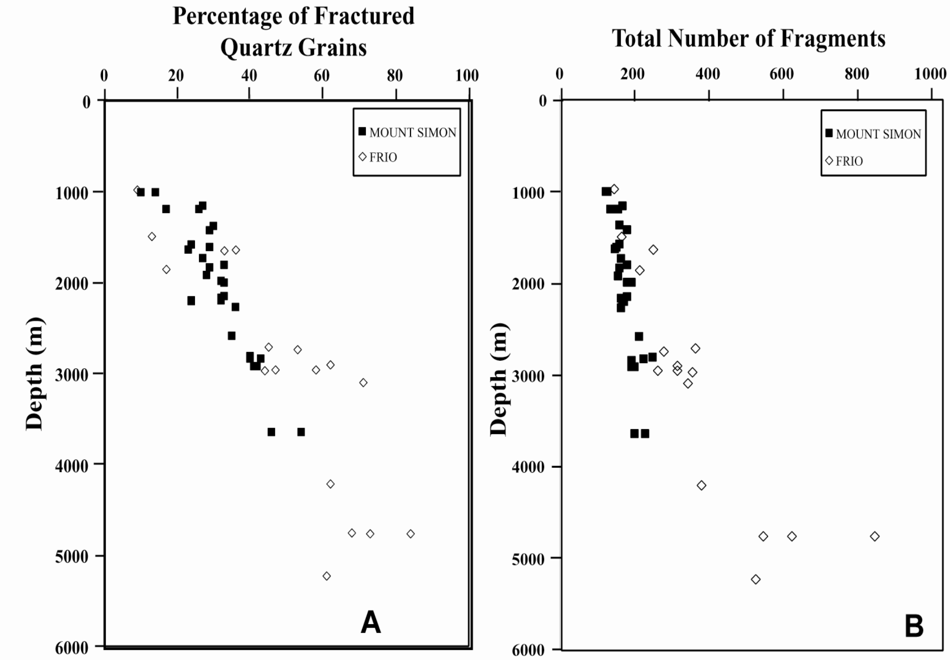

Figure 8. A) The x axis represents the percentage of fractured quartz grains. The percentage of fractured quartz grains increases with depth for both the Frio and Mount Simon Formations. T-test result (3.3) demonstrates a significant difference between Frio and Mount Simon trends. B) The x axis represents the total number of fragments for each sample, taking into consideration individual pieces of a once whole grains and unfractured grains (one fragment). Grain fracturing results in an increase in the number of fragments (total) among the grains counted (fractured + unfractured).

influencing the particle size distribution. For each sample, the number of fragments produced by brittle deformation of each quartz grain is summed per sample. The number of fragments per sample increases with depth for both formations (Fig. 8B).

Maximum burial depths for the Mount Simon samples were calculated using the hybrid model presented by Rowan et al. (2002). Maximum burial depths were also calculated using the burial only model and present depths (Rowan et al., 2002). When comparing the percentage of fractured grains versus depth, it is apparent that the hybrid model developed by Rowan et al. (2002) agrees best with the Frio Formation trend (Fig. 9).

Grain Size Relationship

The average number of fragments derived from fractured grains versus average depositional grain size reveals contrasting trends for fracture dependency on grain size in the two formations. Regression lines were constructed with the *y*-axis (average grain size) as the dependent variable. Data for the Frio Formation show a positive slope (r^2=0.58) indicating that samples containing larger grains, on average, are more intensely fractured (Fig. 10). However, the data for the Mount Simon show that the number of fragments is independent of initial grain size. An artifact of the positive trend for the Frio is that the deeper samples are more coarse grained, and grains size has been demonstrated to control fracturing

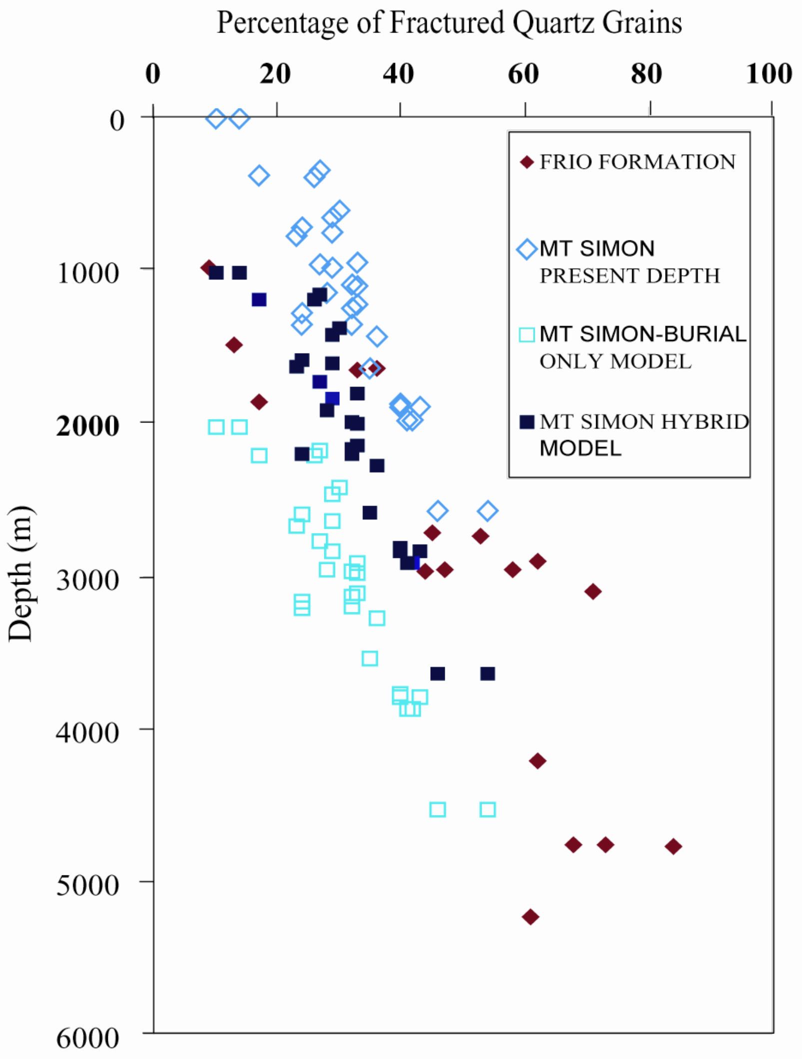

Figure 9. Percentage of fractured quartz grains versus depth for Frio and Mount Simon formations. Maximum depths for the Mount Simon Formation samples were calculated using the hybrid model of Rowan et al. (2002). Using the hybrid model to calculate maximum burial depth of the Mount Simon yields a trend that most closely matches the trend of the Frio Formation.

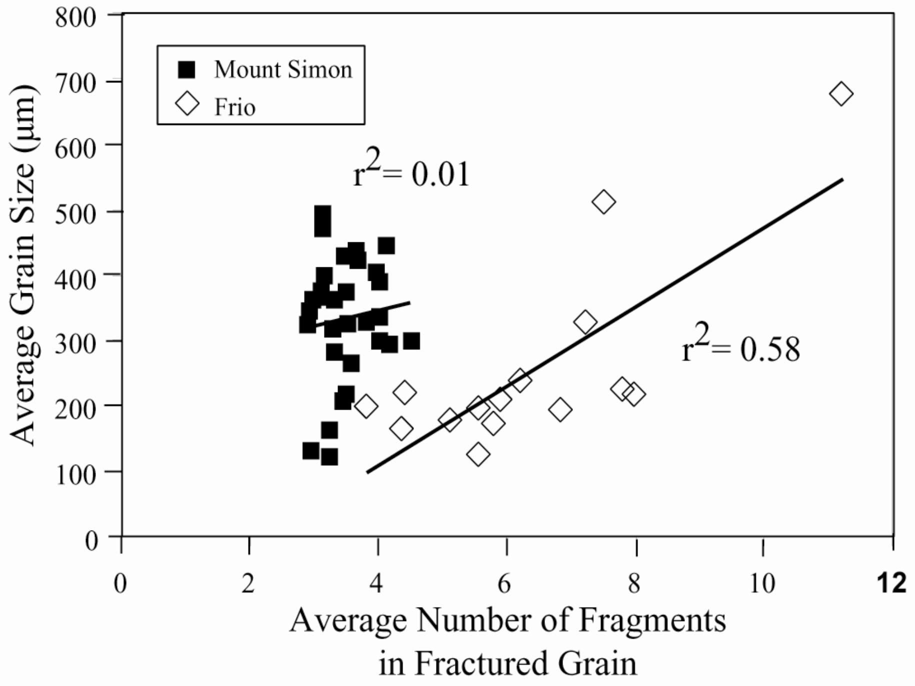

Figure 10. Influence of grain size in brittle deformation. Regression lines are constructed with average grain size on the y axis as the dependent variable. In the Frio Formation, the average number of fragments in a fractured grain is greater for larger grains than for smaller ones. Such a trend is lacking in the Mount Simon Formation.

(see Table 1). However, categorizing samples by their grain size, sample sets for the same grain size still show an increase in grain fracturing with depth suggesting that the trend of percentage of fractured quartz grains with depth is independent of grain size (Fig. 11).

Degree of Fracturing in a Fractured Grain

The ratio of the number of fragments derived from fractured grains to the percent of all grains that were in each sample is plotted versus depth to give an idea of fractured grains at shallow depth are more fractured than fractured grains at greater depth. The degree of fracturing of a single grain in both the Mount Simon and Frio Formations shows no significant depth correlation (Fig. 12). Instead, individual fractured grains at shallow depths exhibit the same number of fragments after fracturing as fractured grains at greater depth. Cross-cutting relationships visible in color CL images from the Frio and the Mount Simon show that most microfractures form before quartz overgrowth precipitation, and some during and after quartz overgrowth cementation (Fig. 13). Few grains show microfractures that crosscut one another (Fig. 13C, D, and E), suggesting that microfracturing can still occur during burial and quartz cementation but is not as common as pre-quartz cementation fracturing.

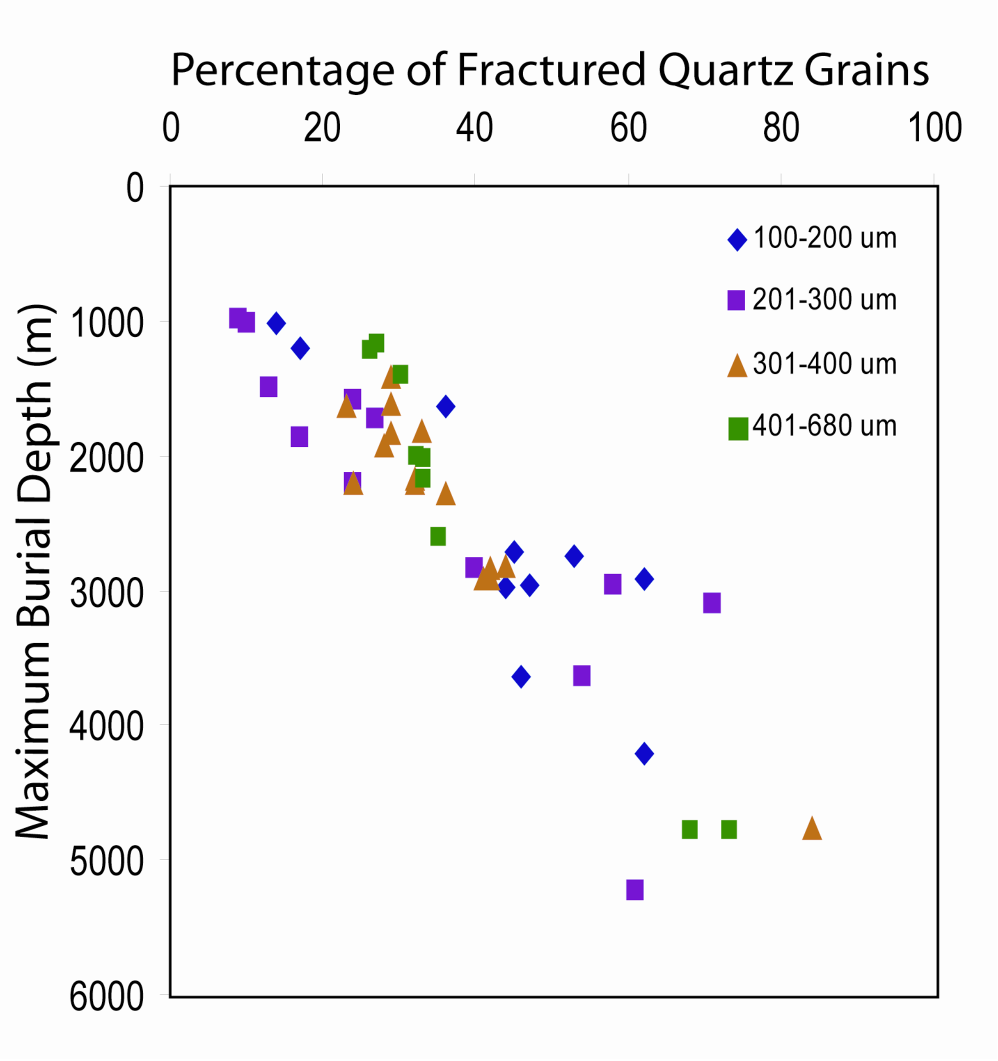

Figure 11. Percentage of fractured quartz grains versus maximum burial depth. Samples are categorizing samples by their grain size. Sample sets for the same grain size still show an increase in grain fracturing with depth suggesting that the trend of percentage of fractured quartz grains with depth is independent of grain size.

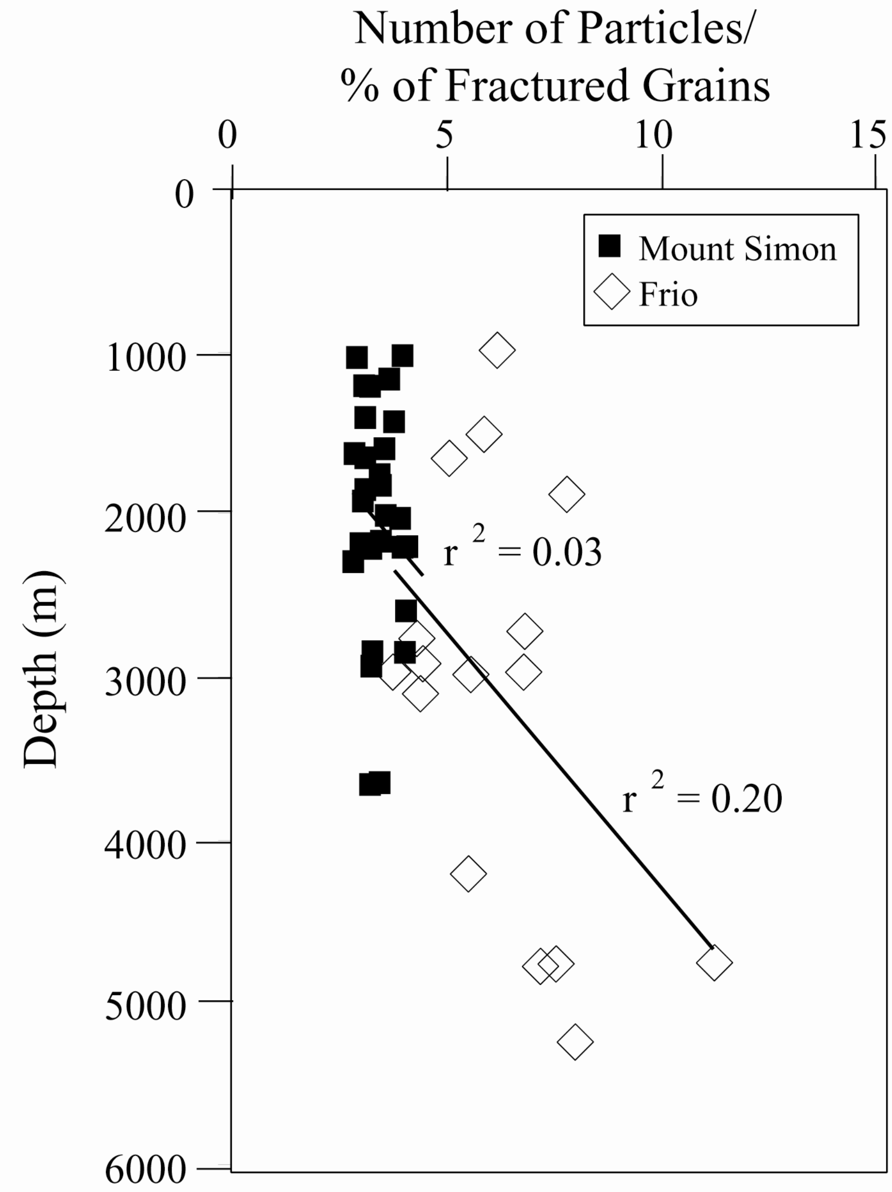

Figure 12. The extent of fragmentation of a fractured grain does not vary significantly throughout the studied depth ranges for the Frio and Mount Simon formations. Fractured grains at shallow depth have a degree of shattering similar to grains from greater depth, suggested by the low r^2 value, although the number of shattered grains increases with depth

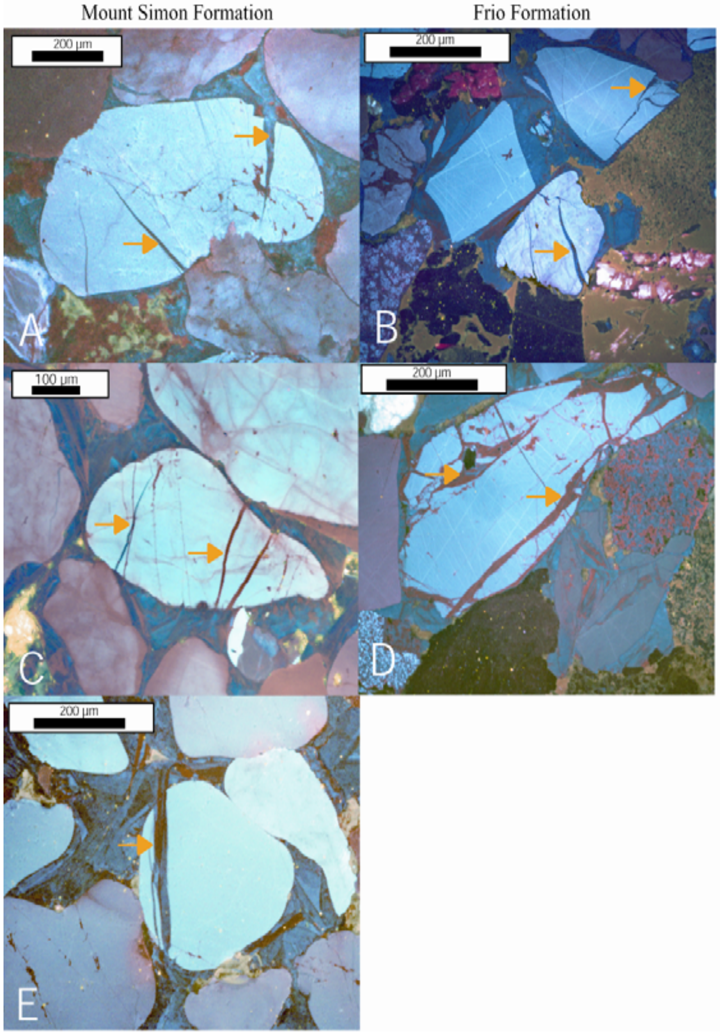

Figure 13. Wedge-shaped fractures in A and B contain quartz cement of the same generation as overgrowth cement (dark blue CL). The dark blue luminescent quartz represents the first episode of cementation (arrows). Images C, D, and E illustrate that at least two episodes of fracturing and cementation can be deciphered using CL color. In all three cases, fractures filled with dark blue and red luminescent quartz cement are observed. The dark blue cement represents the first episode, and the red cement is the second episode, because the red cement crosscuts the blue cement. This demonstrates that fracturing proceeds progressively during burial.

Quantitative Evaluation of Brittle Deformation

The opening-mode (extensional) microfractures in these samples cause expansion of grains into the adjacent primary pore space, creating intragranular pore space. Surface area of the quartz grain is thereby increased. The fresh surfaces created by fracturing are favored for quartz cement nucleation (e.g., Chuhan et al., 2002; Dunn, 1994; Reed and Laubach, 1996), and thus, intragranular pore space is prone to becoming filled with quartz cement. In conventional point counting methods under light microscopy, the cement within the intragranular fractures appears as grain volume, although it is in fact intragranular cement (Fig. 14). Accurate IGV determinations in samples containing fractured grains must include the amount of authigenic quartz within microfractures (intragranular cement).

To determine the average amount of intragranular cement, photomicrographs (SEM-CL) of thirty randomly selected fractured grains representing all depths sampled were obtained for each formation (Appendix D). Grain size can play a role in the degree of fracturing and subsequently can control the amount of authigenic quartz sequestered within the grain (Fig. 10). For this reason, a grid approximately 3-4 times smaller than the grain diameter was randomly applied to the grain image, yielding a measurement that is unbiased by grain size. Each grain was point counted (300- 400 grid intersections) to quantify

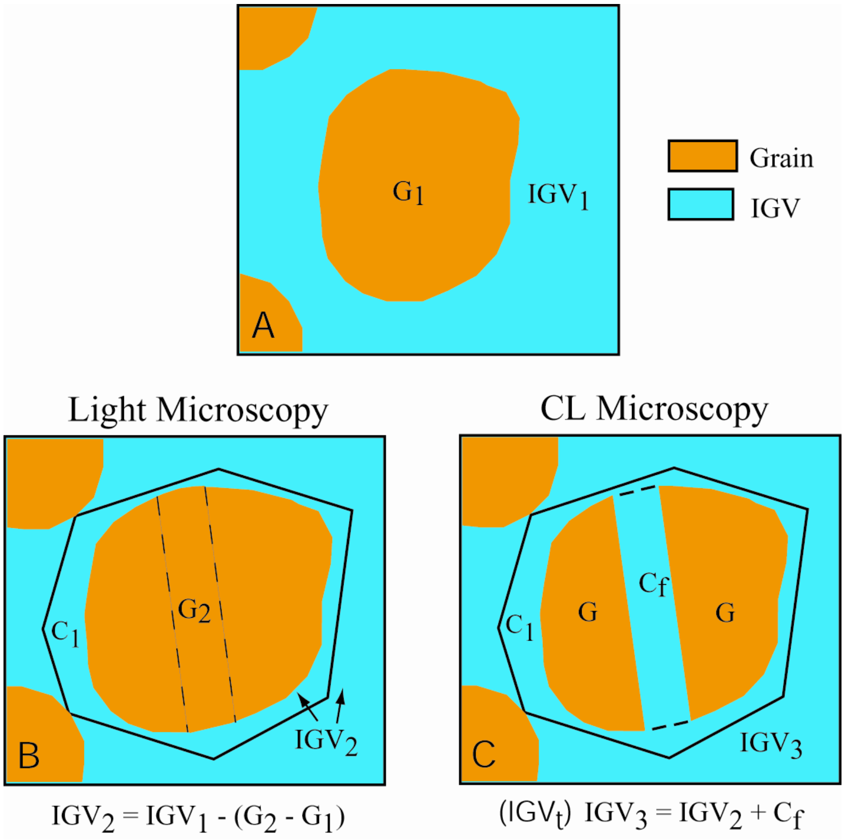

Figure 14. Simplified diagram explaining volume relationships that arise from grain fracturing. A) Grain before fracturing. IGV$_1$ = pore space. B, C) Grain after fracturing. Because the fracture is opening-mode, the grain volume, as seen in conventional light microscopy (B), has been inflated into space that was previously part of the IGV. The apparent grain volume has increased and the IGV has decreased by a volume equal to the volume in the fracture. Here IGV$_2$ = pore space + intergranular cement. The true grain volume (as seen in CL). C$_1$ represents the intergranular cement. (C) is equal to the grain volume (as seen in light microscopy) minus the volume of cement in the fracture (C$_f$). The true IGV is equal to the IGV (as measured in light microscopy) plus the C$_f$. Here IGV$_3$ = pore space + intergranular cement + cement in fracture.

the amount of intragranular cement localized within the fracture(s). Intersections were tabulated either as detrital or authigenic quartz. After each point-count set, the grid was reapplied to another random area of the grain by rotation of the image and an additional set of 300-400 points was tabulated (Fig. 15). A total of 5 samplings were averaged. The values for all thirty fractured grains were then averaged to obtain the overall value of intragranular quartz cement for each formation. A key point is that fractured grains at shallow depth are fragmented to the same degree as fractured grains at great depth (Figure 12, Tables 3 and 4), and therefore, application of this averaged single value across the entire sample set for the formation is valid.

The amount of intragranular cement within fractured grains ranges from 4.1% to 35% (average 15%) for the Frio Formation and 1.3 to 17 % (average 5.2%) for the Mount Simon Formation.

IGV

Intergranular volume (IGV), a measure of grain proximity, is conventionally calculated as the sum of primary porosity, intergranular cement, and detrital matrix (Paxton et al., 2002). All values for IGV are in represented in rock bulk volume. IGV in well-sorted sand is around 40% at the time of deposition (Graton and Fraser, 1935). Void space in sandstones is reduced during burial by compaction and cementation (volume of cement = C). These processes

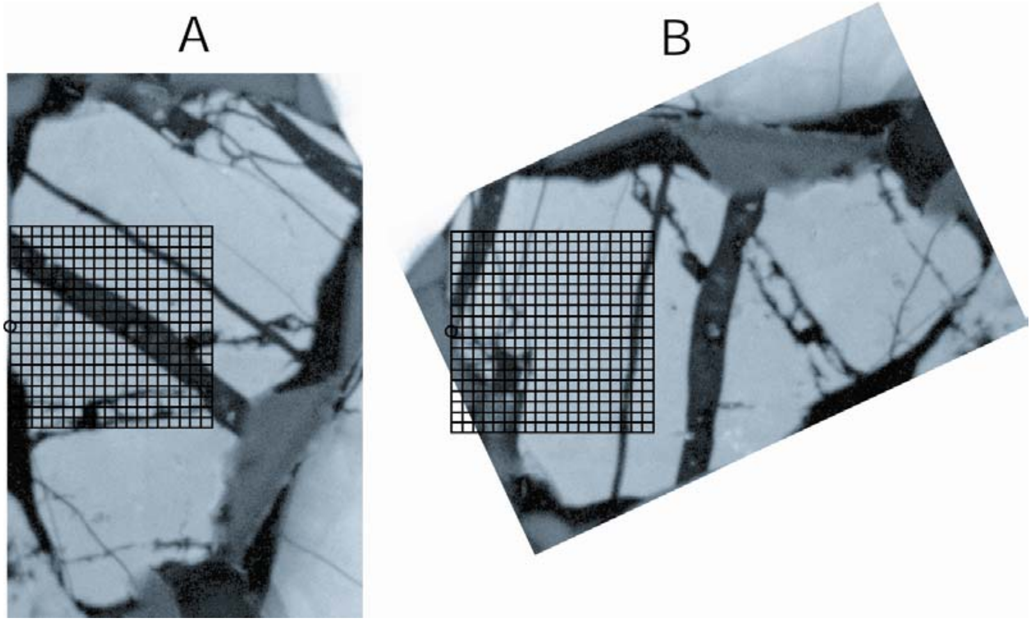

Figure 15. Example of grid pattern overlaid on randomly oriented grain. This technique is used to quantify the amount of intragranular quartz cement localized in grain fractures. The quantification is unbiased with respect to grain size because the grid is much smaller than the average grain (A). Each grain is randomly oriented by rotation followed by alignment of the grid to the left side of the grain (B). A) zero degree rotation and B) 65 degree rotation.

Table 3. Compilation of Frio Formation data used to calculate the amount of IGV destroyed by brittle deformation plus attendant quartz cementation and the amount that brittle deformation influences COPL and CEPL. Data for 15 of the 17 samples are shown. See text for explanation.

Sample #	**Sample Depth (m)**	**% Fractured Qtz Grains** A	**% Detrital Qtz** B	**% Fractured Grains** A x B = G_{frac}	**Rock Vol Const of Frac. Fill** G_{frac} x 0.15 = C_f	**% IGV Present** IGV_c	**% Total Cement** C	**% $COPL_1$**	**% $CEPL_1$**	**$Icomp_1$**
3233	982	9	8.82	0.79	0.12	28.31	13.69	16.31	11.46	0.59
4908	1496	13	22.86	2.97	0.44	20.85	6.53	24.19	4.95	0.83
6105	1861	17	20.54	3.49	0.52	31.93	31.68	11.85	27.92	0.30
8910	2716	45	29.55	13.30	1.97	30.81	30.81	13.28	26.72	0.33
9001	2744	53	35.48	18.81	2.78	15.14	6.95	29.30	4.91	0.86
9120	2963	47	44.28	20.81	3.08	30.32	25.18	27.57	18.24	0.60
9547	2910	62	28.12	17.43	2.58	26.85	1.23	13.89	1.06	0.93
9710	2960	58	40.39	23.43	3.47	26.85	3.48	17.98	2.85	0.86
9743	2970	44	42.86	18.86	2.79	27.83	27.83	16.86	23.14	0.42
10169	3100	71	24.33	17.27	2.56	21.17	11.92	23.89	9.07	0.72
13833	4216	62	24.05	14.91	2.21	27.34	24.05	17.42	19.86	0.47
15617	4760	68	62.78	42.69	6.32	22.58	11.41	22.50	8.84	0.72
15620	4761	73	77.48	56.56	8.37	17.82	16.83	26.99	12.29	0.69
15640	4767	84	46.52	39.07	5.78	24.38	22.39	20.66	17.76	0.54
17154	5229	61	22.94	14.00	2.07	19.45	7.73	25.51	5.76	0.82
Averages		**51.13**	**35.40**	**20.29**	**3.00**	**24.78**	**16.11**	**20.55**	**12.99**	**0.64**

Table 3 continued.

Sample #	Sample Depth (m)	% IGV TRUE	% new total cement	% $COPL_2$	% $CEPL_2$	$Icomp_2$			$I_{grain\ expansion}$	I_{cement}
		C_f+IGV_c=IGV_t	C+C_f=C_t				$COPL_1$- $COPL_2$	$CEPL_2$- $CEPL_1$	$_1$	$C_f/(C_f + C)$
3233	982	28.42	13.81	16.17	11.57	0.58	0.14	0.02	0.01	0.01
4908	1496	21.29	6.97	23.77	5.31	0.83	0.42	0.03	0.02	0.06
6105	1861	32.45	32.20	11.18	28.60	0.28	0.67	0.21	0.06	0.02
8910	2716	32.78	32.78	10.75	29.25	0.28	2.54	0.78	0.19	0.06
9001	2744	17.92	9.73	26.90	7.11	0.84	2.40	0.17	0.08	0.29
9120	2963	33.40	28.26	9.91	25.46	0.57	2.80	0.70	0.10	0.11
9547	2910	29.43	3.81	14.98	3.24	0.91	3.31	0.04	0.24	0.68
9710	2960	30.31	6.95	13.90	5.98	0.82	4.08	0.14	0.23	0.50
9743	2970	30.62	30.62	13.52	26.48	0.36	3.34	0.93	0.20	0.09
10169	3100	23.72	14.48	21.34	11.39	0.69	2.55	0.30	0.11	0.18
13833	4216	29.55	26.26	14.84	22.36	0.42	2.59	0.62	0.15	0.08
15617	4760	28.90	17.73	15.62	14.96	0.62	6.88	0.79	0.31	0.36
15620	4761	26.19	25.20	18.71	20.48	0.58	8.28	1.39	0.31	0.33
15640	4767	30.16	28.17	14.09	24.20	0.42	6.57	1.47	0.32	0.21
17154	5229	21.52	9.80	23.55	7.49	0.80	1.97	0.15	0.08	0.21
Averages		**27.78**	**19.12**	**16.61**	**16.26**	**0.60**	**3.24**	**0.52**	**0.16**	**0.21**

Table 4. Compilation of Mount Simon Formation data to calculate the amount of IGV destroyed by brittle deformation plus attendant quartz cementation and the amount that brittle deformation influences COPL and CEPL. All 30 samples are represented. See text for explanation.

Sample #	**% Frac. Qtz Grains**	**% Det. Qtz**	**% Fractured Grains**	**Rock Vol Const of Frac Fill**	**% IGV Present**	**% Total Cement**	**% COPL1**	**% CEPL1**	**Icomp1**
	A	B	A x B = Gfrac	Gfrac x 0.052 = Cf	IGVc	C			
71901-2	10	67.00	6.70	0.35	15.30	1.50	29.16	1.06	0.96
71901-9	14	34.50	4.83	0.25	24.50	11.80	20.53	9.38	0.69
1164	27	66.80	18.04	0.94	25.50	13.80	19.46	11.11	0.64
1277	17	71.30	12.12	0.63	17.80	15.30	27.01	11.17	0.71
1288	26	62.30	16.20	0.84	34.80	34.80	7.98	32.02	0.20
2019	30	85.60	25.68	1.34	10.10	3.80	33.26	2.54	0.93
2166	29	63.30	18.36	0.95	24.40	14.30	20.63	11.35	0.65
2384	24	71.30	17.11	0.89	19.30	13.80	25.65	10.26	0.71
2480	29	72.00	20.88	1.09	23.00	13.30	22.08	10.36	0.68
2562	23	78.70	18.10	0.94	19.80	12.00	25.19	8.98	0.74
3134.5	33	79.30	26.17	1.36	19.80	17.80	25.19	13.32	0.65
3177	27	71.10	19.20	1.00	23.20	15.00	21.88	11.72	0.65
3224	29	77.10	22.36	1.16	19.90	14.10	25.09	10.56	0.70
3581.5	32	63.30	20.26	1.05	24.40	14.30	20.63	11.35	0.65
3619	33	81.50	26.90	1.40	16.00	15.80	28.57	11.29	0.72
3793	28	78.30	21.92	1.14	18.70	13.60	26.20	10.04	0.72
4038	33	77.10	25.44	1.32	18.80	15.50	26.11	11.45	0.70
4119	32	73.10	23.39	1.22	22.10	12.60	22.98	9.70	0.70
4226	24	74.30	17.83	0.93	24.90	15.20	20.11	12.14	0.62
4469	32	73.80	23.62	1.23	20.00	14.00	25.00	10.50	0.70
4477	24	78.70	18.89	0.98	15.10	9.20	29.33	6.50	0.82
4720	36	76.20	27.43	1.43	16.80	10.80	27.88	7.79	0.78
5404	35	79.10	27.69	1.44	14.70	13.50	29.66	9.50	0.76
6154	44	83.50	36.74	1.91	14.00	12.50	30.23	8.72	0.78
6235	42	87.00	36.54	1.90	9.70	9.00	33.55	5.98	0.85
6241	40	84.80	33.92	1.76	13.80	12.80	30.39	8.91	0.77

Table 4 continued.

Sample #	**% Frac. Qtz Grains**	**% Det. Qtz**	**% Fractured Grains**	**Rock Vol Const of Frac Fill**	**% IGV Present**	**% Total Cement**	**% COPL1**	**% CEPL1**	**Icomp1**
	A	B	A x B = Gfrac	Gfrac x 0.052 = Cf	IGVc	C			
6497	42	78.70	33.05	1.72	19.10	15.80	25.83	11.72	0.69
6500	41	85.50	35.06	1.82	10.50	8.20	32.96	5.50	0.86
8466	54	76.80	41.47	2.16	13.30	13	30.80	9.00	0.77
8468	46	82.80	38.09	1.98	9.00	8.3	34.07	5.47	0.86
Avgs	**31.20**	**74.49**	**23.80**	**1.24**	**18.61**	**13.18**	**25.91**	**9.98**	**0.72**

Sample #	**% IGV TRUE**	**% new total cement**	**% COPL2**	**% CEPL2**	**Icomp2**	**Δ COPL**	**Δ CEPL**	**Igrain expan.**	**Icement**
	Cf+IGVc=IGVt	C+Cf=Ct				COPL1-COPL2	CEPL2-CEPL1	Δ COPL/COPL1	Cf/(Cf + C)
71901-2	15.65	1.85	28.87	1.31	0.96	0.29	0.25	0.01	0.19
71901-9	24.75	12.05	20.26	9.61	0.68	0.27	0.23	0.01	0.02
1164	26.44	14.74	18.44	12.02	0.61	1.03	0.91	0.05	0.06
1277	18.43	15.93	26.44	11.72	0.69	0.56	0.55	0.02	0.04
1288	35.64	35.64	6.77	33.23	0.17	1.20	1.20	0.15	0.02
2019	11.44	5.14	32.25	3.48	0.90	1.01	0.94	0.03	0.26
2166	25.35	15.25	19.62	12.26	0.62	1.01	0.91	0.05	0.06
2384	20.19	14.69	24.82	11.04	0.69	0.83	0.78	0.03	0.06
2480	24.09	14.39	20.96	11.37	0.65	1.11	1.01	0.05	0.08
2562	20.74	12.94	24.30	9.80	0.71	0.89	0.82	0.04	0.07
3134.5	21.16	19.16	23.90	14.58	0.62	1.29	1.27	0.05	0.07
3177	24.20	16.00	20.85	12.66	0.62	1.03	0.94	0.05	0.06
3224	21.06	15.26	23.99	11.60	0.67	1.10	1.04	0.04	0.08
3581.5	25.45	15.35	19.51	12.36	0.61	1.12	1.01	0.05	0.07
3619	17.40	17.20	27.36	12.49	0.69	1.21	1.21	0.04	0.08
3793	19.84	14.74	25.15	11.03	0.70	1.05	1.00	0.04	0.08

Table 4 continued.

Sample #	**% IGV TRUE**	**% new total cement**	**% COPL2**	**% CEPL2**	**Icomp2**	**Δ COPL**	**Δ CEPL**	**Igrain expan.**	**Icement**
	Cf+IGVc=IGVt	C+Cf=Ct				COPL1-COPL2	CEPL2-CEPL1	Δ COPL/COPL1	Cf/(Cf + C)
4038	20.12	16.82	24.88	12.64	0.66	1.22	1.18	0.05	0.08
4119	23.32	13.82	21.76	10.81	0.67	1.22	1.11	0.05	0.09
4226	25.83	16.13	19.11	13.05	0.59	1.00	0.90	0.05	0.06
4469	21.23	15.23	23.83	11.60	0.67	1.17	1.10	0.05	0.08
4477	16.08	10.18	28.50	7.28	0.80	0.83	0.78	0.03	0.10
4720	18.23	12.23	26.63	8.97	0.75	1.26	1.18	0.05	0.12
5404	16.14	14.94	28.45	10.69	0.73	1.21	1.19	0.04	0.10
6154	15.91	14.41	28.65	10.28	0.74	1.59	1.56	0.05	0.13
6235	11.60	10.90	32.13	7.40	0.81	1.43	1.42	0.04	0.17
6241	15.56	14.56	28.94	10.35	0.74	1.45	1.44	0.05	0.12
6497	20.82	17.52	24.22	13.27	0.65	1.61	1.56	0.06	0.10
6500	12.32	10.02	31.57	6.86	0.82	1.39	1.36	0.04	0.18
8466	15.46	15.16	29.03	10.76	0.73	1.77	1.76	0.06	0.14
8468	10.98	10.28	32.60	6.93	0.82	1.47	1.46	0.04	0.19
Avgs	**19.85**	**14.42**	**24.79**	**11.05**	**0.69**	**1.12**	**1.07**	**0.05**	**0.10**

are known as compactional porosity loss (COPL) and cementational porosity loss (CEPL). Conventional calculations of these processes are as follows (Lundegard, 1992; Ehrenberg, 1995):

$$\mathrm{COPL} = \frac{P_i - (100 - P_i) \bullet \mathrm{IGV}}{100 - \mathrm{IGV}} \qquad (3)$$

and

$$\mathrm{CEPL} = (P_i - \mathrm{COPL}) \bullet \frac{C}{\mathrm{IGV}} \qquad (4)$$

where the initial porosity (P_i) = 0.40.

Tables 2 and 3 tabulate the values for COPL and CEPL obtained for the Frio and Mount Simon Formations, as well as the index of compaction(I_{comp}), which equals the ratio of compactional porosity loss to total porosity loss:

$$I_{comp} = \frac{\mathrm{COPL}}{\mathrm{COPL} + \mathrm{CEPL}} \qquad (5)$$

Compaction is the predominant contributor to porosity loss in both the Frio and Mount Simon sandstones. Eleven out of 15 Frio samples have I_{comp} values greater than 0.5 and an overwhelming 29 out of 30 samples of the Mount Simon have I_{comp} values greater than 0.5. Because compaction is so important in porosity reduction, it is interesting to consider the quantitative partitioning of specific mechanisms that operate in compaction, in particular the role of brittle grain deformation.

As mentioned above, IGV determinations made in light microscopy may be incorrect for samples containing fractured quartz grains, because one cannot measure the intragranular cement (Fig. 14). With CL microscopy, the volume of cement sequestered within detrital grains (C_f) is properly construed as a portion of the cement volume (and a portion of the true IGV) rather than as a portion of the grain volume.

Because quartz grains are predominant among grains that show brittle behavior in the Frio and Mount Simon, multiplying the volume percentage of quartz grains in the whole rock by the volume percentage of fractured quartz grains yields an estimate of the percentage of fractured grains (G_{frac}) in a of sandstone.

$$\text{\% Fractured Qtz Grains} \bullet \text{Qtz (\% whole rock)} = G_{frac} \qquad (6)$$

Multiplying G_{frac} by the average percentage of intragranular quartz cement in the average apparent grain volume (grain as seen in conventional light) yields the percentage of total intragranular cement (C_f) within a volume of sandstone:

$$G_{frac} \bullet \text{Avg. Intragranular Qtz Cement} = C_f \qquad (7)$$

C_f is the percent of the entire rock consisting of intragranular cement, a portion counted as detrital grain volume when evaluating conventional IGV

(IGV_c) values. The true value of IGV (IGV_t), as illustrated in Figure 14, sums C_f as part of the cement rather than the grain volume (C_f is added to IGV_c to get IGV_t).

$IGV_t = IGV_c + C_f$ (8)

C_f and C are added, resulting in a readjusted total cement value (Ct).

$C + C_f = C_t$ (9)

$COPL_2$ and $CEPL_2$ are recalculated using IGV_t. I_{comp2} values for the Frio Formation still show that compaction dominates porosity loss with 10 out of 15 values greater than 0.5 (Table 3). Twenty-nine out of 30 Mount Simon samples have I_{comp2} values greater than 0.5, also suggesting that compaction remains the dominant IGV reducer (Table 4). Changes in COPL and CEPL resulting from the correct use of C_f were calculated as follows:

$COPL_1 – COPL_2 = \Delta$ COPL (10)

$CEPL_2 – CEPL_1 = \Delta$ CEPL (11)

Finally, a measure of the true IGV decline using the corrected IGV value (IGV_t) (by summing quartz cement in grain fractures as cement rather than grain volume) can be given as an index of apparent grain expansion, here defined as:

$\Delta COPL/COPL_1 = I_{grain\ expansion}$ (12)

This ratio reflects COPL change caused by brittle deformation. $I_{grain\ expansion}$ values range from 0.01 to 0.32 in the Frio Formation (Fig. 16A). Values for the Mount Simon Formation range from 0.01 to 0.15, with values generally increasing with depth.

The percentage of quartz cement in fractures for an entire rock is given as:

$$\frac{C_f}{C_f + C} = I_{cement} \qquad (13)$$

The average amount (by volume) of intragranular cement localized within fractures in the Mount Simon Formation is also much less overall than in the Frio Formation. I_{cement} values for the Frio Formation range from 0.01 to 0.68, whereas I_{cement} values for the Mount Simon Formation range from 0.02 to 0.26 generally with larger values at greater depths (Fig. 16B).

DISCUSSION: CONTRASTS IN BRITTLE DEFORMATION

Fracturing of quartz grains in the Frio and Mount Simon Formations increases with depth. The rate of fracture increase with depth differs between the two formations, however. At shallow depths (< 2 km), a larger number of quartz grains are fractured in the quartz-rich Mount Simon sandstones compared to the more lithic-rich Frio sandstone. At deeper depths (below 2 km), more quartz grains are subjected to fracturing in the Frio sandstones than in the Mount Simon sandstones. These differences in fracturing behavior may be related to the ductile behavior of certain Frio lithics, which effectively cushions adjacent quartz grains during the early stages of compaction.

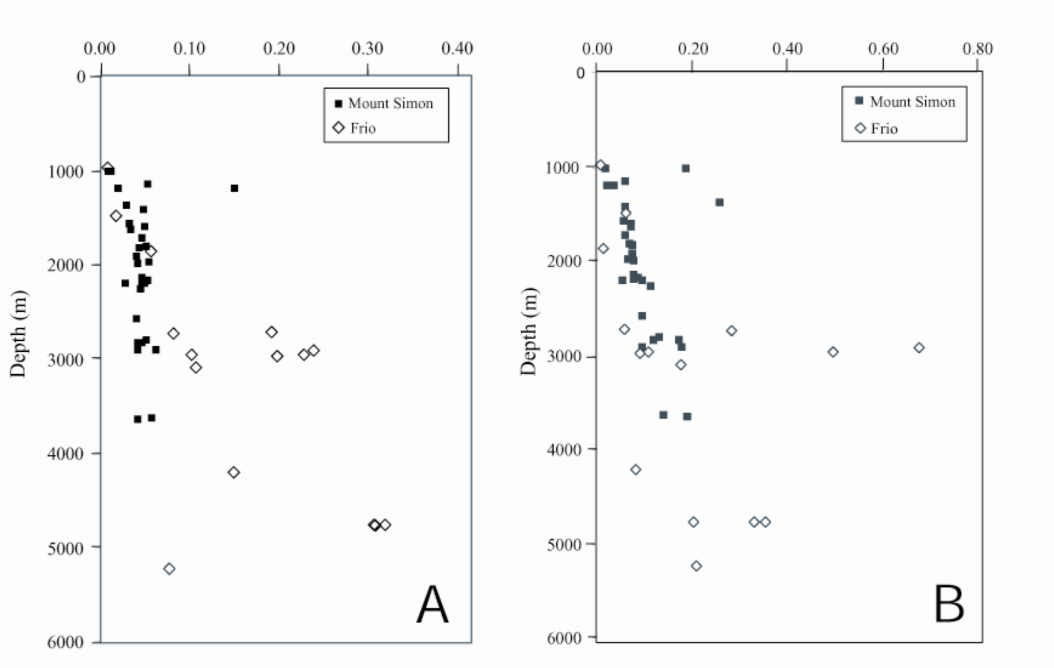

Figure 16. Quantification of the amount of change in quartz cement and COPL values after IGV was reassessed using C_f. A) The x axis represents the values for apparent $I_{grain\ expansion}$. Values of $I_{grain\ expansion}$ increase significantly around 3000 m depth and deeper for the Frio Formation (A). Mount Simon Formation $I_{grain\ expansion}$ values increase only slightly with depth (A). B) The y axis represents values for I_{cement}. Values of I_{cement} generally increase with depth, with the greatest increase in the Frio Formation below ~ 3000 m depth (B).

Differences in brittle grain behavior may also relate to contrasts in geothermal gradients and burial rates between the two formations, as illustrated in a study concerning sandstone rheology and deformation style (Fisher et al., 2003). During burial of the Mount Simon, the average geothermal gradient (from Cambrian to present) in the Illinois basin was higher (~ 36°C/ km in the southern Illinois Basin) (Rowan et al., 2002) than the average geothermal gradient for the South Texas Gulf of Mexico basin (~25°C/ km) (Pfeiffer 1988). Typical of shale-rich sediments deposited at high rates (~1 km/ My), the Frio Formation has been subjected to significantly greater overpressure. In the southern Texas Gulf Coast, the top of the overpressure begins at approximately 2600 m depth (Galloway, 1984). In contrast, overpressures in the Illinois Basin probably did not occur because of the low sedimentation rates (~ 30 m/My), low shale content, and relatively high permeability of sandstone aquifers in the Illinois basin compared to the Gulf Coast basin (Bethke et al., 1991).

Because the onset and progress of quartz cementation is predominantly a function of time-temperature history (Lander and Walderhaug, 1999), the higher geothermal gradient in the Mount Simon Formation, perhaps abetted by the slower depositional rate, allowed initiation of quartz cementation at a shallower depth (around 2 km, Fishman, 1997) compared to the Frio (around 3 km, Land, 1984). Fluid inclusion analyses demonstrate that quartz overgrowths in the Mt.

Simon formed from saline fluids at temperatures greater than 100°C (Fishman, 1997) despite the shallow depth of cementation.

Timing of cementation relative to burial is apparently a key influence on grain fracturing. The onset of quartz cementation has a profound effect on the mechanical properties of sand, as grain contact surfaces become effectively enlarged and the stresses that occur at inter-grain point contacts are correspondingly reduced (Dewhurst and Jones, 2003; Gallagher et al., 1974). Thus, the early onset of quartz cementation within the Mt. Simon led, ultimately, to a lesser degree of grain fracturing at great depths than is observed in the Frio.

Differences in fracture aperture and style can be also attributed to the different burial and thermal histories of the sandstones. The wider, more wedge-shaped fractures in the Frio reflect the greater displacements of grain fragments that could occur in the presence of lesser amounts of quartz cement and greater primary porosity. The thinner apertures and straighter traces of fractures in the Mt. Simon are consistent with fracturing that proceeded under conditions of greater material rigidity resulting from quartz cement. The combined attributes of greater fracture abundance and greater fracture aperture leads, naturally, to the overall greater values for I_{cement}, $I_{grain\ expansion}$, and C_f observed in the Frio. For example, C_f values in samples from the Frio Formation (Table 3) below ~ 3000 m depth range between 2 and 8%. However, Mount Simon C_f values are generally around 2% below ~ 2500 m. This shows that grain expansion can substantially influence porosity reduction below 3000 m in the Frio Formation. In contrast, grain crushing has only a minor influence on porosity below ~2500 m in the Mount Simon Formation.

Experimental measurements using a Hertzian fracture model (Frank and Lawn, 1967) show that the critical effective pressure for the onset of grain crushing of quartz-rich sandstone is influenced by grain size and porosity (Wong, 1990). The critical effective pressure needed for grain fracturing decreases with increasing porosity and grain size. Compaction experiments using unconsolidated quartz-rich sands (Chuhan et al., 2002; Gallagher et al., 1987; Lade et al., 1996; Gallagher et al., 1974; Borg et al., 1960; Brzesowsy, 1995; Zhang et al., 1990) find a similar grain-size control on grain fracturing. Michibayashi (1996) observes the same grain size control for natural feldspar having undergone mylonitization. The widespread explanation of size dependent brittle deformation of grains is due to the fact that larger particles contain more flaws or defects, and they have a higher probability of the defect being present in a particle that will break (Lade, 1996). The occurrence of flaws may be dependent on the quartz grain provenance, where grains sourced from a metamorphic region may contain more flaws that grains from a plutonic or volcanic source area. However, no studies exist that have investigated this point.

CONCLUSIONS

- Mechanical compaction occurs in sandstones across a wide range of depths. This study shows that the degree of fracturing of quartz grains with depth displays a trend that differs between the Frio and the Mount Simon. Contrasts in the trends are probably controlled by the vastly different burial histories of the Gulf of Mexico and Illinois basins, respectively. The timing of cementation and sandstone composition also play a role in the development of grain fracturing, where quartz cementation commenced at shallower depths in the Mount Simon and at greater depths in the Frio.
- The lack of correlation between the ratio of fragments in fractured grains/ percentage of fractured grains versus burial depth suggests that the intensity of fracturing within individual fractured grains is independent of depth. Although fractured grains are more abundant at deeper depths, the degree of crushing of the individual fractured grains is similar for both shallow and deep samples. Accordingly, the measured amount of intragranular quartz cement within any given fractured grain is also independent of depth.
- Failure to recognize authigenic quartz in microfractures (C_f) as cement rather than grain volume (i.e., using light microscopy instead of CL

images) in fractured, quartz-rich sandstone units, leads to inaccurate estimations of IGV and consequently, of COPL and CEPL. Correct COPL values for Mount Simon grains have a 1.0 to 15 % difference from conventional COPL values. For the Frio the difference ranges between 1.0 and 32%. The difference in corrected CEPL values for the Mount Simon and Frio Formation ranges from 2.0 to 19% and 1.0 to 68% respectively. Corrected values of COPL and CEPL (taking into account C_f) still reveal compaction to be the main contributor to porosity loss in both units.

- Conventional methods of IGV, COPL, and CEPL estimation underestimate the importance of quartz cementation in porosity loss.
- Microfracture geometry and crosscutting relationships revealed by CL images show that initiation of microfracturing occurs throughout burial, before and during quartz cementation.
- Burial history and timing of cementation influence geometry and aperture of microfractures. A higher average geothermal gradient and slower depositional rates in the Illinois Basin appears to have promoted quartz cementation at shallower depths in the Mount Simon sandstones than in the Frio sandstones. The stress at contacts is therefore less for quartz grains in the Mt. Simon because the contact area increased owing to more

cement, thus causing intragranular fractures to be thinner and straighter. In contrast, a relatively low geothermal gradient in the Gulf of Mexico Basin combined with higher burial rates caused sandstones of the Frio Formation to reach greater burial depths before reaching the quartz cementation window. In the Frio stress at grain/grain contacts caused extensive development of microfractures that exhibit relatively wide apertures and wedge-shaped form.

- This study demonstrates that grain fracturing and its attendant quartz cementation can influence porosity reduction in sandstones. The depth at which fracturing becomes influential is different for the two formations studied. Intragranular cement occluding microfractures is more abundant in the Frio Formation. In the Frio Formation below ~ 3000 m depth, C_f (volume of intragranular cement) values range between 2 and 8%. For the Mount Simon samples, values are around 2% for depths greater than 2,500 m.
- The IGV increase related to grain fracturing and cementation (here defined as $I_{grain\ expansion}$) generally increases with depth. In the same way, the amount of quartz cement related to fracturing (here defined by the parameter I_{cement}) also tends to increase with depth. As a consequence of this, inaccuracy in the calculation of values for IGV, COPL, and CEPL (if

grain fracturing and intragranular cement are not taken into account) are progressively larger in samples from increasing burial depth.

Chapter 3: Using Models to Understand Influences on Brittle Deformation of Quartz Grains

Diagenetic modeling, commonly used for reservoir quality prediction, is used to reconstruct the timing of quartz cement in the context of burial and uplift history. The mechanical behavior of grains is very much controlled by the geologic history. By using the diagenetic model Touchstone™, one can simulate temperature and pressure history, and consequently, the timing and depth of significant quartz cement emplacement, which affects the rock properties such as porosity, permeability, density, bulk modulus, and shear modulus. Thus, modeling the timing and depth of the occurrence of quartz cementation, can aid in understanding the controls on grain breakage. Results from modeling can be used to validate or reject hypotheses suggested from petrographic data alone. Here, the application of diagenetic modeling contrasts with reservoir quality prediction, because the emphasis is on extracting information on the timing and depth of quartz cementation, rather than on predicting present day porosity.

Contrasts in the fracture trends with maximum burial depths between the Frio and Mount Simon Formations and the differences in fracture morphology are hypothesized in the previous section to be dependent on the timing of quartz cementation which, in turn, is governed by burial rate and geothermal gradient differences between the Frio (Gulf of Mexico Basin) and the Mount Simon (Illinois Basin) together with compositional and textural differences (Frio= lower quartz grain content and larger grains size). As noted in Chapter 2, rapid burial and an average lower geothermal gradient has resulted in commencement of quartz cementation at greater depth in the Frio sandstones compared to the more slowly buried Mount Simon sandstones, which have been subjected to a higher geothermal gradient resulting in cementation at shallower depths. An added complexity in controlling the differences in fracture abundance is the age of the sandstones, where Mount Simon Formation sandstones have been deposited for a longer period of time compared to the Frio Formation sandstones, and therefore influenced by pressure solution. Quartz grains in deeper samples, for both formations, are more extensively fractured than those at shallower depths because they are buried more deeply before the onset of quartz cementation. For the Frio sandstones the influence of fluid overpressure on grain fracturing is unclear. Thus, modeling adds a more quantitative perspective to our understanding of the timing and depth of quartz cementation and effective stress levels.

TIMING OF QUARTZ CEMENT VERSUS GRAIN FRACTURING: PETROGRAPHIC OBSERVATIONS

Quartz cementation is expected to stabilize the grain framework and inhibit grain fracturing. Petrographic observation shows that most compaction fractures within quartz grains form before or during substantial (intergranular) quartz cementation. Cathodoluminescence textures indicate that *most* intragranular fractures do not cross-cut overgrowths but do show that cementation and intragranular fracture cementation is continuous. This textural evidence suggests that most of fracturing precedes significant cementation (Fig. 17). Shallowly buried quartz grains exhibiting intragranular grain fractures are generally filled with quartz cement but lack cementation on external grain surfaces (Fig. 18), indicating faster surface area normalized growth rates on fracture surfaces compared to grain surfaces. The fracture surface is fresh and clean allowing quartz cement to nucleate and grow within the fracture, whereas the external grain surface may contain irregularities and detrital particles that slow the rate of quartz precipitation. While it could be argued that these fractures are inherited (and some may well be), however, the fracture morphology and characteristic dark cement luminescence suggests that these are compaction fractures having formed after sediment deposition.

In deeper subsurface samples (where quartz cementation is ubiquitous) some grains (< 5%) exhibit fractures that transect overgrowths, showing that some fracturing post-dates the initiation of quartz cementation. The volume of quartz cement required to prohibit a significant amount of brittle deformation.

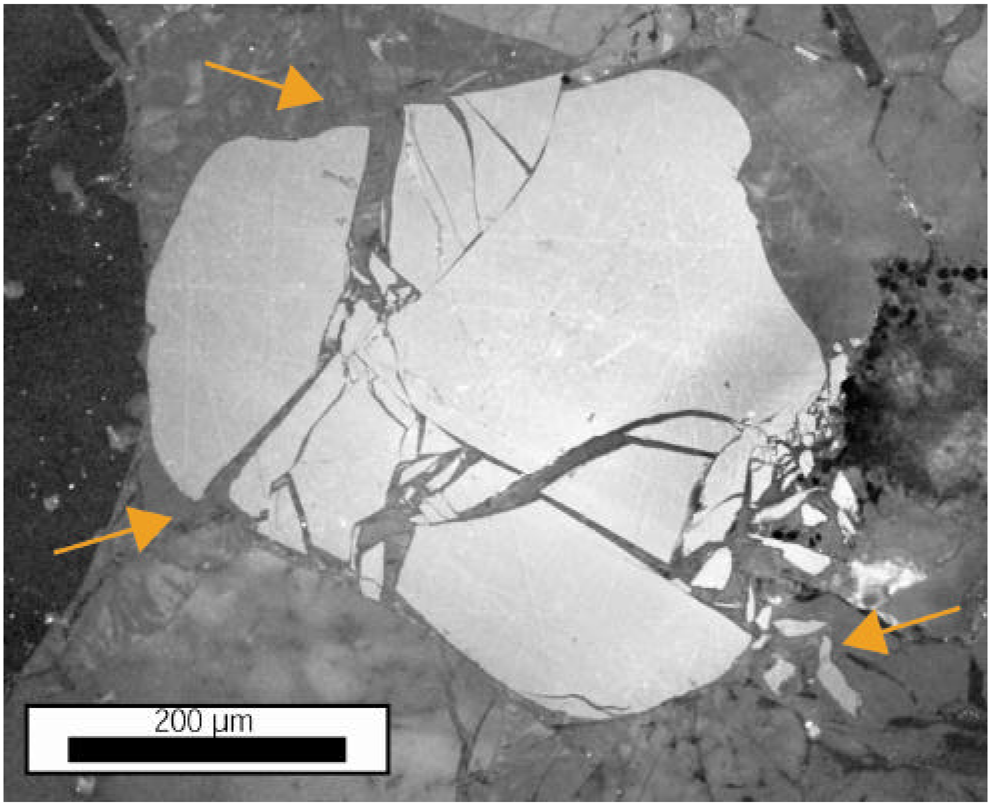

Figure 17. Frio sample 15620. CL image showing fractured quartz grain (center). Fractures have been filled with cement. Arrows indicate areas of fracture filled quartz cement continuous with overgrowth quartz cement suggesting contemporaneous precipitation of quartz cement and fracturing of quartz grains.

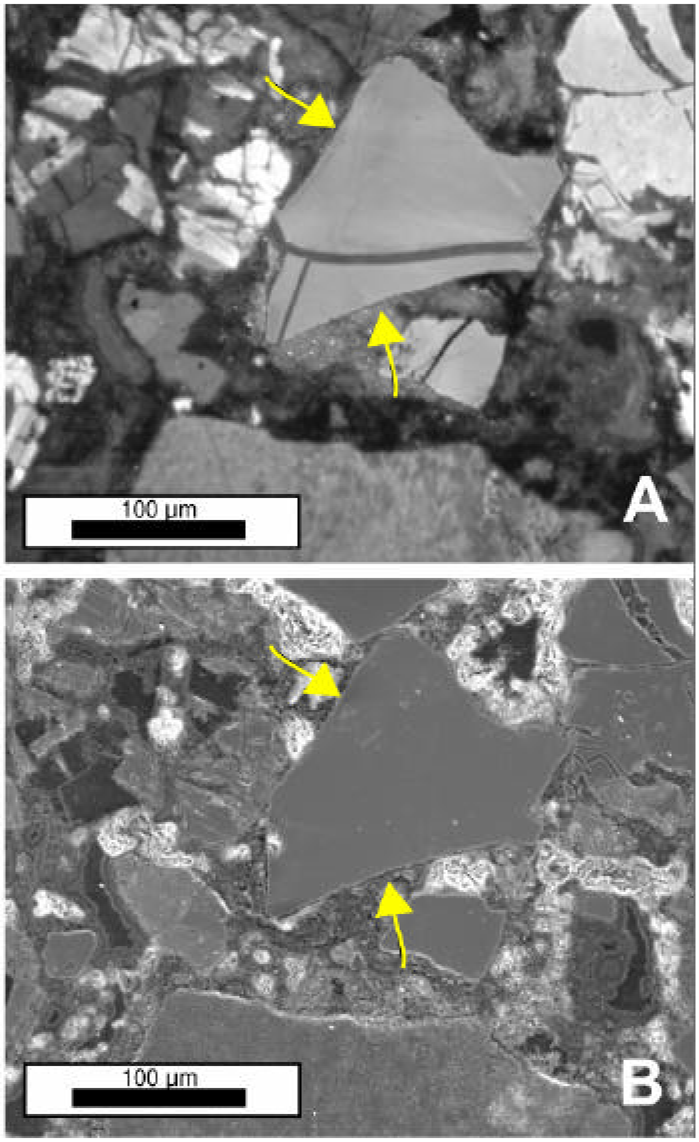

Figure 18. Frio sample 3223, from 982 m depth. A) CL image of grain exhibiting fractures filled with quartz cement. B) SEI image showing continuous smooth surface of grain, indicating that fractures are filled with quartz. There are two reasons for lack of quartz overgrowth precipitation. Clays and by products from dissolved grains (partially dissolved feldspar in upper left and corner) prohibit quartz from precipitation around the grain and low temperatures at this depth (~ 50°C).

MODELING REVIEW

Touchstone combines aspects of process-oriented and empirical or effect-oriented models. Empirical or effect-oriented models typically involve single and multiple variable statistical fits to datasets (Byrnes, 1994; Bloch and Helmold, 1994). Regression equations derived from large data sets are then used to predict porosity and permeability in geologically analogous situations. This type of modeling approach is popular because computation requirements are low and models are easily built. On the other hand, geochemical reaction-transport modeling incorporates forward modeling, where the reaction-transport model is governed by thermodynamic and kinetic expressions resulting in equilibrium prediction, with fluid flow and solute transport. Reaction transport models require large computational power and often there are discrepancies between thermodynamically predicted and observed constituents of natural rocks (e.g., Walderhaug, 1994). Touchstone is a "hybrid" forward numeric model that uses process-oriented forward models that contain terms that are optimized empirically using textural, compositional, and burial history data from natural sandstones. The important controls on quartz cement abundance are temperature history and surface area for cement nucleation. The model utilizes empirically determined rate constants for quartz cementation and assumes simple thermal precipitation kinetics (discussed below). A variety of results using Exemplar™, another "hybrid" modeling approach, have shown that this modeling method, with some limitations and adjustments, is an emerging tool for diagenetic modeling and reservoir quality prediction (Awwiller and Summa, 1997; Lander and Walderhaug, 1997; Lander et al., 1997a and 1997b; Bonnell et al., 1998a, and 1998b; Lander and Walderhaug, 1999; Souza, 2000).

Basin models were constructed using Genesis^{TM} to generate time-temperature history for the Frio Formation. Information on the burial history for the Illinois Basin was used from a recently published basin model by Rowan et al. (2002).

Basin Modeling

Basin modeling was conducted to retrieve temperature history data. Data necessary for the basin models were retrieved from well-logs and other data for each well, which include mud weights, bottom-hole temperatures, circulation times, stratigraphy, and gross lithology for the Frio Formation. Although vitrinite reflectance data are scarce they provide a useful tool in interpreting temperature history. Not all information was found for all wells used and some interpolation was done for a few wells. See Appendix E for complete list of measured and estimated input data used for basin modeling.

Additional input parameters incorporated into the basin models are surface temperature through time and heat flow from the basement. Surface temperature decreases through time beginning in the Oligocene from 19 ° to 15 °C at present for the Frio (Habicht, 1979). Modeled surface temperature through time from the Cambrian is more variable, fluctuating from icehouse to green house periods between 30 and 12 °C spanning the Paleozoic, Mesozoic and Cenozoic eras in the Illinois Basin (Habicht, 1979). Basal heat flow for the Frio Formation remains constant through time at 35 mW/m^2 and heat production rates for Oligocene sandstones and mudstones are 1.19 and 1.72 $\mu W/m^3$ respectively. These are heat production values used for the south Texas, Gulf of Mexico for matching temperature data (McKenna and Sharp, 1998). For the Mount Simon Formation, the heat flow began at 62.5 mW/m^2 and increased for a short time during the Permian (an estimated value of 155 mW/m^2) as a result of a short lived magmatic event from 272 to 270 my (Rowan et al., 2002).

Using a complete suite of initial estimates for the model input parameters, simulations were run and the results compared to available calibration data including estimated temperatures and vitrinite reflectance. Averages of lithology abundances were refined, such that relative abundances of shales, shaley-sand, sandy-shales, and sand abundances were slightly adjusted for a better match between measured and modeled temperature. A good model is one where measured and modeled parameters overlap (Fig. 19).

The majority of temperatures matched between ± 5°C, however, there are a substantial number of measurements that fall out of this range. In most cases, measured temperatures are lower than modeled temperatures. Most likely the true temperatures are higher than the measured temperatures because it can be assumed that waters are not in equilibrium with the formation when recorded. Also, a questionable datum occurs where temperature decreases with depth such as in the Gerdts Well (Fig. 20). Bottom hole temperature data retrieved from well logs match other such data from south Texas (e.g. McKenna and Sharp, 1998).

Effective Stress and Overpressure Development in the Frio Formation

Effective stress is the difference between total stress and the "neutral" stress of the water in the voids. As a rock mass undergoes burial the effective stress increases due to the load of the overburden sediments. However, the effective stress can be reduced by the force of the water counteracting the weight of the rock mass, a condition called "overpressure". In the Frio, rapid deposition of shale (half of its depositional volume being water) results in compactional disequilibrium and overpressuring at shallow depths.

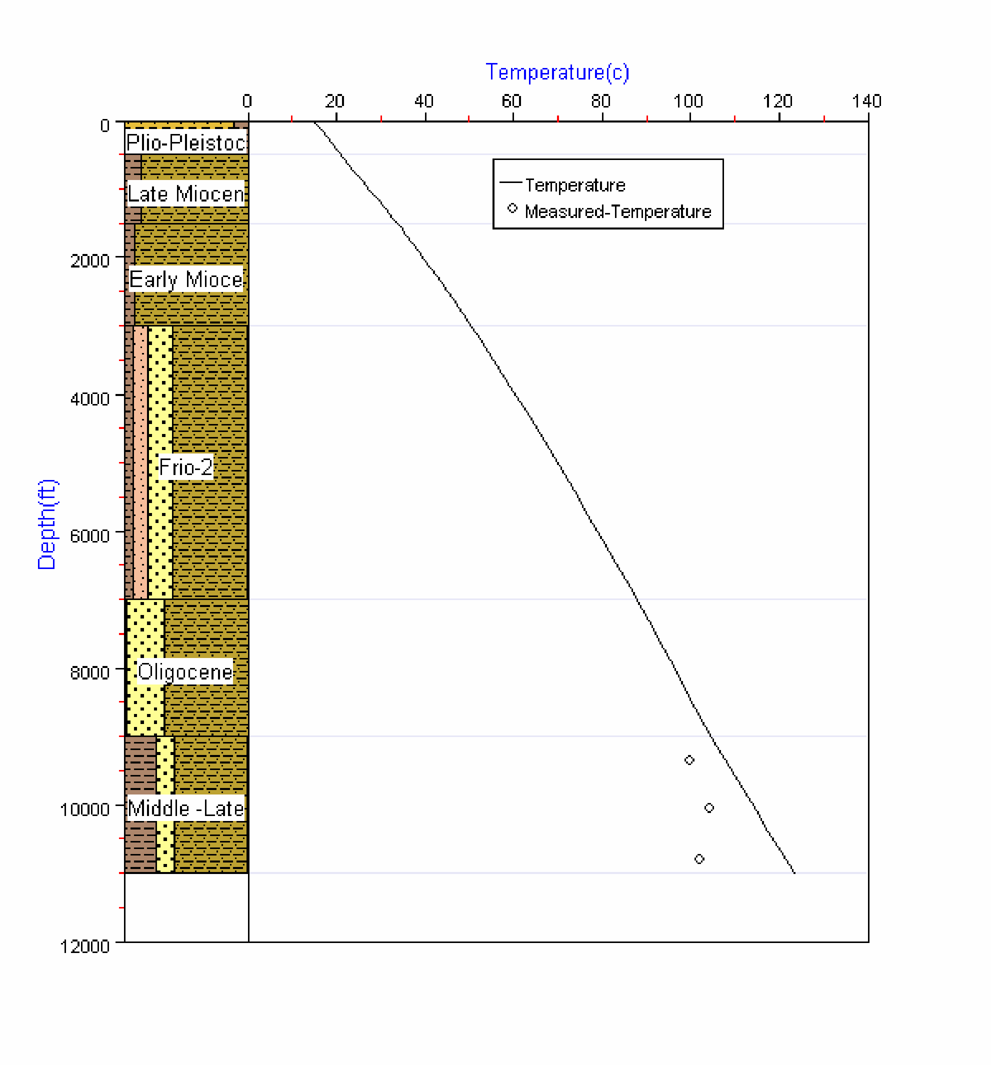

Figure 19. Genesis^{TM}-generated plot showing measured data as points and modeled data depicted as a line for the Gerdts Well, Gulf of Mexico Basin. Modeled temperature data are near but do not exactly match the measured data. Measured data are commonly lower than the actual temperature because measured temperatures are generally not equilibrated to the formation temperature when measured.

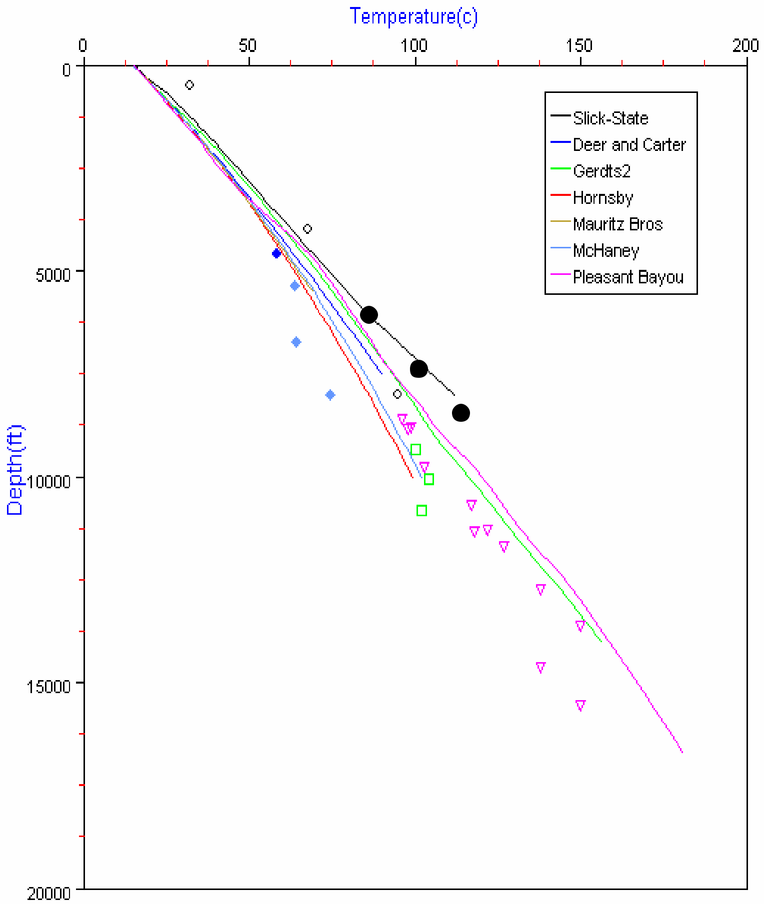

Figure 20. Modeled versus measured subsurface bottom hole temperatures with depth for all wells in the Frio. Data points represent measured values and lines depict the modeled fluid pressures with depth. Commonly modeled temperatures are higher than measured temperatures, especially deeper in the subsurface. Solid data points represent bottom hole temperature from south Texas (McKenna and Sharp, 1998).

Today the effective stress is variable for Frio sandstones and strongly dependent on depth of burial and location in the south Gulf of Mexico Basin. At greater depths (within the overpressure zone), samples display much lower effective stress values, demonstrating the general existence of overpressure below ~ 2900 m depth at present , in agreement with trends documented in the literature (e.g., Galloway, 1984) (Fig 21).

Extensive numerical models have been built to understand the geopressure evolution of the Gulf of Mexico basin (Blanchard, 1987; Bethke, 1989; Harrison and Summa, 1991). The general outcomes of these models are in agreement and demonstrate that extensive overpressure development began in the late Miocene and early Pliocene (Fig. 22). The implication of these results is that many Tertiary formations have only become strongly overpressured in the last 2-3 My, and that the formations have been essentially at near-normal pressures for most of their burial history (Blanchard, 1987; Bethke, 1989; Harrison and Summa, 1991). Effective stress calculations for the Frio are essentially normally pressured through time, with a rapid decrease in recent time according to Harrison and Summa (1991), where the pressure gradient is increases from 12 to 16 MPa/km between 3 and 5 km. Above 3 km, the sediments remain normally pressured (Fig. 21)

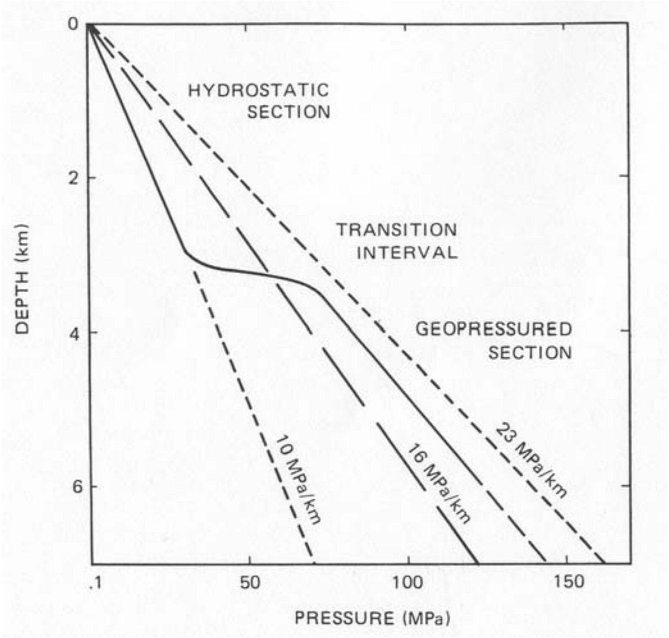

Figure 21. Generalized present day nearshore pore pressure-depth trend in Gulf of Mexico basin sediments. Above 3 km, the sediments are normally pressured. The transition interval spans only a few hundred meters. Below this transition zone sediments are overpressured (modified from Bethke, 1986).

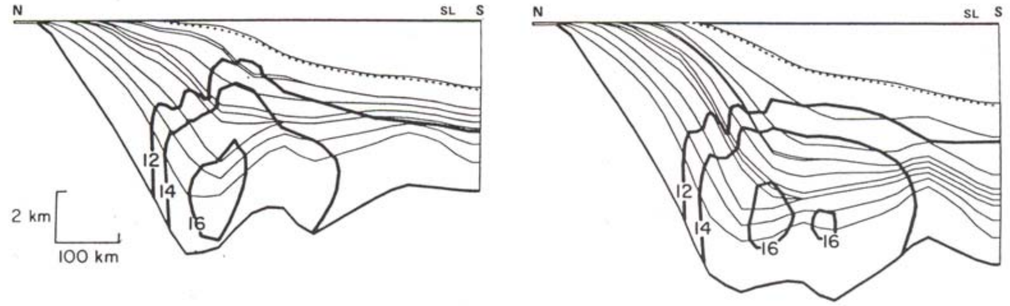

Oligocene (31 m.y.)

Miocene (5.2 m.y.)

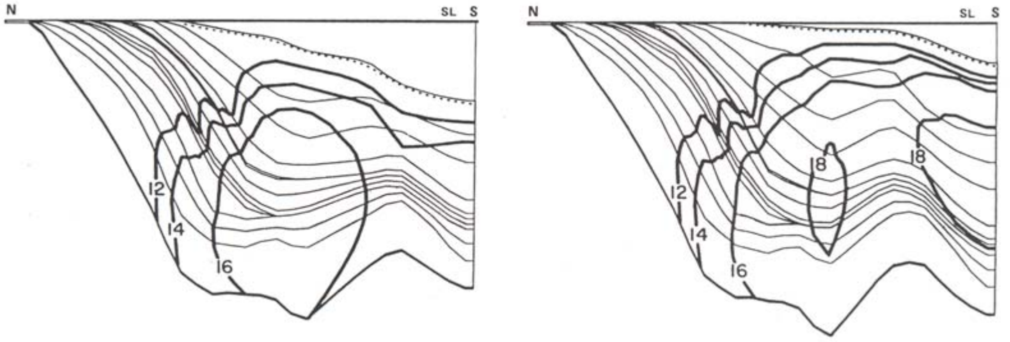

Pliocene (1.8 m.y.)

Present

Figure 22. Modeled hydraulic gradient contours from Oligocene time through to the present. Calculations by Harrison and Summa (1991) and Bethke (1989) show a small deep core of high pore pressure located beneath the major depocenters from Oligocene to Miocene. Extensive overpressure development began in late Miocene to early Pliocene times. North location on the cross section is located onshore and south location in the central part of the Gulf of Mexico (modified from Harrison and Summa, 1991).

Touchstone Modeling

Touchstone^{TM} uses a compaction model and mineral precipitation equations that are empirically calibrated, emphasizing the modeling of compaction and quartz cementation. Input parameters necessary for modeling include a well-constructed basin model that takes into account decompaction and structural restoration of the basin, heat flow modeling and thermal reconstruction and effective stress history. See Appendix F for complete list of input variables through time. Petrographic data is vital for modeling and includes sandstone composition and texture data such as grain size distribution and sorting, as well as grain coating information. Petrographic modal data includes porosity, grain types (36 subcategories), matrix (6 subcategories), cements (29 subcategories) and replacement cements (16 subcategories) (Lander and Walderhaug, 1999; Bonnell and Lander, 2002 GCAGS).

The Touchstone compaction model considers effective stress to be the primary driving force for compaction. Effective stress is defined as the difference between the lithostatic pressure and fluid pressure and corresponds to the gravitational stress transmitted through the solid portion of the rock. Thus, this stress considers the effects both of burial depth and fluid overpressure on compaction. It incorporates the effect of framework grain types and pore-filling materials on sandstone mechanical strength. Touchstone uses the following compaction function (Lander and Walderhaug, 1999):

$$IGV = IGV_f + (\Phi_0 + m_0 - IGV_f)e^{\beta\sigma es} \qquad (14)$$

where IGV is the summation of primary porosity, cement in primary pores and detrital matrix (volume fraction), IGV_f is the stable packing configuration (volume fraction), Φ_0 is the depositional porosity (volume fraction), m_0 is the initial proportion of matrix material (volume fraction), β is the exponential rate of IGV decline with effective stress (MPa^{-1}), and σ_{es} is the maximum effective stress (MPa).

Three parameters in equation 12 affect compaction simulations: (1) IGV_f; (2) β; and (3) depositional porosity. Additionally, compaction is retarded as a function of the abundance and mechanical properties of pore-filling cement and matrix using a proprietary algorithm.

IGV_f is defined as the minimum possible IGV, or in other words, the stable packing arrangement. As a general rule, the IGV_f term exerts the strongest control on the present-day prediction of IGV.

The β term is the exponential rate of IGV decline through burial as a function of increasing effective stress. Lander and Walderhaug (1999) however found that β can generally be considered a constant value of 0.06 MPa^{-1} for a fairly broad range of sandstone compositions.

Depositional porosities vary between environments of deposition, but also within depositional environments. Numerous studies using natural sands show that depositional porosity in river sands ranges from 41% (Pryor, 1973) to as high as 48% (Atkins and McBride, 1992). Although depositional porosity is largely independent of sandstone composition, it is strongly controlled by texture. IGV_0 and F_0 values for each sample are determined from the sample's mean grain size, sorting, and detrital matrix abundance using the proprietary algorithm that is based on unpublished experiments conducted by GEOCOSM in collaboration with R.E. Larese.

The key parameters for estimation of quartz cementation in Touchstone™ are the kinetics of quartz precipitation, the detrital quartz surface area available for quartz nucleation, and the temperature history. Walderhaug (1994, 1996) has demonstrated that the quartz precipitation rate is highly dependent upon temperature using an empirical method. Touchstone has the capability to model kinetics of precipitation of quartz based on the Arrhenius equation, which is commonly used for representing temperature-dependent rates of both organic and inorganic chemical reactions:

$$K=A_e^{-Ea/RT} \qquad (15)$$

where,

K is the rate of quartz precipitation per unit surface area (mole/cm^{2}s)
A_0 is a pre-exponential constant (mole/cm^{2}s)

E_a is the activation energy (kcal/mole)
R is the real gas constant (8.314 J $mole^{-1}$ K^{-1})
T is temperature (Kelvin).

Touchstone makes several major assumptions during diagenetic modeling: (1) quartz cement precipitation is the rate-limiting factor, considering all three mechanisms involved, i.e., dissolution, transport, and precipitation; (2) formation water is assumed to be saturated or supersaturated with respect to silica, i.e. an unlimited supply of silica, which is the case for most subsurface waters (Land and Milliken, 2000); (3) the surface area available for quartz cement precipitation is a function of the grain size, extent of coating on quartz grains, the volume portion of quartz grains, as well as the overall rock porosity. The quartz cement algorithm is defined as (R. Lander, personal communication 2004):

$$Q_c = M/e\ [P_q\ 6/D]\ \gamma K \Delta t \qquad (16)$$

where Pq is the volume fraction of rock with quartz grains in the model framework of reference, M is the molecular weight of quartz (60.09 g/mol), e is the density of quartz (2.65 g/cm^2), γ is the diagenetic surface area reduction coefficient, and D is the quartz grain diameter. K is the rate per unit surface area from equation 14 and Δt is the elapsed time. The γ term is a function of grain coating, compaction, and cementation (R. Lander, personal communication 2004).

Touchstone Calibration and Optimization

When the model is run with user supplied input variables, parameters can be optimized for better correlation between measured and modeled results. Each grain and cement type is given a value to describe its ability to compact (IGV_f and γ). IGV_f values range from 35 to 0, where values for ductile fragments are in the lower end of the range and rigid grains will have values on the upper end of the range. Gamma for cements ranges between 0 and 4 where 4 represents the rigid cement end-member such as quartz and 0 represents the ductile end member such as pore-filling clays. When optimizing, a range of values for each parameter can be defined to restrict values to geologically reasonable ranges. This is an iterative process and can be run as long as necessary to decrease error to a minimum.

RESULTS

For the Frio, 93 % of modeled quartz cement volumes and intergranular porosities fall within 4% bulk volume of the measured values. All Mount Simon Formation modeled values for intergranular volume and quartz cement abundances are within 4% increments of the measured values resulting in a good fit between measured and modeled parameters.

Frio Formation

Timing of Quartz Cementation and Subsurface Temperature

Quartz cement is the dominant cement type within the Frio, although shallow samples contain little to no cement (Milliken et al., 1981; Land, 1984). The general increase in quartz cement with depth in Frio samples is consistent with the temperature-dependent kinetics for quartz precipitation. Present day subsurface temperatures versus depth plots illustrate that temperature increases with depth (Fig. 23). The distribution of quartz cement is also a function of the heterogeneous sandstone composition and cement types, where shallow samples exhibit early calcite and zeolite cements related in large part to volcanic rock composition. Clay rims and matrix on and around detrital quartz grains are also common in Frio sandstones, reducing the surface area for quartz cement precipitation.

The timing and depths for specific quartz cement abundances were extracted from Touchstone simulation where the kinetics of quartz precipitation were adjusted to match present-day values and the IGV_f term in equation 14 was adjusted to match the measured value. The reconstructed depths where quartz cement volume reached 0.5%, 1.0%, and 2% are used to determine if the presence and abundance of quartz cement influences fracturing. These arbitrary levels of quartz cement volumes are used to evaluate the control of quartz cementation on grain fracturing, because logically, a small percent of cement can significantly stabilize the framework. Although plots for percentage of quartz grains fractured

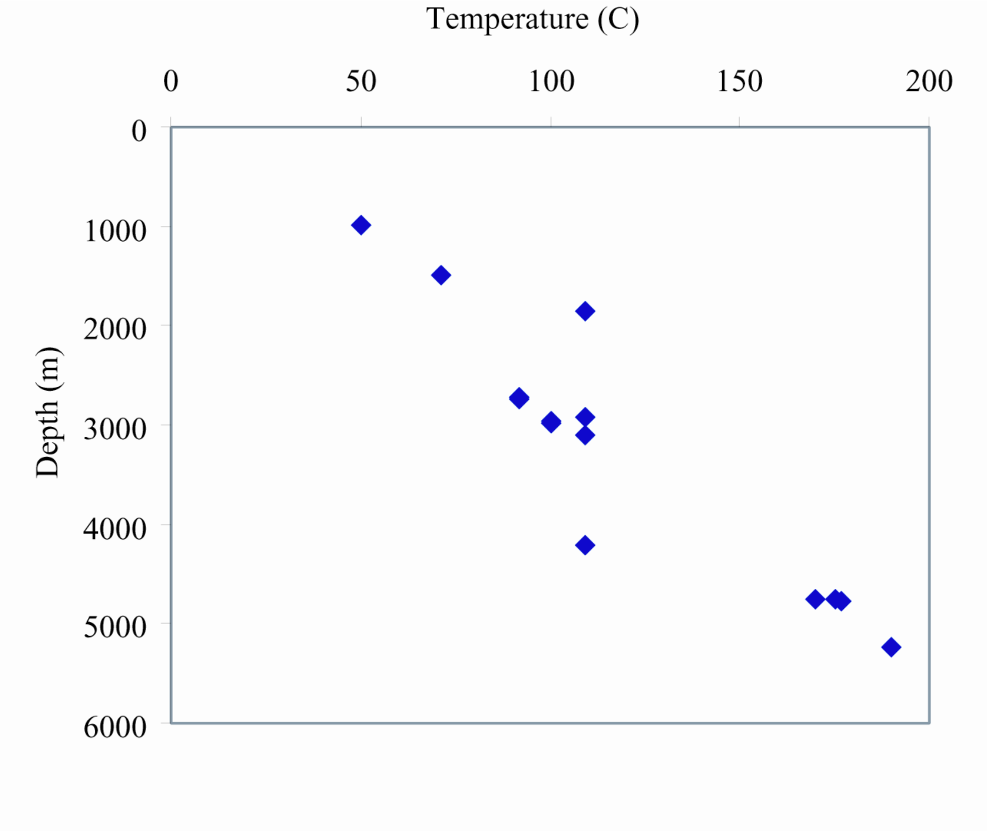

Figure 23. Well-log derived temperature data versus depth at present time in the Frio Formation. Temperature increases linearly with depth. Deeper samples have more quartz cement than shallower samples, because they were buried earlier and reached the quartz cementation window before shallower samples

versus depth at 0.5%, 1.0%, and 2% quartz cement, all show positive correlations, the best statistical fit is for the depth at 2% quartz cement compared to depth at 0.5% quartz cement results (Fig. 24). A correlation between temperatures at 2% quartz cement versus the percentage of fractured quartz grains is most likely affected by the depth dependence for fractured quartz grains (Fig. 25).

In the Frio, deeper samples were buried very rapidly and the onset of quartz cementation did not occur until near-maximum depth. Not all samples contain quartz cement but samples below 2700 m that exhibit quartz cement (10 out of 11 samples) reached the 0.5% quartz cementation window between the present and 24.6 Ma. For samples at depths greater than 2700 m with at least 2% quartz cement (8 out of 11 samples), the 2% quartz cementation threshold was reached between 4 and 23 Ma, at temperatures ranging from 84 to 177 °C. Samples below 4700 m are naturally much hotter and therefore mostly reached 2% quartz cement much sooner after burial (14-21 Ma) than samples above this depth (4-17 Ma) (Table 5).

Effective Stress

Overpressure can be produced by the following processes: (1) increase of compressive stress, (2) changes in volume of the pores fluid or rock matrix, and (3) fluid movement or buoyancy (Osborne and Swarick, 1997). Results from Harrison and Summa (1991) demonstrate that geopressures in the Gulf of Mexico

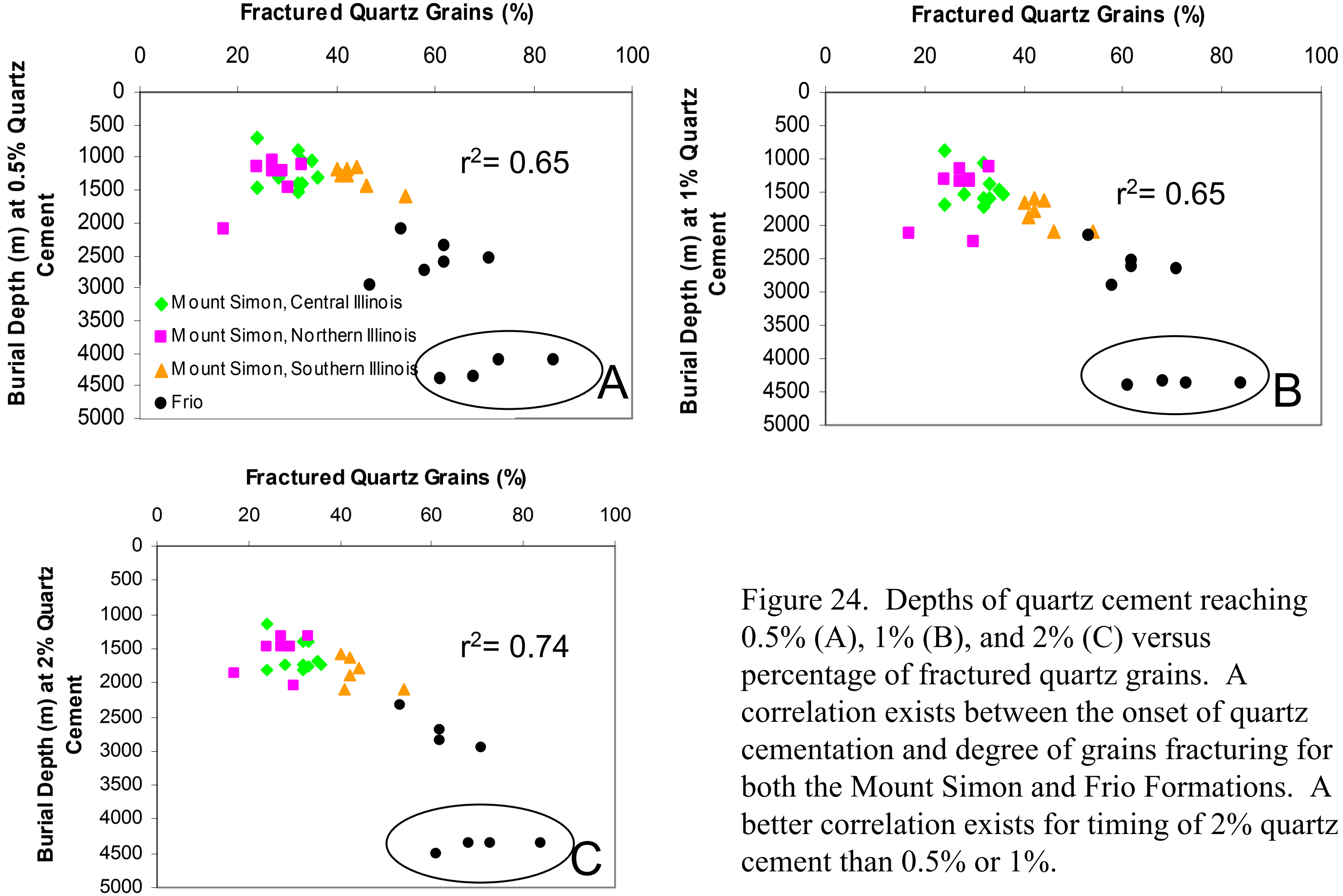

Figure 24. Depths of quartz cement reaching 0.5% (A), 1% (B), and 2% (C) versus percentage of fractured quartz grains. A correlation exists between the onset of quartz cementation and degree of grains fracturing for both the Mount Simon and Frio Formations. A better correlation exists for timing of 2% quartz cement than 0.5% or 1%.

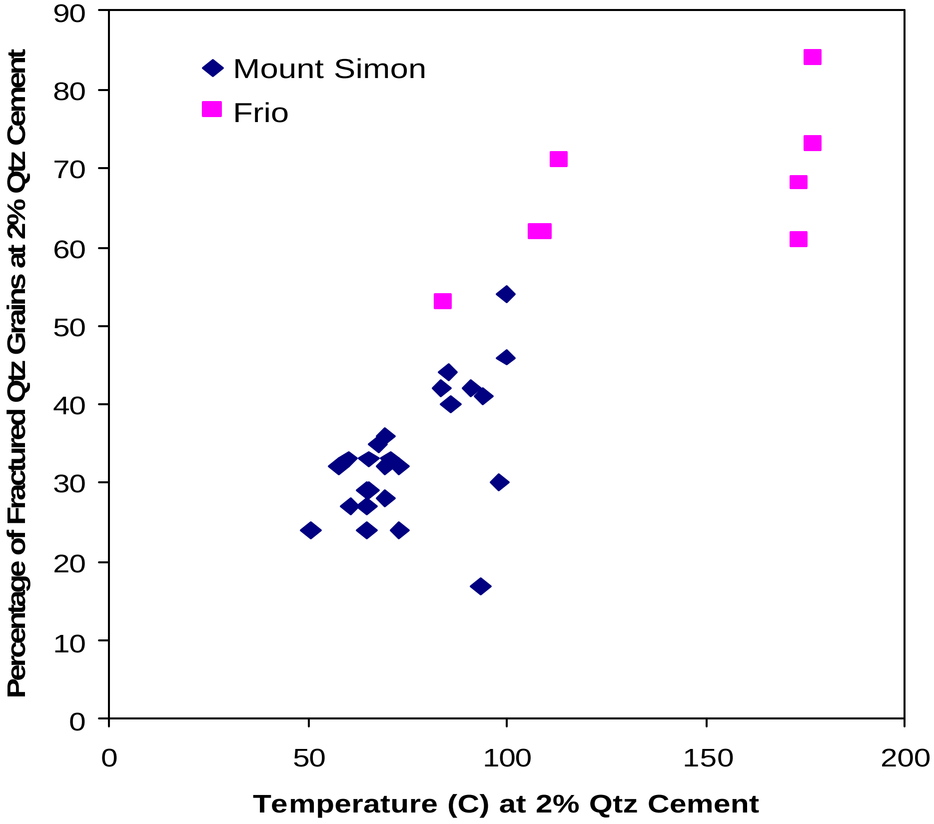

Figure 25. A temperature versus depth plot at 2% quartz cement. Temperature increases linearly with depth.

Table 5. Time, depth, and partial temperatures at intervals of 0.5%, 1%, and 2% quartz cement in the Frio Formation

Frio		0.5% qtz cement			1% quartz cement			2% quartz cement			
sample	% qtz frac.	time*	depth*	Eff. Stress*	time*	depth*	Eff. Stress*	time *	depth*	Eff. Stress	Temp*
3223	9										
4908	13										
6105	17										
8910	45										
9001	53	22	2110	23.3	20	2164	24.3	14.2	2325	25.7	84.04
9547	62	19.9	2370	26.2	14.1	2520	27.8	4.24	2842	31.4	109.49
9710	58	15.37	2729	31.2	5.3	2918	32.2				
9720	47	0	2963	34.6							
9744	44										
10169	71	20.8	2557	28.2	16.01	2668	29.5	7	2956	32.6	113.72
13833	62	23.7	2611	28.8	21.78	2616	28.9	17.9	2693	29.7	108.29
15617	68	22.7	4354	48.1	20.66	4352	48.1	16.6	4352	48.1	173.63
15620	73	24.6	4098	45.3	23.7	4367	48.2	22.1	4357	48.1	177.16
15640	84	24.6	4105	45.3	23.7	4373	48.3	22.7	4364	48.2	177.16
17154	61	21.67	4410	48.7	19.6	4404	48.6	23.7	4500	49.7	173.41

*time=My, depth=m, effective stress=MPa, temperature=C

Blanks denotes no data for quartz cement basin can be accounted for largely by compaction disequilibrium. The requirements for compactional geopressures to be developed are: (1) low permeability sediments, (2) thick shale sequences, (3) sedimentation rates of >1 mm/yr for overpressure reaching lithostatic gradients and > 0.1 mm/yr for moderate overpressure sediments. The relative importance of smectite to illite conversion and its associated expulsion of water are still debated, but are being increasingly recognized as an important contributor to overpressure development (Osbourne and Swarbrick, 1997; Alnes et al., 1998). The smectite-to-illite transition is temperature-controlled and commences at 95° C (Lynch, 1997), and with an average geothermal gradient of 30° C/km, it does not begin to play a role in overpressure until ~ 3km burial depth. There is evidence that the smectite to illite reaction in is a source for silica in associated sandstones (Lynch 1997). Quartz cementation has also been suggested as a cause of overpressure. Quartz cementation itself is insensitive to fluid overpressure (McLaughlin et al., 1996). As quartz precipitates the pore volume is reduced, displacing fluid, possibly contributing to overpressure (Helset et al., 2002). In addition, hydrocarbon maturation, also may contribute to overpressure development at temperatures in excess of 90ºC (Perry and Hower, 1970; Johns and Shimoyama, 1972).

The timing of diagenetic reactions is important to know in reference to overpressure development during the burial and uplift history. A fluid flow and pressure development model for Miocene sediments in the Southern Louisiana Gulf Coast demonstrates that quartz and illite contribute substantially to the present day overpressure and the most rapid rate of overpressure increase occurred between 10 and 5 Ma (Helset et al., 2002).

A correlation exists between effective stresses at 2% bulk volume quartz cement versus percentage of fractured quartz grains, thus making sense with a late overpressure development (post quartz cementation for deeper samples) as discussed in the literature (Blanchard, 1987; Bathke, 1989; Harrison and Summa, 1991) (Fig 22).

Mount Simon Formation

Timing of Quartz Cementation

Quartz cement is the most abundant and in some cases the only authigenic phase documented in the Mount Simon samples. All samples, with the exception of one, have >2% quartz cement. The modeled temperature at which 2% quartz cement volume was reached ranges from 50 °C to 100 °C (Fig. 25) and depths range between 1196 m and 2093 m. Both of these ranges are much lower than for the Frio. Two percent quartz cementation was reached between 192 and 376 Ma (with two exceptions), which is between 139 and 323 My after deposition.

The fact that more quartz cement is present in the Mount Simon Formation compared to the Frio Formation at a given maximum burial depth is a function of:

(1) greater nucleation surface area due to greater quartz grain abundance and lower grain coating coverage and (2) longer thermal exposure.

Effective Stress

Effective stress increases linearly with depth, given that there is no overpressure development in the Mount Simon, as expected given the slow burial rate for the Mount Simon Formation (Fig. 26).

Effects of Non-Quartz Cements

Non-quartz cements range from 0 to 34% in the Frio and Mount Simon, predominantly consisting of calcite cement, which formed early during burial. Calcite cement when present in the Mount Simon is only found in shallow samples (0-34%) is present in almost all Frio samples from all depths (0-30%). To understand the influence of non-quartz cement on grain fracturing, a plot was generated to determine the abundance of non-quartz cement at the time of significant quartz cement abundance with respect to the degree of fracturing in each sample (Fig. 27). There does not seem to be a trend with the amount of non-quartz and the extent of grain fracturing, as shown by samples with high abundance of non-quartz fractured to the same extent as a sample exhibiting little to no non-quartz cement. It could be that the assumption that calcite cement occurred early for all samples is false, but this goes against petrographic observations. If non-quartz cements precipitated contemporaneous with quartz

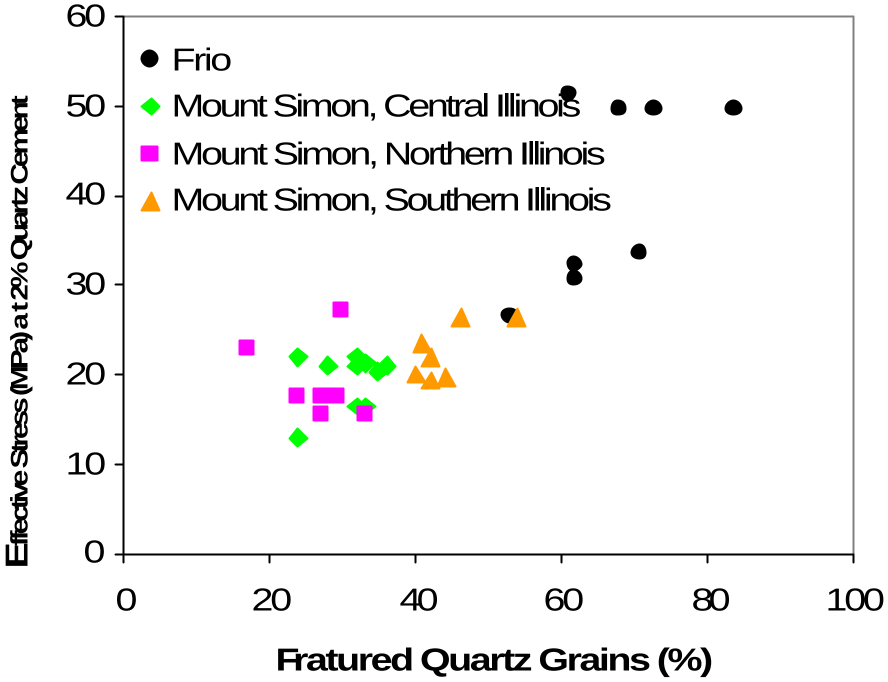

Figure 26. A positive correlation exists for effective stress at 2% quartz cement volume versus percentage of fractured quartz grains. Effective stress is calculated for normally pressured sediments at a given depth.

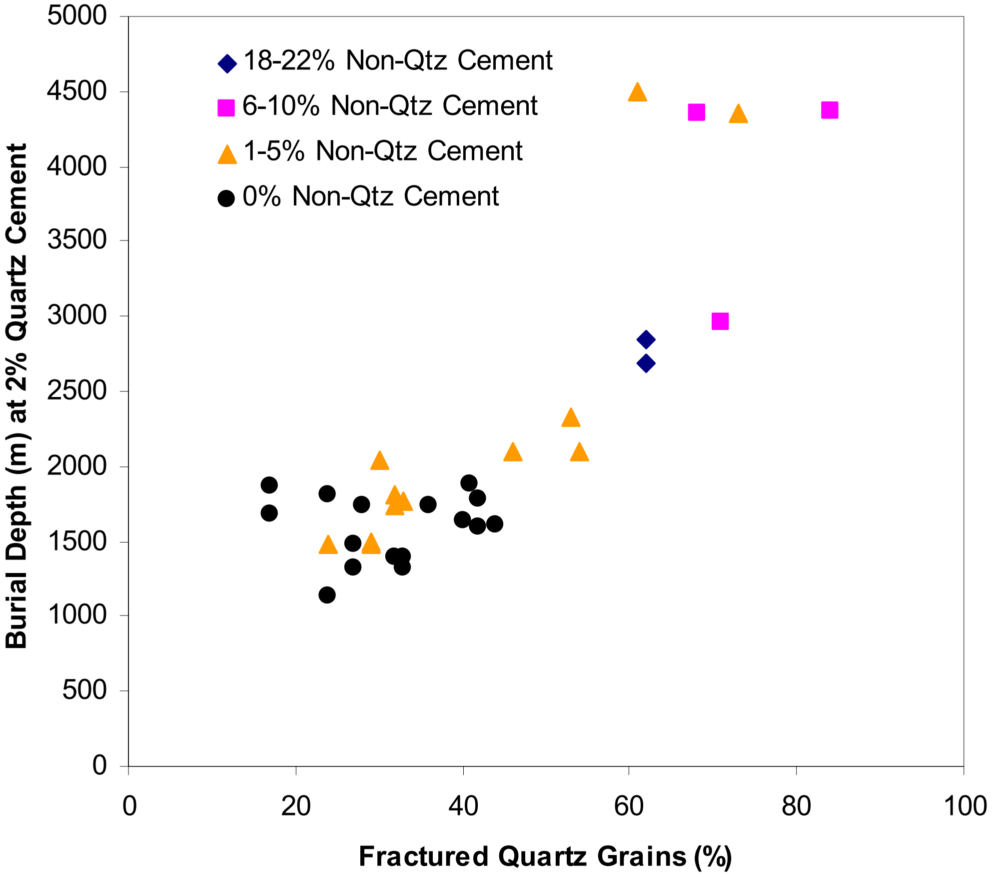

Figure 27. The abundance of non-quartz cement at depth where 2% quartz cement was reached. No correlation exists between the amount of non-quartz cement and the extent of quartz grain fracturing at the onset of cementation.

then non-quartz cements could act as a framework stabilizing agent. It is uncertain to elucidate the exact role of calcite cement also because it is not found in samples from all depths and is present in random amounts.

Cementation and Overpressure Influences on Grains Fracturing in the Frio Formation

Modeling results show that for samples presently > 4700 m depth (and more fractured), quartz cementation reached a critical 2% volume at > 4300 m burial depth and between 14-23 Ma, approximately 7-14 My after deposition. Therefore most fracturing likely occurred during the 7-14 My following deposition and during rapid burial before the framework was strengthened enough by cementation to halt considerable brittle deformation.

Quartz cementation for deeper samples occurred early in their burial history, suggesting that *most* grain fracturing is also an early phenomenon (after considerable depth was achieved) rather than a continuing process, where *most* fracturing occurs in the first few million years after deposition. The samples that are the deepest and most fractured also had the least amount of quartz cement at any given depth. Consequently, they were probably less rigid when exposed to effective stress and has the fastest effective stress/m.y., resulting in more fracturing. Fracturing is not completely halted during the later burial history as observed in thin-section by fractures transecting quartz overgrowth cement.

However, fracturing may slow down after burial and cementation commences, as suggested by the small percentage (<5%) of fractures crosscutting overgrowths.

Conceptual Model for Brittle Deformation

Figure 24 shows a better statistical correlation between the percentage of fractured quartz grains and the burial depth at 2% quartz cement than at 0.5% and 1% quartz cement, suggesting that fracturing proceeds where there are very small volumes of quartz cement. The four deepest samples in the Frio show a large distribution of fractured quartz grains for very similar depths (4300-4700 m). A plot of the percentage of fractured quartz grains versus total present volume of quartz cement for the samples in this depth range yields a positive trend, such that the more fractured samples contain more quartz cement (Fig. 28). Samples with more quartz cement also have a larger proportion of quartz grains, inherently behaving more brittly compared to samples with fewer quartz grains and more ductile grains that promote a cushioning effect within the framework. Both of these points indicate that small amounts of quartz cement may actually encourage brittle deformation. A very small amount may prohibit grain sliding and rotation, as well as increase the rigidity of the framework, thus enhancing brittle grain deformation. Quartz cementation continues and after a significant volume of quartz cement has precipitated, grain fracturing ceases.

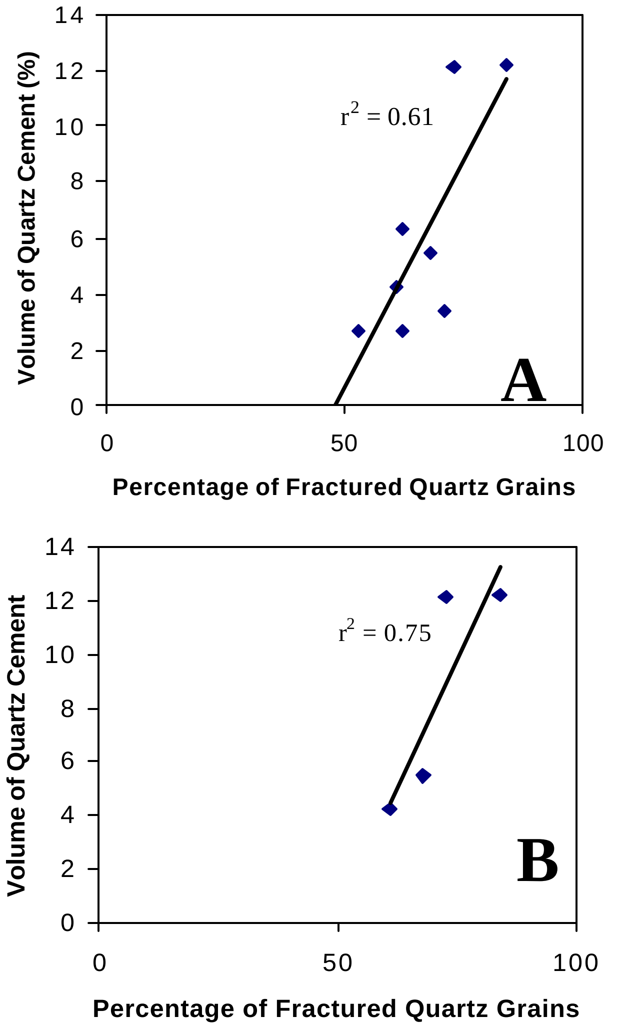

Figure 28. A) Plotting total present amount of intergranular quartz cement versus percentage of fractured quartz grains shows a positive correlation. B) the trend is stronger for the deepest samples (between 4300-4700 m), which did not show a trend between depth at 2% quartz cement and fractured quartz grain percentage, suggesting that the presence of more quartz cement may actually encourage brittle grains deformation.

Interestingly, experimental compaction literature only mentions cement as a grain stabilizing agent. Experimental studies show that cement has a large influence on grain and glass bead breakage, with cement stabilizing the framework and thus broadening the stress concentrations at grain-grain contacts and lessening the chance for fracture (Bruno and Nelson, 1991; Dvorkin et al., 1994; Yin and Dvorkin, 1994; Wong and Wu, 1995; Menendez et al., 1996). However, cement varies in compositions, distribution, and amount. Cement, even in small quantities, significantly increases the strength of granular material. The amount is maybe less important than the location where cement is deposited, for example, small amounts of cement precipitation close to grain-grain contacts is the most effective inhibitor of grain breakage (Bernabe and Hayes, 1992). The material properties of the cement and its geometry are also important. Where documented, the volumes of cement in these experimental studies range from ~3 to 10%. However, this study has looked at the effects of lower volumes of cement on grain fracturing.

The volume of quartz cement that changes the sandstone properties from encouraging brittle grain fracturing to inhibiting grain fracturing is not known but probably is 2 volume % or more . It may also be expected that with large amounts of quartz cement and high effective stress, the fracture style changes from intragranular to transgranular fracturing. During transgranular fracturing, cement has substantially increased the rigidity of the framework grains, so that they behave as one mass, transmitting stresses through continuously aligned grains. Intragranular fractures were predominantly observed in this study.

Here, a conceptual model is proposed that encompasses ideas discussed above (Fig. 29): (1) during the initial stages of burial grain sliding and rotation dominates compaction with little grain breakage occurring because grains are loose and free to move and rearrange as stresses are exerted on them (Fig. 29B). (2) Later during burial, a small amount of quartz cement (<2%) stabilizes the framework reducing the amount of slippage between grains and they begin to exhibit brittly behavior when stress accumulates at grain-grain contacts. The volume of cement is too small to hinder grain breakage and it actually promotes grain breakage (Fig. 29C). (3) After some time, a significant amount of quartz cement has precipitated to counteract all stresses and it stabilizes the framework to alleviate any significant brittle deformation (Fig. 29D). (4) As the differential stresses become very large (by influence of very deep burial or perhaps tectonism), the strength of the bonding cement between the grains is overcome resulting in transgranular fractures (Fig. 29E).

Mount Simon Formation

Variation in Fracture Trend and Style Compared to the Frio

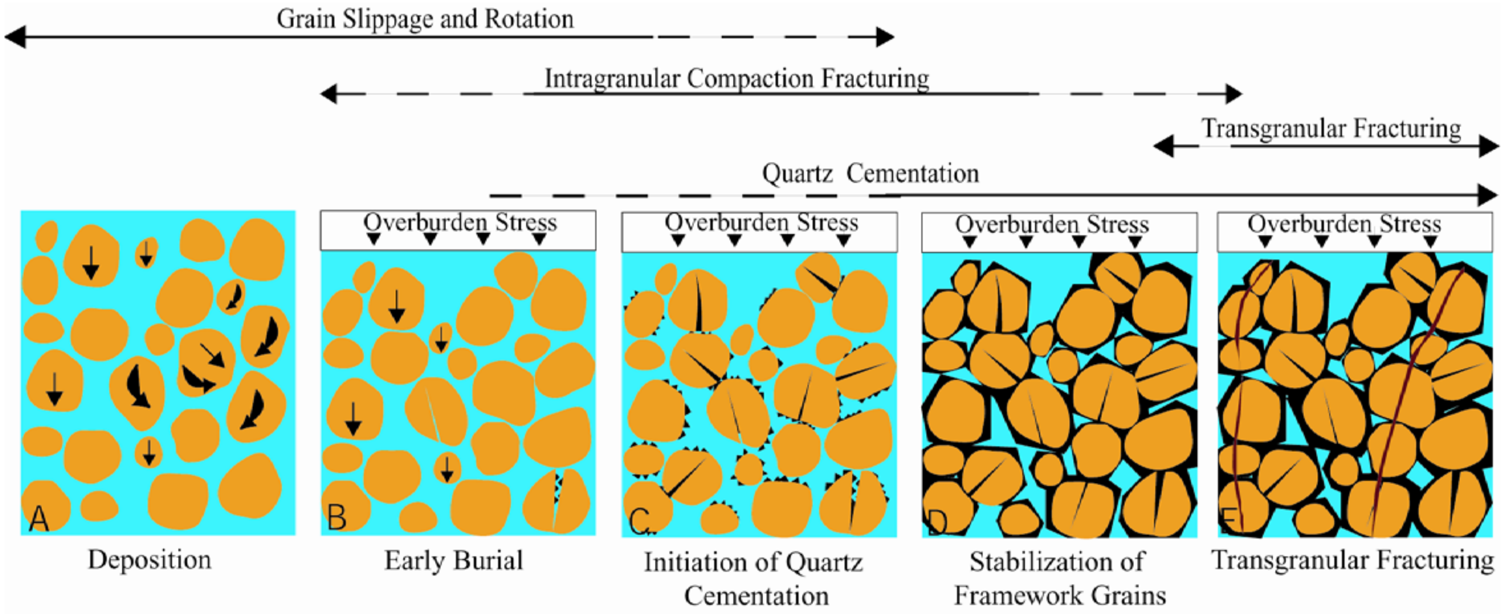

Figure 29. Sequence of schematics illustrating progressive brittle deformation characteristsics with increasing burial and volume of cement. A) Quartz sand upon deposition exhibits high depositional porosity. B) During early burial, compaction is mostly manifested by grain roation and slippage and some brittle deformation. Arrows in A and B show movement and rotation directions of grains. C) After sufficient temperatures are reached to initiate quartz cementation, the framework grains become more rigid by small amounts of incipient overgrowh precipitation, encouraging brittle deformation of grains. D) After significant amount of quartz precipitates, the rigidity of the framework increases so that fracturing slows down. E) Quartz cmeent continues to precipitate. However, if the differential stresses in the rock become large (as by deeper burial or the influence of tectonic stress), transgranular fracturing occurs.

Quartz cementation volumes reached 0.5, 1.0, and 2% volume at shallower depths in the Mount Simon compared to the Frio (Tables 5 and 6). This observation suggests that the depth reached when quartz cementation begins to proliferate could be a control on the different fracture styles between the Mount Simon and the Frio, where shallower cementation produces thin-straight trace fractures and the deeper onset of quartz cementation allows for wider apertures. IGV differences, with lower IGV's for the Mount Simon samples (18.6%) compared to the Frio (24.8%) (Tables 3 and 4) may also control the differences in fracture styles as well as the presence or absence of pressure solution in theMount Simon and Frio Formation respectively, which in essence influences the IGV.

In the Mount Simon formation, a 2% volume of quartz cementation was not reached until 139-323 Ma after deposition and thus, the sand grains were buried far longer than the Frio Formation (5-26 Ma) grains. One would presume that more fracturing may have occurred over a longer time interval, before quartz cement commenced in the Mount Simon, but results do not suggest this. However, the Mount Simon exhibits pressure solution and the Frio shows no evidence of chemical compaction. It has been proposed by observation, modeling and experimentation that brittle processes may play a role in pressure solution (Gratz, 1991; den Brok and Spiers, 1991; Milliken, 1994). It is unclear to what extent brittle processes may contribute to pressure solution, especially in the

Table 6. Time, depth, and partial temperatures at intervals of 0.5%, 1%, and 2% quartz cement in the Mount Simon Formation.

Mount Simon			**0.5% qtz cement**			**1% quartz cement**			**2% quartz cement**		
	sample	**% qtz frac.**	**time***	**depth***	**Eff. Stress***	**time***	**depth***	**Eff. Stress***	**time ***	**depth***	**Temp***
Central	3581.5	32	408.0	1389	16.5	372.0	1608	19.3	333.3	1735	69.8
	3619	33	438.0	1056	11.8	408.0	1389	16.5	372.0	1389	65.6
	3793	28	415.5	1306	15.3	384.0	1537	18.4	333.3	1735	69.8
	4038	33	408.0	1389	16.5	372.0	1608	19.3	320.0	1763	70.6
	4119	32	384.0	1537	18.4	346.7	1706	20.7	302.7	1811	72.8
	4226	24	396.0	1465	17.4	360.0	1677	20.3	302.7	1811	72.8
	4469	32	460.3	888	9.7	438.0	1056	11.8	408.0	1389	57.7
	4477	24	482.7	711	7.6	460.3	888	9.7	430.5	1139	51.0
	4720	36	415.5	1306	15.3	384.0	1537	18.4	333.3	1735	69.8
	5404	35	438.0	1056	11.8	396.0	1465	17.4	360.0	1677	67.9
Northern	1164	27	423.0	1035	12.0	360.0	1170	13.6	268.0	1321	60.5
	1277	17	261.9	2095	24.2	247.3	2116	24.9	192.3	1864	93.6
	2019	30	302.7	1460	17.2	247.3	2236	26.6	206.1	2043	98.5
	2166	29	423.0	1212	14.0	384.0	1315	15.4	285.3	1475	64.9
	2384	24	423.0	1136	13.0	384.0	1315	15.4	285.3	1475	64.9
	2480	29	423.0	1212	14.0	360.0	1342	15.7	268.0	1489	65.6
	3134.5	33	460.3	1117	12.8	438.0	1136	13.0	384.0	1315	60.4
	3177	27	423.0	1212	14.0	360.0	1342	15.7	285.3	1475	64.9
Southern	6154	44	392.0	1150	13.5	376.0	1315	15.6	350.0	1614	85.1
	6235	42	392.0	1180	13.9	376.0	1344	16.0	340.0	1780	91.0
	6241	40	392.0	1182	14.0	376.0	1346	16.1	350.0	1645	86.1
	6497	42	392.0	1273	15.2	376.0	1436	17.3	360.0	1593	83.8
	6500	41	392.0	1286	15.4	360.0	1605	19.6	340.0	1881	94.2
	8466	54	418.0	1600	19.4	392.0	1941	24.2	376.0	2093	99.8
	8468	46	428.0	1418	16.8	408.0	1781	22.1	376.0	2093	99.8

*time=my, depth=m, effective stress=MPa, temperature=C

Mount Simon. Samples demonstrate much lower IGV's (18.4%) than can be achieved by compaction alone (Paxton et al., 2002), which may be evidence for the occurrence of pressure solution. Lower overall IGVs compared to the Frio (24.8%) prohibit less opening of fractures, resulting in the observed thin fracture apertures observed in the Mount Simon.

The initiation of significant quartz cement precipitation can explain the differences between fracture styles and morphology between the two formations. It is suggested in the most of the Gulf of Mexico that the onset of overpressure occurred late (2-3 Ma) by predominantly compaction disequilibrim. The effective stresses for these samples were much higher than in the Mount Simon, resulting in more fracturing. Calculating the effective stress and plotting them against depth at 2% quartz cement, shows a positive correlation. Samples subjected to higher effective stresses are more severely fractured than samples at lower effective stresses that exhibit less fracturing, suggesting that overpressure occurred later during the burial history (Fig. 26).

CONCLUSIONS

- A conceptual model for brittle deformation and the effects of quartz cementation is proposed to explain trends of grain fracturing observed in the Frio Formation. Utilizing Touchstone, the depth at which a volume of quartz cement of interest is reached is retrieved. Combined observational quantification and quartz cement modeling results indicate that a very small amount of quartz cement (0.5%–2%) promotes brittle grain deformation, whereas a larger (=2%) quartz cement volume reduces grain fracturing. More data are needed to substantiate this conceptual model fully, as no proper control on the effective stress history exists for the Frio. To validate the model, a larger data set is needed for statistical significance. To grasp the influences on varying amounts of cement on grain breakage, the optimal data set should be compositionally similar and have been subjected to similar effective stress with a range in quartz cement volumes. However, results for the Frio look promising and further study should be conducted to substantiate them.

- For the Frio, a larger number of quartz grains are fractured in deeper samples than at shallow depths. Three factors may control this observation: (1) overpressure developed late, after grains had been subjected to high effective stresses (deeper burial) for some time. (2) Considering that overpressure developed late, present deeper samples also had small amounts of cement after deep burial. The influence of very small amounts of quartz cement combined with higher effective stresses and loading rates may have lead to more grain fracturing for deeper samples compared to shallow ones. (3) Composition and texture influences the amount of fractured grains in deep samples, where compositionally quartz-rich samples with coarser grain sizes are more fractured than samples containing more lithics. Fracturing is more extensive for samples with a higher brittle grain content.

- Fracturing in the Mount Simon and Frio formations occurred before 2% quartz cement was precipitated, evidenced by very few fractures (<5%) crosscutting quartz cement around original detrital grain surfaces. However, few fractures that *do* cross-cut the overgrowths suggesting that fracturing is not completely halted by modest cementation.
- The differences in grain fracturing trends with depth and fracture morphologies between the Frio and Mount Simon formations can be attributed to: (1) depth and timing of quartz cementation commencement, caused quartz cementation to occur more deeply in the Frio than in the Mount Simon, allowing for more and wider fractures and apertures in the Frio; (2) IGV differences, where lower IGV's in the Mount Simon resulted in less possibility of expansion of fractures into the pore space, hence thinner fracture apertures.
- Non-quartz cements do not affect the grain fracturing by halting grain breakage. However, it is uncertain to what degree a cement phase influences grain stabilization or not. It is uncertain to tell the exact role of

calcite cement also because it is not found in samples from all depths and is present in random amounts.

IMPLICATIONS

Ultimately, it is desirable to be able to predict the timing of fracturing in the subsurface in order to predict reservoir quality. The timing of fracturing can be critical, because fractures, when open, provide avenues for fluid flow, whereas when sealed they reduce porosity. Conventional models that ignore knowledge of fracturing may either over- or under-predict reservoir quality. Understanding the occurrence of fracturing can aid in the prediction of porosity distribution or occlusion, especially in deeper reservoirs.

Chapter 4: Structural Diagenesis Along the Pine Mountain Overthrust: Using Scanned Cathodoluminescence to Elucidate Particle Size, Cement Distribution, and Texture of Cataclastic Sandstones

In this chapter scanned SEM-CL imaging is used to examine a cataclasite containing deformed sandstones and to retrieve particle size distributions, cement occurrence and abundance, and texture of cataclastic pieces. Particle size distributions (PSD's) of deformed crystalline and granular rocks in both natural settings and experiments have been found to evolve through cataclasis toward a self similar distribution following a power law with fractal dimensions (*D*) ranging from 1.7 to >5 (e.g., Sammis et al., 1987; Blenkinsop, 1991; Rawling and Goodwin, 2003). The power law equation is

$y=ax^D$ (17)

where y is the intercept of the best fit line on the y-axis representing the cumulative frequency of grain size, a is a constant, x is the intercept of the best fit line on the x-axis where y representing the mean of the size range, and D is the slope of the line and the power law exponent (Marone and Scholz, 1989). It has been widely observed that the average three dimensional *D* for clastic gouge rocks is approximately 2.6. Fourteen samples of natural quartz-rich fault gouges found in the Pine Mountain Overthrust, Eastern Kentucky, have *D*-values ranging from 2.5 to 3.2 with an average of 2.8 for particle sizes ranging <1 µm to 1 mm.

Common methods used to determine particle size distributions are either: (1) sieve analysis to determine weight abundance for each grain size or (2) direct measurements from a 2-D thin-section using plane light microscopy and corrected to 3-D dimensions. For this study, a scanning electron microscope (SEM) equipped with a cathodoluminescence (CL) detector was used to collect high-magnification images that allow discrimination between detrital and authigenic quartz, therefore resulting in the quantification and measurement of smaller fragments than previous methods. This imaging method also provides insight on the timing of deformation and quartz cementation, by revealing cross-cutting relationships between fractures and cement stratigraphy. In addition, this high-magnification imaging technique suggests a smaller comminution ("grinding") limit for quartz than previously observed. At the least, this very small apparent grinding limit shows that one must be aware that determining the minimum particle size may, in fact, be limited by the resolution of the measurement technique.

Quantitative data like *D*-values and comminution limit sizes in gouges can also provide information on reservoir quality properties such as the evolution of porosity and permeability. Cataclasis drastically decreases pore aperture in sandstone as a result of grain and overgrowth spalling (Pittman, 1981). Decrease in particle size can result in significant local reduction of porosity and permeability in reservoir rocks, which can create flow barriers within reservoirs (Jamison and Stearns, 1982; Antonellini and Aydin, 1994).

Crushing of quartz grains increases the surface area to volume ratio of the rock by producing a large number of fine quartz particles. Increase in surface area is expected to influence quartz cementation. Exploration of the link between grain size and quartz cementation was conducted using Touchstone™ diagenetic modeling software. Touchstone™ can utilize grain size-dependent activation energy for calculating quartz cement precipitation that results in faster growth of quartz cement per surface unit area around coarser grains compared to finer grains, consistent with observations of Makowitz and Sibley (2001). Characterizing the distribution of quartz cement in deformed rocks compared to undeformed (outside the fault zone) rocks nearby and may help to determine if these deformed zones act as silica importers or exporters. Through combining petrographic observations and Touchtone modeling results, it is possible to constrain the timing of cementation and deformation. Understanding the relationship between deformation and cementation is important for assessing the hydrological role of faults (e.g., fluid conduits versus seals).

INTRODUCTION TO FRAGMENTATION

As discussed in the previous chapters, fragmentation (or crushing, fracturing) of natural granular material is a function of numerous parameters, such as grain size (Borg et al., 1960, Gallagher, 1974; 1987, Zhang, 1990, Brzesowsky, 1995, Lade et al, 1996, Chuhan et al, 2002, Makowitz and Milliken, 2003), particle shape (Pittman, 1981; Michibayashi, 1996; Cladouhos, 1999; Tang et al., 2001), porosity (Dunn et al., 1973; Wong et al., 1990; Zhang et al, 1990; Bernabe and Hayes, 1992), cement presence, type and amount (Dunn et al., 1973; Bruno and Nelson, 1991; Bernabe and Hayes, 1992, Dvorkin et al, 1994; Yin and Dvorkin, 1994; Wong and Wu, 1995; Menedez et al., 1996; David et al, 1998), sandstone composition (Makowitz and Milliken; 2003; Lander, personal communication) and follows opening -mode I fracture style. Particle size distributions of cataclasites commonly follow a fractal distribution in terms of the number of particles versus their size. Mathematically this means that the relationship between particle size and frequency is described as power law (straight line between the two parameters on a double log plot).

Cataclasis is a common deformation mechanism in the upper crust and typically occurs under conditions of high deviatoric stress, low temperature, and low confining pressure (Mitra, 1988). Particle-size distributions in natural catacaslites from lithified sedimentary and crystalline rocks have been studied by Sammis et al. (1987), Sammis and Biegel (1989), An and Sammis (1994), and Monzawa and Otsuki (2003), and show an average *D* of 2.6, which Sammis et al. (1987) state as the “steady-state” PSD. Experimental cataclasis simulations of unlithified sand (Marone and Scholz, 1989), sandstone (Sammis and Biegel, 1989), and numerical simulations (Morgan and Boettcher, 1999) find *D*-values in agreement with natural cataclasites. A study from cataclasis simulation suggests that reduction in particle size is correlated to total strain for relatively small strains (? ranges between 0 and 3.3) (Marone and Scholz, 1989). Some of the earliest cataclasis experiments by Engelder (1974) show that the proportion of finer fragments increases with displacement and confining pressure. The PSD's for naturally deformed and poorly lithified sediments, subjected to a lower confining pressure (~ 7 to 11) have *D* ranging between 1.7 and 2.1 (Rawling and Goodwin, 2003).

Sammis et al.(1987) propose that the significance of *D* equaling 2.6 as a result of comminution is that this is the value at which the likelihood of breaking a given grain increases when neighboring grains are of like size, which is consistent with "survivor" grains observed in deformation bands (Milliken and Reed, 2002). Sammis et al. (1987) suggests that the significance of 2.6 is that the probability of same-size grains being adjacent to each other becomes smallest at this value, meaning that the sorting is lowest at this value.

It has been documented and numerically simulated that as the comminution process continues, the probability for fragment to break diminishes as the average fragment size approaches the grinding limit for that designated mineralogy (An and Sammis, 1994; Ozkan and Ortoleva, 2000). The suggested grinding limit for quartz is 1.7 µm (Kendall, 1978; Prasher, 1987); however, other experimental results indicate the minimum size may actually be larger (6.8 µm) for quartz (Hadizadeh and Johnson, in press). Fragmentation comes to a halt in regions of the deformed zone where particle-size has reached the mineral grinding limit. A larger than steady state D (2.6) can be caused by the grinding limit effect, where particles pile up at this limit (An and Sammis, 1994). It has been suggested that the grinding limit occurs because finer particle-size fractions might accommodate more strain by rolling (Morgan and Boettcher, 1999). This is consistent with deformation bands, in which particles derived from a common grain have rotated and moved parallel with the shear direction (Milliken and Reed, 2002).

For clarification purposes, although the term “fault gouge” is used by some authors describing rocks deformed within fault zones, but because of its variation in meaning in the literature, either deformed sandstone or cataclasite are used as terms in describing the PMO fault rock.

REGIONAL AND LOCAL GEOLOGY

Geologic History of the Appalachian Basin

The Appalachian basin is a multi-stage foreland basin bounded by Taconic (450 Ma, Ordovician), Acadian (410-380 Ma, Devonian), and Alleghenian (320-

260 Ma, Carboniferous) overthrusts in the adjacent Appalachian Mountains. The Alleghenian Pennsylvanian-Permian orogeny is the most important deformation event in terms of present structure and depositional style (Quinlan, 1984). The Alleghenian produced a series of overthrusts (striking in a generally easterly to northeasterly direction) associated with the closing of the Iapetan Sea and the assembly of Pangea. Overthrust loads in the Appalachian Mountain system caused flexural downwarping of the lithosphere (Tankard, 1986; Beaumont et al. 1987). Erosion of the thrust sheets resulted in unloading and rebound of the lithosphere.

Systematic variability in thermal history exists across the Appalachian Basin as indicated by spatial variations of apatite cooling ages (Johnsson, 1986) and vitrinite reflectance on a regional scale (Nuccio, 1997). With controversy surrounding the possibility of fluids influencing existing thermal markers, the question arises whether thermal fluids overprinted shallowly buried sediments resulting in an erroneous depth indicator or if thermal indicators are diagnostic of true burial depth suggesting greater amounts of erosion. Uplift history constrains somewhat the possible fluid types that have interacted with the basin fill during burial diagenesis.

Several studies have documented the increasing regional thermal maturity from west to east across the northern, central and southern Appalachian basin.

This is attributed to the increasing thickness and increasing burial of sediments from west to east, with greatest values toward the orogen (Johnsson, 1986; O'Hara et al., 1990; Roden, 1990; Hower and Rimmer, 1991; Nuccio, 1997). On a local scale, O'Hara et al. (1990) used the Pennsylvanian Fire Clay Coal to decipher thermal trends on both sides of the Pine Mountain Overthrust (PMO) and used results to document the uplift history. Isograds follow the trace of the PMO with lower values in the hanging wall suggesting rapid cooling after thrust-sheet emplacement (> 3 km/Ma). This is inconsistent with apatite fission track data from the northern part of the PMO, suggesting that cooling did not commence until the Jurassic, with temperature remaining >60°C until the Late Cretaceous to Miocene (Boettcher and Milliken, 1994). Their data are consistent with apatite fission-track data from southwestern Virginia and Pennsylvania (Roden, 1990; Roden et al., 1993). Triassic-Jurassic age unroofing is contemporaneous with extension along the Atlantic continental margin. On the other hand, a regional study including the PMO of eastern Kentucky, using coal (Pennsylvanian age) rank trends suggests that uplift occurred in Early to mid Cretaceous (Hower and Rimmer, 1991).

Although variability exists in the timing of uplift using different methods, maximum burial depth values are in general agreement. Maximum temperatures experienced by the Pennsylvanian sandstones in the northern PMO exceeded

110°C ± 20°C and maximum burial depth of 3 km (Boettcher and Milliken, 1994), while O'Hara et al (1990) estimates 2.9-3.1 km maximum burial depth of Pennsylvanian age clay of the entire PMO locality. South of the PMO, in southwestern Virginia, Ordovician rocks indicate a maximum burial and maximum temperature of 3.4 km and 120°C respectively (Roden, 1990). Data from north (Virginia, West Virginia, and Maryland) of the PMO from Devonian age rocks have identical values (Roden et al., 1993).

Pine Mountain Overthrust

The PMO is the western-most Alleghenian-age structure in the Valley and Ridge Province crossing Virginia, Tennessee, and Kentucky and is considered to be a classic example of structural style in fold and thrust belts. It is contemporaneous with the Early Permian Appalachian orogeny (275 Ma), also deforming orogenically-derived clastic sediments of the Breathitt Group and Lee Formation deposited previous to deformation. The structural geometry consists of an east-northeast-striking major thrust that climbs from a detachment in the Cambrian Rome Formation through successively younger units and flattens into a detachment in the Devonian Chattanooga Formation, eventually reaching to the surface (Mitra, 1988). The surface exposure of the thrust sheet consists of a rectangular block about 125 mi (200 km) long and 25 mi (40 km) wide, bounded to the northwest by the Pine Mountain thrust and to the southeast by the Wallen

Valley and Hunter Valley thrusts (Mitra, 1988). The thrust sheet terminates to the southwest and northeast at two primary tear faults, the Jacksboro and Russell Fork faults, respectively. The total displacement associated with the Pine Mountain thrust system decreases from about 21.3 km (70,000 ft) at the southwestern end to less than 3.0 km (10,000 ft) at the northeastern end (Mitra, 1988).

Pennsylvanian Sandstones

Lower and Middle Pennsylvanian Breathitt and Lee formations quarztose sandstones are present in extensive outcrops along the Pine Mountain Overthrust (Fig. 32 for sample locations). The Lee Formation is composed of massive, largely quartzose sandstone and quartz-pebble sandstones, whereas the Breathitt Formation is the dominant coal-bearing formation and is made up of lithic sandstones, siltstones, shales, coal beds and underclays. The Lee Formation occurs as channel-fills and as large sandstone belts that flowed to the south (Greb and Chestnut, 1996). The largest portion of Lee sandstones occurs as four large sandstone lenses within the lower part of the Breathitt Group. The belts are approximately 80 km wide and 150 m thick and composed of a number of sandstone beds, typically 20-30 m thick. Lithologies of the Breathitt Group represent inland sea-fill (bay-fill) and coastal lowland environments, including distributary and meandering fluvial systems and swamps. See Appendix G for complete sample location descriptions.

Mineralogy and Diagenesis

Source rocks for Lee and Breathitt sandstones are composed of older siliciclastic, carbonate sedimentary, crystalline basement rocks and dominant mica-rich metamorphic lithologies (Fu et al., 1994). Products of diagenetic alteration include quartz, calcite and kaolinite cements, feldspar alteration (by albite, calcite, ankerite and kaolinite) and dissolution of primary feldspar and brittle and ductile deformation of quartz and feldspar grains and micaceous grains respectively (Milliken, 2001).

The timing of deformation relative to quartz cementation can be elucidated from descriptive information on deformation styles using CL imaging and distribution of quartz cement, illustrating that cementation occurred during and after deformation. Deformed samples collected in the fault zone show quartz cement predominantly localized within grains (*intra*granular) with little quartz cement around detrital grain surfaces (*inter*granular). The extensional style of grain deformation is similar, but more severe, to that seen in the relatively porous Frio Formation (Chapter 2, Gulf of Mexico Basin), with opening mode I style fracturing and extensive localized comminution of grains.

METHODS

Sample Collection

Samples were collected along the PMO spanning the entire 200 km length (Fig. 30). The fault itself is not exposed, only the deformed sandstones in sparsely distributed outcrops. Cataclasites are discontinuous along the PMO and crop out as pods ranging from a few tens to hundreds of meters in length. Sampling proved difficult in the sense that outcrops are highly vegetated. Accessibility to deformed outcrop is also limited because of the steep dip of the beds and cliff faces along the PMO, therefore the majority of samples are from large road cuts or recreation areas containing dirt roads. Cataclasites were identified by their uncharacteristic sandstone appearance: bedding is disturbed and coloration of outcrops appears altered and locally faint semi-linear and anastamosing deformation bands are observed. Fourteen cataclasites were collected from 11 outcrops. Eleven out of 14 deformed samples are quartz-rich Lee Formation and the remaining three are from the more lithic-rich Breathitt Group. Thirty-one undeformed sandstones (not affected by faulting) were also sampled within the region, of which six are from the Lee Formation and 25 from the Breathitt Group.

Imaging Techniques

Conventional methods used to assess particle-size distributions in fault rocks are flawed in the sense that: (1) sieve analyses disaggregates the rock and therefore does not preserve the original spatial relationships and disaggregating

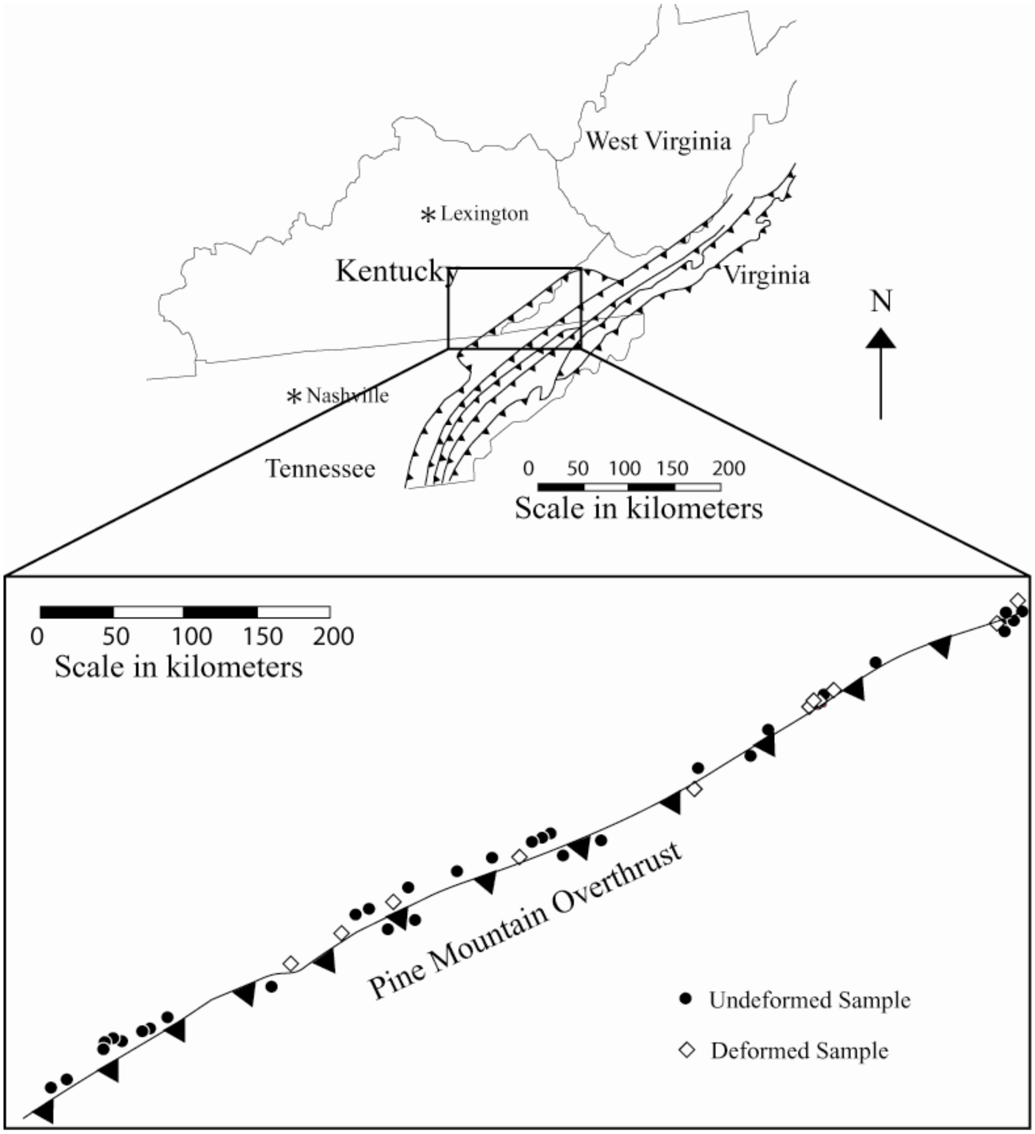

Figure 30. Regional map of the southern Appalachian area showing the PMO as the northeastern-most thrust fault of the southern Appalachian orogen. Zoomed area shows the sample locations of all deformed and undeformed samples used for this study, extending the 200 km length of the PMO.

may produce more and smaller fragments that are not in the original gouge; (2) 2-D thin section measurement using conventional optical microscopy does not provide the magnification necessary to observe the finer fragments and in the case for quartz-cemented quartz-rich cataclasite, the cement cannot be discriminated from the fragments, this may result in inaccurate particle sizes. In addition, only apparent sizes are seen in 2-D and the distribution in 3-D is directly studied.

Particle sizes for this study were obtained from thin-section by scanned cathodoluminescence (CL) imaging on an environmental scanning electron microscope (ESEM). Both color (red, green, and blue=RGB) filter images and panchromatic (black and white) CL images were collected and compiled as collages representing an area of 3.4 mm^2. RGB CL images render more detailed information than panchromatic images, such as the relative timing of cross-cutting fractures and cement (Laubach et al., 2003). However, RGB CL images require a substantially greater acquisition time, therefore, only 50 percent of the images collected are RGB. The ESEM is capable of higher magnification imaging, than conventional methods like microscope-mounted-CL or plane light microscopy.

Because CL imaging discriminates between quartz cement and the quartz grain, the correct apparent fragment size can be measured. This is important because the sandstones are well-cemented, with whole-rock quartz cement values for the deformed samples averaging ~10%. Thin-sections were made from whole rocks, allowing for observation of spatial relationships between fragment and cement. The large volume of cement allows for the preservation of deformation features that may be partially obliterated during the thin-section preparation of less cemented samples.

The term "fragment" is used to describe a piece of an original grain broken by cataclasis, whereas the term "grain" refers to an unfractured sand grain.

Secondary electron imaging was conducted on broken pieces of the gouge using the JEOL T330A SEM at 30 kV accelerating voltage. This was done to retrieve higher resolution information on particle size, where the resolution limit is <0.1 µm.

Data Collection

Once placed on the ESEM, random locations were selected for imaging. The ESEM is a fully automated system allowing for the input of coordinates for precise location or outlining of the thin section in the sample chamber. The *x* and *y* coordinates of the four corners of the thin-section were determined followed by randomly selecting *x* and *y* positions on the thin-sections using a random number generator in Excel™. Four random locations of every thin section were imaged, with each area about 3.4 mm^2, of which one random 3.4 mm^2 collage is used for particle measurement (Fig. 31). The number of fragment sizes measured ranges from 722 to 1590 per thin section, depending on fragment sizes. The presence of

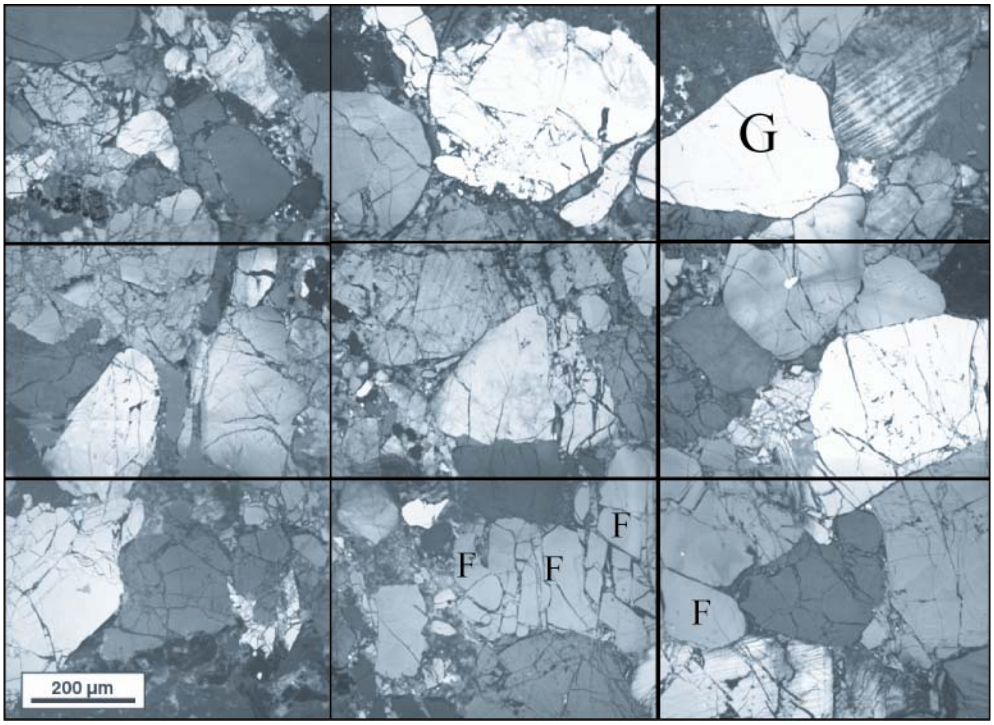

Figure 31. An example of a collage compiling nine SEM-CL images taken at 150x and representing an area of 3.4 mm^2. Sample 38a. Nine images were compiled using Panavue®, an image stitching software. G represents a grain with some fractures. F's represent fragments which are pieces of an original grain.

a larger number of smaller fragments results in more measurements, whereas a larger number of large fragments results in fewer measurements.

It proved too difficult to automate fragment measurements by software image analysis tools because boundaries of the smallest discernible fragments are too ambiguous for automated fragment recognition. Also, for the image analysis tool to work correctly, a fragment of certain luminescence must be surrounded by a dissimilar luminescent fragments or cement, to be distinguished as an individual fragment. The discrimination of the trained user's eye is better for deciphering individual fragments from one another. It proved much easier to manually measure fragments.

The UTHSCSA Image Tool® was used to acquire fragment-size measurements measured manually from images. A grid with nine boxes was overlain on the images to facilitate tracking of fragment measurements (Fig. 31). The ruler in the software program is calibrated to the image scale. Maximum fragment diameters are measured to represent grain size. Each measurement is stored in the program and the compilations of measurements were exported into Excel upon completion of fragment size measurements.

The minimum detectable fragment size using scanned CL imaging in this study is ~ 1 µm. To better quantify fragment sizes, pieces of the deformed sandstone were mounted and imaged in the SEM at magnifications ranging from

2000 to 20,000X, allowing for higher magnification than CL imaging. Larger fragments (> 5 µm) were identified by their concoidal fracture whereas small fragments have euhedral shapes. Prismatic morphology of the smaller fragments indicates that these pieces are covered with euhedral overgrowths (as confirmed by CL-imaging). The maximum lengths of the crystals were recorded for size. The fragment size is smaller than this because crystal size includes the fragment plus the cement.

The actual fragment size is determined by considering a linear grain-size versus quartz cement-abundance relationship, where the larger grains have thicker overgrowths, compared to smaller grains with thinner overgrowths, as documented by Makowitz and Sibley (2001). Fifty random measurements from CL images of the Breathitt and Lee sandstones show this relationship between grain size and overgrowth thickness (Fig. 32). The resulting regression line was then extrapolated down to the 0.1 µm grain size range, showing that the ratio of grain to overgrowth is 5:1. Therefore a crystal of 0.1 µm in size has an overgrowth of 0.017 µm, yielding a true particle size of 0.08 µm.

Quantifying Sandstone Components

Quantification of sandstone constituents was obtained by laying a grid with 400 intersections on each CL collage (used for the PSD analysis). At each intersection, the presence and type of mineralogy (or absence in the case of

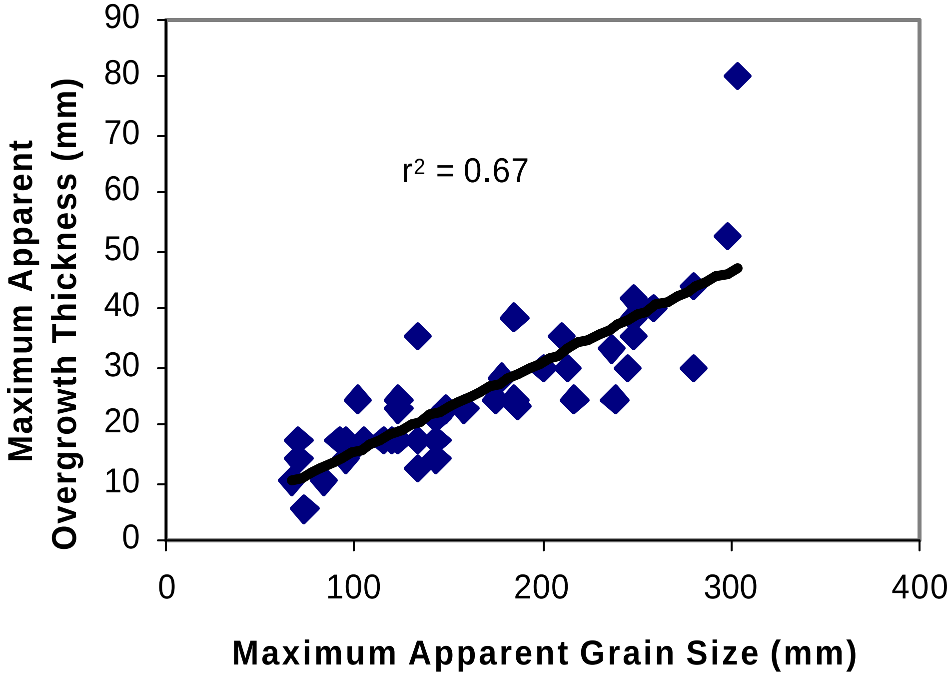

Figure 32. Maximum apparent grain size versus maximum apparent overgrowth thickness. A positive correlation exists between maximum apparent quartz grain size and maximum overgrowth thickness. Considering this relationship, the overgrowth thickness can be approximated by extrapolating the regression line to obtain sizes of fragments that are found underneath overgrowths.

porosity) was tabulated, as is done by conventional points conducted using plane light. Four collages were point counted for each thin section resulting in a total of 1600 point counts per thin section.

Stereological Correction and Plotting Data

Measurements collected from a 2-D thin-section must be corrected for the stereological effect. Grain diameters measured in 2-D represent maximum apparent fragment diameters because grains are sliced randomly during the thin-sectioning process, not necessarily through their centers. A thin section is a small representation of an entire outcrop or hand sample, therefore, it is impossible in thin section to retrieve absolute information on the largest grain size because localities chosen for thin–sectioning may not intersect the maximum fragment size or represent the absolute correct frequency of fragment sizes. The frequency of the smallest fragment sizes is also commonly underestimated because of incomplete sampling due to resolution limitations, a sampling effect called truncation. This is also problematic in measuring fracture aperture spacing from outcrops (Marrett, 1996).

A 3-D model is constructed that takes the above mentioned problems into account (Marrett, 1996). Particle size distributions, following a given power law exponent (in the particle size range measured), are generated for grain sizes measured in 3-D space, following a user-given *D*, and plotted on a double log plot with particle size on the *x*-axis and the cumulative number on the *y*-axis, resulting in a straight line. Next, random slices of the 3-D fragments are calculated, which provides fragment diameters equal to or less than the true diameter (random sliced grain diameters are the apparent grain diameters). A random selection of apparent grain diameters is made and plotted on the double log plot. This plot of randomly picked and sliced grains should result in a similar-shaped plot as for actual pieces measured in 2-D thin section. By changing the *D*, actual measurements taken from thin-section are matched up with the randomly selected and modeled 2-D measurements following the *D*-value chosen. A *D* is sought for which thin-section grain-size measurements match modeled 2-D measurements most closely (Fig. 33).

RESULTS

Particle Size Distribution

Quartz-rich fault gouges deformed within the PMO have particle size distributions following the power law with *D* ranging between 2.5 and 3.2 and average of 2.8 (Table 7). This average correlates well with results by Sammis et al. (1987). The lowest *D* of 2.5 is comparable to the lowest *D*-value found by Sammis et al. (1987) (*D*=2.4). Particle-size measurements for the *undeformed* Breathitt and Lee sandstones follow a normal to slightly-log-normal distribution. Samples derived from the same outcrop (sample 38-a thru 38-c) have values for *D*

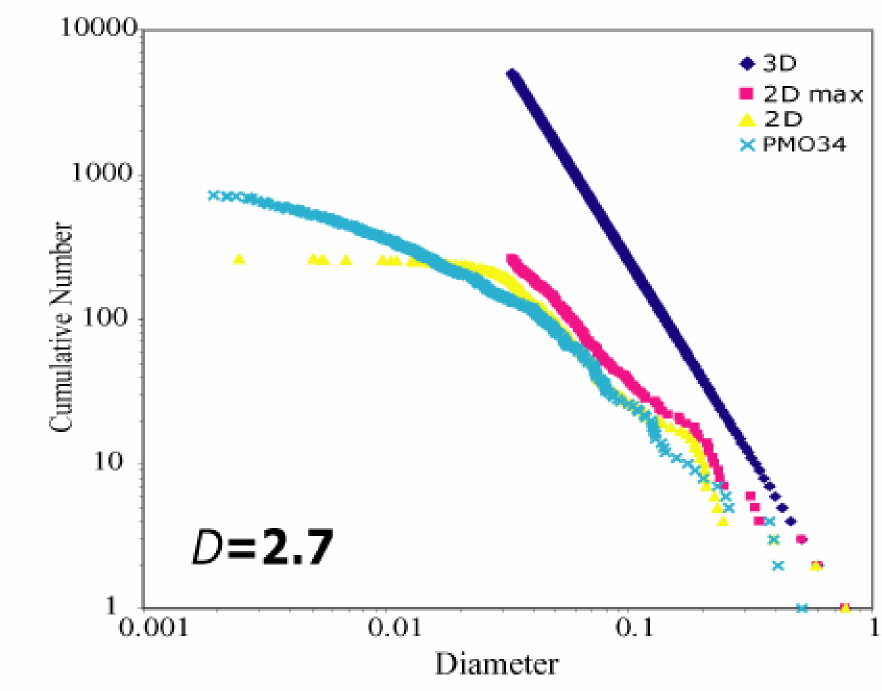

Figure 33. A graph representing the modeled and measurement results for a particle-size distribution. Three-D measurement following D= 2.7, are represented as a straight line on the log-log plot. The modeled 2-D values are represented by the yellow symbols. The red symbols (2-D max) are the upper limit values that 2-D measurements cannot exceed. The turquoise symbols represented 2-D measurements from collages. The 2-D measurements best fit the modeled 2-D values at D=2.7.

Table 7. Particle size distribution data for the 14 deformed samples.

Sample	D-value	Number of counts	Area (mm)
11	2.7	1323	3.4
16	2.8	1309	3.4
16b	2.7	1359	3.4
19	3.0	1426	3.4
23	3.0	948	3.4
34	2.7	1590	3.4
37	2.7	728	3.4
38a	2.9	1401	3.4
38b	2.8	1008	3.4
38c	3.0	1013	3.4
39	2.5	1007	3.4
41	2.7	1422	3.4
44	3.1	948	3.4
50	3.2	727	3.4
Average D	**2.8**		

ranging from 2.8 to 3.0 and an average of 2.9, demonstrating the range of error in measurement.

Values for *D* are independent of displacement across the fault zone, with the southwestern part of the PMO experiencing substantially more displacement compared to the northeastern portion. Sample locations could only be placed in regional context to the fault, exact positions within the fault zone could not be determined. Variability in *D* found in the samples could reflect heterogeneity of strain within the fault zone and not total displacement at a specific locality along the fault zone (Fig. 34).

Spatial Distribution of Particles

Grains within the fault region are all deformed to some degree, with most grains exhibiting extensive fragmentation and fracturing. Some samples have many fragments for which the original grains can be mostly reconstructed, whereas others have undergone more severe deformation, i.e., small fragments rearranged around larger fragments (Fig. 35). In some places, fragments derived from one grain are found within microfractures of another fragment, suggesting that fragments derived from one grain were still mobile (uncemented) at time of crack opening in another nearby fragment.

Some areas investigated have undergone extensive deformation where few original unfractured grains remain. Large “survivor”-like fragments are

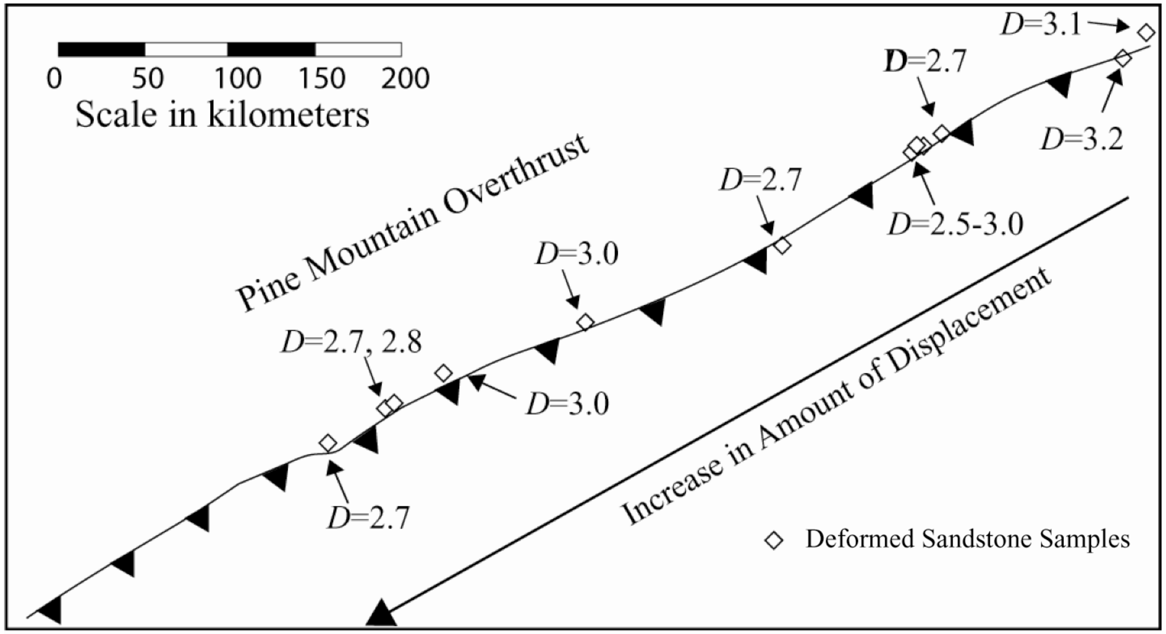

Figure 34. Sample locations for deformed sansdtone samples along the PMO labeled with designated *D*'s. The southern portion of the fault has experienced more displacement than the northern portion of the fault, however, *D* does not vary accordingly, with areas of greater displacement having larger *D* and areas with less displacement with lower *D*. The dependence of *D* could be influenced by the distance of the sample location from the center of the fault.

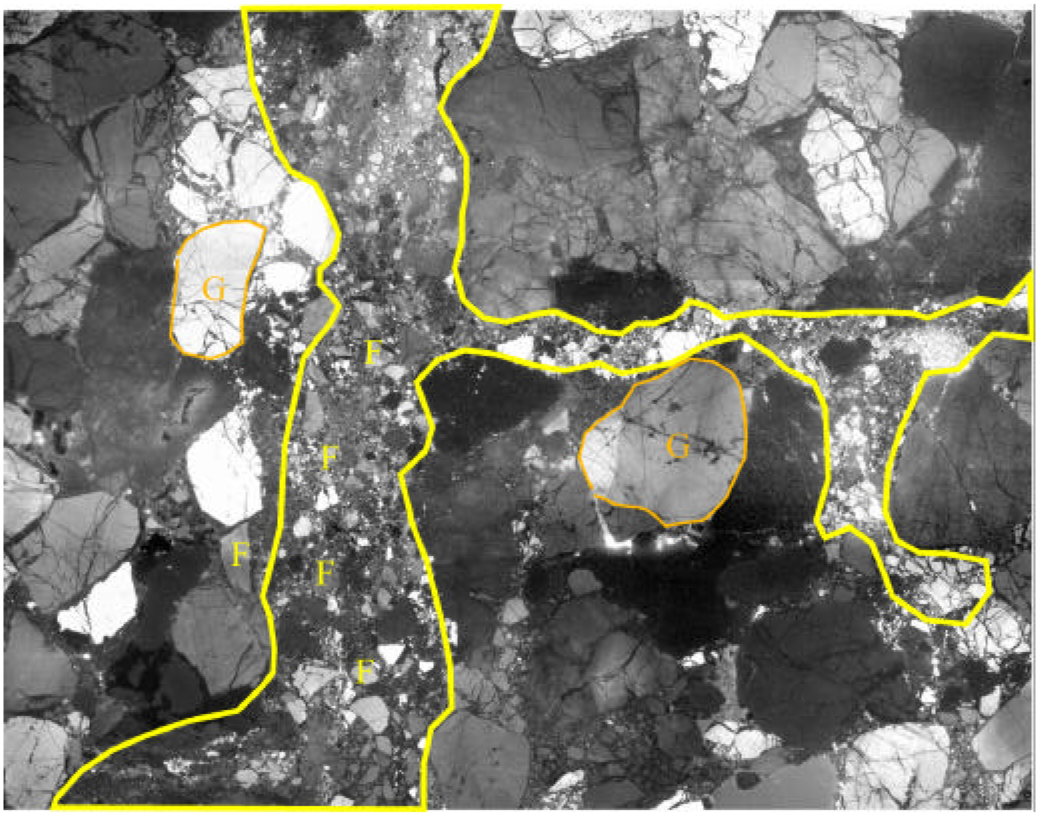

Figure 35. SEM-CL images of cataclasite samples 34. Outlined areas in orange and yellow represent fragments belonging to the same original grain as can be depicted by luminescence color. Fragments marked with yellow and orange “F” symbols depict possible fragments belonging to the same original grain. However, it is difficult to tell this only by luminescence, because the spatial relationships are missing.

embedded in a matrix of finer fragments. These fragments are generally slightly fractured, especially those belonging to the larger size fraction, unlike what has been documented in deformation bands, where “survivor” grains are mostly unfractured (Milliken and Reed, 2003). Deformation bands are prevalent in many samples where fragments have the smallest sizes compared to adjacent less fragmented grains (Fig. 35).

Deformation bands are prevalent in many samples and are localized zones where grains have the smallest particle sizes. Within these deformation bands, in many places, deformation has progressed to such a degree that particles cannot be pieced together to reconstruct the original grain (Fig. 36A). In other places in the same thin-section, pieces have been stretched (by brittle processes) and reconstruction of the original grain is possible, suggesting different episodes of fracturing and movement (Fig. 36B).

Surface Area and Volume of Quartz Cement

Cataclasis and intragranular fracturing increases the surface area/volume ratio in a rock. Increased surface area per volume of rock has the potential for increasing quartz cementation because precipitation is partially controlled by the surface area available (Walderhaug, 1994). If the surface area after fracturing is considered, conventionally one would expect a greater quartz cement volume in deformed sandstones compared to undeformed sandstones. However, when

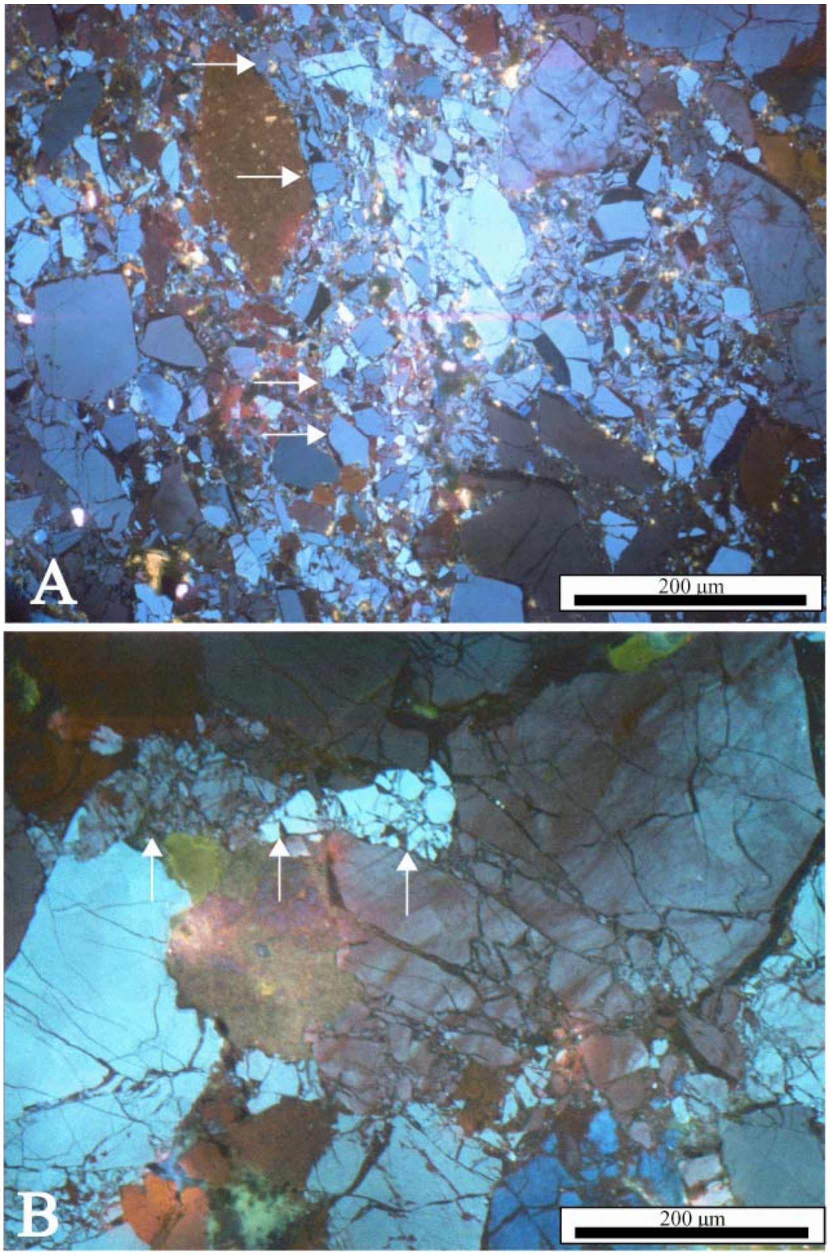

Figure 36. SEM-CL image showing heterogeneity of deformation in sample 38a. A) Area within a large deformation band. Pieces are spread over the entire field of view and are disintegrated to the extent where original grains cannot be reconstructed. B) Area of deformation showing grain expansion or stretching but to a lesser degree than in A. Grain pieces can be reconstructed to form original grain.

comparing average total quartz cement between deformed and undeformed sandstones of both Breathitt and Lee samples, this is not apparent. The average quartz cement volumes for deformed and undeformed Breathitt sandstones are 9.41% and 11.81% respectively (Table 8). For the Lee, volumes of quartz cement between deformed and undeformed samples are 10.68 and 12.44% respectively (Table 9). The differences between deformed and undeformed sandstone samples are approximately ~ 2% for both sandstones, although the difference is slightly greater for the Breathitt than the Lee, perhaps reflecting the smearing of lithics that reduces available quartz surface affect during deformation. T-test result demonstrate that there is no statistically significant difference in the amount of quartz cement between deformed and undeformed sandstones for both the Breathitt Group and the Lee Formation.

The diagenetic model Touchston Version 5.0 was usedto assess predicted quartz cement volumes in coarser-grained undeformed sandstones and the finer fragments found in deformed sandstones. Genesis™ was implemented to model thermal and effective stress histories based on burial and uplift history using apatite fission tracks from samples of the northern region of the Pine Mountain Overthrust (Boettcher and Milliken, 1994). The details of Touchstone™ modeling are discussed in Chapter 3. Fragments in the deformed sandstones

Table 8. Quantitative quartz cement data for the Breathitt Group samples retrieved from point counting CL photomosaics.

Breathitt

Deformed

sample	intergr. quartz cement	intragr. quartz cement	Total qtz cement	
11	5.78	3.99	9.77	
23	4.56	3.21	7.77	
44	6.76	3.94	10.70	
	5.70	**3.71**	**9.41**	**Avgs**

Undeformed

sample	intergr. quartz cement	intragr. quartz cement	Total qtz cement	
1	7.4	1.0	8.4	
2	9.9	0.2	10.1	
3	5.3	3.2	8.5	
4	6.2	1.8	8.0	
5	15.7	0.7	16.5	
7	13.7	0.7	14.4	
8	13.7	0.9	14.6	
9	18.5	0.8	19.3	
13	5.9	2.0	7.8	
15	8.1	0.8	8.9	
21	6.8	2.0	8.8	
22	5.4	1.4	6.8	
24	10.6	3.6	14.1	
25	14.5	1.9	16.4	
26	8.5	1.6	10.1	
27	4.6	1.1	5.7	
30	10.8	1.9	12.7	
31	10.9	1.2	12.1	
35	7.5	4.3	11.8	
36	6.1	1.2	7.3	
40	8.1	1.2	9.3	
48	9.5	1.4	10.9	
49	12.5	2.8	15.3	
51	16.8	0.9	17.6	
52	18.9	1.0	19.9	
	10.23	**1.57**	**11.8**	**Avgs**
			0.19	**t value**

Table 9. Quantitative quartz cement data for the Lee Formation samples retrieved from point counting CL photomosaics.

Lee

Deformed

sample	Formation	intergr. quartz cement	intragr. quartz cement	Total qtz cement	
16	**L**	4.8	4.0	8.8	
16B	**L**	3.5	9.5	12.9	
19	**L**	6.4	8.2	14.6	
34	**L**	1.1	9.4	10.6	
37	**L**	3.2	6.4	9.6	
38a	**L**	1.6	10.9	12.5	
38b	**L**	3.0	5.4	8.4	
38ba	**L**	2.5	6.1	8.6	
39	**L**	3.3	7.9	11.2	
41	**L**	0.8	7.9	8.7	
50	**L**	4.4	7.3	11.7	
	avgs	**3.14**	**7.55**	**10.68**	**Avgs**

Undeformed

sample	Formation	intergr. quartz cement	intragr. quartz cement	Total qtz cement	
17	**L**	10.5	1.5	12.1	
18	**L**	12.0	1.0	13.0	
42	**L**	7.3	3.8	11.2	
45	**L**	9.7	1.2	10.9	
46	**L**	10.1	1.1	11.2	
47	**L**	15.0	1.3	16.3	
	avgs	**10.78**	**1.66**	**12.44**	**Avgs**
				0.27	**t value**

measured by CL range between 1µm and 1 mm, with average particle sizes < 50 µm.

Two Touchstone models have been run, one with a single activation energy for all grain sizes and one with changing activation energy with grain size. Results are not profoundly different between the two models, but there is a better match between measured and modeled quartz cement volumes when activation energy is varied dependent on grain size (Fig. 37).

Distribution of Quartz Cement

On average, in deformed sandstone samples, larger volumes of quartz cement are occurs within fractured grains or between fragments (*intra*granularly) rather than around detrital grains (intergranularly), with average volume percentages of intragranular quartz cement = 6.7 and intergranular quartz cement = 3.7. Undeformed sandstones, outside of the fault zone, have less cement localized intragranularly rather than intergranularly with average volume percentages of 1.6 and 10.3 respectively (Fig. 38). In the deformed Breathitt sandstones there is more quartz cement located *inter*granularly than *intra*granularly. The average for deformed samples is strongly influenced by Lee samples (Tables 8 and 9).

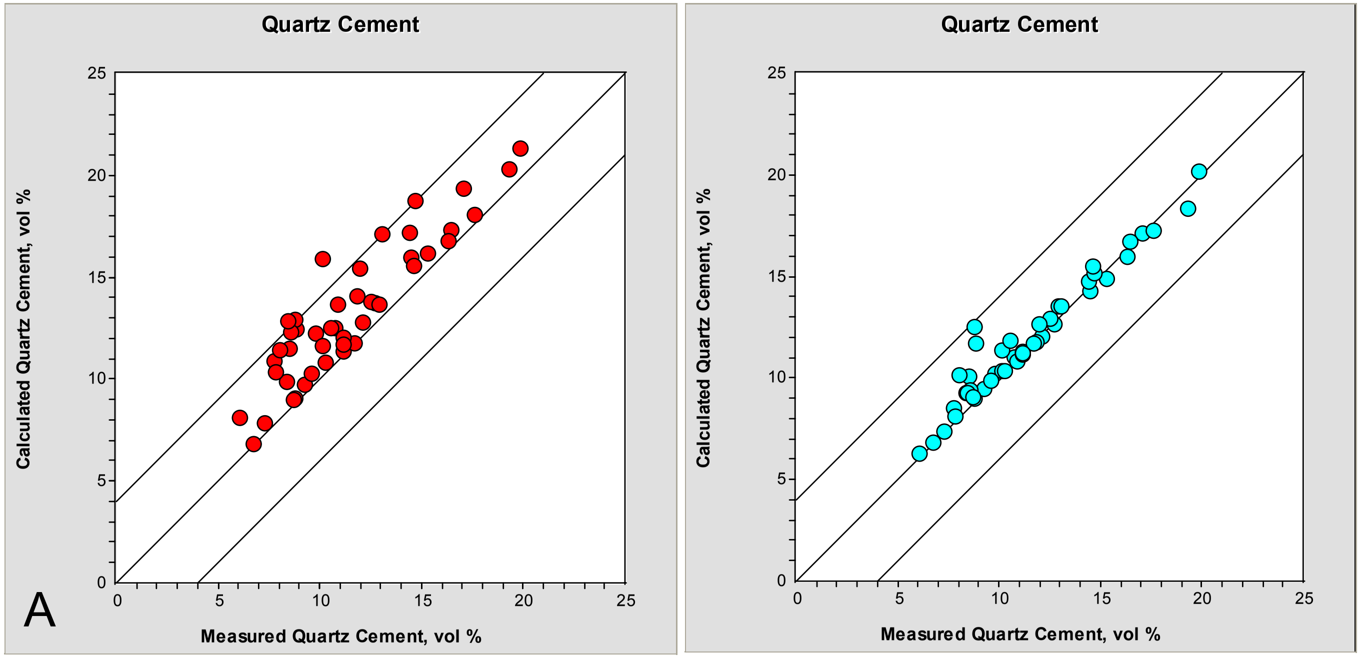

Figure 37. Calculated versus measured quartz cement in bulk rock volume. A) Touchstone using one activation energy for all grain sizes and B) using activation energy as a function of grain size. A better match results from the latter of the models.

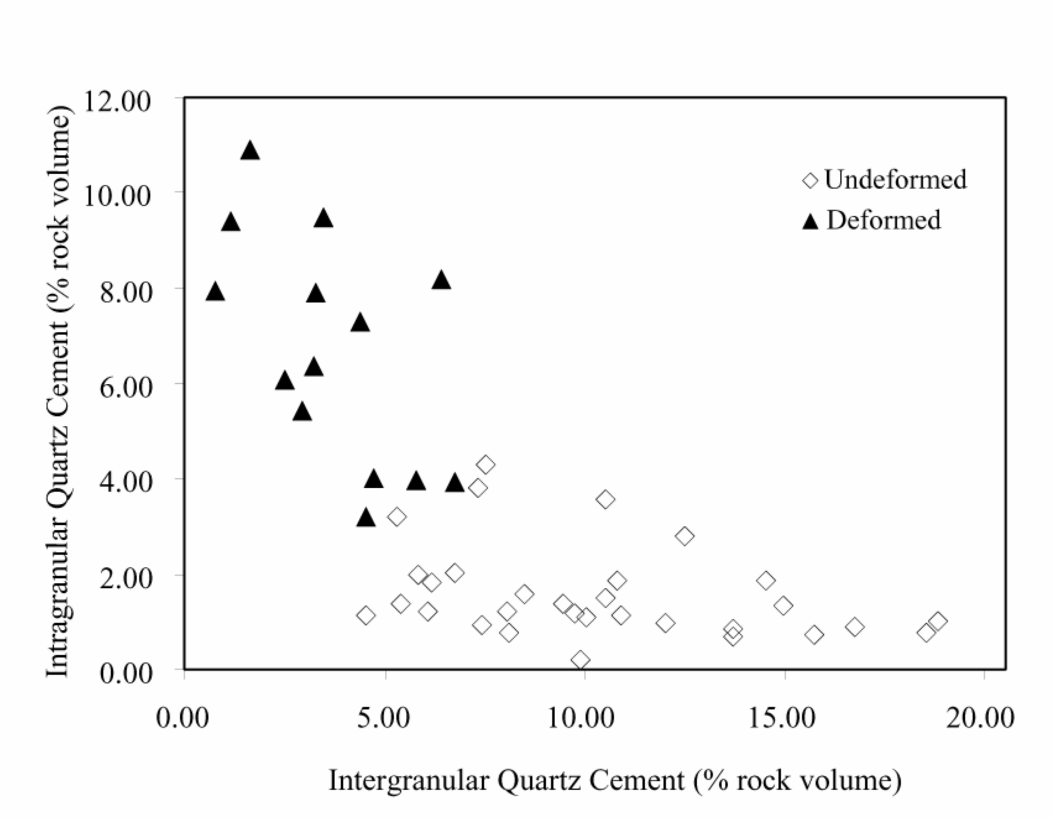

Figure 38. Plot showing the amounts of intergranular quartz (localized around original detrital quartz grains) and intragranular quartz cement (localized between fragments of cataclasized grain pieces and within fractures). More intergranular quartz cement is found in deformed sandstone samples than in undeformed sandstone samples, whereas more intragranular quartz cement is found in deformed sandstone samples than in undeformed sandstone samples. This plot suggests that deformation occurred after approximately 4.7% quartz cement had precipitated. This is the average volume of intergranular quartz cement within deformed sandstones. After deformation, porosity is redistributed and less space is available for intergranular quartz cement precipitation.

Comparing Deformed and Undeformed IGV_t

Upon quantification of quartz cement, including quartz cement localized within comminuted areas and fractures, the IGV's are calculated. Chapter 2 shows how to determine true IGV (IGV_t) values by a few simple mathematical steps, not reviewed here. IGV_t between deformed and undeformed sandstone counterparts does not largely vary when comparing average values. In Breathitt samples, the average IGV_t values for undeformed and deformed samples are 14.5 and 12.0 respectively. For Lee samples, IGV_t values for undeformed and deformed samples are 14.8 and 12.8 (Fig. 39). However, t-test results demonstrate that for both Breathitt and Lee sandstones, there is a statistically significant difference between IGV_t values for undeformed and deformed sandstones. Pressure solution has played a major role in the reduction of IGV reduction in all samples, but here we are mainly concerned in contrasting undeformed versus deformed. Tables 10 and 11 demonstrates how important it is to use microscale CL imaging to determine IGV_t because these true values can vary significantly from the conventional IGV (IGV_c) values, by substantially underestimating IGV, especially for deformed sandstones. It is somewhat surprising that IGV_t values, although statistically different, only differ by ~2.0%, where deformation has occurred on a regional tectonic scale (large offsets), compared to the highly localized zones (little offset) represented as deformation

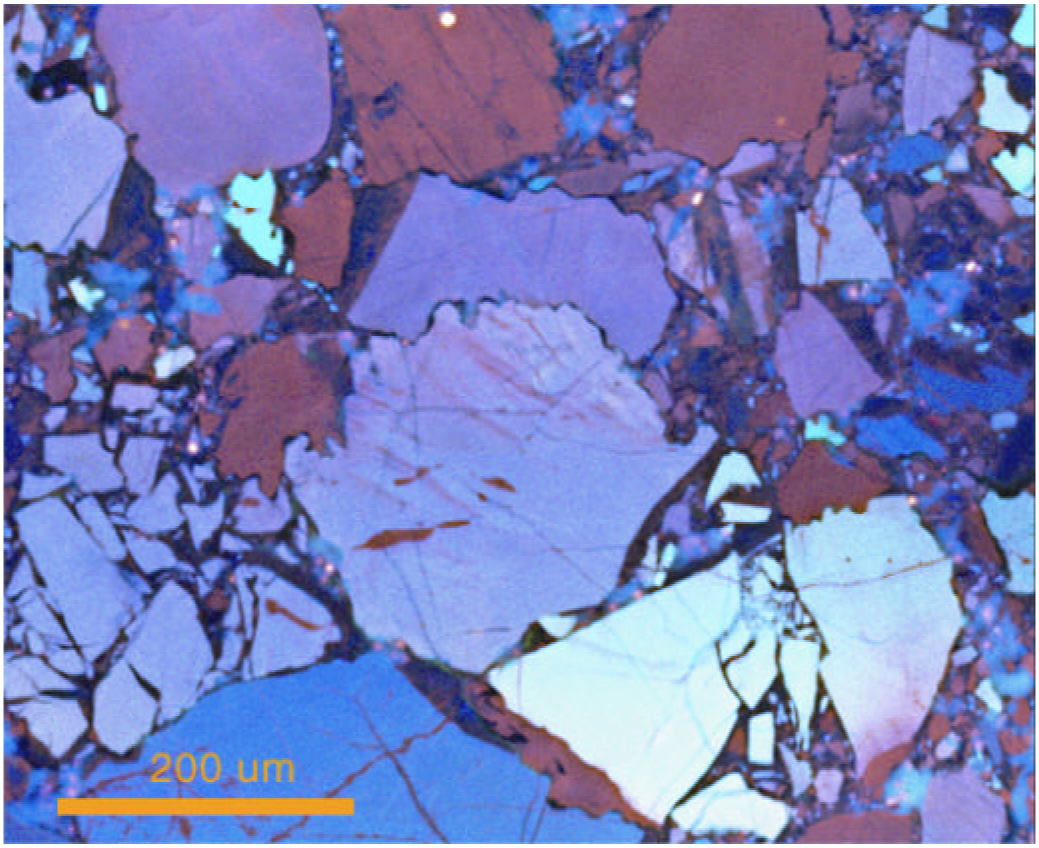

Figure 39. SEM-CL image of cataclasite sample 38b. Examples of pressure solution in deformed sandstone samples. Evidence of pressure solution is ubiquitous. Sutured grain boundaries are common in undeformed and deformed sandstone samples.

Table 10. True and conventional IGV values for the Breahtitt Group samples.

Undeformed Breathitt

	Conventional IGV	True IGV	Difference
	9.2	10.1	0.9
	11.4	11.6	0.2
	8.8	12.0	3.2
	10.0	11.8	1.8
	16.7	17.4	0.7
	18.0	18.7	0.7
	20.6	21.5	0.9
	20.3	21.0	0.8
	10.3	12.3	2.0
	11.9	12.7	0.8
	7.0	9.0	2.0
	5.5	6.9	1.4
	13.0	16.6	3.6
	18.1	19.9	1.9
	17.9	19.5	1.6
	7.4	8.5	1.1
	12.5	14.4	1.9
	12.0	13.2	1.2
	11.7	16.0	4.3
	6.9	8.1	1.2
	8.7	9.9	1.2
	14.2	15.6	1.4
	14.4	17.2	2.8
	17.4	18.3	0.9
	20.4	21.4	1.0
Avgs	**13.0**	**14.5**	**1.6**

Deformed Breathitt

	Conventional IGV	True IGV	Difference
	8.4	12.3	4.0
	7.8	11.0	3.2
	8.6	12.6	3.9
Avgs	**8.3**	**12.0**	**3.7**
t value		**21.2**	

Table 11. True and conventional IGV values for the Lee Formation samples.

	Undeformed Lee		
	Conventional IGV	True IGV	Difference
	15.11	16.63	1.52
	17.63	18.62	0.99
	8.83	12.65	3.82
	10.66	11.85	1.19
	10.83	11.92	1.09
	15.92	17.25	1.33
Avgs	**13.2**	**14.8**	**1.7**

	Deformed Lee		
	Conventional IGV	True IGV	Difference
	9.38	13.38	4
	4.16	13.64	9.48
	7.32	15.51	8.19
	3.1	12.52	9.42
	3.88	10.24	6.36
	3.51	14.41	10.9
	9.28	14.72	5.44
	8.23	14.31	6.08
	3.4	11.29	7.89
	1.01	8.95	7.94
	4.38	11.69	7.31
Avgs	**5.2**	**12.8**	**7.5**
t value		**1.1**	

bands where similar results have been documented (Milliken and Reed, 2002; Milliken and Reed, 2004).

Measuring Small Particle Sizes

Secondary electron imaging of the cataclasites show a ubiquitous presence of sub-micron-size crystals (Fig. 40). Samples 11 and 38b were imaged at high magnification, ranging between 1000x and 20,000x. Although a large number of small particles (~ 1 µm) are measured by CL, many particles are below the resolution of CL imaging capabilities.

Using secondary electron imaging, euhedral crystal size measurements range between 0.1 µm and 2.9 µm with an average of 0.56 µm. Under each overgrowth (crystal) is the seed crystal formed by brittle deformation, which has been calculated to be 83% of the size of the particle plus overgrowth. It is certainly feasible that fragment sizes are present below this minimum size measured. Figure 41 demonstrates that the solubility of a fragment does not drastically increase until >0.01µm. In comparison to other comminution limits found, results here are mostly likely more realistic.

Quartz Cement Stratigraphy

Quartz cement in both undeformed and deformed sandstone samples displays luminescence in three colors: red, dark-blue, and light-blue. These different colors likely arise from differing trace element compositions in the

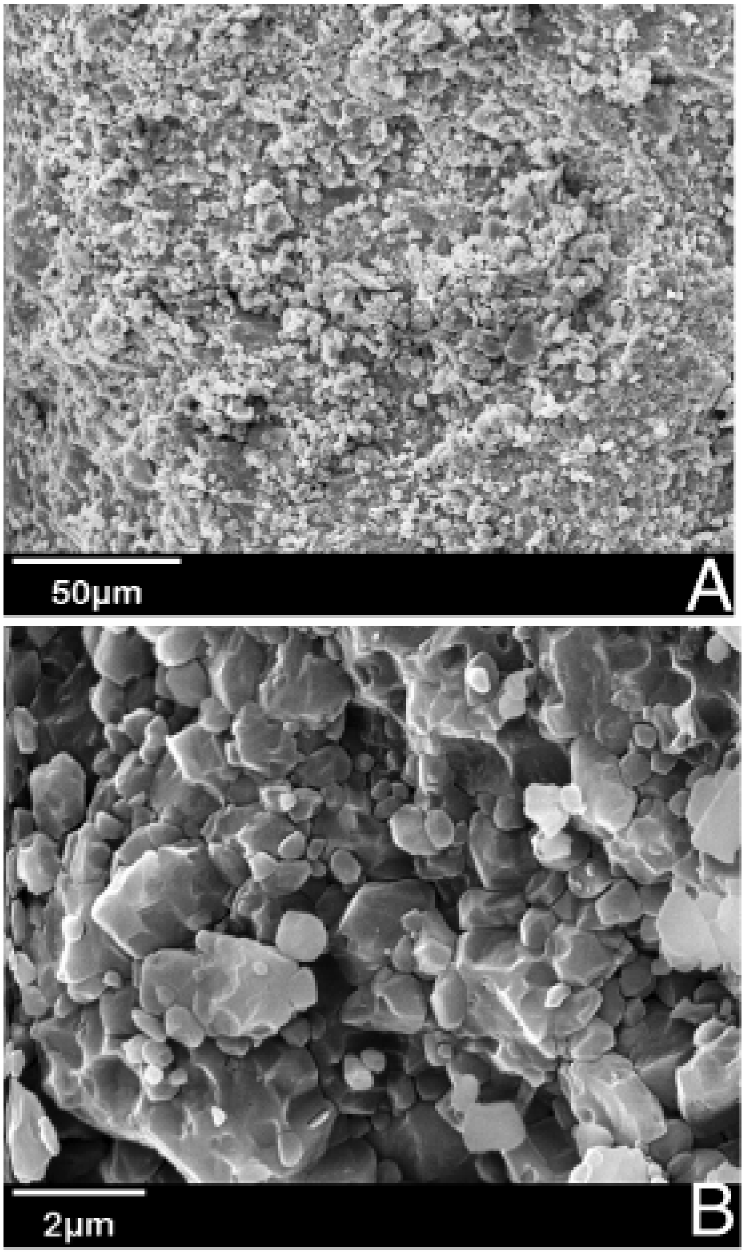

Figure 40. Secondary electron images of whole gouge cataclasite sample 11 show ubiquitous micron and sub-micron crystals. A) At magnification 2000x and B) at magnification 10,000x. These are fragments overprinted by quartz cement (overgrowths).

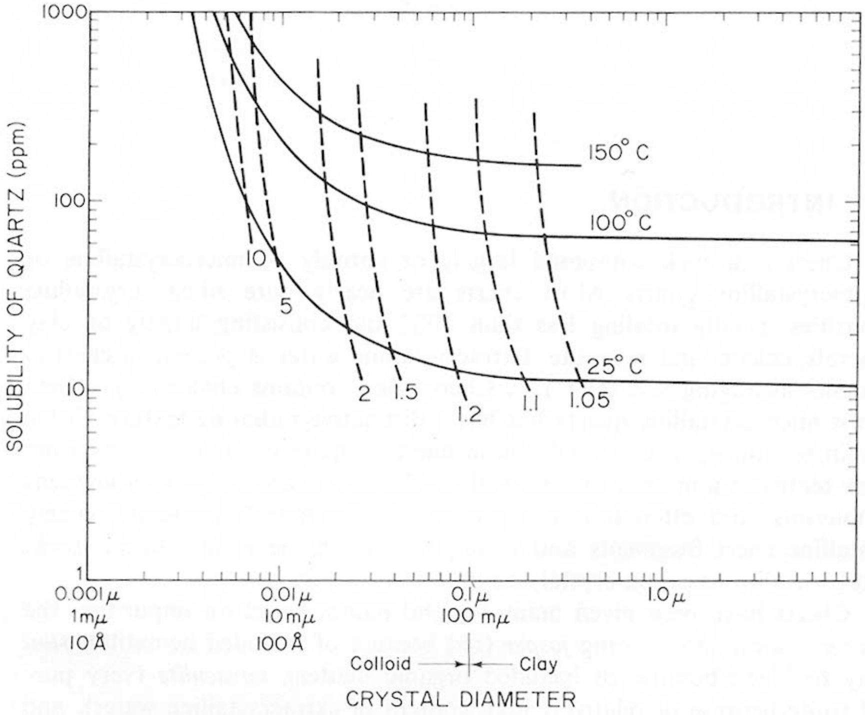

Figure 41. Relationship between solubility of quartz and crystal size at 25°C, 100°C , and 150°C . Dashed lines are contours indicating solubility increase as a function of temperature. Modified from Blatt, Middleton and Murray (1972).

quartz and represent different episodes of cementation. Red cement is commonly overgrown by dark blue cement (Fig. 42). Red cement is not as pervasive as the dark-blue cement and also cannot be found on all grains. Some fractures are filled with red cement but most are filled by the dark-blue quartz (Fig. 43). In some places, dark-blue cement-filled fractures cross-cut red cement-filled fractures (Fig. 44). The majority of cement that precipitates between detrital grains and within detrital grain pieces belongs to the dark-blue-luminescing cement variety. Light-blue cement is also less common than the dark-blue cement, but it generally precipitates over the dark-blue cement, illustrating a third and final episode of quartz cementation (Fig. 45). This latter cement type is rarely present within fractures. See Appendix H for complete quantitative data.

Timing of Intergranular Quartz Cement Precipitation in Deformed Samples

An average of 4.7% quartz in deformed sandstone occurs intergranularly. It is assumed by petrographic evidence that this amount of quartz cement precipitated before deformation. The "age" of this level of cement could constrain timing of the PMO (Tables 8 and 9, Fig. 38). CL imaging shows that many overgrowths around detrital grains are fractured, suggesting that intergranular quartz cementation occurred before sandstones were subjected to deformation. As in Chapter 3, Touchstone™ is used to determine the timing of a specific volume of quartz cement in deformed samples. Volumes of *inter*granular

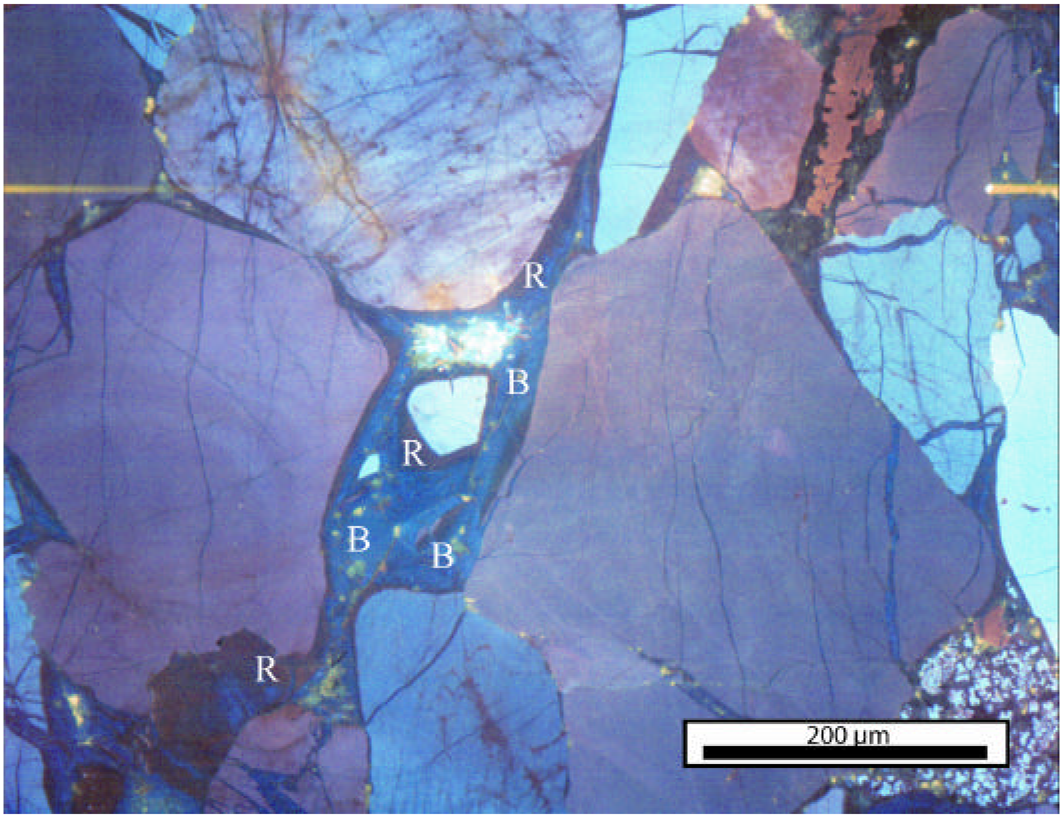

Figure 42. SEM-CL image of cataclasite sample 23 showing red luminescing quartz cement predating dark-blue luminescing cement. Rims of red cement (R) surround most detrital grain surfaces. The later dark-blue luminescing cement (B) filled most of the pore space and in the pores around the central small quartz grain.

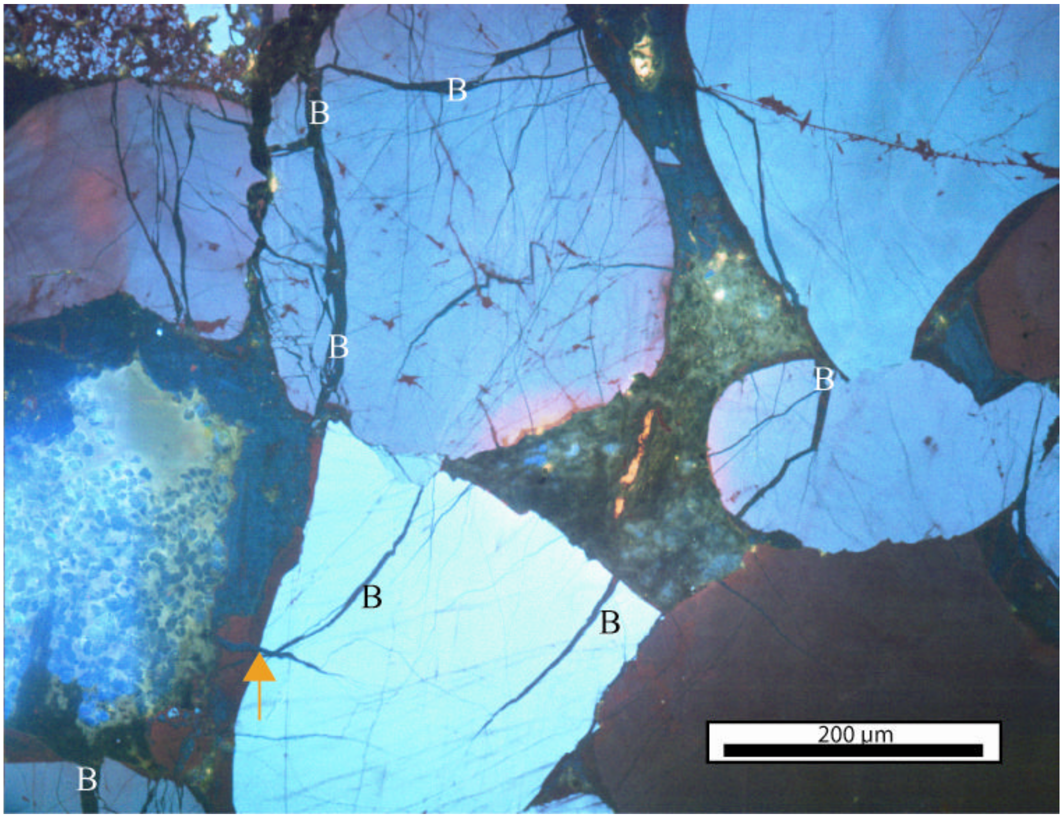

Figure 43. SEM-CL image of cataclasite sample 50 showing fractures filled with dark-blue luminescent cement (B). Some blue-cement filled fractures cross-cut red luminescent overgrowth cement (arrow), suggesting that deformation of the grain occurred after red cement precipitation and during blue cement precipitation. The blue cement filling the fracture (arrow) is continuous with the blue overgrowth cement.

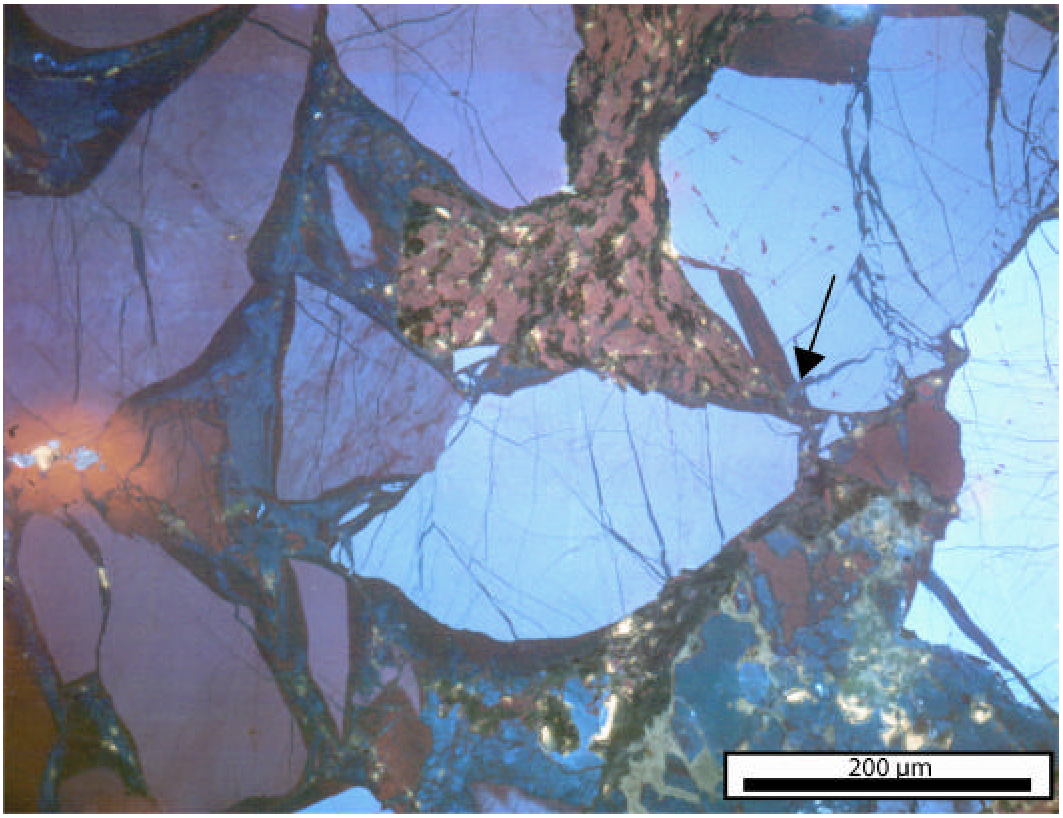

Figure 44. SEM-CL image of cataclasite sample 50 showing cross-cutting relationships where dark-blue cement filled fractures cross-cut younger red cement filled fractures (arrow). Also, red luminescent quartz cement is ubiquitous around detrital quartz grains, illustrating that red predates pore-filling blue quartz.

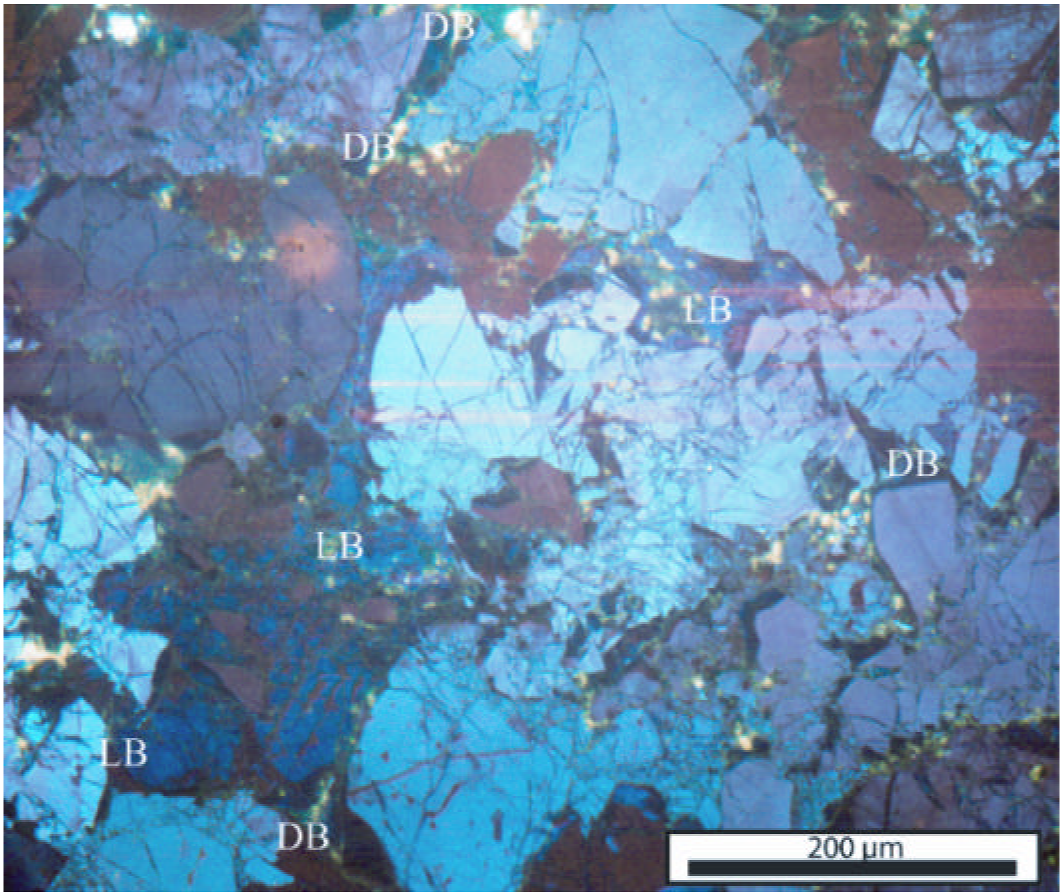

Figure 45. SEM-CL image of cataclasite sample 34 showing light-blue cement (LB) is the most uncommon quartz cement type and is found localized in thin-sections around dark-blue cement (DB), suggesting that it precipitated after dark-blue and red cements.

quartz cement ranges between 0.8 and 6.7% (Tables 8 and 9). These volumes of intergranular cement were precipitated between 263 and 278 Ma and an average of 266 Ma (Table 12). This agrees well with published dates (275 Ma) on the timing of PMO movement (Tankard, 1986)

CONCLUSIONS

High magnification and resolution CL imaging of a quartz-rich fault gouge provides more precise information on grain size, cement volumes, and distribution of cement than available by conventional plane light microscopy or even microscope mounted CL apparatuses.

- Particle-size distributions from 2-D (with 3-D correction) measurements show that the Lee Formation and Breathitt Group sandstones follow the power law distribution with an average fractal dimension D=2.8, similar to what has been found by Sammis et al. (1987).
- Pieces of the cataclasized grains within the PMO have particles one order of magnitude smaller than that reported for grinding limit values for quartz from experiments and natural gouges. This demonstrates the utility of SEM-CL imaging to obtain particle-size data.
- Distinguishing between quartz cement localized *inter*granularly and *intra*granularly combined with petrographic observation and modeling of quartz cement, provides information on the timing of deformation.

Breathitt and Lee sandstones are interpreted to have been deformed earliest 278 Ma and latest by 263 Ma with an average age of 266 Ma. These dates are consistent with the published date on this timing of PMO movement at 275 Ma.

- Differences in IGV_t values between deformed and undeformed sandstones within the PMO indicate that mechanical compaction was not substantially more active in reducing porosity within deformed versus undeformed rocks. This is contrary to conventional thought, where zones of comminution and cataclasis are strictly thought of as severely compacted zones, not highly cemented zones.
- Initial results from Touchstone modeling and petrographic quantification of quartz cement show that perhaps deformed rocks with large number of small fragments are not necessarily more prone to quartz cementation than coarser-grained undeformed rocks, because of the rapid reduction in nucleation surface area with quartz precipitation. Further work must be done to verify if this statement holds in other faulted sandstones. However, if it is found that quartz cementation isn't more profound for deformed sandstones as a result of grain-size dependency for quartz cementation, then this has great predictive power for faults behaving as fluid conduits or barriers.

Table 12. Timing of intergranular quartz cement volumes for deformed samples.

Lee Deformed sample	**Intergr. quartz cement (%)**	**Timing of Precipitation (my)**	
16	4.75	266	
16B	3.46	270	
19	6.44	262	
34	1.14	278	
37	3.22	268	
38a	1.63	278	
38b	2.96	270	
38c	2.50	272	
39	3.27	270	
41	0.76	280	
50	4.38	268	
	3.14	**271**	**avgs**

Breathitt Deformed sample	**Intergr. quartz cement (%)**	**Timing of Precipitation (my)**	
11	5.78	263	
23	4.56	263	
44	6.76	263	
	5.7	**263**	**avgs**
		269 my	**overall avg**

Appendix A

Well information, grain texture, and point count data for Frio Formation samples

Appendix A. Well information, grain texture, point count data for Frio Formation samples.

				Grain Texture		
Sample	Well	Well Unit	Burial Depth (m)	Mean Gr Size (mm)	Sorting (Trask)	Gr Coating (%)
3223	Jack Brown	Frio	982	0.24	1.18	100.00
4908	Slick State	Frio	1496	0.21	0.39	100.00
6105	Seeligson	Frio	1861	0.22	0.44	20.00
8910	Baffin State	Frio	2716	0.19	0.59	20.00
9001	Hornsby	Frio	2744	0.17	0.69	20.00
9547	Gerdts	Frio	2963	0.20	0.50	50.00
9710	McHaney	Frio	2910	0.20	0.56	50.00
9720	McHaney	Frio	2960	0.19	0.50	80.00
9744	McHaney	Frio	2970	0.20	0.74	100.00
10169	Gerdts	Frio	3100	0.22	0.58	40.00
13833	McCullough	Frio	4216	0.13	0.38	20.00
15617	Pleasant Bayou	Frio	4760	0.51	0.65	40.00
15620	Pleasant Bayou	Frio	4761	0.68	0.65	20.00
15640	Pleasant Bayou	Frio	4767	0.33	0.58	40.00
17154	Copano State	Frio	5229	0.22	0.50	40.00

Appendix A. Well information, grain texture, point count data for Frio Formation samples continued.

				GRAINS		
	Porosity		Matrix	Quartz	Feldspar	
Sample	**Intergr Por**	**Sec Por**	**Matrix, undiff**	**Mono Quartz**	**K- feldspar**	**Plag**
3223	14.62	3.25	0.00	8.82	12.99	3.48
4908	14.32	3.52	0.00	22.86	9.30	4.02
6105	0.25	0.00	0.00	20.54	20.54	2.48
8910	0.00	0.51	0.00	29.55	2.78	2.78
9001	8.19	5.21	0.00	35.48	3.72	0.74
9547	4.89	2.69	0.24	28.12	8.07	1.22
9710	25.62	3.20	0.00	40.39	10.10	0.74
9720	13.68	4.23	0.00	44.28	4.98	0.25
9744	0.00	1.23	0.00	42.86	8.62	0.74
10169	8.76	4.62	0.49	24.33	2.19	3.65
13833	3.29	3.54	0.00	24.05	0.25	11.90
15617	11.17	1.49	0.00	62.78	0.99	1.99
15620	0.99	0.74	0.00	77.48	1.24	0.00
15640	1.74	6.72	0.25	46.52	0.75	2.74
17154	11.72	7.23	0.00	22.94	3.49	2.99

Appendix A. Well information, grain texture, point count data for Frio Formation samples continued.

	SRFs				Volcanic Rock Fragments	
Sample	**Shale/Silt RF**	**Chert**	**Carb RF**	**SRF Undiff**	**Andesitic**	**Altered**
3223	1.62	2.55	1.62	0.00	15.78	21.58
4908	0.00	6.03	11.56	0.25	15.08	6.53
6105	0.50	3.47	4.95	0.25	9.65	4.95
8910	0.00	4.29	6.06	0.00	16.16	6.06
9001	0.00	1.24	2.73	0.00	26.30	9.18
9547	0.00	5.13	5.38	0.00	13.69	5.13
9710	0.00	2.71	0.00	0.00	9.61	6.40
9720	0.00	1.74	0.25	1.00	13.18	12.19
9744	0.00	2.71	0.00	0.00	9.11	6.40
10169	0.00	2.92	1.46	0.00	32.85	27.00
13833	0.00	1.77	3.80	0.00	19.24	7.85
15617	0.00	0.99	0.00	0.25	6.95	1.99
15620	0.00	1.49	0.00	0.00	0.99	0.25
15640	0.00	0.75	0.00	0.00	12.44	5.72
17154	0.00	3.74	4.99	0.00	25.69	8.48

Appendix A. Well information, grain texture, point count data for Frio Formation samples continued.

		CEMENTS				
		Quartz	Carbonate	Clay Minerals		Other Cement
Sample	**VRF Undiff**	**Quartz cmt**	**Calcite**	**Chlorite**	**Kaolinite**	**Pyrite**
3223	0.00	0.00	3.02	0.00	0.23	0.00
4908	0.00	0.00	1.76	0.00	0.50	0.00
6105	0.74	0.00	26.98	0.00	0.00	0.74
8910	0.00	0.00	30.05	0.00	0.00	0.00
9001	0.00	2.73	2.98	0.00	0.00	0.00
9547	0.00	2.69	22.49	0.00	0.00	0.00
9710	0.00	1.23	0.00	0.00	0.00	0.00
9720	0.00	0.75	0.25	0.00	0.00	0.00
9744	0.00	0.25	25.86	0.00	0.00	0.00
10169	0.00	3.41	7.79	0.00	0.00	0.00
13833	0.00	6.33	17.72	0.00	0.00	0.00
15617	0.00	5.46	5.21	0.00	0.00	0.00
15620	0.00	12.13	2.72	0.74	0.25	0.25
15640	0.00	12.19	6.22	0.00	3.48	0.00
17154	1.00	4.24	0.50	0.00	1.75	0.25

Appendix A. Well information, grain texture, point count data for Frio Formation samples continued.

Sample	K-spar cmt	Zeolite	FeO	Cmt Undiff	Other Relacements	
					Pyrite	Undiff
3223	0.00	10.44	0.00	0.00	0.00	0.00
4908	0.00	2.76	0.00	1.51	0.00	0.00
6105	0.00	0.50	3.22	0.25	0.00	0.00
8910	0.00	0.25	0.51	0.00	0.00	1.01
9001	0.00	0.00	1.24	0.00	0.00	0.25
9547	0.00	0.00	0.00	0.00	0.00	0.24
9710	0.00	0.00	0.00	0.00	0.00	0.00
9720	0.25	1.74	0.50	0.00	0.00	1.49
9744	0.00	0.00	1.72	0.00	0.00	0.49
10169	0.49	0.00	0.24	0.00	0.00	0.24
13833	0.00	0.00	0.00	0.00	0.25	0.00
15617	0.00	0.00	0.74	0.00	0.00	0.00
15620	0.00	0.00	0.74	0.00	0.00	0.00
15640	0.00	0.00	0.25	0.25	0.00	0.00
17154	0.50	0.00	0.25	0.25	0.00	0.00

Appendix B

Well information, grain texture, and point count data for Mount Simon Formation samples

Appendix B. Well information, grain texture, and point count data for Mount Simon Formation samples.

				Grain Texture		
Sample	**Well**	**Well Unit**	**Burial Depth (m)**	**Mean Grain Size (mm)**	**Sorting (Trask)**	**Grain Coating (%)**
1164	Northern Illinois	Mount Simon	1162	0.42	0.64	10
1277	Northern Illinois	Mount Simon	1196	0.16	0.55	60
1288	Northern Illinois	Mount Simon	1200	0.49	0.66	0
2019	Northern Illinois	Mount Simon	1381	0.48	0.77	80
2166	Northern Illinois	Mount Simon	1426	0.33	0.51	0
2384	Northern Illinois	Mount Simon	1586	0.27	0.71	0
2480	Northern Illinois	Mount Simon	1615	0.35	0.62	0
3135	Northern Illinois	Mount Simon	1814	0.38	0.63	0
3177	Northern Illinois	Mount Simon	1734	0.21	0.48	0
3225	Northern Illinois	Mount Simon	1842	0.37	0.75	0
3582	Central Illinois	Mount Simon	1992	0.44	0.84	0
3619	Central Illinois	Mount Simon	2003	0.40	1.04	0
3793	Central Illinois	Mount Simon	1922	0.37	0.82	0
4038	Central Illinois	Mount Simon	2152	0.43	0.71	10
4119	Central Illinois	Mount Simon	2176	0.37	0.73	0
4226	Central Illinois	Mount Simon	2209	0.33	0.72	40
4469	Central Illinois	Mount Simon	2201	0.32	0.78	0
4477	Central Illinois	Mount Simon	2203	0.29	0.78	20
4720	Central Illinois	Mount Simon	2277	0.32	0.66	0
5404	Central Illinois	Mount Simon	2589	0.45	0.72	0
6154	Southern Illinois	Mount Simon	2817	0.30	0.66	0
6235	Southern Illinois	Mount Simon	2842	0.39	0.53	20
6241	Southern Illinois	Mount Simon	2844	0.28	0.68	20
6497	Southern Illinois	Mount Simon	2922	0.36	0.56	20
6500	Southern Illinois	Mount Simon	2933	0.33	0.65	40
8466	Southern Illinois	Mount Simon	3646	0.22	0.91	60
8468	Southern Illinois	Mount Simon	3647	0.12	0.59	20

					GRAINS	
	Porosity		Matrix		Quartz	Feldspar
Sample	Intergr Por	Sec Por	Detrital clay rims	Matrix, undiff	Undiff Qtz gr	K- feldspar
1164	10.50	7.50	0.25	0.25	66.75	1.00
1277	1.25	3.00	0.25	0.00	71.25	8.50
1288	0.00	0.50	0.00	0.00	62.50	0.00
2019	4.28	4.79	0.00	0.50	85.64	0.00
2166	7.54	9.05	0.25	0.75	63.32	4.02
2384	4.50	3.25	0.00	0.00	71.25	6.75
2480	8.50	4.50	0.00	0.00	72.00	1.00
3135	0.50	0.75	0.00	1.25	79.25	0.00
3177	8.23	5.49	0.00	0.00	71.07	0.25
3225	4.79	1.26	0.00	0.50	77.08	1.51
3582	7.54	9.05	0.25	0.75	63.32	4.02
3619	0.25	0.00	0.00	0.00	81.50	1.25
3793	5.12	0.00	0.00	0.00	78.26	0.51
4038	2.38	0.95	0.00	0.00	77.14	3.81
4119	9.22	2.67	0.00	0.24	73.06	2.18
4226	8.73	0.50	0.00	0.75	74.31	0.50
4469	0.75	2.00	0.00	4.00	73.75	0.50
4477	0.00	0.50	0.00	5.94	78.71	0.25
4720	1.75	6.27	0.00	3.51	76.19	0.00
5404	0.50	1.75	0.00	0.50	79.05	4.49
6154	0.25	0.75	0.00	1.00	83.46	2.01
6235	0.25	0.25	0.00	0.25	87.03	2.99
6241	1.00	0.00	0.00	0.00	84.75	1.00
6497	2.23	1.49	0.00	0.00	78.71	1.24
6500	0.25	0.50	0.00	1.50	85.54	2.49
8466	0.25	0.00	0.00	0.00	76.75	9.75
8468	0.00	0.50	0.00	0.75	82.75	7.25

Sample	Sand RF	Chert	Carb RF	Minerals Mica Undiff	Quartz Quartz cmt	Carbonate Calcite
1164	0.00	0.00	0.00	0.00	13.75	0.00
1277	0.25	0.25	0.00	0.00	3.00	0.00
1288	0.00	0.00	2.25	0.00	0.50	34.25
2019	0.25	0.25	0.00	0.00	3.27	0.00
2166	0.25	0.00	0.00	0.00	13.57	0.00
2384	0.00	0.00	0.00	0.00	12.00	0.00
2480	0.00	0.00	0.00	0.00	12.75	0.00
3135	0.50	0.00	0.00	0.00	17.75	0.00
3177	0.00	0.00	0.00	0.00	14.96	0.00
3225	0.00	0.00	0.00	0.00	13.35	0.00
3582	0.25	0.00	0.00	0.00	13.57	0.00
3619	0.25	0.00	0.00	0.00	15.75	0.00
3793	0.00	0.00	0.00	0.00	13.55	0.00
4038	0.00	0.00	0.00	0.24	11.43	0.00
4119	0.00	0.00	0.00	0.00	9.95	0.00
4226	0.00	0.00	0.00	0.00	10.72	0.00
4469	0.00	0.00	0.00	0.00	14.00	0.00
4477	0.25	0.25	0.00	0.00	9.16	0.00
4720	0.00	0.00	0.00	0.00	10.78	0.00
5404	0.25	0.00	0.00	0.00	13.47	0.00
6154	0.00	0.00	0.00	0.00	12.28	0.00
6235	0.00	0.00	0.00	0.25	8.73	0.00
6241	0.50	0.00	0.00	0.00	12.75	0.00
6497	0.50	0.00	0.00	0.00	15.10	0.00
6500	0.25	0.25	0.00	0.00	8.23	0.00
8466	0.00	0.00	0.00	0.00	11.75	0.00
8468	0.25	0.00	0.00	0.00	7.00	0.00

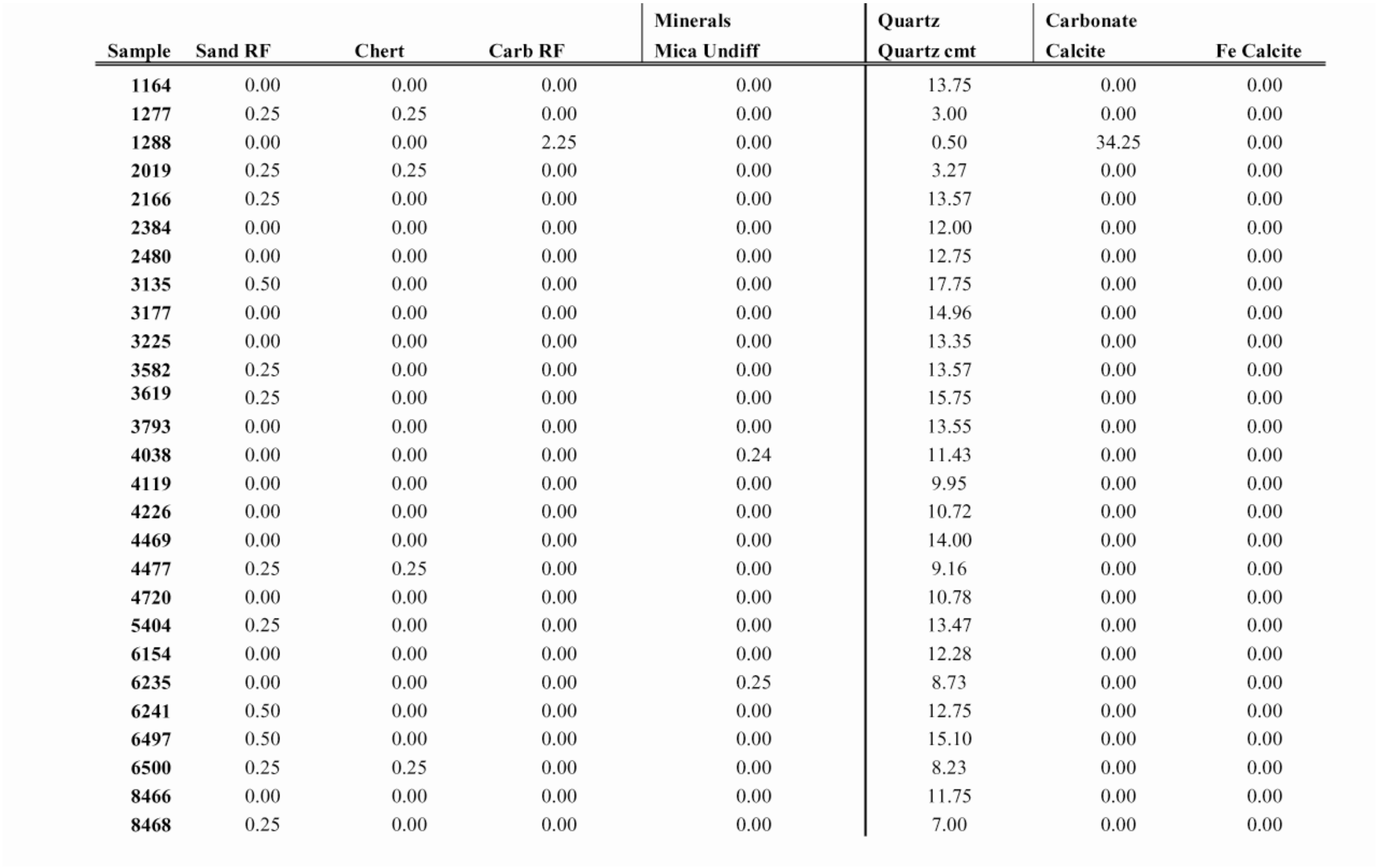

Sample	Sand RF	Chert	Carb RF	Minerals	Quartz	Carbonate	
				Mica Undiff	Quartz cmt	Calcite	Fe Calcite
1164	0.00	0.00	0.00	0.00	13.75	0.00	0.00
1277	0.25	0.25	0.00	0.00	3.00	0.00	0.00
1288	0.00	0.00	2.25	0.00	0.50	34.25	0.00
2019	0.25	0.25	0.00	0.00	3.27	0.00	0.00
2166	0.25	0.00	0.00	0.00	13.57	0.00	0.00
2384	0.00	0.00	0.00	0.00	12.00	0.00	0.00
2480	0.00	0.00	0.00	0.00	12.75	0.00	0.00
3135	0.50	0.00	0.00	0.00	17.75	0.00	0.00
3177	0.00	0.00	0.00	0.00	14.96	0.00	0.00
3225	0.00	0.00	0.00	0.00	13.35	0.00	0.00
3582	0.25	0.00	0.00	0.00	13.57	0.00	0.00
3619	0.25	0.00	0.00	0.00	15.75	0.00	0.00
3793	0.00	0.00	0.00	0.00	13.55	0.00	0.00
4038	0.00	0.00	0.00	0.24	11.43	0.00	0.00
4119	0.00	0.00	0.00	0.00	9.95	0.00	0.00
4226	0.00	0.00	0.00	0.00	10.72	0.00	0.00
4469	0.00	0.00	0.00	0.00	14.00	0.00	0.00
4477	0.25	0.25	0.00	0.00	9.16	0.00	0.00
4720	0.00	0.00	0.00	0.00	10.78	0.00	0.00
5404	0.25	0.00	0.00	0.00	13.47	0.00	0.00
6154	0.00	0.00	0.00	0.00	12.28	0.00	0.00
6235	0.00	0.00	0.00	0.25	8.73	0.00	0.00
6241	0.50	0.00	0.00	0.00	12.75	0.00	0.00
6497	0.50	0.00	0.00	0.00	15.10	0.00	0.00
6500	0.25	0.25	0.00	0.00	8.23	0.00	0.00
8466	0.00	0.00	0.00	0.00	11.75	0.00	0.00
8468	0.25	0.00	0.00	0.00	7.00	0.00	0.00

Appendix C

Fracture information for Frio and Mount Simon Formations

Appendix C. Comprehensive fracture data for the Frio and Mount Simon Formations.

Sample	**3223**				**Sample**	**4908**			
	Grain size (um)	**# of fracs**	**Frac. Wdt (um)**	**# of pieces (2d)**		**Grain size (um)**	**# of fracs**	**Frac. widths (um)**	**# of pieces (2d)**
1	534	0			**1**	220	0		
2	289	4	4.2		**2**	181	0		
3	311	0			**3**	195	0		
4	154	0			**4**	254	0		
5	328	0			**5**	377	0		
6	274	2	5.79		**6**	176	0		
7	237	0			**7**	219	0		
8	507	0			**8**	125	0		
9	259	0			**9**	145	0		
10	347	0			**10**	208	0		
11	206	2	1.93		**11**	214	0		
12	501	0			**12**	194	0		
13	326	0			**13**	343	7	9.2, 3.52, 1.3	11
14	411	0			**14**	196	0		
15	475	0			**15**	174	0		
16	510	6	<1		**16**	241	1	3.4	2
17	724	0			**17**	202	0		
18	394	5	3.22		**18**	209	0		
19	234	0			**19**	266	0		
20	490	0			**20**	262	0		
21	152	0			**21**	126	0		
22	152	0			**22**	230	0		
23	231	1	2.41		**23**	308	0		
24	233	0			**24**	166	0		
25	160	0			**25**	328	0		
26	333	0			**26**	180	3	2.12	2
27	131	0			**27**	224	0		

3223	Grain size (um)	# of fracs	Frac. wdt (um)	# of pieces (2d)	4908	Grain size (um)	# of fracs	Frac. widths (um)	# of pieces (2d)
28	154	0			**28**	189	0		
29	190	0			**29**	141	4		
30	382	0			**30**	146	0		
31	859	0			**31**	153	0		
32	716	0			**32**	98.8	0		
33	523	0			**33**	217	1	8.46	
34	413	0			**34**	420	0		
35	188	0			**35**	165	0		
36	257	0			**36**	168	0		
37	282	1	12.7		**37**	334	0		
38	181	0			**38**	136	0		
39	185	0			**39**	406	0		
40	241	0			**40**	159	0		
41	234	0			**41**	226	0		
42	228	0			**42**	121	0		
43	240	0			**43**	225	0		
44	263	0			**44**	121	0		
45	405	0			**45**	305	0		
46	232	0			**46**	244	0		
47	221	0			**47**	196	3	<1	6
48	137	0			**48**	67.7	0		
49	198	0			**49**	183	0		
50	273	0			**50**	163	0		
51	166	0			**51**	141	0		
52	192	0			**52**	110	1	4.76	2
53	180	0			**53**	140	0		
54	239	0			**54**	215	3	0.871	5
55	153	0			**55**	99.4	0		
56	139	0			**56**	251	0		

3223	Grain size (um)	# of fracs	Frac. wdt (um)	# of pieces (2d)
57	128	0		
58	616	0		
59	287	0		
60	404	0		
61	264	0		
62	185	0		
63	131	0		
64	187	0		
65	301	0		
66	516	0		
67	296	0		
68	149	0		
69	362	0		
70	222	0		
71	536	0		
72	306	0		
73	155	0		
74	317	0		
75	155	0		
76	382	0		
77	467	0		
78	265	0		
79	628	0		
80	331	0		
		21	**total**	
	307	**2.33**	**avgs**	

4908	Grain size (um)	# of fracs	Frac. widths (um)	# of pieces (2d)
57	138	0		
58	258	0		
59	220	0		
60	205	0		
61	193	0		
62	184	0		
63	257	0		
64	169	0		
65	84.5	0		
66	246	0		
67	212	0		
68	145	0		
69	260	0		
70	229	0		
71	275	0		
72	128	0		
73	166	2	1.51	3
74	147	0		
75	156	0		
76	264	0		
77	223	1		
78	147	0		
79	247	4		
80	137	0		
81	228	0		
82	150	0		
83	207	0		
84	352	0		

4908	**Grain size (um)**	**# of fracs**	**Frac. widths (um)**	**# of pieces (2d)**
85	203	0		
86	181	0		
87	149	0		
88	374	0		
89	229	4	<1	5
90	317	0		
91	323	0		
92	126	0		
93	134	0		
94	228	0		
95	219	0		
96	244	0		
97	123	0		
98	74.8	0		
99	261	1	4.34	2
100	55.5	0		
		35.00	total	
	204	2.69	avgs	

Sample	5385			
	Grain size (um)	# of fracs	Frac. wdt (um)	# of pieces (2d)
1	138	0		
2	136	0		
3	195	1	2.84	
4	277	0		
5	160	0		
6	149	1	8.62	
7	111	0		
8	120	2	<1	
9	128	0		
10	132	1	<1	
11	180	0		
12	259	10	5.71, 4.73, 1.78	
13	167	1	1.39	
14	205	5	1.59	
15	168	5	2.9	
16	131	0		
17	111	0		
18	245	0		
19	160	0		
20	182	0		
21	197	4	2.61	
22	166	0		
23	142	0		
24	179	10	2.79	
25	246	0		
26	242	6	4.4	
27	138	0		

Sample	5439			
	Grain size (um)	# of fracs	Frac. widths (um)	# of pieces (2d)
1	277	1	1.31	
2	393	1	9.08	2
3	240	0		
4	195	0		
5	266	0		
6	248	0		
7	225	0		
8	255	0		
9	113	1	1.86	1
10	371	1	1.93	
11	310	4	13.8, 9.26, 4.07	5
12	179	0		
13	171	0		
14	116	0		
15	240	1	9.67	2
16	188	2	8.41, 6.27	3
17	237	3	<1	4
18	241	3	2.38	4
19	241	0		
20	152	25	3.37, <1	>20
21	199	0		
22	227	0		
23	254	2	3.62, <1	1
24	228	0		
25	218	0		
26	319	2	5.18	3
27	222	0		

5385	**Grain size (um)**	**# of fracs**	**Frac. wdt (um)**	**# of pieces (2d)**	**5439**	**Grain size (um)**	**# of fracs**	**Frac. widths (um)**	**# of pieces (2d)**
28	166	1	<1		**28**	411	0		
29	182	2	<1		**29**	176	0		
30	149	0			**30**	144	0		
31	173	0			**31**	317	0		
32	169	4	2.38		**32**	105	0		
33	194	0			**33**	159	0		
34	160	0			**34**	238	1	4.9	1
35	232	0			**35**	313	2	26.8, 2.66	4
36	217	1	<1		**36**	307	2	7.91	3
37	172	0			**37**	304	3	<1	3
38	139	2	<1		**38**	199	1	2.19	2
39	103	0			**39**	362	0		
40	168	0			**40**	144	0		
41	156	0			**41**	220	0		
42	149	1	3.68		**42**	68.6	0		
43	186	0			**43**	339	0		
44	96	0			**44**	233	0		
45	114	0			**45**	189	0		
46	184	0			**46**	178	0		
47	169	2	2.81		**47**	208	0		
48	121	0			**48**	358	5	31.4, 27, 12.4	8
49	154	0			**49**	198	0		
50	186	0			**50**	253	0		
51	141	0			**51**	233	>20	2.56, 1.56	>20
52	180	0			**52**	222	0		
53	116	0			**53**	89.2	1	2.33	2
54	62.9	1	<1		**54**	159	0		
55	135	0			**55**	133	0		
56	192	0			**56**	322	0		

5385	Grain size (um)	# of fracs	Frac. wdt (um)	# of pieces (2d)	5439	Grain size (um)	# of fracs	Frac. widths (um)	# of pieces (2d)
57	185	0			**57**	223	0		
58	128	0			**58**	73.5	0		
59	156	0			**59**	304	0		
60	107	1	<1		**60**	228	0		
61	172	1	<1		**61**	178	0		
62	176	0			**62**	279	0		
63	173	0			**63**	292	1	8.44	2
64	124	0			**64**	361	2	<1	3
65	153	0			**65**	360	3	2.9, <1	2
66	156	7	2.6		**66**	160	0		
67	214	0			**67**	259	3	10.5, <1	4
68	166	5	2.33		**68**	283	0		
69	237	2	2.79		**69**	312	0		
70	145	1	5		**70**	264	3	21.2, 1.74, 1.74	5
71	338	2	1.69		**71**	314	2	<1	1
72	122	0			**72**	299	0		
73	159	0			**73**	167	0		
74	149	0			**74**	201	0		
75	163	0			**75**	227	0		
76	221	1	<1		**76**	253	0		
77	252	3	5.28, 2.09		**77**	139	0		
78	136	0			**78**	293	0		
79	123	2	1		**79**	259	1	<1	1
80	129	0			**80**	178	0		
	13314	**85**	**total**		**81**	73.3	0		
	166	**1.06**	**avgs**		**82**	239	0		
					83	251	1	1.59	2
					84	304	2	3.25, 2.33	3

5439	**Grain size (um)**	**# of fracs**	**Frac. widths (um)**	**# of pieces (2d)**
85	219	2	5.02, 1.95	1
86	135	1	<1	2
87	145	1	8.11	2
88	167	1	8.35	2
89	146	0		
90	180	0		
91	262	0		
92	201	0		
93	147	1	1.74	2
94	328	0		
95	241	8	21.1, 3.88, 3.96	12
96	200	0		
97	288	0		
98	234	0		
99	261	0		
100	336	0		
	23171	**93**	**total**	
	232	**0.93**	**avgs**	

Sample	6105				Sample	8910			
	Grain size (um)	# of fracs	Frac. Wdt (um)	# of pieces (2d)		Grain size (um)	# of fracs	Frac. widths (um)	# of pieces (2d)
1	182	0			**1**	190	2	3.34, 2.7	
2	167	0			**2**	221	1	11.8	
3	229	0			**3**	363	3	25.2, 13.3, 9.31	
4	89.1	0			**4**	206	1	20.4	
5	158	0			**5**	155	0		
6	115	4	1.58	5	**6**	235	4	0.5	
7	113	1	<1	2	**7**	183	0		
8	233	0			**8**	135	0		
9	436	0			**9**	177	0		
10	273	1	19.9	2	**10**	88	1	15.9	
11	205	3	1.93	3	**11**	154	3	1.93	
12	212	0			**12**	211	0		
13	246	0			**13**	136	2	3.26, 1.93	
14	263	0			**14**	239	0		
15	248	1	1.93	2	**15**	190	3	1.59, 3.38	
16	290	0			**16**	199	0		
17	274	5	7.29, 2.0	5	**17**	177	0		
18	228	0			**18**	104	0		
19	214	0			**19**	101	2	9.31, 6.35	
20	297	9	1.86, 1.86	9	**20**	152	3	2.9	
21	273	0			**21**	277	4	1.42	
22	143	0			**22**	282	0		
23	259	0			**23**	149	0		
24	182	0			**24**	297	11	2.23, 1.41, 3.11	
25	266	2	4.87	3	**25**	157	3	11.8, 5.21	
26	154	0			**26**	313	3	2.32	
27	134	0			**27**	185	0		

6105	Grain size (um)	# of fracs	Frac. wdt (um)	# of pieces (2d)	8910	Grain size (um)	# of fracs	Frac. widths (um)	# of pieces (2d)
28	149	0			**28**	136	0		
29	415	0			**29**	226	1	3.26	
30	180	0			**30**	382	0		
31	338	0			**31**	142	0		
32	262	0			**32**	80.5	0		
33	203	0			**33**	176	0		
34	227	1	<1	2	**34**	276	0		
35	190	0			**35**	133	2	2.33, 1.73	
36	192	0			**36**	144	0		
37	90.3	0			**37**	162	2	10.8, 4.64	
38	279	0			**38**	347	1	0.901	
39	118	0			**39**	205	6	2.74, 5.5, 3.61	
40	225	0			**40**	192	12	13.2, 10.9, 9.05, 3.98	
41	194	0			**41**	235	0		
42	234	0			**42**	189	2	3.19, 1.39	
43	368	0			**43**	85.7	0		
44	199	4	6.75. 1.9	5	**44**	108	0		
45	267	0			**45**	315	25	2.6, 4.74, 4.81, 4.5	
46	134	0			**46**	107	0		
47	168	0			**47**	271	25	18.1, 14.2, 2.81	
48	333	0			**48**	342	0		
49	224	3	6.88, 2.,38	5	**49**	311	0		
50	114	0			**50**	229	0		
51	273	0			**51**	224	3	2.81	
52	340	0			**52**	164	3	3.61	
53	130	0			**53**	328	14	6.53, 6.8, 6.33	
54	141	2	<1	2	**54**	72.1	5	3.53, 2.6, 1.58	
55	245	1	2.42	1	**55**	198	2	1.3, 2.6	
56	197	0			**56**	172	0		

6105	Grain size (um)	# of fracs	Frac. wdt (um)	# of pieces (2d)	8910	Grain size (um)	# of fracs	Frac. widths (um)	# of pieces (2d)
57	285	0			**57**	262	0		
58	290	0			**58**	221	3	7.13, 1.58	
59	214	0			**59**	143	0		
60	423	2	<1	3	**60**	190	3	4.68, 2.33	
61	141	3	<1	5	**61**	236	0		
62	293	0			**62**	368	3	7.11, 1.95, 1.95	
63	220	0			**63**	309	0		
64	394	0			**64**	166	3	7.97, 5.4, 2.7	
65	298	0			**65**	219	0		
66	267	0			**66**	241	5	<1	
67	186	0			**67**	59.9	0		
68	288	0			**68**	311	0		
69	292	0			**69**	283	0		
70	198	0			**70**	231	0		
71	192	0			**71**	257	0		
72	170	0			**72**	286	2	2.83, 2.12	
73	336	0			**73**	40	0		
74	242	0			**74**	137	4	2.79, 2.03, 1.54	
75	157	0			**75**	123	1	5.44	
76	252	0			**76**	141	0		
77	203	0			**77**	173	0		
78	311	0			**78**	176	0		
79	218	2	4.18	3	**79**	152	2	2.42	
80	150	0			**80**	180	7	2.79, 8.29, 2.33	
81	402	0			**81**	127	0		
82	150	0			**82**	186	0		
83	266	0			**83**	54.2	0		
84	337	25	5.93, 6.51, 12.3	>25	**84**	94.5	0		

6105	**Grain size (um)**	**# of fracs**	**Frac. wdt (um)**	**# of pieces (2d)**	**8910**	**Grain size (um)**	**# of fracs**	**Frac. widths (um)**	**# of pieces (2d)**
85	238	0			**85**	207	1	2.79	
86	211	0			**86**	172	0		
87	155	0			**87**	277	2	2.38	
88	145	0			**88**	162	0		
89	41.4	0			**89**	92.9	4	6.6, 5.58, 3.9	
90	240	1	<1	1	**90**	239	0		
91	151	0			**91**	133	0		
92	205	0			**92**	178	1	2.08	
93	294	0			**93**	53.1	1	3.28	
94	169	0			**94**	198	0		
95	206	0			**95**	159	0		
96	228	0			**96**	257	1	12.9	
97	200	0			**97**	382	0		
98	282	0			**98**	285	0		
99	273	0			**99**	236	0		
100	166	0			**100**	225	0		
	22692	**70**	**total**			**19851**	**192**	**total**	
	227	**4.12**	**avg**			**199**	**4.27**	**avg**	

Sample	9001				Sample	9547			
	Grain size (um)	# of fracs	Frac. wdt (um)	# of pieces (2d)		Grain size (um)	# of fracs	Frac wdt (um)	# of pieces (2d)
1	191	0			**1**	219	2	0.866	3
2	121	1	1.86	2	**2**	188	0		
3	270	10	3.16, 2.09, 1.54	13	**3**	273	1	1.03	2
4	123	10	1.65, 0.901	13	**4**	201	2	4.5, 3.48	
5	104	1	1.59	2	**5**	201	0		
6	128	0			**6**	348	3	4.24, 2.01	2
7	201	0			**7**	361	25	18.1, 7.11, 10.2	>25
8	214	0			**8**	225	5	3.67, 3.11, 2.72	5
9	174	0			**9**	148	0		
10	131	1	<1	2	**10**	295	7	2.09, 4.95	8
11	147	0			**11**	250	1	2.6	2
12	182	2	2.54, <1	3	**12**	329	6	4.84, 5.23, 3.38	8
13	149	1	<1	2	**13**	326	2	<1	2
14	65.4	0			**14**	317	4	5.18	4
15	148	0			**15**	268	0		
16	103	2	4.92. 1.81	3	**16**	333	1	27.5	2
17	235	25	5.74, 4.6	>25	**17**	299	0		
18	102	0			**18**	243	6	11.6, 9.11, 1.81	5
19	179	1	8.21	2	**19**	391	8	3.96, 0.995, 2.89	9
20	268	6	6.07, 2.79	7	**20**	312	6	12.7, 9.88, 3.66	5
21	138	1	3.12	2	**21**	256	0		
22	195	3	2.23, 3.09	4	**22**	91.2	1	2.09	2
23	190	0			**23**	289	11	9.74, 12, 11.6, 3.49	6
24	121	0			**24**	100	0		
25	218	1	1.69	2	**25**	164	1	<1	1
26	232	3	5.16, 2.23	4	**26**	180	5	15.4, 11, 5.86	6
27	108	2	2.84, 2.32	3	**27**	117	2	<1	3

9001	Grain size (um)	# of fracs	Frac wdt (um)	# of pieces (2d)	9547	Grain size (um)	# of fracs	Frac wdt (um)	# of pieces (2d)
28	157	0			**28**	271	1	7.78	2
29	185	0			**29**	171	2		
30	135	6	4.59, 3.12, 3.39	10	**30**	86.8	0		
31	86.1	0			**31**	186	2	5.43	3
32	97.5	0			**32**	72.4	0		
33	158	4	3.67, 3.85	3	**33**	280	1	7.65	2
34	163	1	<1	1	**34**	207	7	2.09, <1	9
35	140	0			**35**	230	0		
36	238	4	<1	7	**36**	156	0		
37	187	1	1.04	2	**37**	239	7	3.81, 5.69	9
38	145	4	9.43, 2.54, 1.27	5	**38**	259	1	1.58	
39	107	1	<1	1	**39**	283	7	6.9, 4.38, 2.97	5
40	171	0			**40**	196	1	3.61	2
41	151	0			**41**	212	4	6.83, 4.34, 1.58	5
42	162	3	5.69, 4.5	3	**42**	142	0		
43	140	4	7.84, 1.81	5	**43**	400	0		
44	156	4	3.86, 13, 7.1, 8.8	5	**44**	80.1	2	6.72, 3.13	3
45	131	2	2.23, 3.16	3	**45**	223	4	4.87, <1	5
46	94.4	0			**46**	156	5	18.6, 3.49, 3.08	5
47	132	5	2.33, 2.23	7	**47**	337	2	7.42, 7.07	2
48	161	4	4.85	2	**48**	90.7	0		
49	245	0			**49**	256	2	1.3, <1	3
50	69.5	0			**50**	129	0		
51	168	0			**51**	257	0		
52	162	1	1.37	2	**52**	183	2	2.23 , <1	3
53	166	0			**53**	134	0		
54	204	0			**54**	225	3	3.38, 6.59	4
55	156	5	3.12, 2.39, 1.74	4	**55**	359	5	6.15, 26.4, 4.18	6
56	165	8	12.2, 4.34, 2.09, 4.98	6	**56**	51.4	0		

9001	Grain size (um)	# of fracs	Frac wdt (um)	# of pieces (2d)	9547	Grain size (um)	# of fracs	Frac wdt (um)	# of pieces (2d)
57	463	0			**57**	326	3	14.6, <1	2
58	140	0			**58**	166	3	28.7, 3.52	4
59	315	10	4.3, 8.74, 7.06	14	**59**	268	4	0.78, 10.1, 6.85	5
60	208	0			**60**	359	0		
61	192	8	12.4, 8.5, 5.24	14	**61**	289	3	7.46, 5.46	2
62	131	0			**62**	134	0		
63	141	0			**63**	317	0		
64	158	2	3.12, 3.02		**64**	315	0		
65	203	0			**65**	85.6	0		
66	160	16	10.4, 3.02, 3.91	>25	**66**	84.1	3	3.62, <1	3
67	125	0			**67**	203	2	<1	2
68	152	0			**68**	142	1	4.37	2
69	189	1	3.62	2	**69**	332	3	19, 8.71, 4.71	5
70	197	0			**70**	136	4	2.7, 2.07, 1.46	5
71	154	2	<1	3	**71**	95.1	0		
72	193	0			**72**	93.7	2	4.16, 2.6	3
73	87.2	1	1.98		**73**	292	0		
74	165	0			**74**	175	2	8.41, 1.3	2
75	150	1	2.45	1	**75**	414	0		
76	294	2	3.83, 2.12	2	**76**	294	0		
77	184	9	15.2, 13.2, 7.65	10	**77**	124	0		
78	168	0			**78**	143	0		
79	165	1	<1	2	**79**	81.8	0		
80	122	3	8.92, 2.12	4	**80**	100	0		
81	167	0			**81**	163	0		
82	109	4	7.07, 6.66	6	**82**	123	0		
83	198	12	15.4, 4.59, 4.85	13	**83**	113	1	5.2	
84	155	3	10.8	1	**84**	94.8	8	9.75, 4.65, 2.19	13

9001	Grain size (um)	# of fracs	Frac wdt (um)	# of pieces (2d)
85	132	0		
86	177	5	<1	3
87	75.6	0		
88	335	1	12.6	2
89	182	0		
90	171	1	11.1	2
91	214	0		
92	132	0		
93	92.6	0		
94	302	0		
95	159	0		
96	226	4	15.2, 7.41, 3.61	6
97	205	2	12, 2.78	2
98	111	0		
99	101	0		
100	121	2	4.82. <1	3
	16691	**217**	**total**	
	167	**4.09**	**avg**	

9547	Grain size (um)	# of fracs	Frac wdt (um)	# of pieces (2d)
85	274	3	<1	2
86	379	9	23.2, 13.9, 6.88	11
87	235	2	8.41, 10.7	3
88	314	5	6.17, 8.27, 4.9	3
89	174	6	9.15, 5.74, 4.82	5
90	125	0		
91	176	1	2.38	1
92	118	0		
93	108	1	5.46	2
94	177	0		
95	140	11	3.81, 2.6, 6.28	10
96	110	2	4.27, 3.04	3
97	123	0		
98	277	6	<1	11
99	284	1	<1	2
	21074	**243**	**total**	
	213	**3.92**	**avg**	

Sample	9710				Sample	9720			
	Grain size (um)	# of fracs	Frac. wdt (um)	# of pieces (2d)		Grain size (um)	# of fracs	Frac. wdt (um)	# of pieces (2d)
1	147	1	1.69		**1**	188	0		
2	359	0			**2**	155	0		
3	190	5	1.69		**3**	132	25	17.9	
4	210	0			**4**	145	3	3.54	
5	121	0			**5**	160	1	4.63	
6	150	0			**6**	137	0		
7	211	1	<1		**7**	172	25	10.1	
8	135	1	<2		**8**	114	0		
9	233	2	<3		**9**	78.8	0		
10	212	5	<4		**10**	147	1	3.5	
11	172	0			**11**	92	0		
12	197	5	1.74, <1		**12**	260	25	3.37	
13	187	0			**13**	122	4	2.41	
14	193	2	7.63, <1		**14**	114	0		
15	63.9	2	2.84, <1		**15**	142	0		
16	203	2	16.1, 6.66		**16**	251	0		
17	93.9	0			**17**	142	0		
18	189	1	<1		**18**	229	1	8.1	
19	139	5	2.45, 2.11		**19**	272	0		
20	368	0			**20**	95.9	0		
21	114	0			**21**	116	0		
22	251	1	4.34		**22**	137	0		
23	266	1	<1		**23**	132	0		
24	70.2	2	1.19		**24**	164	3	2.12	
25	163	4	5.83, 1.04		**25**	155	0		
26	188	2	12.1, 2.7		**26**	236	25	6.86, 3.13	
27	178	0			**27**	202	3	<1	

9710	Grain size (um)	# of fracs	Frac. Wdt (um)	# of pieces (2d)	9720	Grain size (um)	# of fracs	Frac. Wdt (um)	# of pieces (2d)
28	112	0			**28**	187	2	<1	
29	179	4	2.08		**29**	185	25	4.78, 3.25	
30	237	0			**30**	162	8	9.57, 5.79	
31	166	0			**31**	283	3	8.2, 6.88, 6.08	
32	385	4	9.35, 3.8		**32**	277	1	1.69	
33	164	1	4.6		**33**	150	0		
34	295	1	9.29		**34**	169	1	10	
35	291	6	<1		**35**	132	0		
36	130	0			**36**	134	0		
37	124	0			**37**	153	0		
38	209	3	<1		**38**	175	10		
39	122	2			**39**	93.2	1	<1	
40	187	0			**40**	320	2	5.03, 4.03	
41	54.1	1			**41**	140	3	1.54	
42	229	3	<1		**42**	130	2	<1	
43	194	0			**43**	121	0		
44	272	5	5.92, 4.13		**44**	205	1	3.18	
45	92.9	0			**45**	164	0		
46	195	2	1.16, 6.33		**46**	163	4	<1	
47	193	1	2.32		**47**	158	0		
48	341	8	6.49, 7.72, 10.6		**48**	118	0		
49	216	4	2.56, <1		**49**	188	0		
50	140	0			**50**	248	0		
51	122	0			**51**	185	4	1.81	
52	87.8	2			**52**	194	0		
53	190	0			**53**	205	0		
54	136	2	3.18		**54**	200	0		
55	141	1	<1		**55**	202	1	3.5	
56	239	7	4.28, 2.77		**56**	262	0		

9710	Grain size (um)	# of fracs	Frac. Wdt (um)	# of pieces (2d)	9720	Grain size (um)	# of fracs	Frac. Wdt (um)	# of pieces (2d)
57	181	0			**57**	236	2	3.42, 2.41	
58	195	0			**58**	264	2	1.21	
59	210	1	5.45		**59**	187	0		
60	87.4	1	<1		**60**	192	4	2.61	
61	189	1	2.39		**61**	176	2	3.62	
62	262	0			**62**	226	7	<1	
63	158	0			**63**	163	0		
64	277	3	1.35		**64**	239	0		
65	281	25	<1		**65**	157	2	3.32	
66	195	0			**66**	278	25	7.06, 3.68, 2.42	
67	156	0			**67**	183	0		
68	149	0			**68**	191	5	<1	
69	164	2	2.08, 2.54		**69**	152	0		
70	190	0			**70**	135	1	2.72	
71	204	7	2.34, <1		**71**	161	0		
72	216	0			**72**	128	1	2.89	
73	143	0			**73**	176	25	1.93	
74	179	4	<1		**74**	113	0		
75	126	0			**75**	249	0		
76	214	4	<1		**76**	179	1	6.68	
77	206	13	2.84, 2.44		**77**	245	0		
78	120	0	0		**78**	204	0		
79	238	1	4.4		**79**	231	25	2.36, 3.09	
80	140	0			**80**	184	2	<1	
81	158	4	<1		**81**	243	3	2.33, 0.847	
82	159	3	3.89, 2.74		**82**	122	0		
83	100	9	4.46		**83**	209	0		
84	113	8	<1		**84**	167	4	6.03, 2.59, 1.7	

9710	Grain size (um)	# of fracs	Frac. wdt (um)	# of pieces (2d)	9720	Grain size (um)	# of fracs	Frac. wdt (um)	# of pieces (2d)
85	123	0			**85**	184	0		
86	182	1	<1		**86**	171	5	2.19, 2.66, 2.66	
87	133	0			**87**	355	8	9.62, 7.7, 1.39	
88	127	3	5.32		**88**	144	0		
89	185	3	<1		**89**	184	0		
90	191	0			**90**	206	3	4.94, 2.34	
91	285	3	4.06, 2.25		**91**	189	0		
92	208	0			**92**	226	6	3.04, 1.02	
93	57.7	1	2.33		**93**	163	0		
94	181	0			**94**	122	5	3.26, 5.45, 2.59	
95	162	2	9.3		**95**	223	0		
96	241	3	4.13, 4.13		**96**	168	0		
97	253	2	2.89, 1.11		**97**	135	0		
98	157	0			**98**	123	0		
99	169	1	1.04		**99**	143	0		
100	133	0			**100**	196	0		
	18246	**204**	**total**				**322**	**total**	
	182	**3.52**	**avg**			**179**	**3.22**	**avgs**	

Sample	9743				Sample	10169			
	Grain size (um)	# of fracs	Frac. wdt (um)	# of pieces (2d)		Grain size (um)	# of fracs	Frac. Wdt (um)	# of pieces (2d)
1	203	0			**1**	220	1	3.47	
2	230	2	2.58, 3.99		**2**	181	15	9.12, 21.5, 10.4, 3.39	
3	165	1	4.76		**3**	195	13	7.15, 14.7, 10.5	
4	266	0			**4**	254	11	20.3, 15.6, 15.03	
5	280	2	1.51, 0.482		**5**	377	7	23.9, 13.3, 15.1	
6	97.4	25	1.96		**6**	176	1	2.78	
7	288	0			**7**	219	6	2.42, 4.39, 0.5	
8	145	0			**8**	125	8	4.37,5.63, 1.8	
9	269	0			**9**	145	0		
10	181	2	1.04		**10**	208	3	10	
11	281	2	1.19, 1.37		**11**	214	2	31.7, 11.9	
12	53.7	0			**12**	194	2	2.23, 4.29	
13	319	0			**13**	343	1	5.49	
14	144	0			**14**	196	0		
15	107	0			**15**	174	0		
16	175	0			**16**	241	0		
17	108	2	<1		**17**	202	0		
18	241	3	21.3, 3.47, 2.16		**18**	209	4	3.37, 1.39, 1.69	
19	137	1	2.11		**19**	266	0		
20	127	0			**20**	262	5	6.54, 3.39	
21	138	0			**21**	126	9	4.68, 3.37, 1.81	
22	168	2	3.16, 5.11		**22**	230	2	4.18, 1.78	
23	161	0			**23**	308	4	5.31	
24	185	2	5.11, 3.34		**24**	166	7	10, 6.38, 3.87	
25	317	0			**25**	328	1	13.5,	
26	139	2	6.46, 5.35		**26**	180	4	5.57	
27	208	0			**27**	224	2	<1	

9743	Grain size (um)	# of fracs	Frac. wdt (um)	# of pieces (2d)	10169	Grain size (um)	# of fracs	Frac. Wdt (um)	# of pieces (2d)
28	136	0			**28**	189	7	4.92	
29	223	0			**29**	141	8	3.73, 2.38, 1.16	
30	190	0			**30**	146	0		
31	254	0			**31**	153	3	4.75, 3.11, 2.32	
32	238	0			**32**	98.8	2	4.89	
33	233	2	<1		**33**	217	3	21.89, 1	
34	189	8	2.81, 2.82, 1.65		**34**	420	8	7.24, 6.75, 4.43	
35	307	25	22.4, 18.3		**35**	165	4	5.02	
36	124	0			**36**	168	0		
37	170	3	5.78		**37**	334	0		
38	167	3	2.08, 2.79		**38**	136	4	4.73, 1.59	
39	113	0			**39**	406	1	3.53	
40	193	2	6.24, 1.92		**40**	159	5	6.75, 7.63	
41	276	6	4.81, 2.01, 2.41		**41**	226	4	<1	
42	131	0			**42**	121	0		
43	218	2	2.41, 2.23		**43**	225	0		
44	148	0			**44**	121	0		
45	276	3	1.93, 1.0		**45**	305	3	7.27, 1.35	
46	270	1	3.02		**46**	244	4	2.98	
47	253	3	4.34, 0.434		**47**	196	1	<1	
48	283	1	1.16		**48**	67.7	1	1.55	
49	122	0			**49**	183	3	9.88, 2.72	
50	282	3	131		**50**	163	3	3.54, 2.89, 2.32	
51	175	25	6.5, 25.8, 13.7		**51**	141	0		
52	135	0			**52**	110	3	2.07	
53	167	0			**53**	140	0		
54	230	2	5.07, 3.92		**54**	215	5	3.81, 1.59, 1.73	
55	262	1	1		**55**	99.4	0		
56	183	25	5.86, 2.89		**56**	251	2	4.95, 0.796	

9743	Grain size (um)	# of fracs	Frac. wdt (um)	# of pieces (2d)	10169	Grain size (um)	# of fracs	Frac. Wdt (um)	# of pieces (2d)
57	81.8	0			**57**	138	2	13.9, 2.91	
58	151	0			**58**	258	0		
59	118	1	3.54		**59**	220	5	4.02, 1.98	
60	72.3	0			**60**	205	1	1.48	
61	168	0			**61**	193	4	4.54, 1.81, 1.69	
62	129	2	<1		**62**	184	3	1.73	
63	193	25	5.19, 4.38, 4.9		**63**	257	0		
64	216	0			**64**	169	0		
65	196	0			**65**	84.5	5	8.13, 1.92, 1.73	
66	194	2	<1		**66**	246	2	6.15	
67	540	2	<1		**67**	212	4	12, 1.69	
68	197	0			**68**	145	3	3.41	
69	322	0			**69**	260	0		
70	151	0			**70**	229	5	4.24, 6.49, 2.66	
71	236	2	5.29, 1.81		**71**	275	0		
72	116	0			**72**	128	0		
73	161	0			**73**	166	0		
74	123	0			**74**	147	2	5.69	
75	183	2	2.33, 1.05		**75**	156	6	4.89, 1.3	
76	145	0			**76**	264	4	8.48, 4.33	
77	176	0			**77**	223	3	5.27, 4	
78	216	4	8.68, 7.23, 6.46, 2.38		**78**	147	0		
79	167	3	2.45		**79**	247	0		
80	236	0			**80**	137	0		
81	165	0			**81**	228	0		
82	244	0			**82**	150	2	2.38, 1.9	
83	117	0			**83**	207	0		
84	223	2	10, 1.31		**84**	352	3	26.7, 8.46	

9743	Grain size (um)	# of fracs	Frac. wdt (um)	# of pieces (2d)	10169	Grain size (um)	# of fracs	Frac. wdt (um)	# of pieces (2d)
85	196	1	1.04		**85**	203	6	10.2, 3.37, 2.7	
86	229	0			**86**	181	0		
87	311	0			**87**	149	8	9.57, 1.21	
88	369	0			**88**	374	5	5.31, 4.82, 1.73	
89	237	0			**89**	229	5	3.38, 3.08	
90	116	0			**90**	317	1	2.79	
91	225	3	3.02, 4.88		**91**	323	2	7.96	
92	150	0			**92**	126	3	2.98	
93	159	1	4.5		**93**	134	4	4.3, 4.1, 6.57	
94	167	25	7.89, 6.67, 1.3		**94**	228	4	1.69	
95	217	3	6.26		**95**	219	9	4.89, 3.48, 2.86	
96	284	0			**96**	244	2	14, 3.67	
97	86.3	0			**97**	123	2	2.72	
98	251	2	4.88, 2.93		**98**	74.8	0		
99	290	0			**99**	261	2	9.96, 14.3	
100	259	0			**100**	55.5	1	9.32	
	19865	**241**	**total**			**20373**	**290**	**total**	
	199	**2.41**	**avgs**			**204**	**4.08**	**avg**	

Sample	13833				Sample	15617			
	Grain size (um)	# of fracs	Frac. wdt (um)	# of pieces (2d)		Grain size (um)	# of fracs	Frac. Wdt (um)	# of pieces (2d)
1	118	3	<1	3	**1**	239	0		
2	52.9	0			**2**	883	7	12, 7.34	
3	160	11	4.34, 3.83, 3.18	>25	**3**	306	0		
4	118	1	<1	2	**4**	782	8	13.9, 7.07, 4.33	
5	101	1	11.7	2	**5**	716	17	10.1, 7.42, 5.2	
6	78.1	1	<1		**6**	1000	15	3.38, 5.91, 3.98	
7	138	0			**7**	715	6	14.8, 9.07, 3.38	7
8	106	1	4.38	2	**8**	812	0		
9	116	1	1.35		**9**	293	3	3.38, 1.51	
10	150	0			**10**	743	3	5.58, 4.53, 4.85	4
11	76.2	0			**11**	943	0		
12	136	16	6.24, 1.33	>25	**12**	335	25	5.86, 3.98, 9.53	
13	132	1	1.11	1	**13**	451	13	9.71, 3.25	
14	142	6	7.65, <1	6	**14**	186	25		
15	118	1	2.45	2	**15**	832	0		
16	110	0			**16**	623	3	2.26,<1	6
17	262	0			**17**	350	8	1.45,<1	
18	133	3	5.59, 1.86, 4.37	4	**18**	767	1	2.97	
19	116	3	1.59	4	**19**	633	2	3.16	
20	146	0			**20**	918	3	1.73, 1.04	3
21	129	0			**21**	106	4	<1	
22	79.8	2	4.24, 3.05	3	**22**	425	0		
23	137	4	1.96, 1.86	2	**23**	306	5	15.1, 4.55, 2.97	6
24	61.8	0			**24**	884	0		
25	113	0			**25**	609	4	4.43, 1.39	
26	120	3	2.89	4	**26**	927	0		
27	125	4	3.68, 1.58	3	**27**	193	0		

13833	Grain size (um)	# of fracs	Frac. wdt (um)	# of pieces (2d)	**15617**	Grain size (um)	# of fracs	Frac. Wdt (um)	# of pieces (2d)
28	136	2	2.78	2	**28**	545	5	8.74, 11.3, 6.84	7
29	128	0			**29**	389	0		
30	121	2	3.86, 1.06	4	**30**	398	2	6.04, 5	3
31	202	4	5.5, 1.95	4	**31**	351	3	3.23, 2.39	4
32	126	0			**32**	850	2	2.26, 5.42	
33	188	4	<1	5	**33**	788	0		
34	72.6	0			**34**	688	5	3.97, 6.21, 21.17	
35	139	3	4.64, 5.43	3	**35**	687	0		
36	132	2	1.16, 1.42	3	**36**	372	0		
37	99.8	5	1.19	3	**37**	856	4	4.98, <1	
38	102	2	<1	3	**38**	104	2	2.23	
39	68.7	0			**39**	650	4	1	
40	114	0			**40**	221	0		
41	144	14	6.85, 11.4, 7.89, 2.66	>25	**41**	351	1	1.33	
42	174	1	1.99	1	**42**	655	4	2.09	2
43	72.4	3	<1	3	**43**	96.9	1		
44	124	9	4.43	9	**44**	355	0		
45	99.7	0			**45**	582	0		
46	282	0			**46**	303	2	21.2, 15.9	3
47	65	3	<1	2	**47**	587	25	5.38, 4.64	
48	131	1	7.97	2	**48**	341	0		
49	79.9	1	5.57	2	**49**	714	2	3.66,<1	
50	187	0			**50**	837	4	23.2, 2.16	4
51	123	1	2.26	1	**51**	851	3	21	
52	151	2	<1	3	**52**	337	2	<1um	3
53	101	2	<1	3	**53**	408	0		
54	165	0			**54**	515	0		
55	93.4	0			**55**	556	2	11.6, 5.8	

56	182	4	6.37, 3.21	5	56	605	4	1.16	2
13833	**Grain size (um)**	**# of fracs**	**Frac. wdt (um)**	**# of pieces (2d)**	**15617**	**Grain size (um)**	**# of fracs**	**Frac. Wdt (um)**	**# of pieces (2d)**
57	74.1	7	3.21		**57**	985	2	1.21	
58	143	0			**58**	506	0		
59	85.3	1	1.96	1	**59**	406	7	5.8, 6.56, 1.35	11
60	122	4	8.47	4	**60**	482	14	10.9, 5.18, 13.4	>25
61	97.6	0			**61**	372	5	6.6, 1.06	
62	98.6	0			**62**	458	11	68.6, 11.7, 4.33	
63	108	0			**63**	520	0		
64	131	7	3.39, 2.05, 2.09	10	**64**	1000	3	<1	
65	161	2	<1	1	**65**	786	3	<1	
66	101	0			**66**	575	9	3.48, 10.6, 16.1, 4.3, 19.4	
67	125	0			**67**	331	25	20, 6.88	
68	95.7	6	3.26	8	**68**	883	3	4.5	
69	104	1	3.41	2	**69**	584	0		
70	75.5	1	7.13	4	**70**	820	1	3.54	
71	121	0			**71**	418	0		
72	169	3	13	3	**72**	357	0		
73	104	0			**73**	700	7	6.81, 11.7, 2.89	
74	166	0			**74**	836	0		
75	128	1	1.35	2	**75**	478	1	10.4	
76	133	1	2.81	2	**76**	523	4	1.81	
77	149	2	<1	2	**77**	803	0		
78	58.8	0			**78**	1120	1	6.81	
79	71.4	2	1.92	3	**79**	67	0		
80	142	3	1.48	2	**80**	522	0		
81	147	17	10.9, 10.4	>25	**81**	384	3	2.82	
82	82.9	0			**82**	299	5	3.22, 1.98	
83	167	3	11.6, 5.36	3	**83**	729	1	2.32	
84	88.9	0			**84**	392	25	5.03, 7.76	>25

13833	Grain size (um)	# of fracs	Frac. wdt (um)	# of pieces (2d)	15617	Grain size (um)	# of fracs	Frac. wdt (um)	# of pieces (2d)
85	151	3	2.7, 3.5	4	**85**	265	6	4.5, 2.97, 1.39, 6	
86	186	1	3.18	1	**86**	555	3	2.57	
87	140	2	<1	2	**87**	369	7	3.48,<1	
88	46.8	2	<1	2	**88**	769	0		
89	90.7	1	<1	1	**89**	313	2	<1	
90	121	0			**90**	713	9	8.76, 12.8, 3.9	
91	155	0			**91**	244	6	6.29, 1.81, 4.4	
92	173	0			**92**	906	0		
93	60.7	1	<1	2	**93**	930	1	<1	
94	131	0			**94**	682	3	1.69	
95	206	0			**95**	392	6	4.69, 3.48	
96	181	0			**96**	498	1	1.74	
97	53.4	3	1.9	3	**97**	601	0		
98	118	4	4.92, 4.24, 4.63	9	**98**	707	25	6.9	
99	127	3	4.24, 4.53, 1.06	4	**99**	475	0		
100	155	7	17.5, 11.3, 2.89	9	**100**	705	2		
	12424	**215**	**total**				**430**	**total**	
	124	**3.47**	**avg**			**564**	**6.32**	**avg**	

Sample	15620				Sample	15640			
	Grain size (um)	# of fracs	Frac. wdt (um)	# of pieces (2d)		Grain size (um)	# of fracs	Frac. Wdt (um)	# of pieces (2d)
1	524	25	8.73, 4.83, 3.42		**1**	243	0		
2	455	1	17.6		**2**	189	9	15.4, 12.3	
3	405	1	1.81		**3**	485	2	<1	
4	673	4	3.55		**4**	520	12	6.49, 5.22	
5	360	1	<1		**5**	632	12	11, 6.04, 5.79	
6	965	2			**6**	430	1	4.83	
7	502	0			**7**	117	3	2.44	
8	299	2	<1		**8**	430	10	<1	
9	610	1	2.16		**9**	518	4	<1	
10	718	25	11.5		**10**	639	1	<1	
11	547	25	9.17, 4.9, 1.74		**11**	467	3	<1	
12	805	3	22.8, 5.57		**12**	370	3	<1	
13	210	3	7.23, 2.89, 0.5		**13**	587	5	2.64, <1	
14	617	2	1.39		**14**	468	12	13.1, 4.07	
15	56.8	0	0		**15**	458	7	19.1, 1.86	
16	500	1			**16**	350	8	3.71	
17	850	3	1.62		**17**	297	4	4.69	
18	477	25	7.52, 5.32, 4.46		**18**	634	6	1.86, 18.2	
19	489	0			**19**	337	10	11.3, 1.41	
20	186	1	2.91		**20**	644	11	7.07, 3.71, 2.82	
21	201	0			**21**	420	15	7.97, 12.1, 8.2	
22	1030	4	7.13, 2.93		**22**	203	5	9.42, 3.09	
23	644	3			**23**	511	3	<1	
24	726	3	10.5, 3.54, 3.96		**24**	271	4	2.26,<1	
25	611	1	<1		**25**	457	0		
26	1170	2	2.61		**26**	207	6	5.83, <1	
27	1050	2	6.51		**27**	309	4	<1	

15620	Grain size (um)	# of fracs	Frac. wdt (um)	# of pieces (2d)	15640	Grain size (um)	# of fracs	Frac. Wdt (um)	# of pieces (2d)
28	284	3	2.33		**28**	192	11	11.1, 6.21, 2.9	
29	337	25			**29**	86.7	3	<1	
30	1120	5	1.93, 1.54		**30**	287	9	14.8, 5.9	
31	330	9	1.9, 2.11		**31**	250	0		
32	754	1	6.84		**32**	159	4	2.9, 1.54	
33	397	0			**33**	534	4	1.39	
34	840	0			**34**	473	4	2.6	
35	297	6	3.73, 3.36, 0.772		**35**	313	2	2.16	
36	386	4	3.61, 1.39		**36**	597	25	19.9, 13.7, 7.58, 6.26	
37	644	0			**37**	439	4	1.3	
38	321	2	<1		**38**	239	0		
39	985	2	4.74		**39**	420	6	8.29, 2.01	
40	748	1	7.4		**40**	214	1	2.16	
41	512	0			**41**	273	6	1.3, 3.52	
42	652	0			**42**	357	1	3.9	
43	434	3	5.57, 3.5, 1.59		**43**	349	3	1.29	
44	745	3	<1		**44**	163	2	4.88, 5.68	
45	788	3	0.696		**45**	464	1	1.73	
46	603	0			**46**	417	2	<1	
47	355	4	2.9, 1.86		**47**	627	8	9, 9.17	
48	752	0			**48**	296	0		
49	446	2	<1		**49**	459	1	5.91	
50	475	10	1.93		**50**	480	0		
51	975	4	4.4		**51**	475	5	6.93, 5.2	
52	376	0			**52**	538	2	<1	
53	864	5	9.62, 1.78		**53**	1030	2	21.4	
54	531	5	11.5, 2.78, 1.93		**54**	382	1	<1	
55	520	9	4.82, 1.28, 1.27		**55**	206	0		
56	862	0			**56**	244	1	3.61	

15620	Grain size (um)	# of fracs	Frac. wdt (um)	# of pieces (2d)	15640	Grain size (um)	# of fracs	Frac. Wdt (um)	# of pieces (2d)
57	712	0			**57**	306	1	5.64	
58	138	4	5.2		**58**	135	0		
59	529	4			**59**	199	2	3.2	
60	772	0			**60**	203	2	1.99	
61	425	7	10.1, 7.35, 5.15		**61**	298	4	3.98, 2.66	
62	373	10	4.92, 3.89, 2.56		**62**	262	1	8.54	
63	461	9	8.16		**63**	246	5	2.97	
64	303	0			**64**	228	1	8.66	
65	567	5	12.3		**65**	487	9	6.46, 4.03	
66	926	15	14.5, 7.96		**66**	287	6	11.4, 2.16	
67	547	0			**67**	198	1	1.3	
68	514	12	9.8, 8.66, 4.83		**68**	628	3	<1	
69	686	0			**69**	611	6	<1	
		312	total		**70**	310	8	7.72	
		4.27	avg		**71**	398	3	1.73	
					72	256	0		
					73	82.2	5	3.88, 1.98	
					74	183	0		
					75	307	0		
					76	472	5	<1	
					77	165	1	7.157	
					78	594	11	8.86, 4.03, 2.97	
					79	428	2	1.29	
					80	200	25	4.9, 5.38	
					81	422	10	6.5, 6.76	
					82	255	1	<1	
					83	709	0		
					84	420	15	3.88,<1	

15640	**Grain size (um)**	**# of fracs**	**Frac. wdt (um)**	**# of pieces (2d)**
85	214	1	1.93	
86	382	4	1.95	
87	601	8	3.98, 7.8	
88	173	1	8.92	
89	212	0		
90	203	2		
91	279	7	11.2, 4.78, 6.51	
92	472	4	11	
93	370	9	3.02	
94	467	1	9.48	
95	554	10	14.5	
96	500	0		
97	426	0		
98	157	2	<1	
99	206	0		
100	150	1	<1	
		445	**total**	
		5.30	**avg**	

Sample	17156			
	Grain size (um)	# of fractures	Frac. widths (um)	# of pieces (2d)
1	286	0		
2	230	0		
3	248	1	2.26	
4	225	25	6.96, 6.53, 4.53	
5	242	3	7.07, 3.62, 1.98	
6	205	0		
7	195	4	2.17	
8	285	0		
9	132	4	1.86	
10	175	25	9.59, 1.35, 1.11	
11	286	0		
12	203	6	7.24, 3.38, 2.6	
13	368	0		
14	234	3	<1	
15	128	1	3.1	
16	158	3	5, 1.21	
17	250	0		
18	300	0		
19	151	25	2.42, 2.7	
20	240	25	3.86, 4.86	
21	322	3	2.08	
22	289	0		
23	263	2		
24	304	4	1.72	
25	231	4	2.34, 1.82, 1.21*	
26	334	0		
27	187	4	5.32, 1.99, 2.12	

17156	Grain size (um)	# of fractures	Frac. widths (um)	# of pieces (2d)
28	280	2	<1	
29	380	0		
30	1.78	0		
31	125	0		
32	363	3	4.43	
33	362	0		
34	241	1	6.47	
35	297	1	4.5	
36	277	0		
37	109	1	2.74	
38	300	0		
39	373	1	4.07	
40	268	3	8.71, 1.16	
41	300	0		
42	188	25	24.2, 24.1, 6.99	
43	199	0		
44	292	3	3.49	
45	297	0		
46	230	25	<1	
47	280	6	3.4, 4.9, 3.02	
48	394	1	11.4	
49	267	3	3.48, 3.25, 2.61	
50	262	3	2.84	
51	184	0		
52	237	1	5.58	
53	145	3	5.82	
54	315	3	3.9	
55	292	0		
56	426	0		

17156	**Grain size (um)**	**# of fractures**	**Frac. widths (um)**	**# of pieces (2d)**
85	421	7	26.5, 9.07, 12.2	
86	254	3	<1	
87	380	2	1.29	
88	203	25	3.55, 2.45	
89	270	2	<1	
90	307	3	5.84, 1.86	
91	152	0		
92	339	0		
93	134	3	5.82	
94	235	1	5.64	
95	207	0		
96	303	5	6.96	
97	344	0		
98	274	5	3.48	
99	403	1	1.39	
100	407	0		
		340	**total**	
		5.57	**avg**	

Appendix D

Photomicrographs of fractured grains used to determine volume of intragranular quartz cement and resulting raw data

APPENDIX D

Quantifying the average amount of intragranular quartz cement in 30 fractured quartz grains from the Mount Simon Formation. One to two fractured grains were randomly selected, resulting in 30 grains analyzed. Between 300-400 point counts were conducted for each grain. Each grain image was rotated randomly five times and point counted.

*= Total Point Counts **=% volume

No	Depth (m)	Sample	Det Qtz	Intragr Qtz	TPC*	Det Qtz**	Intragr Qtz**	Avg Det.Qtz**	Avg Intragr Qtz**
1	1016	**71901-2**	304	31	335	0.91	0.09	**0.91**	**0.09**
			310	23	333	0.93	0.07		
			267	35	302	0.88	0.12		
			257	21	278	0.92	0.08		
			307	24	331	0.93	0.07		
2	1016	**71801-9**	366	36	402	0.91	0.09	**0.93**	**0.07**
			348	10	358	0.97	0.03		
			357	14	371	0.96	0.04		
			349	33	382	0.91	0.09		
			359	33	392	0.92	0.08		
3	1162	**1164**	274	26	300	0.91	0.09	**0.89**	**0.11**
			270	43	313	0.86	0.14		
			235	4	239	0.98	0.02		
			278	48	326	0.85	0.15		
			219	46	265	0.83	0.17		
4	1196	**1277**	356	13	369	0.96	0.04	**0.98**	**0.02**
			393	4	397	0.99	0.01		
			375	2	377	0.99	0.01		
			358	8	366	0.98	0.02		
			326	5	331	0.98	0.02		

No	Depth (m)	Sample	Det Qtz	Intragr Qtz	TPC*	Det Qtz**	Intragr Qtz**	Avg Det.Qtz**	Avg Intragr Qtz**
5	1200	**1288**	246	9	255	0.96	0.04	**0.97**	**0.03**
			352	5	357	0.99	0.01		
			285	6	291	0.98	0.02		
			342	10	352	0.97	0.03		
			249	10	259	0.96	0.04		
6	1381	**2019**	314	5	319	0.98	0.02	**0.99**	**0.01**
			269	3	272	0.99	0.01		
			296	2	298	0.99	0.01		
			365	5	370	0.99	0.01		
			340	7	347	0.98	0.02		
7	1426	**2166**	235	27	262	0.90	0.10	**0.91**	**0.09**
			222	23	245	0.91	0.09		
			217	22	239	0.91	0.09		
			241	23	264	0.91	0.09		
			222	21	243	0.91	0.09		
8	1586	**2480**	231	25	256	0.90	0.10	**0.88**	**0.12**
			272	29	301	0.90	0.10		
			271	47	318	0.85	0.15		
			290	36	326	0.89	0.11		
			278	42	320	0.87	0.13		
9	1615	**2384**	194	10	204	0.95	0.05	**0.96**	**0.04**
			206	10	216	0.95	0.05		
			216	7	223	0.97	0.03		
			215	11	226	0.95	0.05		
			186	9	195	0.95	0.05		

No	Depth (m)	Sample	Det Qtz	Intragr Qtz	TPC*	Det Qtz**	Intragr Qtz**	Avg Det.Qtz**	Avg Intragr Qtz**
10	1640	**2562**	241	60	301	0.80	0.20	**0.85**	**0.15**
			267	41	308	0.87	0.13		
			253	45	298	0.85	0.15		
			265	47	312	0.85	0.15		
			282	45	327	0.86	0.14		
11	1814	**3581**	339	11	350	0.97	0.03	**0.95**	**0.05**
			379	16	395	0.96	0.04		
			340	23	363	0.94	0.06		
			343	24	367	0.93	0.07		
			337	18	355	0.95	0.05		
12	1734	**3134.5**	336	52	388	0.87	0.13	**0.83**	**0.171**
			345	48	393	0.88	0.12		
			277	72	349	0.79	0.21		
			277	72	349	0.79	0.21		
			271	62	333	0.81	0.19		
13	1842	**3177**	255	6	261	0.98	0.02	**0.97**	**0.03**
			312	5	317	0.98	0.02		
			305	9	314	0.97	0.03		
			214	9	223	0.96	0.04		
			251	7	258	0.97	0.03		
14	1992	**3224**	392	4	396	0.99	0.01	**0.98**	**0.02**
			278	3	281	0.99	0.01		
			327	7	334	0.98	0.02		
			342	4	346	0.99	0.01		
			385	14	399	0.96	0.04		

No	Depth (m)	Sample	Det Qtz	Intragr Qtz	TPC*	Det Qtz**	Intragr Qtz**	Avg Det.Qtz**	Avg Intragr Qtz**
15	2003	**3619**	404	9	413	0.98	0.02	**0.94**	**0.06**
			367	18	385	0.95	0.05		
			229	14	243	0.94	0.06		
			336	22	358	0.94	0.06		
			294	29	323	0.91	0.09		
16	1922	**3793**	271	5	276	0.98	0.02	**0.98**	**0.02**
			242	5	247	0.98	0.02		
			223	7	230	0.97	0.03		
			227	7	234	0.97	0.03		
			293	6	299	0.98	0.02		
17	2152	**4038**	357	15	372	0.96	0.04	**0.96**	**0.04**
			352	13	365	0.96	0.04		
			296	15	311	0.95	0.05		
			350	21	371	0.94	0.06		
			277	12	289	0.96	0.04		
18	2176	**4119**	274	3	277	0.99	0.01	**0.99**	**0.01**
			263	1	264	1.00	0.00		
			341	7	348	0.98	0.02		
			342	3	345	0.99	0.01		
			282	7	289	0.98	0.02		
19	2209	**4226**	273	19	292	0.93	0.07	**0.97**	**0.03**
			227	1	228	1.00	0.00		
			254	21	275	0.92	0.08		
			235	2	237	0.99	0.01		
			222	1	223	1.00	0.00		

No	Depth (m)	Sample	Det Qtz	Intragr Qtz	TPC*	Det Qtz**	Intragr Qtz**	Avg Det.Qtz**	Avg Intragr Qtz**
20	2201	**4469**	326	13	339	0.96	0.04	**0.97**	**0.03**
			271	3	274	0.99	0.01		
			311	13	324	0.96	0.04		
			293	12	305	0.96	0.04		
			240	9	249	0.96	0.04		
21	2203	**4477**	369	5	374	0.99	0.01	**0.97**	**0.03**
			411	15	426	0.96	0.04		
			376	12	388	0.97	0.03		
			344	23	367	0.94	0.06		
			370	10	380	0.97	0.03		
22	2277	**4720**	376	13	389	0.97	0.03	**0.96**	**0.04**
			347	13	360	0.96	0.04		
			348	14	362	0.96	0.04		
			339	14	353	0.96	0.04		
			241	9	250	0.96	0.04		
23	2589	**5404**	314	11	325	0.97	0.03	**0.98**	**0.02**
			286	8	294	0.97	0.03		
			301	0	301	1.00	0.00		
			294	10	304	0.97	0.03		
			300	0	300	1.00	0.00		
24	2817	**6154**	269	42	311	0.86	0.14	**0.91**	**0.09**
			316	25	341	0.93	0.07		
			314	43	357	0.88	0.12		
			345	29	374	0.92	0.08		
			313	15	328	0.95	0.05		

No	Depth (m)	Sample	Det Qtz	Intragr Qtz	TPC*	Det Qtz**	Intragr Qtz**	Avg Det.Qtz**	Avg Intragr Qtz**
25	2842	**6235**	242	23	265	0.91	0.09	**0.98**	**0.02**
			314	4	318	0.99	0.01		
			264	0	264	1.00	0.00		
			168	0	168	1.00	0.00		
			301	0	301	1.00	0.00		
26	2844	**6241**	295	2	297	0.99	0.01	**0.98**	**0.02**
			413	8	421	0.98	0.02		
			328	13	341	0.96	0.04		
			354	8	362	0.98	0.02		
			297	0	297	1.00	0.00		
27	2922	**6497**	378	5	383	0.99	0.01	**0.99**	**0.013**
			348	3	351	0.99	0.01		
			377	6	383	0.98	0.02		
			346	4	350	0.99	0.01		
			373	6	379	0.98	0.02		
28	2923	**6500**	288	10	298	0.97	0.03	**0.98**	**0.02**
			381	9	390	0.98	0.02		
			338	6	344	0.98	0.02		
			321	6	327	0.98	0.02		
			355	11	366	0.97	0.03		
29	3646	**8466**	353	19	372	0.95	0.05	**0.94**	**0.06**
			158	12	170	0.93	0.07		
			323	14	337	0.96	0.04		
			367	21	388	0.95	0.05		
			336	26	362	0.93	0.07		

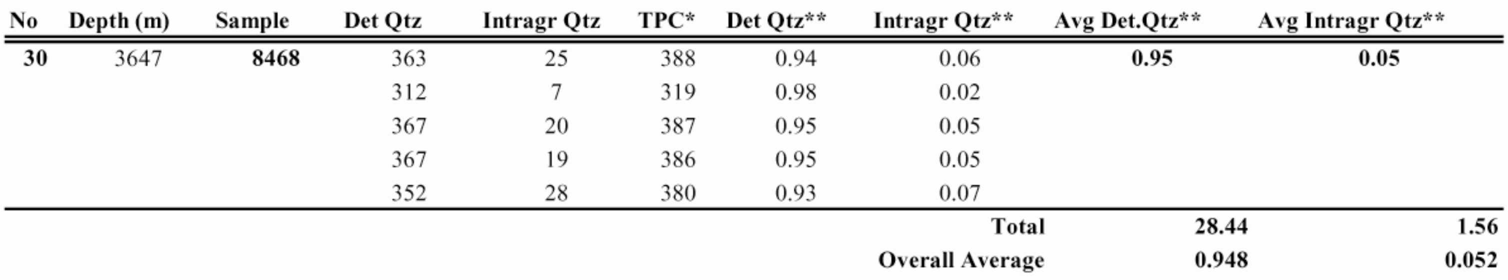

No	Depth (m)	Sample	Det Qtz	Intragr Qtz	TPC*	Det Qtz**	Intragr Qtz**	Avg Det.Qtz**	Avg Intragr Qtz**
30	3647	**8468**	363	25	388	0.94	0.06	**0.95**	**0.05**
			312	7	319	0.98	0.02		
			367	20	387	0.95	0.05		
			367	19	386	0.95	0.05		
			352	28	380	0.93	0.07		
							Total	**28.44**	**1.56**
							Overall Average	**0.948**	**0.052**

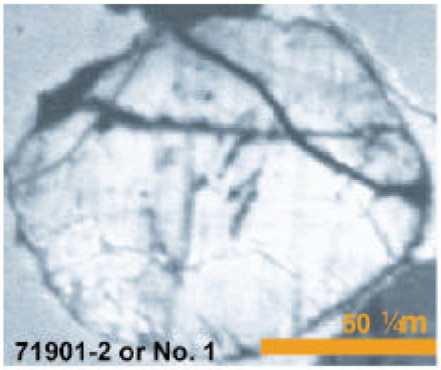
50 ¼m
71901-2 or No. 1

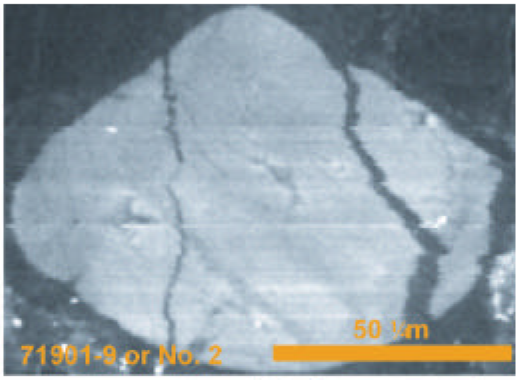
50 ¼m
71901-9 or No. 2

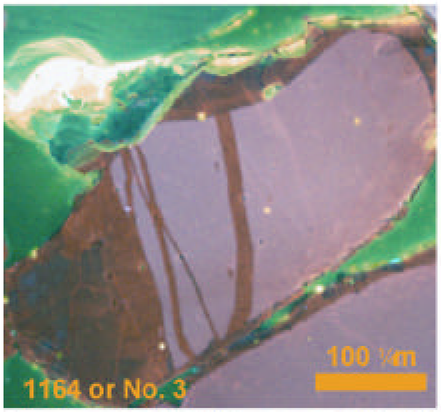
100 ¼m
1164 or No. 3

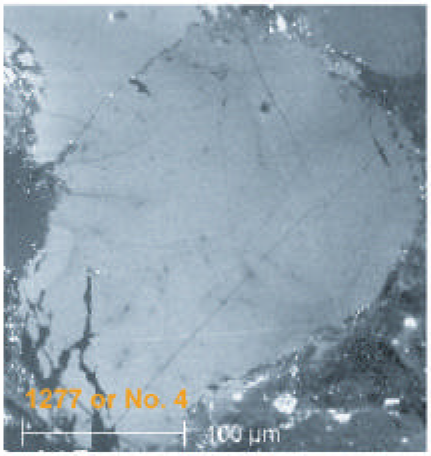
1277 or No. 4
100 µm

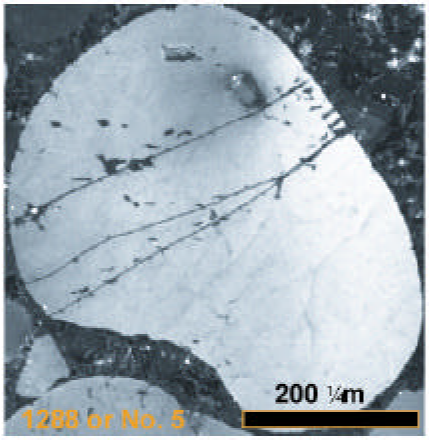
200 ¼m
1288 or No. 5

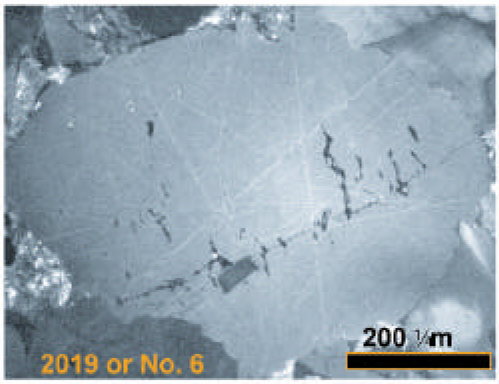
200 ¼m
2019 or No. 6

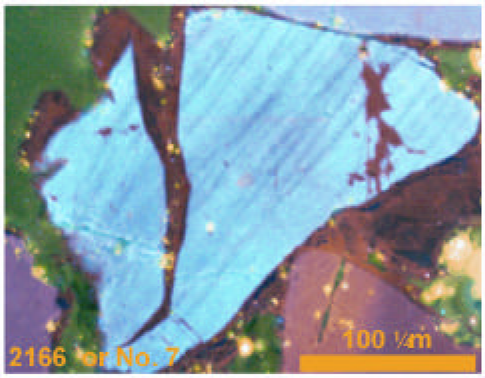
2166 or No. 7
100 ¼m

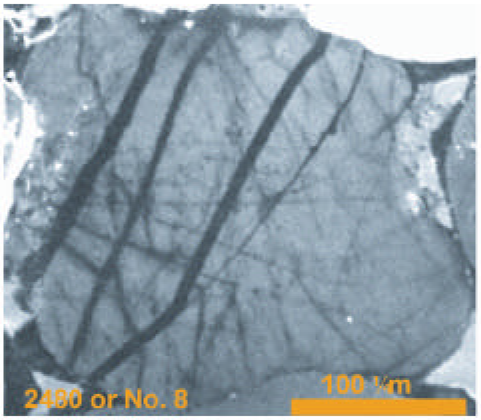
2480 or No. 8
100 ¼m

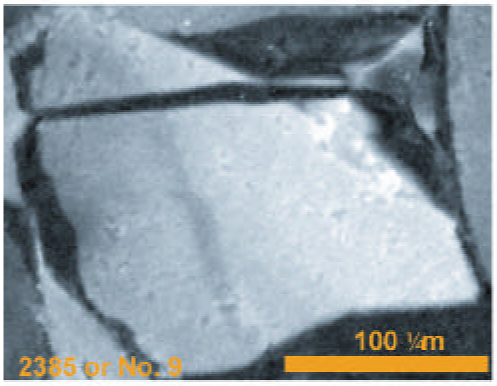
2385 or No. 9
100 ¼m

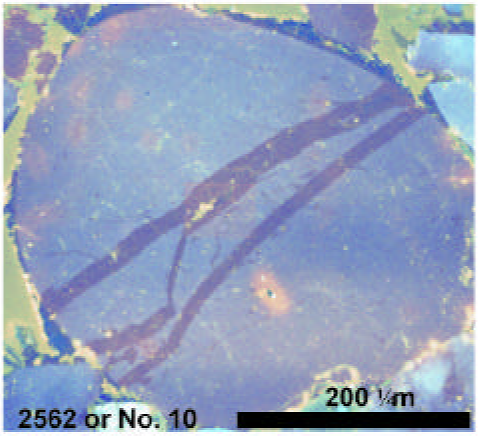
2562 or No. 10
200 ¼m

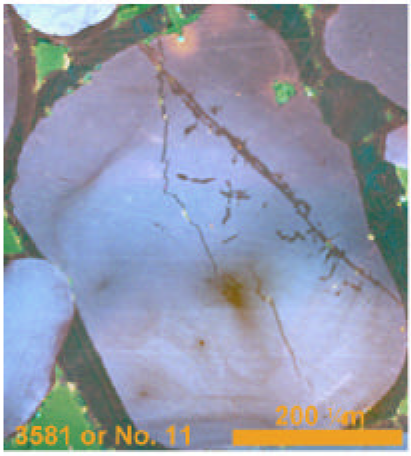
3581 or No. 11
200 ¼m

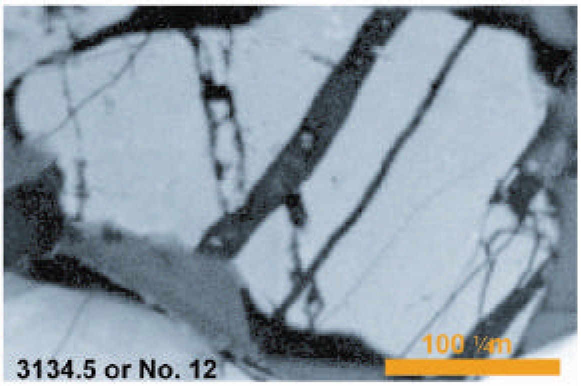
3134.5 or No. 12
100 ¼m

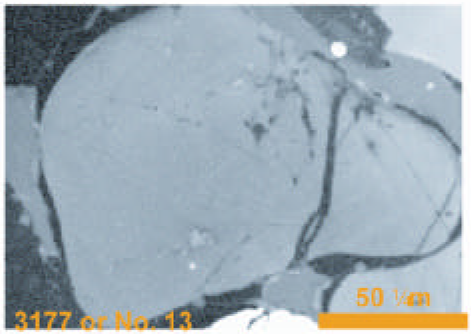
50 µm
3177 or No. 13

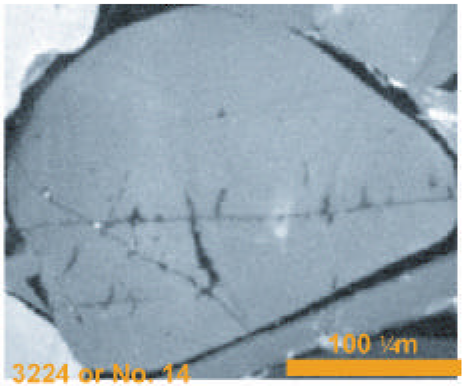
100 µm
3224 or No. 14

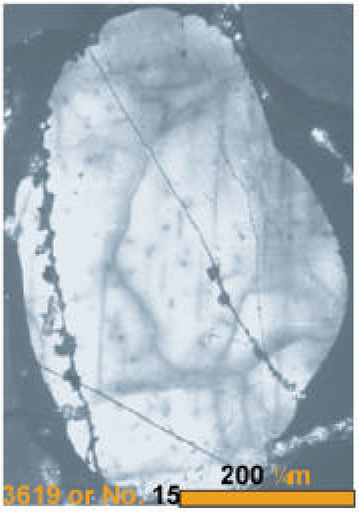
200 µm
3619 or No. 15

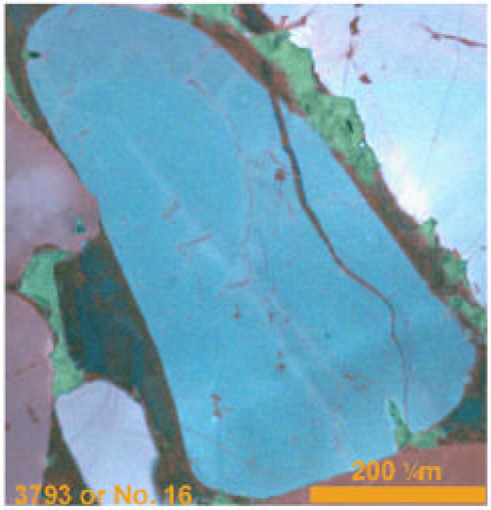
200 µm
3793 or No. 16

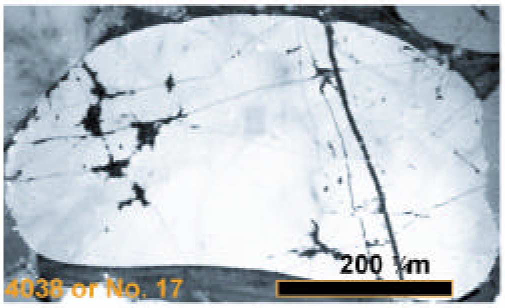
200 µm
4038 or No. 17

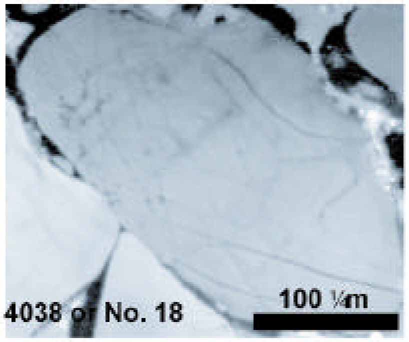
100 µm
4038 or No. 18

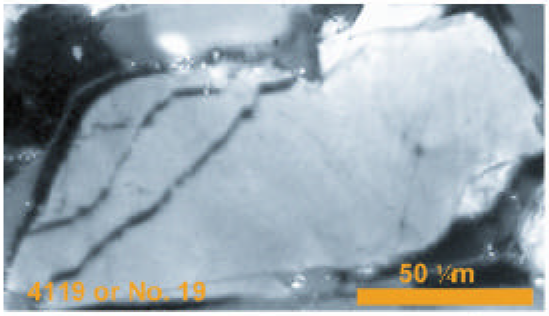
50 ¼m
4119 or No. 19


100 ¼m
4469 or No. 20

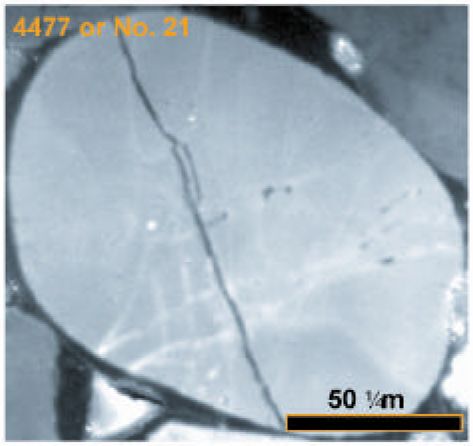
4477 or No. 21
50 ¼m

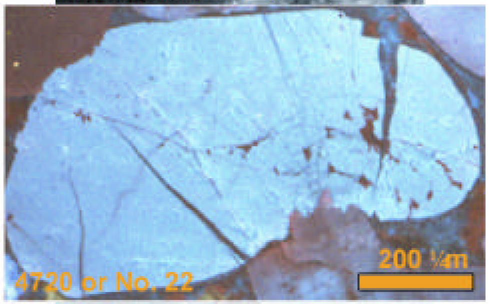
200 ¼m
4720 or No. 22

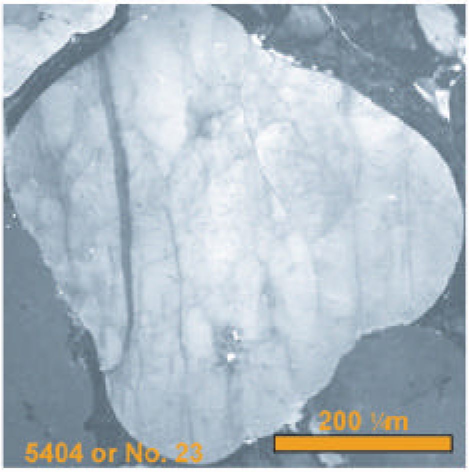
200 ¼m
5404 or No. 23

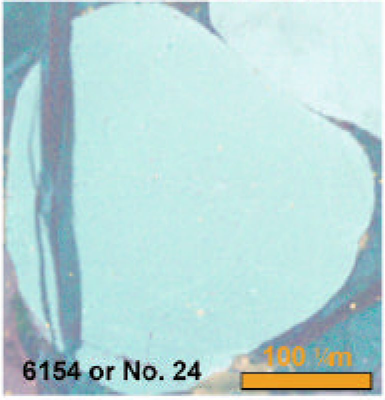
100 ¼m
6154 or No. 24

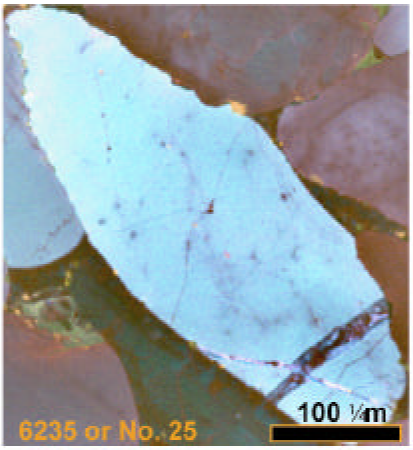
6235 or No. 25
100 ¼m

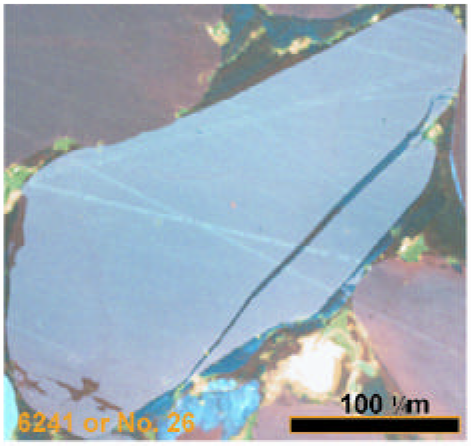
6241 or No. 26
100 ¼m

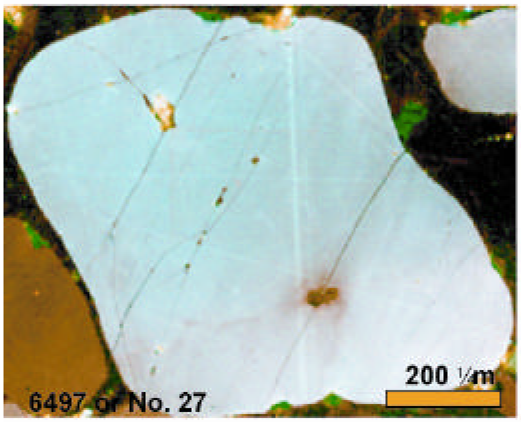
6497 or No. 27
200 ¼m

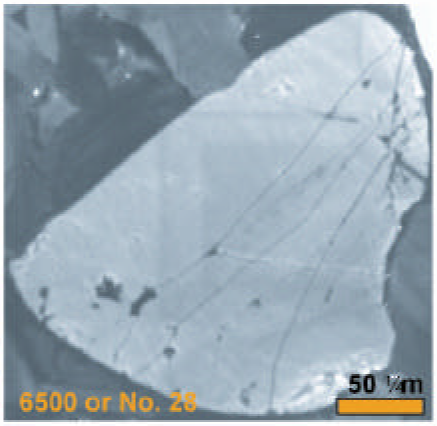
6500 or No. 28
50 ¼m

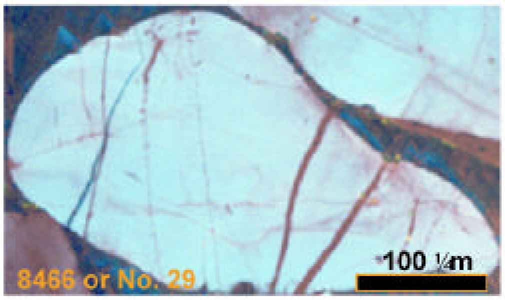
8466 or No. 29
100 ¼m

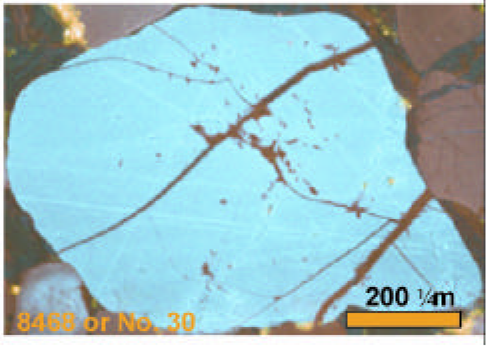
8468 or No. 30
200 ¼m

Appendix E

Measured and inferred values incorporated into Genesis for basin modeling

Appendix E. Values incorporated into Genesis for basin modeling. Measured values are derived from well-logs.

Slick State		**Gerdts**		**McHaney**	
Samples 4908		*Sample 6105, 9547, 10169, 13833*		*Samples 9710, 9720, 9744*	
Depth (m)	**Pressure (MPa)**	**Depth (ft)**	**Pressure (psi)**	**Depth (m)**	**Pressure (MPa)**
156*	2*	2850*	35*	1639*	17*
1219*	17*	3063*	43*	2050*	21*
2438*	46*	3296*	49*	2438*	25*
Depth (m)	**Temp (C)**	**Depth (m)**	**Temp (C)**	**Depth (m)**	**Temp (C)**
156*	32*	2850*	100*	1639*	64*
1219*	68*	3063*	104*	2050*	65*
2438*	95*	3296*	102*	2438*	74*
Time (MY)	**Surface Temp (C)**	**Time (MY)**	**Surface Temp (C)**	**Time (MY)**	**Surface Temp (C)**
50**	19**	50**	19**	50**	19**
34**	19**	34**	19**	34**	19**
16.6**	17**	16.6**	17**	16.6**	17**
5**	16**	5**	16**	5**	16**
1**	15**	1**	15**	1**	15**
Time (MY)	**Heat Flow Mw/m^2**	**Time (MY)**	**Heat Flow Mw/m^2**	**Time (MY)**	**Heat Flow Mw/m^2**
50**	80**	50**	35**	50**	35**
25**	80**	25**	35**	25**	35**
0**	80**	0**	35**	0**	35**

*=Measured values

**= Infered values

Mauritz		**Deer and Carter**		**Hornsby**	
Sample 5385		*Samples 3223,*		*Sample 9001*	
Depth (m)	**Pressure (MPa)**	**Depth (m)**	**Pressure (MPa)**	**Depth (m)**	**Pressure (MPa)**
1639*	17*	1402*	16*	2747*	23*
Depth (m)	**Temp (C)**	**Depth (m)**	**Temp (C)**	**Time (MY)**	**Surface Temp (C)**
1639*	64*	1402*	58*	50**	19**
				34**	19**
Time (MY)	**Surface Temp (C**	**Time (MY)**	**Surface Temp (**	16.6**	17**
50**	19**	50**	19**	5**	16**
34**	19**	34**	19**	1**	15**
16.6**	17**	16.6**	17**		
5**	16**	5**	16**	**Time (MY)**	**Heat Flow Mw/m^2**
1**	15**	1**	15**	50**	35**
				25**	35**
Time (MY)	**Heat Flow Mw/m**	**Time (MY)**	**Heat Flow Mw/**	0**	35**
50**	35**	50**	35**		
25**	35**	25**	35**		
0**	35**	0**	35**		

*=Measured values
**= Infered values

Pleasant Bayou

Samples 15617, 15629, 15649, 17154

Depth (m)	Pressure (MPa)
948*	14*
2600*	72*

Depth (m)	Temp (C)
2626*	96*
2681*	99*
2696*	98*
2981*	103*
3259*	117*
3440*	122*
3463*	118*
3574*	127*
3892*	138*
4161*	150*
4462*	138*
4740*	150*

Depth (m)	Ro
3096.77	0.4
3186.68	0.45
3299.46	0.51
3435.1	0.51
3535.68	0.58
3627.12	0.615
3736.85	0.56
3861.82	0.58

Depth (m)	Ro
4284*	0.61*
4407*	0.61*
4420*	0.61*
4538*	0.61*
4602*	0.61*
4694*	0.61*
4776*	0.61*
4785*	0.61*
4877*	0.61*
4968*	0.63*
5029*	0.63*

Time (MY)	Surface Temp (C)
50**	19**
34**	19**
16.6**	17**
5**	16**
1**	15**

Time (MY)	Heat Flow Mw/m^2
50**	35**
25**	35**
0**	35**

*=Measured values

**= Infered values

All values for the Illinois Basin were derived from Rowan et al (2002).

Southern Illinois Basin		**Central Illinois Basin**		**Northern Illinois Basin**	
Samples 6154, 6235, 6241, 6497, (*8466, 8468*		*Samples 3581.5, 3619, 3793, 4038, 4119,* *4226, 4469, 4477, 4720, 5404*		*Samples 2480, 3134.5, 3177, 3225*	
Depth (m)	**Temp (C)**	**Depth (m)**	**Temp (C)**	**Time (MY)**	**Heat Flow Mw/m^2**
460	38	1837.27	38	0	62.5
1900	93	5249.34	68	25	62.5
				50	62.5
Time (MY)	**Heat Flow Mw/m**	**Time (MY)**	**Heat Flow Mw/**	270	155
0	62.5	0	62.5	272	155
25	62.5	25	62.5	550	62.5
50	62.5	50	62.5		
270	155	270	155	**Time (MY)**	**Surface Temp (C)**
272	155	272	155	0	12
550	62.5	550	62.5	5	14
				40	18
Time (MY)	**Surface Temp (C**	**Time (MY)**	**Surface Temp (**	103	20
0	12	0	12	175	24
5	14	5	14	230	29
40	18	40	18	270	30
103	20	103	20	325	24
175	24	175	24	385	26
230	29	230	29	425	27
270	30	270	30	470	20
325	24	325	24	545	26
385	26	385	26		
425	27	425	27		
470	20	470	20		
545	26	545	26		

Appendix F

Temperature and pressure history data incorporated into Touchstone models

Appendix F. Compilation of temperature, depth, excess pressure, and effective stress data for Frio and Mount Simon Formation Wells generated by Genesis basin models.

Gerdts Well- GOM

Time	**Temperature**		**Depth**		**Pressure (Excess)**		**Effective Stress**	
my	**c**		**ft**		**psi**		**psi**	
	Top	**Base**	**Top**	**Base**	**Top**	**Base**	**Top**	**Base**
30.6	19.0	35.1	0.0	1177.2	0.0	176.7	0.0	255.9
30.3	22.3	40.6	240.5	1612.9	45.3	267.8	41.2	337.9
30.0	28.9	46.0	720.9	2040.4	128.5	375.5	131.1	403.3
29.6	33.3	49.2	1102.8	2365.4	153.6	445.6	264.0	491.2
29.1	36.4	51.6	1433.2	2661.3	191.4	525.9	384.3	568.9
28.7	40.0	54.6	1787.8	2992.1	271.3	616.2	462.3	636.6
28.3	43.5	57.6	2134.0	3316.7	345.1	710.8	546.5	700.0
27.9	46.9	60.6	2473.3	3637.0	421.1	809.1	628.6	759.7
27.4	50.1	63.4	2806.8	3953.8	501.2	910.7	706.5	816.2
27.0	53.3	66.3	3135.4	4267.7	585.7	1015.1	780.0	869.7
26.7	57.3	70.0	3554.0	4677.1	723.4	1166.1	828.4	904.9
26.4	61.4	73.9	3962.2	5076.6	861.5	1318.2	876.6	939.1
26.1	65.4	77.8	4365.3	5471.6	1001.4	1471.2	923.0	972.4
25.8	69.4	81.6	4765.1	5863.9	1143.4	1625.1	967.1	1004.7
25.5	73.3	85.4	5162.3	6254.1	1287.8	1780.0	1009.0	1036.0
25.2	77.2	89.1	5557.4	6642.7	1434.4	1935.8	1048.6	1066.4
24.9	81.0	92.8	5950.6	7029.8	1583.0	2092.5	1086.3	1096.0
24.6	84.7	96.4	6342.2	7415.7	1733.3	2250.0	1122.2	1124.7
24.3	88.4	100.0	6732.3	7800.4	1885.3	2408.3	1156.4	1152.6
24.0	92.1	103.5	7120.9	8184.0	2038.8	2567.4	1189.2	1179.8
23.7	95.7	107.1	7508.1	8566.5	2193.5	2727.2	1220.6	1206.1
22.7	97.2	108.4	7504.0	8548.5	2151.5	2698.7	1315.2	1287.2
21.8	97.0	107.9	7548.9	8581.7	2120.2	2676.7	1399.0	1361.7
20.8	97.0	107.7	7610.1	8632.7	2096.9	2660.2	1474.9	1430.8
19.9	97.3	107.8	7680.2	8693.9	2079.9	2648.3	1544.3	1495.1
18.9	97.6	108.0	7755.9	8761.7	2068.3	2640.6	1608.5	1555.3
17.9	98.1	108.3	7835.4	8834.1	2061.0	2636.5	1668.3	1612.0
17.0	98.6	108.7	7917.6	8909.8	2057.5	2635.5	1724.3	1665.5
16.0	99.1	109.1	8001.8	8988.1	2057.3	2637.3	1777.1	1716.2
15.0	99.7	109.6	8087.5	9068.3	2059.9	2641.6	1826.9	1764.4
14.1	100.3	110.1	8174.3	9150.2	2065.1	2648.2	1874.3	1810.4
13.1	100.9	110.6	8262.0	9233.2	2072.6	2656.8	1919.3	1854.3
12.2	101.6	111.1	8350.4	9317.3	2082.1	2667.3	1962.3	1896.3
11.2	102.2	111.7	8439.4	9402.3	2093.4	2679.5	2003.5	1936.6
10.4	103.1	112.5	8548.4	9508.0	2116.9	2703.6	2038.1	1970.7
9.5	104.0	113.4	8656.0	9612.4	2141.6	2728.8	2071.6	2003.6
8.7	105.0	114.2	8762.9	9716.4	2167.3	2755.0	2103.9	2035.4

Gerdts Well- GOM continued

Time	Temperature		Depth		Pressure (Excess)		Effective Stress	
my	c		ft		psi		psi	
	Top	Base	Top	Base	Top	Base	Top	Base
7.8	105.8	115.1	8869.5	9820.2	2194.1	2782.2	2135.3	2066.3
7.0	106.7	115.9	8975.9	9923.8	2221.9	2810.4	2165.6	2096.3
6.1	107.6	116.7	9082.0	10027.4	2250.5	2839.3	2195.1	2125.5
5.3	108.5	117.5	9188.0	10130.9	2280.0	2869.1	2223.7	2153.8
4.2	108.6	117.7	9235.8	10175.8	2282.8	2872.3	2258.6	2188.4
3.2	108.6	117.6	9289.0	10226.1	2286.9	2876.7	2292.4	2221.8
2.1	108.6	117.5	9344.5	10278.9	2292.0	2882.1	2325.1	2254.2
1.1	108.7	117.5	9401.5	10333.4	2298.1	2888.5	2356.8	2285.6
0.0	108.8	117.6	9459.5	10389.0	2305.2	2895.8	2387.5	2316.1

Hornsby Well GOM

Time	Temperature		Depth		Pressure (Excess)		Effective Stress	
my	c		ft		psi		psi	
	Top	Base	Top	Base	Top	Base	Top	Base
29.1	18.4	20.8	0.0	212.7	0.0	0.8	0.0	83.8
28.8	20.8	25.3	212.7	629.3	1.0	2.7	83.6	251.0
28.5	25.3	29.5	629.4	1029.9	3.1	4.9	250.6	417.9
28.3	29.4	33.3	1030.0	1417.0	5.6	7.6	417.3	584.3
28.0	33.3	37.0	1417.1	1792.7	8.6	11.0	583.4	750.1
27.7	36.9	40.4	1792.8	2158.4	12.3	15.0	748.8	915.2
27.5	40.4	43.7	2158.6	2515.5	16.6	19.7	913.6	1079.7
27.2	43.6	46.8	2515.7	2864.8	21.8	25.2	1077.6	1243.3
26.9	46.8	49.8	2865.1	3207.4	27.7	31.6	1240.8	1406.0
26.6	49.7	52.7	3207.7	3543.8	34.6	38.9	1403.0	1567.9
26.4	52.6	55.4	3544.2	3874.7	42.4	47.2	1564.3	1728.7
26.1	55.4	58.1	3875.2	4200.6	51.4	56.6	1724.5	1888.4
25.8	58.0	60.7	4201.1	4521.9	61.4	67.2	1883.6	2046.9
25.6	60.6	63.2	4522.5	4839.0	72.7	79.1	2041.4	2204.2
25.3	63.1	65.6	4839.7	5152.4	85.4	92.3	2197.9	2360.1
25.0	65.5	67.9	5153.1	5462.2	99.4	107.0	2352.9	2514.5
24.8	67.9	70.3	5463.0	5768.8	115.0	123.2	2506.5	2667.4
24.5	70.2	72.5	5769.6	6072.3	132.1	141.0	2658.5	2818.7
24.2	72.5	74.7	6073.3	6373.1	150.9	160.5	2808.7	2968.3
24.0	74.7	76.9	6374.1	6671.3	171.5	181.8	2957.3	3116.1
23.7	76.8	79.0	6672.4	6967.1	193.9	205.0	3103.9	3262.0
22.8	77.6	79.8	6732.7	7024.4	53.0	56.8	3295.3	3460.6
21.9	78.2	80.3	6820.0	7110.6	29.7	31.5	3368.9	3536.2
21.0	78.9	80.9	6909.7	7199.5	26.7	28.2	3422.3	3589.9

Hornsby Well GOM continued

Time	Temperature		Depth		Pressure (Excess)		Effective Stress	
my	c		ft		psi		psi	
	Top	Base	Top	Base	Top	Base	Top	Base
20.1	79.5	81.6	6999.4	7288.5	27.3	28.8	3471.9	3639.6
19.2	80.2	82.2	7088.6	7377.0	28.8	30.3	3520.8	3688.5
18.3	80.8	82.9	7177.4	7465.1	30.5	32.0	3569.5	3737.1
17.5	81.5	83.5	7265.7	7552.8	32.3	33.9	3618.0	3785.6
16.6	82.1	84.1	7353.6	7640.1	34.3	35.9	3666.4	3833.9
15.7	82.7	84.7	7441.2	7727.0	36.4	38.1	3714.6	3882.1
14.8	83.3	85.3	7528.4	7813.6	38.7	40.4	3762.7	3930.1
13.9	84.0	86.0	7615.3	7899.8	41.1	42.8	3810.6	3978.0
13.0	84.6	86.6	7701.8	7985.8	43.7	45.5	3858.3	4025.7
12.1	85.2	87.2	7788.1	8071.5	46.5	48.3	3905.9	4073.2
11.2	85.8	87.7	7874.2	8157.0	49.4	51.3	3953.2	4120.5
10.4	86.6	88.5	7980.1	8262.3	60.8	62.9	4001.8	4168.8
9.5	87.3	89.3	8083.9	8365.6	68.3	70.6	4054.3	4221.1
8.7	88.1	90.0	8187.1	8468.1	74.2	76.6	4108.3	4275.0
7.8	88.8	90.8	8289.8	8570.1	79.7	82.2	4162.7	4329.3
7.0	89.6	91.5	8392.1	8671.9	85.3	87.8	4217.1	4383.7
6.1	90.3	92.2	8494.1	8773.3	91.0	93.6	4271.3	4437.9
5.3	91.0	92.9	8595.8	8874.4	96.9	99.6	4325.3	4491.8
4.2	91.2	93.1	8651.7	8929.7	76.3	78.6	4384.5	4551.3
3.2	91.3	93.2	8713.1	8990.6	67.3	69.3	4432.0	4599.2
2.1	91.5	93.3	8776.4	9053.4	64.5	66.3	4473.4	4640.8
1.1	91.6	93.5	8840.3	9117.0	64.6	66.2	4511.9	4679.3
0.0	92.0	93.8	8904.6	9180.9	65.9	67.6	4549.0	4716.5

McHaney Well GOM

Time	Temperature		Depth		Pressure (Excess)		Effective Stress	
my	c		ft		psi		psi	
	Top	Base	Top	Base	Top	Base	Top	Base
33.0	18.9	22.0	0.0	272.5	0.0	0.0	0.0	107.0
32.9	22.0	28.0	272.7	803.5	3.7	8.8	103.3	312.2
32.8	28.0	33.5	804.1	1309.1	14.5	19.5	306.5	515.4
32.7	33.5	38.5	1310.3	1794.7	27.9	33.7	507.0	715.2
32.6	38.5	43.2	1796.5	2264.0	45.0	51.5	703.9	911.3
32.6	43.2	47.6	2266.4	2719.9	66.0	73.3	896.8	1103.4
32.5	47.6	51.8	2722.9	3164.4	91.2	99.4	1085.5	1291.4
32.4	51.8	55.7	3168.0	3599.3	120.9	129.8	1269.8	1474.9
32.3	55.8	59.6	3603.5	4026.0	155.2	164.9	1449.5	1653.7
32.2	59.7	63.3	4030.7	4445.4	194.3	204.8	1624.4	1827.8

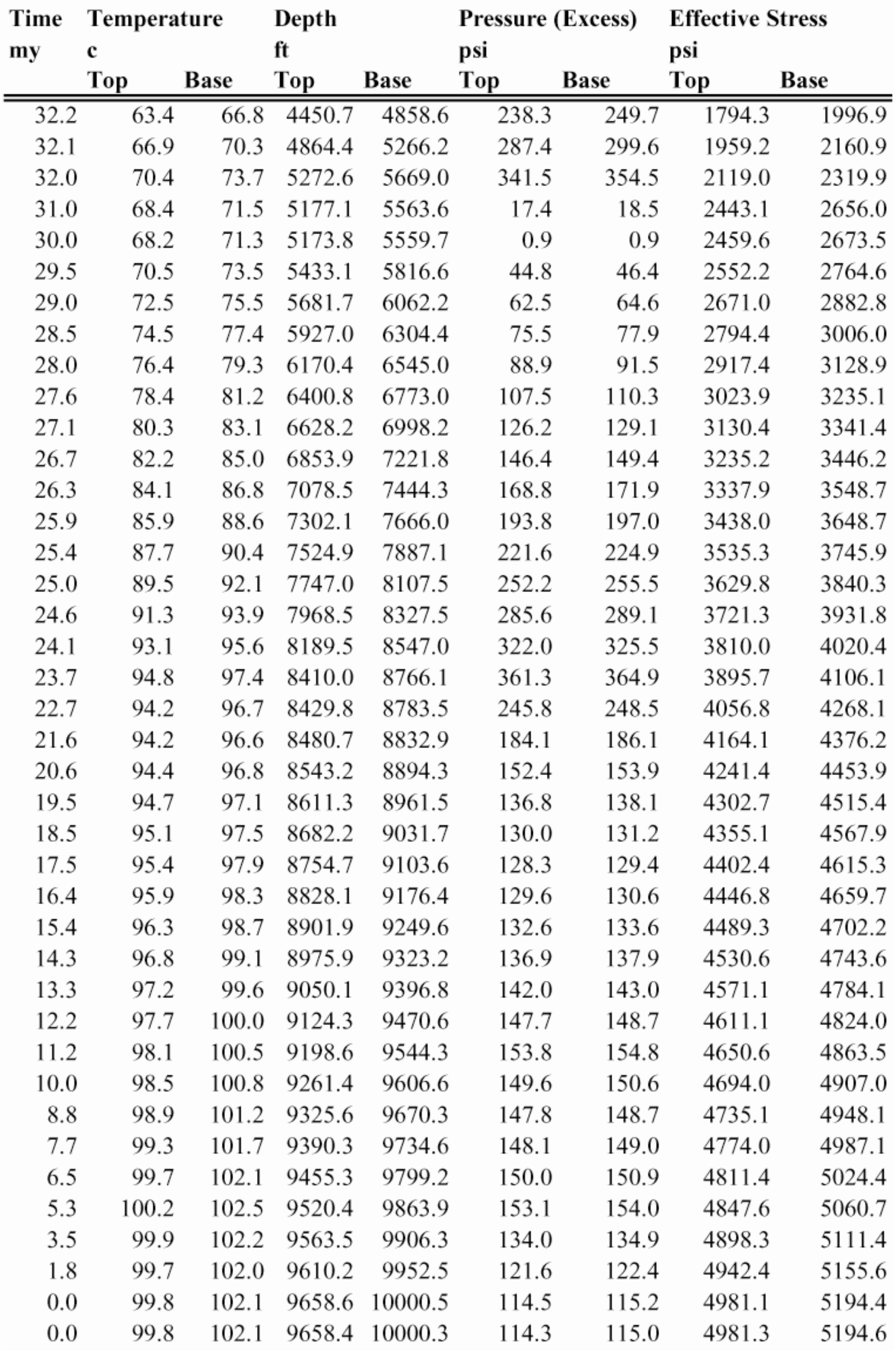

Time	Temperature		Depth		Pressure (Excess)		Effective Stress	
my	c		ft		psi		psi	
	Top	Base	Top	Base	Top	Base	Top	Base
32.2	63.4	66.8	4450.7	4858.6	238.3	249.7	1794.3	1996.9
32.1	66.9	70.3	4864.4	5266.2	287.4	299.6	1959.2	2160.9
32.0	70.4	73.7	5272.6	5669.0	341.5	354.5	2119.0	2319.9
31.0	68.4	71.5	5177.1	5563.6	17.4	18.5	2443.1	2656.0
30.0	68.2	71.3	5173.8	5559.7	0.9	0.9	2459.6	2673.5
29.5	70.5	73.5	5433.1	5816.6	44.8	46.4	2552.2	2764.6
29.0	72.5	75.5	5681.7	6062.2	62.5	64.6	2671.0	2882.8
28.5	74.5	77.4	5927.0	6304.4	75.5	77.9	2794.4	3006.0
28.0	76.4	79.3	6170.4	6545.0	88.9	91.5	2917.4	3128.9
27.6	78.4	81.2	6400.8	6773.0	107.5	110.3	3023.9	3235.1
27.1	80.3	83.1	6628.2	6998.2	126.2	129.1	3130.4	3341.4
26.7	82.2	85.0	6853.9	7221.8	146.4	149.4	3235.2	3446.2
26.3	84.1	86.8	7078.5	7444.3	168.8	171.9	3337.9	3548.7
25.9	85.9	88.6	7302.1	7666.0	193.8	197.0	3438.0	3648.7
25.4	87.7	90.4	7524.9	7887.1	221.6	224.9	3535.3	3745.9
25.0	89.5	92.1	7747.0	8107.5	252.2	255.5	3629.8	3840.3
24.6	91.3	93.9	7968.5	8327.5	285.6	289.1	3721.3	3931.8
24.1	93.1	95.6	8189.5	8547.0	322.0	325.5	3810.0	4020.4
23.7	94.8	97.4	8410.0	8766.1	361.3	364.9	3895.7	4106.1
22.7	94.2	96.7	8429.8	8783.5	245.8	248.5	4056.8	4268.1
21.6	94.2	96.6	8480.7	8832.9	184.1	186.1	4164.1	4376.2
20.6	94.4	96.8	8543.2	8894.3	152.4	153.9	4241.4	4453.9
19.5	94.7	97.1	8611.3	8961.5	136.8	138.1	4302.7	4515.4
18.5	95.1	97.5	8682.2	9031.7	130.0	131.2	4355.1	4567.9
17.5	95.4	97.9	8754.7	9103.6	128.3	129.4	4402.4	4615.3
16.4	95.9	98.3	8828.1	9176.4	129.6	130.6	4446.8	4659.7
15.4	96.3	98.7	8901.9	9249.6	132.6	133.6	4489.3	4702.2
14.3	96.8	99.1	8975.9	9323.2	136.9	137.9	4530.6	4743.6
13.3	97.2	99.6	9050.1	9396.8	142.0	143.0	4571.1	4784.1
12.2	97.7	100.0	9124.3	9470.6	147.7	148.7	4611.1	4824.0
11.2	98.1	100.5	9198.6	9544.3	153.8	154.8	4650.6	4863.5
10.0	98.5	100.8	9261.4	9606.6	149.6	150.6	4694.0	4907.0
8.8	98.9	101.2	9325.6	9670.3	147.8	148.7	4735.1	4948.1
7.7	99.3	101.7	9390.3	9734.6	148.1	149.0	4774.0	4987.1
6.5	99.7	102.1	9455.3	9799.2	150.0	150.9	4811.4	5024.4
5.3	100.2	102.5	9520.4	9863.9	153.1	154.0	4847.6	5060.7
3.5	99.9	102.2	9563.5	9906.3	134.0	134.9	4898.3	5111.4
1.8	99.7	102.0	9610.2	9952.5	121.6	122.4	4942.4	5155.6
0.0	99.8	102.1	9658.6	10000.5	114.5	115.2	4981.1	5194.4
0.0	99.8	102.1	9658.4	10000.3	114.3	115.0	4981.3	5194.6

Deer and Carter Well GOM

Time	Temperature		Depth		Pressure (Excess)		Effective Stress	
my	c		ft		psi		psi	
	Top	Base	Top	Base	Top	Base	Top	Base
23.9	17.8	20.2	0.0	176.1	0.0	9.9	0.0	55.0
23.7	20.2	24.7	176.0	519.5	9.8	28.6	55.1	166.2
23.0	21.4	25.7	282.9	618.9	3.6	11.4	102.8	224.8
22.2	22.6	26.8	388.9	719.4	3.2	9.2	144.7	268.5
21.5	23.8	27.9	493.6	819.0	3.1	8.5	186.2	310.7
20.8	25.0	29.0	597.0	917.8	3.3	8.4	227.5	352.2
20.0	26.1	30.0	699.2	1015.7	3.5	8.6	268.7	393.5
19.3	27.2	31.0	800.2	1112.8	3.8	9.0	309.9	434.5
18.6	28.3	32.0	900.0	1208.9	4.2	9.6	351.0	475.4
17.8	29.3	33.0	998.9	1304.3	4.6	10.2	392.0	516.2
17.1	30.4	33.9	1096.7	1398.8	5.1	11.0	432.9	556.9
16.3	31.4	34.9	1193.5	1492.5	5.7	11.9	473.8	597.5
15.6	32.4	35.8	1289.5	1585.5	6.3	12.9	514.7	637.9
14.9	33.4	36.8	1384.5	1677.8	6.9	13.9	555.5	678.3
14.1	34.4	37.7	1478.7	1769.3	7.6	15.1	596.3	718.7
13.4	35.3	38.6	1572.1	1860.2	8.4	16.3	637.0	758.9
12.7	36.3	39.5	1664.7	1950.3	9.2	17.6	677.6	799.1
11.9	37.2	40.3	1756.5	2039.9	10.0	18.9	718.2	839.1
11.2	38.1	41.2	1847.7	2128.8	10.9	20.4	758.7	879.1
10.5	39.1	42.2	1949.9	2228.7	13.4	24.3	802.4	921.3
9.9	40.2	43.2	2051.2	2327.9	15.0	27.0	847.0	964.8
9.2	41.2	44.1	2151.8	2426.3	16.5	29.5	891.6	1008.4
8.6	42.2	45.1	2251.7	2524.2	18.0	32.0	936.2	1052.1
7.9	43.1	46.0	2350.9	2621.3	19.6	34.6	980.7	1095.6
7.3	44.1	46.9	2449.3	2717.9	21.3	37.3	1025.2	1139.1
6.6	45.1	47.8	2547.1	2813.8	23.0	40.0	1069.7	1182.5
6.0	46.0	48.7	2644.1	2909.1	24.8	42.9	1114.0	1225.8
5.3	46.9	49.6	2740.5	3003.9	26.7	45.8	1158.3	1269.0
4.4	47.3	49.9	2805.2	3067.1	21.9	39.0	1195.1	1308.0
3.5	47.6	50.3	2870.2	3130.9	21.3	37.5	1227.9	1341.5
2.7	47.9	50.6	2935.2	3194.8	21.4	37.4	1259.9	1373.8
1.8	48.2	50.9	3000.0	3258.5	21.8	37.7	1291.7	1405.6
0.9	48.6	51.2	3064.6	3322.1	22.3	38.4	1323.3	1437.1
0.0	49.1	51.7	3129.1	3385.5	22.9	39.2	1354.7	1468.3

Slick-State Well GOM

Time	Temperature		Depth		Pressure (Excess)		Effective Stress	
my	c		ft		psi		psi	
	Top	Base	Top	Base	Top	Base	Top	Base
26.0	18.1	20.6	0.0	175.2	0.0	43.5	0.0	17.1
25.8	20.6	25.7	175.2	523.6	44.4	123.8	16.2	58.1
25.5	25.6	30.5	523.7	864.1	126.1	207.0	55.8	96.0
25.3	30.5	35.1	864.5	1196.6	210.2	294.8	92.8	129.6
25.0	35.1	39.7	1197.5	1524.7	298.7	389.4	125.6	156.1
24.7	39.3	43.7	1511.2	1833.2	383.2	477.9	161.8	188.3
24.4	43.3	47.6	1819.4	2137.0	472.1	569.6	193.6	217.2
24.0	47.2	51.5	2123.4	2437.4	564.5	663.9	221.8	243.6
23.7	51.1	55.2	2424.6	2735.4	659.3	760.2	247.6	267.9
23.0	51.5	55.5	2516.5	2821.5	667.1	769.4	298.2	317.2
22.2	52.5	56.4	2633.2	2933.5	682.7	785.1	341.1	359.8
21.5	53.6	57.4	2750.4	3046.7	701.8	804.5	380.3	399.0
20.8	54.7	58.4	2868.7	3161.5	723.6	826.3	417.0	435.5
20.0	55.7	59.4	2987.6	3277.2	747.3	850.2	451.7	470.0
19.3	56.8	60.4	3106.7	3393.5	772.7	875.8	484.8	502.9
18.6	57.9	61.5	3225.9	3510.1	799.4	902.7	516.5	534.4
17.8	59.0	62.5	3344.9	3626.8	827.2	930.9	547.0	564.7
17.1	60.1	63.6	3463.8	3743.5	856.2	960.1	576.6	593.9
16.3	61.3	64.6	3582.4	3860.0	886.0	990.2	605.1	622.1
15.6	62.4	65.7	3700.7	3976.4	916.7	1021.3	632.9	649.5
14.9	63.5	66.8	3818.7	4092.5	948.1	1053.1	659.8	676.1
14.1	64.6	67.8	3936.3	4208.4	980.3	1085.7	686.0	701.9
13.4	65.7	68.9	4053.5	4324.0	1013.2	1118.9	711.6	727.1
12.7	66.7	69.9	4170.3	4439.3	1046.7	1152.8	736.5	751.6
11.9	67.8	71.0	4286.8	4554.3	1080.8	1187.3	760.8	775.5
11.2	68.9	72.0	4402.8	4669.0	1115.4	1222.4	784.5	798.8
10.2	69.2	72.3	4454.2	4718.6	1114.6	1222.0	815.4	829.2
9.2	69.6	72.7	4510.4	4773.2	1115.0	1222.8	845.0	858.5
8.3	70.1	73.1	4568.1	4829.4	1116.7	1224.7	873.4	886.7
7.3	70.6	73.5	4626.5	4886.4	1119.4	1227.5	900.7	913.8
6.3	71.0	74.0	4685.4	4943.9	1123.2	1231.4	927.0	940.0
5.3	71.5	74.5	4744.5	5001.8	1127.9	1236.1	952.3	965.4
4.2	71.4	74.3	4770.2	5026.2	1119.7	1227.8	978.6	991.8
3.2	71.4	74.2	4798.2	5053.0	1112.4	1220.4	1004.1	1017.3
2.1	71.3	74.1	4827.3	5080.9	1105.9	1213.9	1028.7	1042.0
1.1	71.3	74.1	4856.9	5109.5	1100.3	1208.1	1052.5	1066.0
0.0	71.5	74.3	4887.0	5138.6	1095.3	1203.0	1075.6	1089.2

Pleasant Bayou Well GOM

Time	Temperature		Depth		Pressure (Excess)		Effective Stress	
my	c		ft		psi		psi	
	Top	Base	Top	Base	Top	Base	Top	Base
29.7	18.5	22.1	0.0	312.3	0.0	56.2	0.0	63.4
29.5	22.0	29.1	312.4	936.1	57.7	128.7	61.9	230.0
29.4	29.1	35.7	938.9	1537.3	174.0	278.1	184.7	319.8
29.2	35.6	41.6	1542.3	2114.0	321.0	435.3	276.9	401.8
29.0	41.6	47.4	2123.2	2684.7	483.1	611.5	353.9	464.7
28.8	46.0	51.6	2627.8	3177.3	629.1	769.6	450.9	549.6
28.5	49.1	54.5	3078.1	3618.5	790.8	937.8	532.3	624.5
28.3	57.3	62.5	3801.5	4337.4	986.0	1130.1	571.2	666.3
28.2	66.0	71.1	4482.5	5014.6	1184.5	1325.9	606.9	704.7
28.0	74.6	79.7	5164.0	5692.6	1385.2	1524.1	640.0	740.3
27.8	80.7	85.8	5686.3	6211.8	1592.7	1729.6	671.3	773.6
27.7	84.2	89.2	6051.9	6574.5	1801.9	1937.2	701.1	805.0
27.5	87.5	92.5	6554.6	7074.5	2012.8	2146.6	729.3	834.6
27.3	94.9	99.8	7176.1	7692.4	2166.0	2297.7	769.2	876.7
27.0	102.8	107.6	7757.4	8270.4	2322.1	2451.8	806.2	915.7
26.8	108.8	113.6	8257.5	8767.5	2518.4	2646.2	840.8	952.2
26.5	112.2	116.9	8573.0	9080.3	2717.2	2843.2	873.3	986.4
26.0	121.7	126.3	9376.3	9878.9	2910.0	3032.4	933.2	1049.9
25.9	123.9	128.6	9999.4	10501.1	3188.8	3310.7	944.2	1061.5
25.8	126.4	131.0	10501.8	11002.7	3467.9	3589.2	955.1	1073.0
25.7	129.1	133.6	11112.7	11612.8	3747.3	3868.1	965.8	1084.2
25.6	131.9	136.5	11695.0	12194.3	4027.0	4147.2	976.2	1095.2
25.5	134.8	139.4	12255.8	12754.3	4307.2	4426.9	986.5	1106.0
25.1	145.4	149.9	12718.9	13214.2	4418.3	4535.3	1030.7	1152.8
24.6	153.7	158.2	13138.0	13630.4	4532.7	4647.4	1071.6	1196.0
24.2	161.1	165.5	13593.4	14083.3	4649.9	4762.5	1109.6	1236.2
23.7	167.8	172.2	14021.7	14509.2	4769.7	4880.2	1145.2	1273.8
22.7	174.5	178.8	13993.2	14476.0	4730.7	4837.2	1218.0	1350.7
21.7	175.6	179.8	13990.0	14468.9	4700.0	4803.1	1282.7	1418.7
20.7	175.1	179.2	13984.9	14460.4	4675.6	4775.8	1340.9	1479.9
19.6	174.1	178.2	13979.5	14452.0	4656.4	4754.1	1394.1	1535.5
18.6	173.1	177.1	13980.7	14450.6	4641.3	4736.9	1443.0	1586.6
17.6	172.1	176.1	13985.0	14452.5	4629.9	4723.5	1488.4	1634.0
16.6	171.2	175.2	13992.0	14457.4	4621.4	4713.3	1530.8	1678.0
15.7	170.8	174.8	14096.7	14560.3	4661.7	4752.2	1566.2	1714.8
14.8	170.8	174.7	14200.0	14662.0	4703.8	4793.1	1599.8	1749.7
13.9	170.8	174.7	14303.9	14764.3	4747.6	4835.8	1631.8	1782.8
13.0	170.9	174.8	14408.8	14867.8	4792.8	4879.9	1662.4	1814.4
12.1	171.1	174.9	14514.7	14972.5	4839.3	4925.5	1691.7	1844.6
11.2	171.2	175.1	14621.7	15078.2	4887.0	4972.3	1719.7	1873.6

Pleasant Bayou Well GOM continued

Time	Temperature		Depth		Pressure (Excess)		Effective Stress	
my	c		ft		psi		psi	
	Top	Base	Top	Base	Top	Base	Top	Base
10.0	171.3	175.1	14724.6	15179.5	4933.1	5017.3	1756.6	1911.6
8.7	171.2	175.0	14830.8	15284.2	4981.0	5064.2	1791.7	1947.7
7.5	171.2	175.0	14939.5	15391.4	5030.6	5112.8	1825.2	1982.1
6.2	171.3	175.0	15050.2	15500.8	5081.6	5163.0	1857.1	2014.9
5.0	171.4	175.1	15162.7	15612.1	5134.0	5214.7	1887.8	2046.3
3.8	171.0	174.7	15203.2	15651.4	5152.5	5232.5	1917.4	2076.7
2.5	170.4	174.1	15247.2	15694.3	5172.2	5251.5	1945.9	2105.8
1.3	169.8	173.5	15293.7	15739.7	5192.9	5271.6	1973.4	2133.9
0.0	169.4	173.0	15342.3	15787.3	5214.6	5292.6	1999.9	2161.0

Northern Illinois Wells

Time	Temperature		Depth		Pressure (Excess)		Effective Stress	
my	c		ft		mpa		mpa	
	Top	Base	Top	Base	Top	Base	Top	
482.7	19.5	56.0	0.0	3602.3	0.0	0.0	0.0	12.6
460.3	19.5	56.1	39.7	3665.2	0.0	0.0	0.1	12.8
438.0	19.9	56.2	118.4	3727.5	0.0	0.0	0.3	13.0
423.0	23.4	58.1	438.5	3977.7	0.0	0.0	1.3	14.0
408.0	26.5	60.0	747.1	4225.1	0.0	0.0	2.4	15.1
384.0	27.4	60.4	855.0	4315.1	0.0	0.0	2.7	15.4
360.0	28.1	60.8	960.8	4403.6	0.0	0.0	3.0	15.7
346.7	29.5	61.7	1096.3	4517.1	0.0	0.0	3.4	16.2
333.3	30.8	62.6	1229.1	4629.0	0.0	0.0	3.9	16.6
320.0	32.1	63.4	1359.6	4739.3	0.0	0.0	4.3	17.0
302.7	33.0	64.2	1416.3	4789.0	0.0	0.0	4.4	17.2
285.3	33.9	64.9	1472.2	4838.2	0.0	0.0	4.6	17.3
268.0	34.7	65.6	1527.6	4886.7	0.0	0.0	4.8	17.5
267.1	44.1	74.0	1988.0	5298.8	0.0	0.0	5.9	18.6
266.3	52.1	81.1	2405.0	5672.1	0.0	0.0	7.1	19.8
265.4	59.3	87.4	2792.7	6020.0	0.0	0.0	8.2	21.0
264.5	65.7	93.1	3158.8	6349.8	0.0	0.0	9.4	22.2
263.6	71.7	98.4	3508.3	6666.0	0.0	0.0	10.6	23.4
262.8	77.3	103.4	3844.6	6971.6	0.0	0.0	11.8	24.6
261.9	82.6	108.1	4170.1	7268.6	0.0	0.0	12.9	25.8
261.0	87.6	112.7	4486.5	7558.6	0.0	0.0	14.1	27.0
247.3	82.9	108.0	4263.3	7335.4	0.0	0.0	13.6	26.6
233.5	78.2	103.2	4038.0	7109.5	0.0	0.0	13.1	26.0
219.8	74.0	99.0	3829.0	6899.9	0.0	0.0	12.6	25.5

Northern Illinois Wells continued

Time	Temperature		Depth		Pressure (Excess)		Effective Stress	
my	c		ft		mpa		mpa	
	Top	Base	Top	Base	Top	Base	Top	
206.1	73.5	98.5	3630.7	6701.6	0.0	0.0	12.1	25.0
192.3	71.8	96.8	3436.3	6507.1	0.0	0.0	11.7	24.5
178.6	69.5	94.5	3254.5	6325.1	0.0	0.0	11.2	24.0
164.8	67.2	92.2	3072.7	6143.0	0.0	0.0	10.7	23.5
151.1	65.2	90.2	2901.7	5971.8	0.0	0.0	10.2	23.0
137.4	63.1	88.1	2732.2	5802.1	0.0	0.0	9.7	22.5
123.6	60.1	85.1	2567.1	5636.7	0.0	0.0	9.2	22.0
109.9	57.3	82.3	2406.8	5476.1	0.0	0.0	8.7	21.5
96.2	54.5	79.5	2247.5	5316.4	0.0	0.0	8.2	21.0
82.4	51.9	76.9	2094.7	5163.3	0.0	0.0	7.7	20.5
68.7	47.8	72.7	1941.7	5009.7	0.0	0.0	7.2	20.0
55.0	42.0	66.9	1793.0	4860.2	0.0	0.0	6.7	19.5
41.2	38.3	63.3	1646.2	4713.0	0.0	0.0	6.2	19.0
27.5	35.2	60.1	1501.4	4567.8	0.0	0.0	5.7	18.4
13.7	31.4	56.3	1359.7	4425.6	0.0	0.0	5.2	17.9
0.0	27.3	52.2	1218.1	4283.4	0.0	0.0	4.7	17.4
0.0	27.8	52.7	1250.9	4316.1	0.0	0.0	4.8	17.5

Central Illinois Wells

Time	Temperature		Depth		Pressure (Excess)		Effective Stress	
my	c		ft		mpa		mpa	
	Top	Base	Top	Base	Top	Base	Top	Base
512.8	10.0	24.8	0.0	1349.5	0.0	0.0	0.0	4.3
505.0	12.3	28.5	201.8	1709.7	0.0	0.0	0.6	5.6
493.8	17.2	32.5	557.7	2028.6	0.0	0.0	1.6	6.6
482.7	21.6	36.2	894.4	2333.2	0.0	0.0	2.7	7.6
471.5	25.6	39.6	1216.8	2627.4	0.0	0.0	3.7	8.7
460.3	29.4	42.9	1527.8	2913.3	0.0	0.0	4.7	9.7
449.2	32.9	45.9	1829.5	3192.5	0.0	0.0	5.8	10.7
438.0	36.3	48.8	2123.3	3465.9	0.0	0.0	6.8	11.8
430.5	38.9	51.0	2416.1	3737.6	0.0	0.0	8.0	12.9
423.0	41.5	53.2	2709.2	4011.7	0.0	0.0	9.1	14.1
415.5	44.1	55.5	3000.6	4285.7	0.0	0.0	10.3	15.3
408.0	46.7	57.7	3289.5	4558.7	0.0	0.0	11.5	16.5
396.0	49.8	60.6	3547.5	4805.1	0.0	0.0	12.4	17.4
384.0	52.6	63.2	3796.4	5043.2	0.0	0.0	13.4	18.4
372.0	55.3	65.6	4038.7	5275.4	0.0	0.0	14.3	19.3
360.0	57.8	67.9	4275.8	5503.0	0.0	0.0	15.2	20.3

Central Illinois Wells Cotinued

Time my	Temperature c Top	 Base	Depth ft Top	 Base	Pressure (Excess) mpa Top	 Base	Effective Stress mpa Top	 Base
346.7	58.7	68.9	4374.2	5597.5	0.0	0.0	15.6	20.7
333.3	59.7	69.7	4472.0	5691.5	0.0	0.0	16.0	21.1
320.0	60.7	70.6	4569.2	5785.1	0.0	0.0	16.4	21.5
302.7	63.0	72.8	4730.5	5941.7	0.0	0.0	17.0	22.0
285.3	65.1	74.9	4886.9	6093.5	0.0	0.0	17.5	22.5
268.0	67.1	76.8	5039.4	6241.6	0.0	0.0	18.0	23.1
266.0	73.8	83.4	5377.9	6572.0	0.0	0.0	19.0	24.1
264.0	79.7	89.1	5690.9	6877.5	0.0	0.0	20.1	25.1
262.0	85.0	94.3	5986.4	7165.7	0.0	0.0	21.1	26.2
260.0	89.9	99.0	6268.8	7441.4	0.0	0.0	22.1	27.2
258.0	94.5	103.5	6541.3	7707.4	0.0	0.0	23.2	28.2
244.3	91.0	100.0	6375.6	7541.7	0.0	0.0	22.8	27.9
230.6	87.5	96.5	6208.7	7374.7	0.0	0.0	22.4	27.5
216.9	84.0	93.0	6045.4	7211.2	0.0	0.0	22.1	27.1
203.3	81.0	90.0	5896.1	7061.8	0.0	0.0	21.7	26.7
189.6	78.0	87.0	5746.9	6912.4	0.0	0.0	21.3	26.4
175.9	75.2	84.2	5602.4	6767.8	0.0	0.0	20.9	26.0
162.2	72.6	81.5	5465.2	6630.5	0.0	0.0	20.6	25.6
148.5	69.9	78.9	5328.0	6493.1	0.0	0.0	20.2	25.2
134.8	67.4	76.4	5196.2	6361.2	0.0	0.0	19.8	24.8
121.1	65.1	74.0	5067.9	6232.8	0.0	0.0	19.5	24.5
107.5	62.7	71.7	4939.6	6104.4	0.0	0.0	19.1	24.1
93.8	60.5	69.4	4816.9	5981.5	0.0	0.0	18.7	23.7
80.1	58.3	67.2	4695.5	5860.1	0.0	0.0	18.4	23.4
66.4	56.1	65.1	4574.1	5738.6	0.0	0.0	18.0	23.0
49.8	57.9	66.9	4701.7	5866.2	0.0	0.0	18.3	23.3
33.2	59.7	68.7	4826.2	5990.8	0.0	0.0	18.6	23.6
16.6	61.4	70.4	4948.1	6112.8	0.0	0.0	19.0	24.0
0.0	63.0	72.0	5067.5	6232.2	0.0	0.0	19.3	24.3

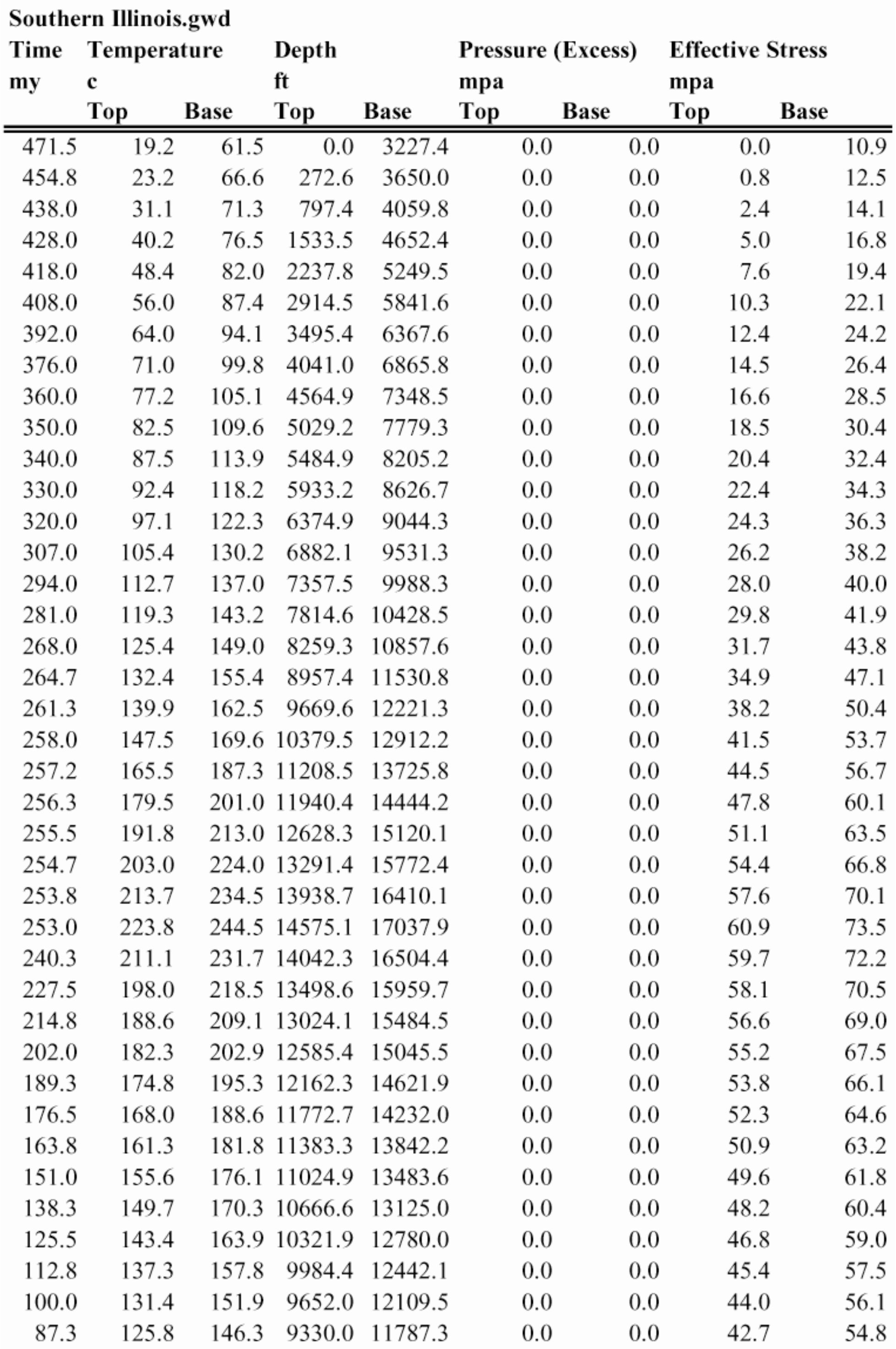

Southern Illinois.gwd

Time my	Temperature c		Depth ft		Pressure (Excess) mpa		Effective Stress mpa	
	Top	Base	Top	Base	Top	Base	Top	Base
471.5	19.2	61.5	0.0	3227.4	0.0	0.0	0.0	10.9
454.8	23.2	66.6	272.6	3650.0	0.0	0.0	0.8	12.5
438.0	31.1	71.3	797.4	4059.8	0.0	0.0	2.4	14.1
428.0	40.2	76.5	1533.5	4652.4	0.0	0.0	5.0	16.8
418.0	48.4	82.0	2237.8	5249.5	0.0	0.0	7.6	19.4
408.0	56.0	87.4	2914.5	5841.6	0.0	0.0	10.3	22.1
392.0	64.0	94.1	3495.4	6367.6	0.0	0.0	12.4	24.2
376.0	71.0	99.8	4041.0	6865.8	0.0	0.0	14.5	26.4
360.0	77.2	105.1	4564.9	7348.5	0.0	0.0	16.6	28.5
350.0	82.5	109.6	5029.2	7779.3	0.0	0.0	18.5	30.4
340.0	87.5	113.9	5484.9	8205.2	0.0	0.0	20.4	32.4
330.0	92.4	118.2	5933.2	8626.7	0.0	0.0	22.4	34.3
320.0	97.1	122.3	6374.9	9044.3	0.0	0.0	24.3	36.3
307.0	105.4	130.2	6882.1	9531.3	0.0	0.0	26.2	38.2
294.0	112.7	137.0	7357.5	9988.3	0.0	0.0	28.0	40.0
281.0	119.3	143.2	7814.6	10428.5	0.0	0.0	29.8	41.9
268.0	125.4	149.0	8259.3	10857.6	0.0	0.0	31.7	43.8
264.7	132.4	155.4	8957.4	11530.8	0.0	0.0	34.9	47.1
261.3	139.9	162.5	9669.6	12221.3	0.0	0.0	38.2	50.4
258.0	147.5	169.6	10379.5	12912.2	0.0	0.0	41.5	53.7
257.2	165.5	187.3	11208.5	13725.8	0.0	0.0	44.5	56.7
256.3	179.5	201.0	11940.4	14444.2	0.0	0.0	47.8	60.1
255.5	191.8	213.0	12628.3	15120.1	0.0	0.0	51.1	63.5
254.7	203.0	224.0	13291.4	15772.4	0.0	0.0	54.4	66.8
253.8	213.7	234.5	13938.7	16410.1	0.0	0.0	57.6	70.1
253.0	223.8	244.5	14575.1	17037.9	0.0	0.0	60.9	73.5
240.3	211.1	231.7	14042.3	16504.4	0.0	0.0	59.7	72.2
227.5	198.0	218.5	13498.6	15959.7	0.0	0.0	58.1	70.5
214.8	188.6	209.1	13024.1	15484.5	0.0	0.0	56.6	69.0
202.0	182.3	202.9	12585.4	15045.5	0.0	0.0	55.2	67.5
189.3	174.8	195.3	12162.3	14621.9	0.0	0.0	53.8	66.1
176.5	168.0	188.6	11772.7	14232.0	0.0	0.0	52.3	64.6
163.8	161.3	181.8	11383.3	13842.2	0.0	0.0	50.9	63.2
151.0	155.6	176.1	11024.9	13483.6	0.0	0.0	49.6	61.8
138.3	149.7	170.3	10666.6	13125.0	0.0	0.0	48.2	60.4
125.5	143.4	163.9	10321.9	12780.0	0.0	0.0	46.8	59.0
112.8	137.3	157.8	9984.4	12442.1	0.0	0.0	45.4	57.5
100.0	131.4	151.9	9652.0	12109.5	0.0	0.0	44.0	56.1
87.3	125.8	146.3	9330.0	11787.3	0.0	0.0	42.7	54.8

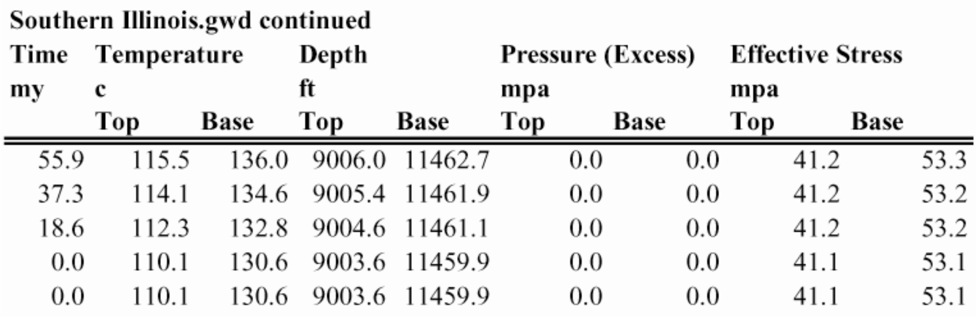

Southern Illinois.gwd continued

Time	Temperature		Depth		Pressure (Excess)		Effective Stress	
my	c		ft		mpa		mpa	
	Top	Base	Top	Base	Top	Base	Top	Base
55.9	115.5	136.0	9006.0	11462.7	0.0	0.0	41.2	53.3
37.3	114.1	134.6	9005.4	11461.9	0.0	0.0	41.2	53.2
18.6	112.3	132.8	9004.6	11461.1	0.0	0.0	41.2	53.2
0.0	110.1	130.6	9003.6	11459.9	0.0	0.0	41.1	53.1
0.0	110.1	130.6	9003.6	11459.9	0.0	0.0	41.1	53.1

Appendix G

Pine Mountain Overthrust sample location descriptions

Appendix G. Sample location descriptions and miscellaneous data collected in the field. Not all samples collected were ultimately used for the fault gouge study. More precise locations are marked on topo maps and geologic maps. Ask A.M. for maps.

Sample PMO 1

Located outside of Jelico, TN along highway 25W. See topo sheet for exact location. Undeformed sample of Breathitt Formation. Two joint sets associated with this location:

N72W/Dip 77 NE

N20W/ Dip 62 NE

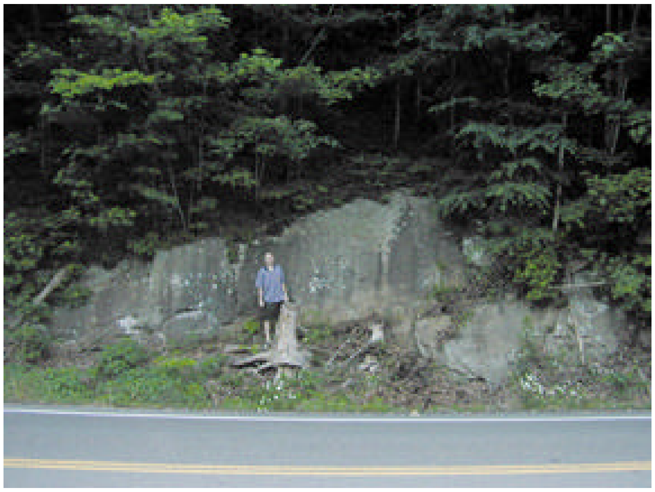

PMO 1 Outcrop. Jason for scale.

Sample PMO 2

Located on Doc Siler Rd.. Undeformed Breathitt sandstone. Strike and dip of bedding N80W/5-10 (Right hand rule). Very shallow dip almost horizontal.

Sample PMO 3

located on Mud Creek Lot Rd. 4-wheel drive road going south (see Kentucky Road Map). Strike and dip S35W/20SW. 2 joint sets: N2E/78, S 85W/76

PMO 3. Astrid for scale on outcrop. Joint sets clearly visible.

Sample PMO 4
Henry Bowlin Gap. See Kentucky road map for location. Located on dirt road off of 1595. Clearly near to fault. Steeply dipping beds, convoluted and bedding detection uncertain. Two strike and dips taken:
N72E
One joint set parallel to bedding, others are
NS/72 W
N76W/58N

PMO 4. Jason taking strike and dip.

Sample PMO 5
Henry Bowlin Gap. Coal Seams present. Approximately ½ mile past sample 4 (see road map). Shallowly dipping. Relatively undeformed compared to sample 4. Fine grained, unsure if it will be useful. Strike and dip
S30W/18W

PMO 5. Jason taking sample. Coal seams visible as dark lineations.

Sample PMO 6
Henry Bowlins Gap. Approximately ½ mile past sample 5. Dead end. Large outcrop of shale and some intermixed coal. At base is coal rich sediment and top of outcrop is sandier
Photo:

PMO 6. Jason standing on shale debris with resistant sandstone beds lying above.

Sample PMO 7
Along highway 92. See Kentucky road map for location. Massively bedded. Relatively undeformed with localized deformation containing brecciation. Contains evidence for fluid flow such as liesegang bands. Strike and dip S8E/17E

PMO 7. Liesegang bands are ubiquitous at this sample locality.

Sample PMO 8

Along highway 92. See Kentucky road map for location. Massively bedded. Contains slickensides and liesegang bands. Few hundred meters from location 7. Strike and dip same as for sample 7.

Sample PMO 9
Along highway 92. Exact location on Kentucky road map. Approximately 200 m from Bell County line. Appears less deformed than previous stops.

Sample PMO 10
Pineville railroad outcrop. Same as Kitty's number 18 stop. Possibly affected by Dorton fault branch zone. Breathitt undeformed. Thinnly to massivly bedded. Strike and dip N55W/18E
Several joints see scratch field notes as well as photo 2 below
N60W/88NE
S59E/40 SW
S20W/58 NW

PMO 10. Massive bed dipping to right.

Sample PMO 11
Railroad cut along 221. See Kentucky road map for exact location. Questionable association with Pine Mtn. Overthrust fault, potential association with another fault. Massively bedded

Sample PMO 12
Undeformed Lee and Breathitt Formation. See Kentucky Road map for exact location
1 mile West from western most HW 840 and HW 119 intersection at town of Tremont.
Strike and dip N65E ± 10/ 35 S. Two samples collected: lower more fine grained (A) and upper more coarse grained (B).

PMO 12. Jason and Gordon on outcrop.

Sample PMO 13
Along HW 119. Undeformed Lee and Breathitt sandstone. See Kentucky road map for exact locations. Obvious channel sands, containing coal seams.

PMO 13. Large scale outcrop with car for scale. Obvious sand filled in channels.

Sample PMO 14
Along HW 119. Shortly before 2012 going west. Undeformed Lee and Breathitt sandstones. Strike and dip N30E/ 10SE.

Sample PMO 15
Along HW 119 going east. One mile before 25E intersection Stopped in "Save A Lot" parking lot. Undeformed Lee Formation. Massive sandstone with interbedded shale. Changes in dip due to irregular surface. Strike and Dip N55W/25SW.

PMO 15. Gordon taking strike and dip. Can see the variation of dip in sandstone due to cross bedding.

Sample PMO 16
On HW 221. Two miles east from sample location 11. See local regional geology map for exact location. Deformed Lee, within the imbricate fault system. Massive sandstone, uncertain if this rock is in place. Strike and dip EW ±10/25S

Sample PMO 17
0.7 miles east from location 16 on HW 221. Deformed massive channel Lee sandstone. For exact location see local geology map. Strike and dip
N80E/30SE. Weathers orange to dark gray.

PMO16. Jason for scale on outcrop

Sample PMO 18
100 yards east from sample 17. Massive deformed Lee sandstone member. Exact location on local geology map. Strike and dip N25E/ 44SE.

Sample PMO 19
On HW 221. Massive sandstone, undergone deformation. Lee sandstone. Approximately 0.5 miles northeast of location 18. 1000 yards past railroad crossing on HW 221 going NE. Extensive fracturing and jointing.

Sample PMO 20
Railroad cut on HW 221. According to geomap, should be imbricated but is relatively flat lying. Thick shale beds with sandstone lenses. Strike and dip N80E/14N
Light gray sandstone bed contains rip up clasts of surrounding ss material.

PMO 20. Gordon for scale on outcrop.

PMO 20. Astrid with light gray sandstone lenses.

Sample PMO 21
Located on HW221 just past 421 intersection north of Harlan city. Undifferentiated Breathitt sandstone. Contorted bedding. Perhaps overturned. Soft sediment deformation as well.

PMO 21. Jason and Gordon for scale on outcrop. Obvious convoluted bedding, possibly soft sediment deformation

Sample PMO 22
Located on HW 221 1 mile east of intersection 2009. Massive jointing, large scale cross-bedding. No deformation visible. Some jointing. Strike and dip
N30e/10 NW

Sample PMO 23
Located on HW 221, next to Pine Mountain Church. See local geology map and Kentucky road map for exact location. According to map. Undifferentiated Breathitt. Samples contains lineation indicating fracturing. Slippage surface. Liesegang bands.

PMO 23. Jason and Gordon for scale on outcrop

Sample PMO 24

Located on HW 221, approximately 1 mile before Pine Mountain community. Undifferentiated Breathitt. Exact location on Nolansburg Quadrangle and Kentucky Road Map. Collected two pieces. Geology map indicates steep and often indeterminate dip. Localized veins.

PMO 24. Close-up of deformation bands in ss.

Sample PMO 25

On HW 221, approximately 100 feet before 510 intersection. Location on Nolansburg Geologic quadrangle map and Kentucky road map. Undifferentiated Breathitt according to geology map. Almost vertical bedding. Some areas brittle. Strike and dip N45E/73NW.

PMO 25. Massive bedded. Joint pattern is clearly visible.

Sample PMO 26
HW 510, 1 mile northeast past 221 junction. Crossing into Letcher Co. See Kentucky road map and Nolansburg geologic quadrangle map for exact location. Undifferentiated Breathitt according to geo map. Strike and dip EW/37N.

Sample PMO 27
HW510. See Kentucky road map or Nolansburg geological quadrangle for exact location. Overturned bedding according to map. Shale fragments within sandstone. Strike and dip N85E/42SE

Sample PMO 28
On HW 510 near Gilley community. On large Geologic map, an imbicated thrust system is illustrated with deformed Lee ss within. This locality it is thinny-bedded. Strike and dip N85E/70N

Sample PMO 29
HW 463 south of Gordon. See Kentucky Road map for exact location. Could be deformed due to imbrication. Iron Manganese fracture surface coating on joints. Strike and dip N80E/27S

PMO 29. Outcrop with Jason and Gordon for scale.

PMO 29. Iron oxide coating in fractures

Sample PMO 30
On HW 522 going SW between Chad and Hiram communities. See Kentucky road map for detailed location. Undeformed Breathitt and Lee sandstone

Sample PMO 31
On HW 522 , traveling SW, past Totz. See Kentucky road map for detailed location. Undeformed Breathitt and Lee sandstone. Thin to medium bedding/ generally horizontal with little dip.

Sample PMO 32
On HW 522, 2-3 miles SW of stop 31. See Kentucky road map for detailed location. Undeformed Breathitt and Lee sandstone. Thin to medium bedding/ generally horizontal with little dip.
Photo: 1) Massive sandstone bedding (6-10-02-32-1)

Sample PMO 33
Exact location not noted. Presumably near Gatin community on HW 119 approximately 1 mile from 421 intersection. Undeformed Breathitt and Lee sandstone. Massive and well-cemented. Strike and dip N75E/22 SE

PMO 33. Massive bedded roadcut.

Sample PMO 34

On HW 931, 1 mile SW before Cowan. Location estimated on Kentucky road map. Massive outcrop, subjected to soft sediment deformation, however beds still have recognizable attitude. Deformed? Probably not! Strike and dip EW/ 24 S

PMO 34. Soft sediment deformation.

Sample PMO 35

On HW 931, about 0.5 mile NE of intersection 160. Liesegang banding,jointing, slickensides, soft sediment deformation. Lots of iron and magnesium in fracture seal. Strike and dip N80E/8S


PMO 35. Gordon and vertical jointing.

Sample PMO 36
On small side road (1862) near Mayking and HW 119 near Whitesburg. See Kentucky road map. Undeformed Breathitt and Lee sandstone. Contains liesegang banding. This is the only place we were threatened!!!!

Samples 37-39 collected along same road cut, along a 200 yard stretch. See original field notes for sketch.

Sample PMO 37
In Payne Gap on HW 119. One mile (West) before intersection 23. Severely deformed as indicated by regional geology map. Deformed Lee within imbricate fault system. Angular breccia pieces in ss matrix. Strike and dip N80E/34 N !!!


PMO 37. Deformed outcrop of Lee sandstone.

PMO 37. Close-up of brecciation

Sample PMO 38
In Payne Gap on HW 119. Approximately 100 yards west from location 37. Mud clasts in sandy matrix, possibly rip up clasts, depositional feature?

PMO 38. Rip-up clasts?

Sample PMO 39
In Payne Gap on HW 119. Approximately 200 yards west from location 37. Deformed Lee
Strike and dip
N80E/33N

Sample PMO 40
Intersection 119 and 23. Between Payne Gap and Jenkins. Outcrop on 23 south bound, north of 119. Deformed Lee. Coal seams present. Iron staining in area lying above coal seam, see photo. Strike varies between E/W and E/NE. Dips vary between 5-35 south.

PMO 40. Jason on outcrop for scale.

Sample PMO 41

On 3086 in Jenkins, Approximately 300 yards west from intersection 3086/805. Location marked on Kentucky road map. Deformed Lee.

PMO 41.

Sample PMO 42

HW 197, 1 mile east past 805/197 intersection. See Kentucky road map for exact location. Undeformed Lee. Almost flat lying bedding. Strike and dip N40E/ 7NW.

PMO 42. Massive bedded

Sample PMO 43
HW 197, exact location unknown, approximate location on Kentucky road map. Road across from Marathon gas station on HW 197. Bedding cannot be exactly deciphered from fractures. Deformed Lee. Regional geo map shows imbricate zone in this area. Best shot at strike and dip: N50E/50SW.

Between sample 44 and 45. 0.25 mile distance between samples and extreme change in dip
Sample PMO 44
On HW80 NE of Breaks interstate park in Virginia side near Kentucky/Virginia boarder. Exact location on Elkhorn City toposheet or Kentucky road map. Deformed Lee Breathitt. Strike and dip (questionable) N50E/66S.

Sample PMO 45
On road intersecting HW80 from a NE direction. Undeformed Breathitt and Lee sandstone. 0.25 miles north of last location (Good pair). Strike and dip N50E/ 5S.

Starts off in Breaks Interstate Park, Virginia.
Ask for geologic guide at visitor information center. Numbers with Asterisks denote number in guide.
Sample PMO 46
Breaks Interstate Park along Geological train by their location 26*. Conglomeratic zone where failure occurred. Perhaps preferential zone of faulting where coarser material preferential zone of faulting, more porosity, allowing fluid flow. Strike and dip EW/20S.

PMO 46. Coarse grained Lee sandstone. Pebbles visible below power bar.

Sample PMO 47

100 yards N/NE from stop 46 on Geological trail. Strike and dip indicate a quick shift in direction. Next to park marker 23*. Strike and dip N50W/23SW.

PMO 47.

Sample PMO 48

Beginning of Geological Trail. Relatively flat lying and undeformed. Strike and dip N25W/14SW.

Sample PMO 49
Prospector's trail in Breaks Interstate Park. Conglomeratic, pebbles evenly distributed. 2 set of prominent fractures, 1 set vertical and second set horizontal. Very well cemented. Strike and dip N35W/30SW

PMO 49. Gordon taking strike and dip.

PMO 49. Vertical fracture with Gordon.

Sample PMO 50
Prospector's Trail. Highly cemented ss. Deformed Conglomerate.

PMO 50.

Sample PMO 51
Prospector's Trail. Undeformed. Strike and dip
N65W/10SW

Near Whitesburg
Sample PMO 52
On HW 119, south of Whitesburg. Deformed Breathitt. See Kentucky road map for location.
Strike and dip E/NE/30S but dip varies considerably

PMO 52. Large outcrop image of the Gumbles

Appendix H

Quantitative data collected from CL image collages for PMO samples

APPENDIX H.

Pine Mountain Overthrust CL pointcount compilations.

Four 1 x1 mm areas of each thin section were selected at random and were point counted. The four point-counted areas were then averaged to retrieve an average value for each category. The summations of the four areas are listed below and their resulting averages.

Sample	**State of deformation: Undeformed**						**Sandstone: Breathitt**	
No.: PMO 01	Qtz Grain	Kaolinite	Lithic RF	Feldspar	FeO	**Inter**gran. Qtz Cement	**Intra**gran. Qtz Cement	Prim. Porosity
Area 1	76.07	0.25	7.81	6.80	0.00	6.55	1.51	1.01
Area 2	73.68	0.00	16.04	1.50	0.00	7.02	0.75	1.00
Area 3	73.79	0.76	11.20	3.05	0.00	8.91	1.02	1.27
Area 4	76.94	2.59	9.84	2.85	0.00	7.25	0.52	0.00
Averages	**75.12**	**0.90**	**11.22**	**3.55**	**0.00**	**7.43**	**0.95**	**0.82**
Min. Value	73.68	0.00	7.81	1.50	0.00	6.55	0.52	0.00
Max. Value	76.94	2.59	16.04	6.80	0.00	8.91	1.51	1.27
Max. Difference	**3.26**	**2.59**	**8.23**	**5.30**	**0.00**	**2.36**	**0.99**	**1.27**
Min. Dev. from Avg.	**1.44**	**0.90**	**3.41**	**2.05**	**0.00**	**0.88**	**0.43**	**0.82**
Max. Dev. from Avg.	**1.82**	**1.69**	**4.82**	**3.25**	**0.00**	**1.47**	**0.56**	**0.45**

Sample	**State of deformation:** **Undeformed**						**Sandstone:** **Breathitt**	
No.: **PMO 02**	Qtz Grain	Kaolinite	Lithic RF	Feldspar	FeO	**Inter**gran. Qtz Cement	**Intra**gran. Qtz Cement	Prim. Porosity
Area 1	65.47	0.26	16.11	2.56	0.00	14.07	0.26	1.28
Area 2	68.80	0.28	19.22	2.23	0.00	8.36	0.28	0.84
Area 3	68.80	0.00	20.00	0.53	0.00	8.53	0.27	1.87
Area 4	71.79	0.00	17.32	0.84	0.00	8.66	0.00	1.40
Averages	**68.72**	**0.13**	**18.16**	**1.54**	**0.00**	**9.90**	**0.20**	**1.34**
Min. Value	65.47	0.00	16.11	0.53	0.00	8.36	0.00	0.84
Max. Value	71.79	0.28	19.22	2.56	0.00	14.07	0.28	1.87
Max. Difference	**6.31**	**0.28**	**3.11**	**2.02**	**0.00**	**5.71**	**0.28**	**1.03**
Min. Dev. from Avg.	**3.24**	**0.13**	**2.05**	**1.01**	**0.00**	**1.55**	**0.20**	**0.51**
Max. Dev. from Avg.	**3.07**	**0.14**	**1.06**	**1.02**	**0.00**	**4.16**	**0.08**	**0.52**

Sample	**State of deformation:** **Undeformed**						**Sandstone:** **Breathitt**	
No.: **PMO 03**	Qtz Grain	Kaolinite	Lithic RF	Feldspar	FeO	**Inter**gran. Qtz Cement	**Intra**gran. Qtz Cement	Prim. Porosity
Area 1	84.89	1.01	5.04	1.51	0.00	4.53	1.76	1.26
Area 2	83.72	1.03	1.81	0.52	0.00	8.01	4.65	0.26
Area 3	80.46	3.60	6.17	0.26	0.00	4.88	2.06	2.57
Area 4	80.31	2.30	4.09	3.07	0.00	3.84	4.35	2.05
Averages	**82.34**	**1.99**	**4.28**	**1.34**	**0.00**	**5.32**	**3.20**	**1.53**
Min. Value	80.31	1.01	1.81	0.52	0.00	3.84	1.76	0.26
Max. Value	84.89	3.60	6.17	3.07	0.00	8.01	4.65	2.57
Max. Difference	**4.58**	**2.59**	**4.36**	**2.55**	**0.00**	**4.17**	**2.89**	**2.31**
Min. Dev. from Avg.	**2.04**	**0.98**	**2.47**	**0.82**	**0.00**	**1.48**	**1.44**	**1.28**
Max. Dev. from Avg.	**2.54**	**1.61**	**1.89**	**1.73**	**0.00**	**2.69**	**1.45**	**1.04**

Sample	**State of deformation: Undeformed**						**Sandstone: Breathitt**	
No.: PMO 04	Qtz Grain	Kaolinite	Lithic RF	Feldspar	FeO	**Inter**gran. Qtz Cement	**Intra**gran. Qtz Cement	Prim. Porosity
Area 1	79.29	3.79	4.04	1.77	0.00	4.80	2.53	3.79
Area 2	74.69	1.00	17.29	0.00	0.00	3.26	2.01	1.75
Area 3	81.06	1.77	2.27	2.78	0.00	8.33	2.02	1.77
Area 4	82.41	0.50	6.53	0.75	0.00	8.29	0.75	0.75
Averages	**79.36**	**1.77**	**7.53**	**1.32**	**0.00**	**6.17**	**1.83**	**2.02**
Min. Value	74.69	0.50	2.27	0.00	0.00	3.26	0.75	0.75
Max. Value	82.41	3.79	17.29	2.78	0.00	8.33	2.53	3.79
Max. Difference	7.73	3.29	15.02	2.78	**0.00**	5.08	1.77	3.03
Min. Dev. from Avg.	**4.68**	**1.26**	**5.26**	**1.32**	**0.00**	**2.91**	**1.07**	**1.26**
Max. Dev. from Avg.	**3.05**	**2.02**	**9.76**	**1.45**	**0.00**	**2.16**	**0.70**	**1.77**

Sample	**State of deformaiton: Undeformed**						**Sandstone: Breathitt**	
No.: PMO 05	Qtz Grain	Kaolinite	Lithic RF	Feldspar	FeO	**Inter**gran. Qtz Cement	**Intra**gran. Qtz Cement	Prim. Porosity
Area 1	77.37	0.00	3.91	1.12	0.00	15.92	0.00	1.68
Area 2	69.87	0.00	7.53	3.38	0.00	17.66	1.04	0.52
Area 3	67.67	1.50	12.78	0.25	0.00	17.29	0.50	0.00
Area 4	74.55	0.00	12.08	0.00	0.00	12.08	1.29	0.00
Averages	**72.37**	**0.38**	**9.08**	**1.19**	**0.00**	**15.74**	**0.71**	**0.55**
Min. Value	67.67	0.00	3.91	0.00	0.00	12.08	0.00	0.00
Max. Value	77.37	1.50	12.78	3.38	0.00	17.66	1.29	1.68
Max. Difference	**9.71**	**1.50**	**8.87**	**3.38**	**0.00**	**5.58**	**1.29**	**1.68**
Min. Dev. from Avg.	**4.70**	**0.38**	**5.17**	**1.19**	**0.00**	**3.66**	**0.71**	**0.55**
Max. Dev. from Avg.	**5.01**	**1.13**	**3.71**	**2.19**	**0.00**	**1.92**	**0.58**	**1.13**

Sample	**State of deformation: Undeformed**						**Sandstone: Breathitt**	
No.: PMO 07	Qtz Grain	Kaolinite	Lithic RF	Feldspar	FeO	**Inter**gran. Qtz Cement	**Intra**gran. Qtz Cement	Prim. Porosity
Area 1	69.25	4.89	8.91	0.86	0.00	15.23	0.57	0.29
Area 2	67.83	4.29	13.67	0.80	0.00	12.33	0.80	0.27
Area 3	78.72	1.86	3.72	0.53	0.00	12.50	1.06	1.60
Area 4	74.54	3.45	6.37	0.00	0.00	14.85	0.27	0.53
Averages	**72.59**	**3.62**	**8.17**	**0.55**	**0.00**	**13.73**	**0.68**	**0.67**
Min. Value	67.83	1.86	3.72	0.00	0.00	12.33	0.27	0.27
Max. Value	78.72	4.89	13.67	0.86	0.00	15.23	1.06	1.60
Max. Difference	**10.89**	**3.02**	**9.95**	**0.86**	**0.00**	**2.90**	**0.80**	**1.33**
Min. Dev. from Avg.	**4.76**	**1.76**	**4.44**	**0.55**	**0.00**	**1.40**	**0.41**	**0.40**
Max. Dev. from Avg.	**6.14**	**1.26**	**5.51**	**0.31**	**0.00**	**1.50**	**0.39**	**0.93**

Sample	**State of deformation: Undeformed**						**Sandstone: Breathitt**	
No.: PMO 08	Qtz Grain	Kaolinite	Lithic RF	Feldspar	FeO	**Inter**gran. Qtz Cement	**Intra**gran. Qtz Cement	Prim. Porosity
Area 1	72.32	6.27	5.48	0.00	0.00	14.36	0.78	0.78
Area 2	67.36	7.57	10.18	0.00	0.00	12.27	0.78	1.83
Area 3	70.97	0.81	8.33	0.27	0.00	17.74	1.34	0.54
Area 4	72.93	9.12	6.08	0.00	0.00	10.77	0.55	0.55
Averages	**70.90**	**5.94**	**7.52**	**0.07**	**0.00**	**13.79**	**0.87**	**0.93**
Min. Value	67.36	0.81	5.48	0.00	0.00	10.77	0.55	0.54
Max. Value	72.93	9.12	10.18	0.27	0.00	17.74	1.34	1.83
Max. Difference	**5.57**	**8.31**	**4.70**	**0.27**	**0.00**	**6.97**	**0.79**	**1.29**
Min. Dev. from Avg.	**3.53**	**5.13**	**2.04**	**0.07**	**0.00**	**3.01**	**0.31**	**0.39**
Max. Dev. from Avg.	**2.03**	**3.18**	**2.66**	**0.20**	**0.00**	**3.96**	**0.48**	**0.90**

Sample	**State of deformation:** **Undeformed**						**Sandstone:** **Breathitt**	
No.: **PMO 09**	Qtz Grain	Kaolinite	Lithic RF	Feldspar	FeO	**Inter**gran. Qtz Cement	**Intra**gran. Qtz Cement	Prim. Porosity
Area 1	62.73	0.52	11.02	1.57	0.00	23.36	0.52	0.26
Area 2	69.52	0.76	8.82	4.28	0.00	15.62	1.01	0.00
Area 3	67.25	4.50	4.00	7.50	0.00	16.25	0.50	0.00
Area 4	74.93	0.80	4.27	0.00	0.00	18.93	1.07	0.00
Averages	**68.61**	**1.65**	**7.03**	**3.34**	**0.00**	**18.54**	**0.77**	**0.07**
Min. Value	62.73	0.52	4.00	0.00	0.00	15.62	0.52	0.00
Max. Value	74.93	4.50	11.02	7.50	0.00	23.36	1.07	0.26
Max. Difference	**12.20**	**3.98**	**7.02**	**7.50**	**0.00**	**7.74**	**0.54**	**0.26**
Min. Dev. from Avg.	**5.88**	**1.12**	**3.03**	**3.34**	**0.00**	**2.92**	**0.25**	**0.07**
Max. Dev. from Avg.	**6.32**	**2.85**	**4.00**	**4.16**	**0.00**	**4.82**	**0.29**	**0.20**

Sample	**State of deformation:** **Deformed**						**Sandstone:** **Lee**	
No.: **PMO 11**	Qtz Grain	Kaolinite	Lithic RF	Feldspar	FeO	**Inter**gran. Qtz Cement	**Intra**gran. Qtz Cement	Prim. Porosity
Area 1	88.75	0.25	2.50	0.00	0.00	2.00	6.50	0.00
Area 2	76.34	3.56	11.20	0.00	0.00	2.29	6.62	0.00
Area 3	81.82	5.19	1.82	0.00	0.00	8.57	2.60	0.00
Area 4	86.67	1.28	0.77	0.77	0.00	10.26	0.26	0.00
Averages	**83.39**	**2.57**	**4.07**	**0.19**	**0.00**	**5.78**	**3.99**	**0.00**
Min. Value	76.34	0.25	0.77	0.00	0.00	2.00	0.26	0.00
Max. Value	88.75	5.19	11.20	0.77	0.00	10.26	6.62	0.00
Max. Difference	**12.41**	**4.94**	**10.43**	**0.77**	**0.00**	**8.26**	**6.36**	**0.00**
Min. Dev. from Avg.	**7.06**	**2.32**	**3.30**	**0.19**	**0.00**	**3.78**	**3.74**	**0.00**
Max. Dev. from Avg.	**5.36**	**2.62**	**7.13**	**0.58**	**0.00**	**4.48**	**2.62**	**0.00**

Sample	**State of deformation:** Undeformed						**Sandstone:** Breathitt	
No.: PMO 13	Qtz Grain	Kaolinite	Lithic RF	Feldspar	FeO	**Inter**gran. Qtz Cement	**Intra**gran. Qtz Cement	Prim. Porosity
Area 1	55.44	6.84	18.23	6.58	0.00	7.34	5.06	0.51
Area 2	70.00	2.00	23.25	3.00	0.00	1.25	0.50	0.00
Area 3	70.60	6.03	12.56	1.26	0.00	8.79	0.75	0.00
Area 4	58.84	1.85	13.72	17.41	0.00	6.07	1.58	0.53
Averages	**63.72**	**4.18**	**16.94**	**7.06**	**0.00**	**5.86**	**1.98**	**0.26**
Min. Value	55.44	1.85	12.56	1.26	0.00	1.25	0.50	0.00
Max. Value	70.00	6.84	23.25	17.41	0.00	8.79	5.06	0.53
Max. Difference	**14.56**	**4.99**	**10.69**	**16.16**	**0.00**	**7.54**	**4.56**	**0.53**
Min. Dev. from Avg.	8.28	2.33	4.38	5.81	**0.00**	4.61	1.48	0.26
Max. Dev. from Avg.	6.28	2.66	6.31	10.35	**0.00**	2.93	3.09	0.27

Sample	**State of deformation:** Undeformed						**Sandstone:** Breathitt	
No.: PMO 15	Qtz Grain	Kaolinite	Lithic RF	Feldspar	FeO	**Inter**gran. Qtz Cement	**Intra**gran. Qtz Cement	Prim. Porosity
Area 1	73.77	4.16	3.38	1.30	0.00	13.77	0.26	3.38
Area 2	70.25	0.00	12.75	6.75	0.00	7.25	0.50	2.50
Area 3	79.85	0.00	10.71	0.00	0.00	6.38	1.28	1.79
Area 4	84.42	0.00	1.76	4.27	0.00	5.03	1.01	3.52
Averages	**77.07**	**1.04**	**7.15**	**3.08**	**0.00**	**8.10**	**0.76**	**2.79**
Min. Value	70.25	0.00	1.76	0.00	0.00	5.03	0.26	1.79
Max. Value	84.42	4.16	12.75	6.75	0.00	13.77	1.28	3.52
Max. Difference	**14.17**	**4.16**	**10.99**	**6.75**	**0.00**	**8.74**	**1.02**	**1.73**
Min. Dev. from Avg.	**6.82**	**1.04**	**5.39**	**3.08**	**0.00**	**3.08**	**0.50**	**1.01**
Max. Dev. from Avg.	**7.35**	**3.12**	**5.60**	**3.67**	**0.00**	**5.66**	**0.52**	**0.72**

Sample	**State of deformation: Deformed**						**Sandstone: Lee**	
No.: PMO 16	Qtz Grain	Kaolinite	Lithic RF	Feldspar	FeO	**Inter**gran. Qtz Cement	**Intra**gran. Qtz Cement	Prim. Porosity
Area 1	82.75	0.25	4.25	1.25	0.00	5.00	3.75	2.75
Area 2	85.00	0.00	0.50	1.00	0.00	4.75	5.50	3.25
Area 3	82.50	1.50	1.75	3.50	0.00	3.75	1.75	5.25
Area 4	81.00	0.00	0.00	5.00	0.00	5.50	5.00	3.50
Averages	**82.81**	**0.44**	**1.63**	**2.69**	**0.00**	**4.75**	**4.00**	**3.69**
Min. Value	81.00	0.00	0.00	1.00	0.00	3.75	1.75	2.75
Max. Value	85.00	1.50	4.25	5.00	0.00	5.50	5.50	5.25
Max. Difference	**4.00**	**1.50**	**4.25**	**4.00**	**0.00**	**1.75**	**3.75**	**2.50**
Min. Dev. from Avg.	**1.81**	**0.44**	**1.63**	**1.69**	**0.00**	**1.00**	**2.25**	**0.94**
Max. Dev. from Avg.	**2.19**	**1.06**	**2.63**	**2.31**	**0.00**	**0.75**	**1.50**	**1.56**

Sample	**State of deformation: Deformed**						**Sandstone: Lee**	
No.: PMO 16b	Qtz Grain	Kaolinite	Lithic RF	Feldspar	FeO	**Inter**gran. Qtz Cement	**Intra**gran. Qtz Cement	Prim. Porosity
Area 1	79.75	0.51	4.30	0.00	0.00	6.84	8.10	0.51
Area 2	82.00	0.00	0.25	0.50	0.00	5.00	12.00	0.25
Area 3	80.15	0.00	0.25	8.04	0.00	2.01	8.79	0.75
Area 4	90.23	0.00	0.00	0.00	0.00	0.00	9.02	0.75
Averages	**83.03**	**0.13**	**1.20**	**2.14**	**0.00**	**3.46**	**9.48**	**0.57**
Min. Value	79.75	0.00	0.00	0.00	0.00	0.00	8.10	0.25
Max. Value	90.23	0.51	4.30	8.04	0.00	6.84	12.00	0.75
Max. Difference	**10.48**	**0.51**	**4.30**	**8.04**	**0.00**	**6.84**	**3.90**	**0.50**
Min. Dev. from Avg.	**3.28**	**0.13**	**1.20**	**2.14**	**0.00**	**3.46**	**1.38**	**0.32**
Max. Dev. from Avg.	**7.19**	**0.38**	**3.10**	**5.91**	**0.00**	**3.37**	**2.52**	**0.19**

Sample	**State of deformation:** **Undeformed**						**Sandstone:** **Lee**	
No.: **PMO 17**	Qtz Grain	Kaolinite	Lithic RF	Feldspar	FeO	**Inter**gran. Qtz Cement	**Intra**gran. Qtz Cement	Prim. Porosity
Area 1	80.32	4.52	0.27	0.00	0.00	12.50	1.60	0.80
Area 2	84.13	1.32	0.00	0.00	0.00	11.90	1.32	1.59
Area 3	81.23	6.94	0.77	0.00	0.00	8.74	2.31	0.00
Area 4	87.04	2.82	0.00	0.00	0.00	9.01	0.85	0.28
Averages	**83.18**	**3.90**	**0.26**	**0.00**	**0.00**	**10.54**	**1.52**	**0.67**
Min. Value	80.32	1.32	0.00	0.00	0.00	8.74	0.85	0.00
Max. Value	87.04	6.94	0.77	0.00	0.00	12.50	2.31	1.59
Max. Difference	**6.72**	**5.62**	**0.77**	**0.00**	**0.00**	**3.76**	**1.47**	**1.59**
Min. Dev. from Avg.	**2.86**	**2.58**	**0.26**	**0.00**	**0.00**	**1.80**	**0.67**	**0.67**
Max. Dev. from Avg.	**3.86**	**3.04**	**0.51**	**0.00**	**0.00**	**1.96**	**0.79**	**0.92**

Sample	**State of deformation:** **Undeformed**						**Sandstone:** **Lee**	
No.: **PMO 18**	Qtz Grain	Kaolinite	Lithic RF	Feldspar	FeO	**Inter**gran. Qtz Cement	**Intra**gran. Qtz Cement	Prim. Porosity
Area 1	81.42	3.05	0.76	0.25	0.00	12.47	1.53	0.51
Area 2	81.61	7.51	1.04	0.00	0.00	9.33	0.26	0.26
Area 3	78.47	5.18	0.00	0.00	0.00	14.17	1.36	0.82
Area 4	81.96	4.51	0.00	0.00	0.00	12.20	0.80	0.53
Averages	**80.87**	**5.06**	**0.45**	**0.06**	**0.00**	**12.04**	**0.99**	**0.53**
Min. Value	78.47	3.05	0.00	0.00	0.00	9.33	0.26	0.26
Max. Value	81.96	7.51	1.04	0.25	0.00	14.17	1.53	0.82
Max. Difference	**3.49**	**4.46**	**1.04**	**0.25**	**0.00**	**4.84**	**1.27**	**0.56**
Min. Dev. from Avg.	**2.39**	**2.01**	**0.45**	**0.06**	**0.00**	**2.71**	**0.73**	**0.27**
Max. Dev. from Avg.	**1.10**	**2.45**	**0.59**	**0.19**	**0.00**	**2.13**	**0.54**	**0.29**

Sample	**State of deformation: Deformed**						**Sandstone: Lee**	
No.: PMO 19	Qtz Grain	Kaolinite	Lithic RF	Feldspar	FeO	**Inter**gran. Qtz Cement	**Intra**gran. Qtz Cement	Prim. Porosity
Area 1	77.50	0.00	5.00	0.25	0.00	9.50	6.25	1.50
Area 2	81.70	0.00	2.26	0.00	0.00	5.01	10.28	0.75
Area 3	82.75	0.00	1.50	0.00	0.00	7.50	7.50	0.75
Area 4	87.00	0.00	0.00	0.00	0.00	3.75	8.75	0.50
Averages	**82.24**	**0.00**	**2.19**	**0.06**	**0.00**	**6.44**	**8.19**	**0.88**
Min. Value	77.50	0.00	0.00	0.00	0.00	3.75	6.25	0.50
Max. Value	87.00	0.00	5.00	0.25	0.00	9.50	10.28	1.50
Max. Difference	**9.50**	**0.00**	**5.00**	**0.25**	**0.00**	**5.75**	**4.03**	**1.00**
Min. Dev. from Avg.	**4.74**	**0.00**	**2.19**	**0.06**	**0.00**	**2.69**	**1.94**	**0.38**
Max. Dev. from Avg.	**4.76**	**0.00**	**2.81**	**0.19**	**0.00**	**3.06**	**2.08**	**0.62**

Sample	**State of deformation: Undeformed**						**Sandstone: Breathitt**	
No.: PMO 21	Qtz Grain	Kaolinite	Lithic RF	Feldspar	FeO	**Inter**gran. Qtz Cement	**Intra**gran. Qtz Cement	Prim. Porosity
Area 1	60.81	0.00	21.88	5.85	0.00	10.43	0.76	0.25
Area 2	78.20	0.00	12.81	8.72	0.00	5.72	1.63	0.00
Area 3	77.26	0.00	12.14	2.58	0.00	5.17	2.58	0.26
Area 4	74.61	0.00	12.69	3.63	0.00	5.70	3.11	0.26
Averages	**72.72**	**0.00**	**14.88**	**5.20**	**0.00**	**6.76**	**2.02**	**0.19**
Min. Value	60.81	0.00	12.14	2.58	0.00	5.17	0.76	0.00
Max. Value	78.20	0.00	21.88	8.72	0.00	10.43	3.11	0.26
Max. Difference	**17.39**	**0.00**	**9.74**	**6.14**	**0.00**	**5.26**	**2.35**	**0.26**
Min. Dev. from Avg.	**11.91**	**0.00**	**2.74**	**2.61**	**0.00**	**1.59**	**1.26**	**0.19**
Max. Dev. from Avg.	**5.48**	**0.00**	**7.00**	**3.52**	**0.00**	**3.68**	**1.09**	**0.07**

Sample	**State of deformation:** Undeformed						**Sandstone:** Breathitt	
No.: PMO 22	Qtz Grain	Kaolinite	Lithic RF	Feldspar	FeO	**Inter**gran. Qtz Cement	**Intra**gran. Qtz Cement	Prim. Porosity
Area 1	54.31	0.00	32.49	7.36	0.00	3.81	2.03	0.00
Area 2	67.03	0.00	20.98	3.27	0.00	7.36	1.63	0.00
Area 3	68.58	0.00	25.68	0.00	0.00	4.37	1.09	0.27
Area 4	77.01	0.00	16.04	0.00	0.00	6.15	0.80	0.00
Averages	**66.73**	**0.00**	**23.80**	**2.66**	**0.00**	**5.42**	**1.39**	**0.07**
Min. Value	54.31	0.00	16.04	0.00	0.00	3.81	0.80	0.00
Max. Value	77.01	0.00	32.49	7.36	0.00	7.36	2.03	0.27
Max. Difference	**22.69**	**0.00**	**16.44**	**7.36**	**0.00**	**3.55**	**1.23**	**0.27**
Min. Dev. from Avg.	**12.42**	**0.00**	**7.76**	**2.66**	**0.00**	**1.61**	**0.59**	**0.07**
Max. Dev. from Avg.	**10.27**	**0.00**	**8.69**	**4.70**	**0.00**	**1.94**	**0.64**	**0.20**

Sample	**State of deformation:** Deformed						**Sandstone:** Breathitt	
No.: PMO 23	Qtz Grain	Kaolinite	Lithic RF	Feldspar	FeO	**Inter**gran. Qtz Cement	**Intra**gran. Qtz Cement	Prim. Porosity
Area 1	81.47	2.79	4.82	1.02	0.00	6.60	3.30	0.00
Area 2	74.28	4.20	9.19	3.67	0.00	6.30	2.36	0.00
Area 3	73.23	5.05	10.86	4.80	0.00	3.79	2.27	0.00
Area 4	78.81	0.78	13.70	0.00	0.00	1.55	4.91	0.26
Averages	**76.95**	**3.20**	**9.64**	**2.37**	**0.00**	**4.56**	**3.21**	**0.06**
Min. Value	73.23	0.78	4.82	0.00	0.00	1.55	2.27	0.00
Max. Value	81.47	5.05	13.70	4.80	0.00	6.60	4.91	0.26
Max. Difference	**8.24**	**4.28**	**8.87**	**4.80**	**0.00**	**5.05**	**2.64**	**0.26**
Min. Dev. from Avg.	**3.72**	**2.43**	**4.82**	**2.37**	**0.00**	**3.01**	**0.94**	**0.06**
Max. Dev. from Avg.	**4.52**	**1.85**	**4.05**	**2.43**	**0.00**	**2.04**	**1.70**	**0.19**

Sample	**State of deformation:** **Undeformed**						**Sandstone:** **Breathitt**	
No.: **PMO 24**	Qtz Grain	Kaolinite	Lithic RF	Feldspar	FeO	**Inter**gran. Qtz Cement	**Intra**gran. Qtz Cement	Prim. Porosity
Area 1	70.00	6.05	7.89	0.00	0.00	12.89	2.63	0.53
Area 2	66.93	1.84	16.54	0.00	0.00	8.40	3.94	0.00
Area 3	68.69	0.76	9.60	0.00	0.00	13.64	3.79	0.00
Area 4	81.30	0.78	6.75	0.00	0.00	7.27	3.90	0.00
Averages	**71.73**	**2.36**	**10.19**	**0.00**	**0.00**	**10.55**	**3.56**	**0.13**
Min. Value	66.93	0.76	6.75	0.00	0.00	7.27	2.63	0.00
Max. Value	81.30	6.05	16.54	0.00	0.00	13.64	3.94	0.53
Max. Difference	**14.37**	**5.30**	**9.78**	**0.00**	**0.00**	**6.36**	**1.31**	**0.53**
Min. Dev. from Avg.	**4.80**	**1.60**	**3.44**	**0.00**	**0.00**	**3.28**	**0.93**	**0.13**
Max. Dev. from Avg.	**9.57**	**3.70**	**6.34**	**0.00**	**0.00**	**3.09**	**0.37**	**0.39**

Sample	**State of deformation:** **Undeformed**						**Sandstone:** **Breathitt**	
No.: **PMO 25**	Qtz Grain	Kaolinite	Lithic RF	Feldspar	FeO	**Inter**gran. Qtz Cement	**Intra**gran. Qtz Cement	Prim. Porosity
Area 1	70.13	1.30	8.83	0.00	0.00	17.92	1.30	0.52
Area 2	64.30	0.00	10.76	0.00	0.00	13.65	1.57	0.26
Area 3	65.15	2.27	7.58	0.00	0.00	13.89	2.02	2.53
Area 4	68.48	6.98	8.27	0.78	0.00	12.66	2.58	0.26
Averages	**67.02**	**2.64**	**8.86**	**0.19**	**0.00**	**14.53**	**1.87**	**0.89**
Min. Value	64.30	0.00	7.58	0.00	0.00	12.66	1.30	0.52
Max. Value	70.13	6.98	10.76	0.78	0.00	17.92	2.58	2.53
Max. Difference	**5.83**	**6.98**	**3.19**	**0.78**	**0.00**	**5.26**	**1.29**	**2.01**
Min. Dev. from Avg.	**2.71**	**2.64**	**1.28**	**0.19**	**0.00**	**1.87**	**0.57**	**0.37**
Max. Dev. from Avg.	**3.11**	**4.34**	**1.90**	**0.58**	**0.00**	**3.39**	**0.71**	**1.63**

Sample	**State of deformation:** Undeformed						**Sandstone:** Breathitt	
No.: PMO 26	Qtz Grain	Kaolinite	Lithic RF	Feldspar	FeO	**Inter**gran. Qtz Cement	**Intra**gran. Qtz Cement	Prim. Porosity
Area 1	78.57	5.77	4.40	0.00	0.00	10.44	0.82	0.00
Area 2	75.07	11.80	3.75	0.00	0.00	7.77	1.07	0.54
Area 3	71.73	8.80	8.00	0.27	0.00	8.27	2.93	0.00
Area 4	77.26	10.59	2.84	0.26	0.00	7.49	1.55	0.00
Averages	**75.66**	**9.24**	**4.75**	**0.13**	**0.00**	**8.49**	**1.60**	**0.13**
Min. Value	71.73	5.77	2.84	0.00	0.00	7.49	0.82	0.00
Max. Value	78.57	11.80	8.00	0.27	0.00	10.44	2.93	0.54
Max. Difference	**6.84**	**6.03**	**5.16**	**0.27**	**0.00**	**2.95**	**2.11**	**0.54**
Min. Dev. from Avg.	**3.92**	**3.47**	**1.91**	**0.13**	**0.00**	**1.00**	**0.77**	**0.13**
Max. Dev. from Avg.	**2.91**	**2.56**	**3.25**	**0.14**	**0.00**	**1.95**	**1.34**	**0.40**

Sample	**State of deformation:** Undeformed						**Sandstone:** Breathitt	
No.: PMO 27	Qtz Grain	Kaolinite	Lithic RF	Feldspar	FeO	**Inter**gran. Qtz Cement	**Intra**gran. Qtz Cement	Prim. Porosity
Area 1	53.18	6.36	22.65	8.14	0.00	8.14	1.27	0.25
Area 2	78.75	2.00	15.75	1.00	0.00	1.00	1.50	0.00
Area 3	54.06	0.76	30.46	6.85	0.00	6.60	1.27	0.00
Area 4	55.64	2.01	14.79	1.50	0.00	2.51	0.50	0.00
Averages	**60.41**	**2.78**	**20.91**	**4.37**	**0.00**	**4.56**	**1.14**	**0.06**
Min. Value	53.18	0.76	14.79	1.00	0.00	1.00	0.50	0.00
Max. Value	78.75	6.36	30.46	8.14	0.00	8.14	1.50	0.25
Max. Difference	**25.57**	**5.60**	**15.67**	**7.14**	**0.00**	**7.14**	**1.00**	**0.25**
Min. Dev. from Avg.	**7.23**	**2.02**	**6.12**	**3.37**	**0.00**	**3.56**	**0.63**	**0.06**
Max. Dev. from Avg.	**18.34**	**3.58**	**9.55**	**3.77**	**0.00**	**3.58**	**0.36**	**0.19**

Sample	**State of deformation:** Undeformed						**Sandstone:** Breathitt	
No.: PMO 30	Qtz Grain	Kaolinite	Lithic RF	Feldspar	FeO	**Inter**gran. Qtz Cement	**Intra**gran. Qtz Cement	Prim. Porosity
Area 1	79.27	0.00	10.10	1.55	0.00	5.18	3.89	0.00
Area 2	78.00	2.00	3.25	0.50	0.00	14.50	1.75	0.00
Area 3	70.35	0.00	12.31	5.78	0.00	11.06	0.50	0.00
Area 4	68.26	4.53	12.85	0.25	0.00	12.59	1.26	0.25
Averages	**73.97**	**1.63**	**9.63**	**2.02**	**0.00**	**10.83**	**1.85**	**0.06**
Min. Value	68.26	0.00	3.25	0.25	0.00	5.18	0.50	0.00
Max. Value	79.27	4.53	12.85	5.78	0.00	14.50	3.89	0.25
Max. Difference	**11.01**	**4.53**	**9.60**	**5.53**	**0.00**	**9.32**	**3.38**	**0.25**
Min. Dev. from Avg.	**5.71**	**1.63**	**6.38**	**1.77**	**0.00**	**5.65**	**1.35**	**0.06**
Max. Dev. from Avg.	**5.30**	**2.90**	**3.22**	**3.76**	**0.00**	**3.67**	**2.04**	**0.19**

Sample	**State of deformation:** Undeformed						**Sandstone:** Breathitt	
No.: PMO 31	Qtz Grain	Kaolinite	Lithic RF	Feldspar	FeO	**Inter**gran. Qtz Cement	**Intra**gran. Qtz Cement	Prim. Porosity
Area 1	74.68	2.56	6.65	0.51	0.00	14.83	0.77	0.00
Area 2	81.04	0.78	5.97	0.00	0.00	10.91	1.30	0.00
Area 3	77.47	0.00	13.42	0.00	0.00	7.34	1.77	0.00
Area 4	77.72	1.01	7.34	2.53	0.00	10.63	0.76	0.00
Averages	**77.73**	**1.09**	**8.35**	**0.76**	**0.00**	**10.93**	**1.15**	**0.00**
Min. Value	74.68	0.00	5.97	0.00	0.00	7.34	0.76	0.00
Max. Value	81.04	2.56	13.42	2.53	0.00	14.83	1.77	0.00
Max. Difference	**6.36**	**2.56**	**7.44**	**2.53**	**0.00**	**7.49**	**1.01**	**0.00**
Min. Dev. from Avg.	**3.05**	**1.09**	**2.37**	**0.76**	**0.00**	**3.59**	**0.39**	**0.00**
Max. Dev. from Avg.	**3.31**	**1.47**	**5.07**	**1.77**	**0.00**	**3.90**	**0.62**	**0.00**

Sample	**State of deformation:** **Deformed**						**Sandstone:** **Lee**	
No.: **PMO 34**	Qtz Grain	Kaolinite	Lithic RF	Feldspar	FeO	**Inter**gran. Qtz Cement	**Intra**gran. Qtz Cement	Prim. Porosity
Area 1	84.26	0.00	0.25	0.00	0.00	2.79	8.63	4.06
Area 2	87.50	0.00	0.00	0.00	0.00	0.00	12.00	0.50
Area 3	89.00	1.00	0.00	0.00	0.00	0.00	10.00	0.00
Area 4	87.69	2.26	1.26	0.00	0.00	1.76	7.04	0.00
Averages	**87.11**	**0.82**	**0.38**	**0.00**	**0.00**	**1.14**	**9.42**	**1.14**
Min. Value	84.26	0.00	0.00	0.00	0.00	0.00	7.04	0.00
Max. Value	89.00	2.26	1.26	0.00	0.00	2.79	12.00	4.06
Max. Difference	**4.74**	**2.26**	**1.26**	**0.00**	**0.00**	**2.79**	**4.96**	**4.06**
Min. Dev. from Avg.	**2.85**	**0.82**	**0.38**	**0.00**	**0.00**	**1.14**	**2.38**	**1.14**
Max. Dev. from Avg.	**1.89**	**1.45**	**0.88**	**0.00**	**0.00**	**1.65**	**2.58**	**2.92**

Sample	**State of deformation:** **Undeformed**						**Sandstone:** **Breathitt**	
No.: **PMO 35**	Qtz Grain	Kaolinite	Lithic RF	Feldspar	FeO	**Inter**gran. Qtz Cement	**Intra**gran. Qtz Cement	Prim. Porosity
Area 1	71.28	2.05	4.10	7.18	0.00	11.28	4.10	0.00
Area 2	79.78	5.06	2.25	0.56	0.00	8.15	4.21	0.00
Area 3	83.90	3.90	4.68	0.00	0.00	4.42	3.12	0.00
Area 4	65.80	5.74	10.97	5.48	0.00	6.27	5.74	0.00
Averages	**75.19**	**4.19**	**5.50**	**3.31**	**0.00**	**7.53**	**4.29**	**0.00**
Min. Value	71.28	2.05	2.25	0.00	0.00	4.42	3.12	0.00
Max. Value	83.90	5.74	10.97	7.18	0.00	11.28	5.74	0.00
Max. Difference	**12.61**	**3.69**	**8.72**	**7.18**	**0.00**	**6.87**	**2.63**	**0.00**
Min. Dev. from Avg.	**3.91**	**2.14**	**3.25**	**3.31**	**0.00**	**3.11**	**1.18**	**0.00**
Max. Dev. from Avg.	**8.71**	**1.56**	**5.47**	**3.87**	**0.00**	**3.75**	**1.45**	**0.00**

Sample	**State of deformation:** **Undeformed**						**Sandstone:** **Breathitt**	
No.: **PMO 36**	Qtz Grain	Kaolinite	Lithic RF	Feldspar	FeO	**Inter**gran. Qtz Cement	**Intra**gran. Qtz Cement	Prim. Porosity
Area 1	73.03	0.28	19.38	2.81	0.00	4.21	0.28	0.00
Area 2	66.33	0.00	23.72	2.04	0.00	7.14	0.77	0.00
Area 3	48.50	2.75	23.50	13.50	0.00	9.25	2.50	0.00
Area 4	63.89	0.00	21.97	9.09	0.00	3.79	1.26	0.00
Averages	**62.94**	**0.76**	**22.14**	**6.86**	**0.00**	**6.10**	**1.20**	**0.00**
Min. Value	48.50	0.00	19.38	2.04	0.00	3.79	0.28	0.00
Max. Value	73.03	2.75	23.72	13.50	0.00	9.25	2.50	0.00
Max. Difference	**24.53**	**2.75**	**4.34**	**11.46**	**0.00**	**5.46**	**2.22**	**0.00**
Min. Dev. from Avg.	**14.44**	**0.76**	**2.76**	**4.82**	**0.00**	**2.31**	**0.92**	**0.00**
Max. Dev. from Avg.	**10.10**	**1.99**	**1.58**	**6.64**	**0.00**	**3.15**	**1.30**	**0.00**

Sample	**State of deformation:** **Deformed**						**Sandstone:** **Lee**	
No.: **PMO 37**	Qtz Grain	Kaolinite	Lithic RF	Feldspar	FeO	**Inter**gran. Qtz Cement	**Intra**gran. Qtz Cement	Prim. Porosity
Area 1	87.31	0.78	0.00	0.00	0.00	6.99	4.92	0.00
Area 2	93.62	0.51	0.00	0.00	0.00	3.06	2.81	0.00
Area 3	87.25	0.00	0.75	0.00	0.00	2.75	9.25	0.00
Area 4	89.62	1.52	1.27	0.00	0.00	2.03	5.57	0.00
Area 5	88.97	0.00	0.00	0.00	0.00	1.25	9.27	0.50
Averages	**89.35**	**0.56**	**0.40**	**0.00**	**0.00**	**3.22**	**6.36**	**0.10**
Min. Value	87.25	0.00	0.00	0.00	0.00	1.25	2.81	0.00
Max. Value	93.62	1.52	1.27	0.00	0.00	6.99	9.27	0.50
Max. Difference	**6.37**	**1.52**	**1.27**	**0.00**	**0.00**	**5.74**	**6.47**	**0.50**
Min. Dev. from Avg.	**2.10**	**0.56**	**0.40**	**0.00**	**0.00**	**1.96**	**3.56**	**0.10**
Max. Dev. from Avg.	**4.27**	**0.96**	**0.86**	**0.00**	**0.00**	**3.78**	**2.91**	**0.40**

Sample	**State of deformation: Deformed**						**Sandstone: Lee**	
No.: PMO 38a	Qtz Grain	Kaolinite	Lithic RF	Feldspar	FeO	**Inter**gran. Qtz Cement	**Intra**gran. Qtz Cement	Prim. Porosity
Area 1	78.00	0.00	3.50	0.00	0.00	0.00	17.75	0.75
Area 2	86.00	0.00	0.00	0.00	6.75	4.25	3.00	0.00
Area 3	89.00	0.00	0.00	0.00	0.00	0.00	11.00	0.00
Area 4	85.14	0.00	0.76	0.00	0.00	2.27	11.84	0.00
Averages	**84.53**	**0.00**	**1.06**	**0.00**	**1.69**	**1.63**	**10.90**	**0.19**
Min. Value	78.00	0.00	0.00	0.00	0.00	0.00	3.00	0.00
Max. Value	89.00	0.00	3.50	0.00	6.75	4.25	17.75	0.75
Max. Difference	**11.00**	**0.00**	**3.50**	**0.00**	**6.75**	**4.25**	**14.75**	**0.75**
Min. Dev. from Avg.	**6.53**	**0.00**	**1.06**	**0.00**	**1.69**	**1.63**	**7.90**	**0.19**
Max. Dev. from Avg.	**4.47**	**0.00**	**2.44**	**0.00**	**5.06**	**2.62**	**6.85**	**0.56**

Sample	**State of deformation: Deformed**						**Sandstone: Lee**	
No.: PMO 38b	Qtz Grain	Kaolinite	Lithic RF	Feldspar	FeO	**Inter**gran. Qtz Cement	**Intra**gran. Qtz Cement	Prim. Porosity
Area 1	76.14	4.82	0.25	1.52	11.68	2.03	3.55	0.00
Area 2	86.00	0.00	0.00	0.00	6.75	4.25	3.00	0.00
Area 3	90.10	0.00	0.00	0.00	2.03	2.28	5.58	0.00
Area 4	84.56	0.00	2.53	0.00	0.00	3.29	9.62	0.00
Averages	**84.20**	**1.21**	**0.70**	**0.38**	**5.11**	**2.96**	**5.44**	**0.00**
Min. Value	76.14	0.00	0.00	0.00	0.00	2.03	3.00	0.00
Max. Value	90.10	4.82	2.53	1.52	11.68	4.25	9.62	0.00
Max. Difference	**13.96**	**4.82**	**2.53**	**1.52**	**11.68**	**2.22**	**6.62**	**0.00**
Min. Dev. from Avg.	**8.06**	**1.21**	**0.70**	**0.38**	**5.11**	**0.93**	**2.44**	**0.00**
Max. Dev. from Avg.	**5.90**	**3.62**	**1.84**	**1.14**	**6.56**	**1.29**	**4.18**	**0.00**

Sample	**State of deformation: Deformed**						**Sandstone: Lee**	
No.: PMO 38c	Qtz Grain	Kaolinite	Lithic RF	Feldspar	FeO	**Inter**gran. Qtz Cement	**Intra**gran. Qtz Cement	Prim. Porosity
Area 1	90.70	0.00	0.00	0.00	0.00	0.00	9.05	0.25
Area 2	86.00	0.00	0.00	0.00	6.75	4.25	3.00	0.00
Area 3	77.02	0.00	5.56	0.00	8.08	3.03	6.31	0.00
Area 4	83.47	0.00	0.00	0.00	7.86	2.71	5.96	0.00
Averages	**84.30**	**0.00**	**1.39**	**0.00**	**5.67**	**2.50**	**6.08**	**0.06**
Min. Value	77.02	0.00	0.00	0.00	0.00	0.00	3.00	0.00
Max. Value	90.70	0.00	5.56	0.00	8.08	4.25	9.05	0.25
Max. Difference	**13.68**	**0.00**	**5.56**	**0.00**	**8.08**	**4.25**	**6.05**	**0.25**
Min. Dev. from Avg.	**7.28**	**0.00**	**1.39**	**0.00**	**5.67**	**2.50**	**3.08**	**0.06**
Max. Dev. from Avg.	**6.41**	**0.00**	**4.17**	**0.00**	**2.41**	**1.75**	**2.97**	**0.19**

Sample	**State of deformation: Deformed**						**Sandstone: Lee**	
No.: PMO 39	Qtz Grain	Kaolinite	Lithic RF	Feldspar	FeO	**Inter**gran. Qtz Cement	**Intra**gran. Qtz Cement	Prim. Porosity
Area 1	86.87	0.00	0.00	0.00	0.00	4.80	7.83	0.51
Area 2	75.00	0.00	12.00	5.00	0.00	7.25	0.75	0.00
Area 3	89.72	0.00	0.00	0.00	0.00	0.75	9.52	0.00
Area 4	86.25	0.00	0.00	0.00	0.00	0.27	13.48	0.00
Averages	**84.46**	**0.00**	**3.00**	**1.25**	**0.00**	**3.27**	**7.89**	**0.13**
Min. Value	75.00	0.00	0.00	0.00	0.00	0.27	0.75	0.00
Max. Value	89.72	0.00	12.00	5.00	0.00	7.25	13.48	0.51
Max. Difference	**14.72**	**0.00**	**12.00**	**5.00**	**0.00**	**6.98**	**12.73**	**0.51**
Min. Dev. from Avg.	**9.46**	**0.00**	**3.00**	**1.25**	**0.00**	**3.00**	**7.14**	**0.13**
Max. Dev. from Avg.	**5.26**	**0.00**	**9.00**	**3.75**	**0.00**	**3.98**	**5.58**	**0.38**

Sample	**State of deformation:** **Undeformed**						**Sandstone:** **Breathitt**	
No.: **PMO 40**	Qtz Grain	Kaolinite	Lithic RF	Feldspar	FeO	**Inter**gran. Qtz Cement	**Intra**gran. Qtz Cement	Prim. Porosity
Area 1	62.53	1.58	20.84	8.71	0.00	4.49	1.06	0.79
Area 2	75.00	0.00	12.00	5.00	0.00	7.25	0.75	0.00
Area 3	63.57	0.00	18.59	7.04	0.00	8.79	2.01	0.00
Area 4	70.19	0.00	13.55	3.52	0.00	11.65	1.08	0.00
Averages	**67.82**	**0.40**	**16.25**	**6.07**	**0.00**	**8.05**	**1.22**	**0.20**
Min. Value	62.53	0.00	12.00	3.52	0.00	4.49	0.75	0.00
Max. Value	75.00	1.58	20.84	8.71	0.00	11.65	2.01	0.79
Max. Difference	**12.47**	**1.58**	**8.84**	**5.18**	**0.00**	**7.17**	**1.26**	**0.79**
Min. Dev. from Avg.	**5.29**	**0.40**	**4.25**	**2.54**	**0.00**	**3.56**	**0.47**	**0.20**
Max. Dev. from Avg.	**7.18**	**1.19**	**4.60**	**2.64**	**0.00**	**3.61**	**0.79**	**0.59**

Sample	**State of deformation:** **Deformed**						**Sandstone:** **Lee**	
No.: **PMO 41**	Qtz Grain	Kaolinite	Lithic RF	Feldspar	FeO	**Inter**gran. Qtz Cement	**Intra**gran. Qtz Cement	Prim. Porosity
Area 1	91.23	0.00	0.00	0.00	0.00	0.75	7.02	1.00
Area 2	90.73	0.00	0.00	0.00	0.00	0.00	9.27	0.00
Area 3	89.22	0.00	2.76	0.00	0.00	0.50	7.52	0.00
Area 4	89.46	0.00	0.77	0.00	0.00	1.80	7.97	0.00
Averages	**90.16**	**0.00**	**0.88**	**0.00**	**0.00**	**0.76**	**7.94**	**0.25**
Min. Value	89.22	0.00	0.00	0.00	0.00	0.00	7.02	0.00
Max. Value	**91.23**	**0.00**	**2.76**	**0.00**	0.00	**1.80**	**9.27**	**1.00**
Max. Difference	**2.01**	**0.00**	**2.76**	**0.00**	**0.00**	**1.80**	**2.26**	**1.00**
Min. Dev. from Avg.	**0.94**	**0.00**	**0.88**	**0.00**	**0.00**	**0.76**	**0.93**	**0.25**
Max. Dev. from Avg.	**1.07**	**0.00**	**1.87**	**0.00**	**0.00**	**1.04**	**1.33**	**0.75**

Sample	**State of deformation:** Undeformed						**Sandstone:** Lee	
No.: PMO 42	Qtz Grain	Kaolinite	Lithic RF	Feldspar	FeO	**Inter**gran. Qtz Cement	**Intra**gran. Qtz Cement	Prim. Porosity
Area 1	73.25	3.00	10.75	0.00	0.00	12.25	0.75	0.00
Area 2	79.80	1.77	6.82	1.01	0.00	7.58	3.03	0.00
Area 3	87.75	0.00	3.75	0.00	0.00	1.75	6.75	0.00
Area 4	85.00	1.25	1.25	0.00	0.00	7.75	4.75	0.00
Averages	**81.45**	**1.50**	**5.64**	**0.25**	**0.00**	**7.33**	**3.82**	**0.00**
Min. Value	73.25	0.00	1.25	0.00	0.00	1.75	0.75	0.00
Max. Value	87.75	3.00	10.75	1.01	0.00	12.25	6.75	0.00
Max. Difference	**14.50**	**3.00**	**9.50**	**1.01**	**0.00**	**10.50**	**6.00**	**0.00**
Min. Dev. from Avg.	**8.20**	**1.50**	**4.39**	**0.25**	**0.00**	**5.58**	**3.07**	**0.00**
Max. Dev. from Avg.	**6.30**	**1.50**	**5.11**	**0.76**	**0.00**	**4.92**	**2.93**	**0.00**

Sample	**State of deformation:** Deformed						**Sandstone:** Breathitt	
No.: PMO 44	Qtz Grain	Kaolinite	Lithic RF	Feldspar	FeO	**Inter**gran. Qtz Cement	**Intra**gran. Qtz Cement	Prim. Porosity
Area 1	73.25	3.00	10.75	0.00	0.00	12.25	0.75	0.00
Area 2	77.58	3.02	10.33	0.00	0.00	5.29	3.53	0.25
Area 3	87.75	0.00	3.75	0.00	0.00	1.75	6.75	0.00
Area 4	85.00	1.25	1.25	0.00	0.00	7.75	4.75	0.00
Averages	**80.90**	**1.82**	**6.52**	**0.00**	**0.00**	**6.76**	**3.94**	**0.06**
Min. Value	73.25	0.00	1.25	0.00	0.00	1.75	0.75	0.00
Max. Value	87.75	3.02	10.75	0.00	0.00	12.25	6.75	0.25
Max. Difference	**14.50**	**3.02**	**9.50**	**0.00**	**0.00**	**10.50**	**6.00**	**0.25**
Min. Dev. from Avg.	**7.65**	**1.82**	**5.27**	**0.00**	**0.00**	**5.01**	**3.19**	**0.06**
Max. Dev. from Avg.	**6.85**	**1.20**	**4.23**	**0.00**	**0.00**	**5.49**	**2.81**	**0.19**

Sample	**State of deformation:** **Undeformed**						**Sandstone:** Lee	
No.: **PMO 45**	Qtz Grain	Kaolinite	Lithic RF	Feldspar	FeO	**Inter**gran. Qtz Cement	**Intra**gran. Qtz Cement	Prim. Porosity
Area 1	76.23	1.81	12.40	0.78	0.00	7.75	0.78	0.26
Area 2	87.66	0.00	2.85	0.32	0.00	7.91	1.27	0.00
Area 3	66.40	0.81	16.80	2.98	0.00	11.65	1.36	0.00
Averages	**76.76**	**0.87**	**10.68**	**1.36**	**0.00**	**9.11**	**1.13**	**0.09**
Min. Value	66.40	0.00	2.85	0.32	0.00	7.75	0.78	0.00
Max. Value	87.66	1.81	16.80	2.98	0.00	11.65	1.36	0.26
Max. Difference	**21.26**	**1.81**	**13.95**	**2.66**	**0.00**	**3.90**	**0.58**	**0.26**
Min. Dev. from Avg.	**10.36**	**0.87**	**7.84**	**1.04**	**0.00**	**1.35**	**0.36**	**0.09**
Max. Dev. from Avg.	**10.90**	**0.93**	**6.12**	**1.62**	**0.00**	**2.55**	**0.22**	**0.17**

Sample	**State of deformation:** **Undeformed**						**Sandstone:** Lee	
No.: **PMO 46**	Qtz Grain	Kaolinite	Lithic RF	Feldspar	FeO	**Inter**gran. Qtz Cement	**Intra**gran. Qtz Cement	Prim. Porosity
Area 1	84.77	0.76	3.30	0.00	0.00	10.15	1.02	0.00
Area 2	87.79	0.26	0.78	0.00	0.00	9.35	1.82	0.00
Area 3	81.01	1.77	3.54	0.00	0.00	12.41	1.27	0.00
Area 4	87.59	0.00	3.54	0.00	0.00	8.35	0.25	0.25
Averages	**85.29**	**0.70**	**2.79**	**0.00**	**0.00**	**10.07**	**1.09**	**0.06**
Min. Value	81.01	0.26	0.78	0.00	0.00	8.35	0.25	0.00
Max. Value	87.79	1.77	3.54	0.00	0.00	12.41	1.82	0.25
Max. Difference	**6.78**	**1.51**	**2.77**	**0.00**	**0.00**	**4.05**	**1.57**	**0.25**
Min. Dev. from Avg.	**4.28**	**0.44**	**2.01**	**0.00**	**0.00**	**1.71**	**0.83**	**0.06**
Max. Dev. from Avg.	**2.50**	**1.07**	**0.75**	**0.00**	**0.00**	**2.34**	**0.73**	**0.19**

Sample	**State of deformation:** Undeformed						**Sandstone:** Lee	
No.: PMO 47	Qtz Grain	Kaolinite	Lithic RF	Feldspar	FeO	**Inter**gran. Qtz Cement	**Intra**gran. Qtz Cement	Prim. Porosity
Area 1	80.75	3.25	1.50	0.00	0.00	13.50	1.00	0.00
Area 2	77.41	0.00	1.02	4.57	0.00	15.48	1.52	0.00
Area 3	77.32	0.00	4.12	0.00	0.00	17.27	1.03	0.26
Area 4	76.46	0.25	7.85	0.00	0.00	13.67	1.77	0.00
Averages	**77.98**	**0.88**	**3.62**	**1.14**	**0.00**	**14.98**	**1.33**	**0.06**
Min. Value	76.46	0.00	1.02	0.00	0.00	13.50	1.00	0.00
Max. Value	80.75	3.25	7.85	4.57	0.00	17.27	1.77	0.26
Max. Difference	**4.29**	**3.25**	**6.83**	**4.57**	**0.00**	**3.77**	**0.77**	**0.26**
Min. Dev. from Avg.	**1.53**	**0.88**	**2.61**	**1.14**	**0.00**	**1.48**	**0.33**	**0.06**
Max. Dev. from Avg.	**2.77**	**2.37**	**4.23**	**3.43**	**0.00**	**2.29**	**0.44**	**0.19**

Sample	**State of deformation:** Undeformed						**Sandstone:** Breathitt	
No.: PMO 48	Qtz Grain	Kaolinite	Lithic RF	Feldspar	FeO	**Inter**gran. Qtz Cement	**Intra**gran. Qtz Cement	Prim. Porosity
Area 1	84.64	2.08	3.65	0.00	0.00	9.11	0.52	0.00
Area 2	77.69	4.76	7.02	1.00	0.00	8.02	1.50	0.00
Area 3	74.44	6.02	3.26	1.00	0.00	13.03	2.26	0.00
Area 4	81.54	6.15	3.33	0.00	0.00	7.69	1.28	0.00
Averages	**79.58**	**4.75**	**4.31**	**0.50**	**0.00**	**9.46**	**1.39**	**0.00**
Min. Value	74.44	2.08	3.26	0.00	0.00	7.69	0.52	0.00
Max. Value	84.64	6.15	7.02	1.00	0.00	13.03	2.26	0.00
Max. Difference	**10.20**	**4.07**	**3.76**	**1.00**	**0.00**	**5.34**	**1.73**	**0.00**
Min. Dev. from Avg.	**5.14**	**2.67**	**1.06**	**0.50**	**0.00**	**1.77**	**0.87**	**0.00**
Max. Dev. from Avg.	**5.06**	**1.40**	**2.70**	**0.50**	**0.00**	**3.57**	**0.87**	**0.00**

Sample	**State of deformation:** **Undeformed**						**Sandstone:** **Breathitt**	
No.: **PMO 49**	Qtz Grain	Kaolinite	Lithic RF	Feldspar	FeO	**Inter**gran. Qtz Cement	**Intra**gran. Qtz Cement	Prim. Porosity
Area 1	78.80	2.49	2.00	0.00	0.00	14.21	2.49	0.00
Area 2	80.25	5.25	0.00	0.00	0.00	13.75	0.75	0.00
Area 3	75.25	0.00	5.75	1.75	0.00	12.75	4.50	0.00
Area 4	78.25	0.00	9.00	0.00	0.00	9.25	3.50	0.00
Averages	**78.14**	**1.94**	**4.19**	**0.44**	**0.00**	**12.49**	**2.81**	**0.00**
Min. Value	75.25	0.00	0.00	0.00	0.00	9.25	0.75	0.00
Max. Value	80.25	5.25	9.00	1.75	0.00	14.21	4.50	0.00
Max. Difference	**5.00**	**5.25**	**9.00**	**1.75**	**0.00**	**4.96**	**3.75**	**0.00**
Min. Dev. from Avg.	**2.89**	**1.94**	**4.19**	**0.44**	**0.00**	**3.24**	**2.06**	**0.00**
Max. Dev. from Avg.	**2.11**	**3.31**	**4.81**	**1.31**	**0.00**	**1.72**	**1.69**	**0.00**

Sample	**State of deformation:** **Deformed**						**Sandstone:** **Lee**	
No.: **PMO 50**	Qtz Grain	Kaolinite	Lithic RF	Feldspar	FeO	**Inter**gran. Qtz Cement	**Intra**gran. Qtz Cement	Prim. Porosity
Area 1	87.75	0.00	0.00	0.00	0.00	2.50	9.75	0.00
Area 2	86.50	0.00	2.00	0.00	0.00	5.50	6.00	0.00
Area 3	88.50	0.00	0.00	0.00	0.00	2.25	9.25	0.00
Area 4	86.00	0.00	2.50	0.00	0.00	7.25	4.25	0.00
Averages	**87.19**	**0.00**	**1.13**	**0.00**	**0.00**	**4.38**	**7.31**	**0.00**
Min. Value	86.00	0.00	0.00	0.00	0.00	2.50	4.25	0.00
Max. Value	88.50	0.00	2.50	0.00	0.00	7.25	9.75	0.00
Max. Difference	**2.50**	**0.00**	**2.50**	**0.00**	**0.00**	**4.75**	**5.50**	**0.00**
Min. Dev. from Avg.	**1.19**	**0.00**	**1.13**	**0.00**	**0.00**	**1.88**	**3.06**	**0.00**
Max. Dev. from Avg.	**1.31**	**0.00**	**1.38**	**0.00**	**0.00**	**2.88**	**2.44**	**0.00**

Sample	**State of deformation: Undeformed**						**Sandstone: Breathitt**	
No.: PMO 51	Qtz Grain	Kaolinite	Lithic RF	Feldspar	FeO	**Inter**gran. Qtz Cement	**Intra**gran. Qtz Cement	Prim. Porosity
Area 1	68.25	0	10.25	0.25	0.00	20	0.75	0.5
Area 2	80.25	0	4.5	0	0.00	14.75	0.5	0
Area 3	76.25	1.25	4.5	0	0.00	16.75	1.25	0
Area 4	76.5	0.75	5.75	0.5	0.00	15.5	1	0
Averages	**75.31**	**0.50**	**6.25**	**0.19**	**0.00**	**16.75**	**0.88**	**0.13**
Min. Value	68.25	0.00	4.50	0.00	0.00	14.75	0.50	0.00
Max. Value	80.25	1.25	10.25	0.50	0.00	16.75	1.25	0.50
Max. Difference	**12.00**	**1.25**	**5.75**	**0.50**	**0.00**	**2.00**	**0.75**	**0.50**
Min. Dev. from Avg.	**7.06**	**0.50**	**1.75**	**0.19**	**0.00**	**2.00**	**0.38**	**0.13**
Max. Dev. from Avg.	**4.94**	**0.75**	**4.00**	**0.31**	**0.00**	**0.00**	**0.38**	**0.38**

Sample	**State of deformation: Undeformed**						**Sandstone: Breathitt**	
No.: PMO 52	Qtz Grain	Kaolinite	Lithic RF	Feldspar	FeO	**Inter**gran. Qtz Cement	**Intra**gran. Qtz Cement	Prim. Porosity
Area 1	70.45	0.25	5.81	0.25	0.00	20.20	1.01	2.02
Area 2	71.43	0.00	6.63	0.00	0.00	17.86	2.30	1.79
Area 3	69.10	0.00	9.80	0.50	0.00	19.10	0.50	1.01
Area 4	74.50	0.75	5.75	0.00	0.00	18.25	0.25	0.50
Averages	**71.37**	**0.25**	**7.00**	**0.19**	**0.00**	**18.85**	**1.01**	**1.33**
Min. Value	69.10	0.00	5.75	0.00	0.00	17.86	0.25	0.50
Max. Value	74.50	0.75	9.80	0.50	0.00	20.20	2.30	2.02
Max. Difference	**5.40**	**0.75**	**4.05**	**0.50**	**0.00**	**2.34**	**2.05**	**1.52**
Min. Dev. from Avg.	**2.27**	**0.25**	**1.25**	**0.19**	**0.00**	**0.99**	**0.76**	**0.83**
Max. Dev. from Avg.	**3.13**	**0.50**	**2.80**	**0.31**	**0.00**	**1.35**	**1.28**	**0.69**

Bibliography

Aase, N.E., Bjorkum, P.A., and Nadeau, P.H., 1996, The effect of grain-coating microquartz on preservation of reservoir porosity: American Association of Petroleum Geologists Bulletin, v. 80, p. 1654-1673.

Alnes, J.R. and Lilburn, R.A., 1998, Mechanisms for generating overpressure in sedimentary basins: A reevaluation: Discussion: American Association of Petroleum Geologists Bulletin, v. 82, p. 2266-2269.

An, L.-J., and Sammis, C.G., 1994, Particle size distribution of cataclastic fault material from Southern California: A 3D study: Pure and Applied Geophysics, v. 143, p. 203-227.

Antonellini, M., and Aydin, A., 1994, Effect of faulting on fluid flow in porous sandstones: Petrophysical properties: American Association of Petroleum Geologists Bulletin, v. 78, p. 355-377.

Atkins, J.E. and McBride, E.F., 1992, Porosity and packing of Holocene river, dune and beach sands: American Association of Petroleum Geologists Bulletin, v. 76, p.339-355.

Atkinson, B.K., 1987, Introduction to fracture mechanics and its geophysical applications, *in* Atkinson, B.K., ed., Fracture mechanics of rocks: Austin, Academic Press, p. 1-25.

Awwiller, D.N. and Summa, L.L., 1997, Quartz cement volume constraints on burial history analysis: an example from the Eocene of western Venezuela (abs.): American Association of Petroleum Geologists Annual Convention Program Abstracts, p. A6.

Baldwin, B., and Butler, C.O., 1985, Compaction curves: American Association of Petroleum Geologists Bulletin, v. 69, p. 622-626.

Beaumont, C., Quinlan, G.M., and Hamilton, J., 1987, The Alleghanian orogeny and its relationship to the evolution of the eastern interior, North America, *in* Beaumont, C., and Tankard, A.J., eds., Sedimentary Basins and Basin-Forming Mechanisms: Society of Petroleum Geologists, v. 12 p. 425-445.

Bernabe, Y., and Hayes, J.A., 1992, The effects of cement on the strength of granular rocks: Geophysical Research Letters, v. 19, p. 1511-1514.

Berner, R.A., 1980, Early Diagenesis- A Theoretical Approach: Princeton, NJ, Princeton University Press, 242 p.

Bethke, C.M., Reed, J.D., and Oltz, D.F., 1991, Long-range petroleum migration in the Illinois Basin: American Association of Petroleum Geologists Bulletin, v. 75, p. 925-945.

Bethke, C.M., 1986, Inverse hydrologic analysis of the distribution and origin of Gulg coast-type geopressured zones: Journal of Geophyisical Research, v. 91, p. 6535-6545.

Blanchard, P.E., 1987, Fluid Flow in Compacting Sedimentary Basins [Ph.D. thesis]: Austin, Texas, The University of Texas at Austin, 190 p.

Blatt, H., Middelton, G., and Murray, R., 1972 Origin of Sedimentary Rocks: Engelwood Cliffs, New Jersey, Prentice-Hall, Inc., 634 p.

Blenkinsop, T.G., 1991, Cataclasis and processes of particle size reduction: Pure and Applied Geophysics, v. 136, p. 59-87.

Bloch, S., 1991, Empirical prediction of porosity and permeability in sandstones: The American Association of Petroleum Geologists, v. 75, p. 1145-1160.
—, 1994, Importance of reservoir prediction in exploration, *in* Wilson, M.D., ed., Reservoir Quality Assessment and Prediction in Clastic Rocks: Society for Sedimentary Geology (SEPM) Short Course, v. 30, p. 5-8.

Bloch, S., and Helmold, K.P., 1995, Approaches to predicting reservoir quality in sandstones: American Association of Petroleum Geologists Bulletin, v. 79, p. 97-115.

Bloch, S., Lander, R.H., and Bonnell, L., 2002, Anomalously high porosity and permeability in deeply buried sandstone reservoirs: Origin and predictability: American Association of Petroleum Geologists Bulletin, v. 86, p. 301-328.

Boettcher, S.S., and Milliken, K.L., 1994, Mesozoic-Cenozoic unroofing of the southern Appalachian Basin: apatite fission track evidence from Middle Pennsylvanian sandstones: Journal of Geology, v. 102, p. 655-663.

Boiron, M.C., Essarraj, S., Cathalineau, M., and Lespinasse, B.P., 1992, Identification of fluid inclusions in relations to their host microstructural domains in quartz by cathodoluminescence: Geochimica et Cosmochimica Acta, v. 56, p. 175-185.

Boles, J.R., Franks, S., 1979, Clay diagenesis in Wilcox sandstones of southwest Texas: Implications of smectite diagenesis on sandstone cementation: Journal of Sedimentary Petrology, v. 49, p. 55-70.

Bonnell, L.M., Lander, R.H., In prep, Quartz precipitation kinetics vary with sandstone grain size.

—, 2002, Reservoir Quality Prediction: From Deep Water to Tight Gas Sandstones: Gulf Coast Section of Geological Societies Annual Meeting Short Course, Austin, Texas.

Bonnell, L.M., Lander, R.H., and Sundhaug, C., 1998a, Grain coatings and reservoir quality preservation: role of coating completeness, grain size and thermal history (abs.): American Association of Petroleum Geologists, Annual Convention Extended Abstracts, v. 1, p. A81.

Bonnell, L.M., Warren, E.A. and Lander, R.H., 1998b., Reservoir quality prediction through simulation of sandstone diagenesis: Cusiana Field, Eastern Columbia (abs.) American Association of Petroleum Geologists International Conference and Exhibition Extended Abstracts, p.494.

Borg, I.Y., Melvin, F., Handin, J.W., and Donald Val, H., 1960, Experimental deformation of Saint Peter sand--A study of cataclastic flow, Chapter 6, *in* Griggs, D.T., ed., North American Rock Mechanics Syposium, 2: Houston, TX, USA, Geological Society of America, p. 133-191.

Brady, P.V., and Walther, J.V., 1990, Kinetics of quartz dissolution at low temperatures: Chemical Geology, v. 82, p. 253-264.

Brantley, S.L., Evans, B., Hickman, S.H., and Crerar, D.A., 1990, Healing of microcracks in quartz: Implication for fluid flow: Geology, v. 18, p. 136-139.

Bruno, M.S., and Nelson, R.B., 1991, Microstructural analysis of the inelastic behavior of sedimentary rock: Mechanics of Material, v. 12, p. 95-118.

Brzesowsky, R., 1995, Micromechanics of Sand Grain Failure and Sand Compaction [Ph.D. thesis]: Utrecht, Netherlands, Universiteit Utrecht, 180 p.

Burley, S.D., Walsh, J., and Watterson, J., 1991 Active fault participation in the diagenetic modification of sandstone reservoir properties (abs.) American Association of Petroleum Geologists Annual Convention Program Abstracts, v. 75, p. 1407.

Byrnes, A.P., 1994, Empirical methods of reservoir quality prediction, *in* Wilson, M.D., ed., Reservoir Quality Assessment and Prediction in Clastic Rocks: Society for Sedimentary Geology (SEPM) Short Course 30, p. 9-20.

Chuhan, F., Kjeldtad, A., Bjorlykke, K., and Hoeg, K., 2002, Porosity loss in sand by grains crushing- experimental evidence and relevance to reservoir quality: Marine and Petroleum Geology, v. 19, p. 39-53.

Cladouhos, T.T., 1999, Shape preferred orientation of survivor grains in fault gouge: Journal of Structural Geology, v. 21, p. 419-436.

Damberger, H.H., Demir, I., and Pine, J., 1999, Age relationships between coalification, deformation, and geothermal events in the Illinois Basin: Geological Society of America Abstract, Annual Meeting, v. 31, p. 403.

David, C, Menéndez, B., and Bernabé, Y., 1998, Mechanical behavior of synthetic sandstones with varying brittle cement content: International Journal of Mechanical Mineral Science, v. 35, p. 759-770.

den Brok, S.W.J., 1998, Effect of microcracking on pressure-solution strain rate: The Gratz grain-boundary model: Geology, v. 26, p. 915-918.

Dickinson, W.W., and Milliken, K.L., 1995, The diagenetic role of brittle deformation in compaction and pressure solution, Etjo Sandstone, Namibia: Journal of Geology, v. 103, p. 339-347.

Dunn, D.E., LaFountain, L.J., and Jackson, R.E., 1973, Porosity dependence and mechanism of brittle fracture in sandstones: Journal of Geophysical Research, v. 78, p. 2403-2517.

Dunn, T.L., 1994, Recognizing tectonic and compaction driven quartz grain fracturing and annealing in the Almond Formation, Green River basin, Wyoming (abs): American Association of Petroleum Geologists Annual Convention Program Abstracts, v. 3, p. 140.

Dutton, S.P., 1997, Timing of compaction and quartz cementation from integrated petrographic and burial-history analyses, Lower Cretaceous Fall River Formation, Wyoming and South Dakota: Journal of Sedimentary Research, v. 67, p. 186-196.

Dvorkin, J., Nur, A., and Yin, H., 1994, Effective properties of cemented granular materials: Mechanics of Material, v. 18, p. 351-366.

Eberl, D.D., Kile, D.E., and Drits, V.A., 2002, On geological interpretation of crystal size distributions: constant vs. proportionate growth: American Mineralogist, v. 87, p. 1235-1241.

Ehrenberg, S.N., 1989, Assessing the Relative Importance of compaction processes and cementation to reduction of porosity in sandstones: discussion; Compaction and porosity evolution of Pliocene sandstones, Ventura Basin, California: discussion: American Association of Petroleum Geologists, v. 73, p. 1274-1276.

—, 1995, Measuring sandstone compaction from modal analyses of thin-sections: how to do it and what the results mean: Journal of Sedimentary Research, v. A65, p. 369-379.

Elias, B.P., and Hajash, A., 1992, Changes in quartz solubility and porosity due to effective stress; an experimental investigation of pressure solution: Geology, v. 20, p. 451-454.

Engelder, J.T., 1974, Cataclasis and the generation of fault gouge: Geological Society of America Bulletin, v. 85, p. 1515-1522.

Fisher, Q.J., Casey, M., Harris, S.D., and Knipe, R.J., 2003, Fluid-flow of faulted sandstones: The importance of temperature history: Geology, v. 31, p. 965-968.

Fisher, Q.J., Casey, M., Clennell, M.B., and Knipe, R.J., 1999, Mechanical compaction of deeply buried sandstones of the North Sea: Marine and Petroleum Geology, v. 16, p. 605-618.

Fisher, Q.J., Knipe, R.J., and Worden, R.H., 2000, Microstructure of deformed and non-deformed sandstones from the North Sea: implications for the origin of quartz cement in sandstones, *in* Worden, R.H., and Morad, S., eds., Quartz Cementation in Sandstones: International Association of Sedimentologists Special Publication, v. 29, p. 129-146.

Fishman, N.S., 1997, Basin-wide fluid movement in a Cambrian paleoaquifer:evidence from the Mount Simon sandstone, Illinois and Indiana, *in* Montanez, I., Gregg, J.M., and Shelton, K.L., eds., Basin-Wide Diagenetic Patterns: Integrated Petrologic, Geochemical, and Hydrologic Considerations: SEPM Special Publication, v. 57, p. 221-234.

Folk, R., Petrology of Sedimentary Rocks: Hemphill Publishing Company, Austin, Texas, 170 p.

Frank, F.C. and Lawn, B.R., 1967, On the theory of Herzian fracture: Proceedings from the Royal Society of London, v.A229, p. 291-306

Fu, L., Milliken, K.L., and Sharp, J.M.J., 1994, Porosity and permeability variations in fractured and liesegang-banded Brethitt sandstones (Middle Pennsylvanian), eastern Kentucky: diagenetic controls and implications for modeling dual-porosity systems: Journal of Hydrology, v. 154, p. 351-381.

Füchtbauer, H., 1967 Influence of different types of diagenesis on sandstone porosity: diagenetic controls and implications for modeling dual-porosity systems: Proceedings From the 7th World Petroleum Congree, v. 2, p. 353-369.

Gallagher, J.J., 1987, Fractography of sand grains broken by uniaxial compression, *in* Marshall, J.R., ed., Clastic particles; scanning electron microscopy and shape analysis of sedimentary and volcanic clasts: New York, Van Nostrand Reinhold Company, p. 189-228.

Gallagher, J.J., Friedman, M., Handin, J., and Sowers, G.M., 1974, Experimental studies relating to microfracture in sandstone: Tectonophysics, v. 21, p. 203-247.

Galloway, W.E., 1977, Catahoula Formation of the Texas coastal plain: deposition systems, composition, structural development, groundwater flow history, and uranium distribution: Report of Invetigation, v. 87, p. 59.

—, 1984, Hydrogeologic regimes of sandstone diagenesis, *in* McDonald, D.A., and Surdam, R.C., eds., Clastic Diagenesis: American Association of Petroleum Geologists Memoir, v. 37, p. 3-14.

Galloway, W.E., and Hodbay, D.K., 1982, Frio Formation of the Texas Gulf Plain- depositional systems, structural framework, and hydrocarbon distribution: American Association of Petroleum Geologists Bulletin, v. 66, p. 649-688.

Graton, L.C., and Fraser, H.C., 1935, Systematic packing of spheres with particular relation to porosity and permeability: American Association of Petroleum Geologists Bulletin, v. 43, p. 785-909.

Gratz, A., 1991, Solution-transfer compaction of quartzites: Progress toward a rate law: Geology, v. 19, p. 901-904.

Greb, S.F., and Chestnut, D.R.J., 1996, Lower and lower Middle Pennsylvanian to estuarine deposition, central Appalachian Basin; effects of eustacy, tectonics, and climate: Geological Society of America Bulletin, v. 108, p. 303-317.

Groshong, R.H.J., 1988, Low-temperature deformation mechanisms and their interpretation: Geological Society of America Bulletin, v. 100, p. 1329-1360.

Gu, Y., and Wong, T.-F., 1994, Development of shear localization in simulated quartz gouge: effect of cumulative slip and gouge particle size: Pure and Applied Geophysics, v. 143, p. 387-421.

Habicht, J.K.A., 1979, Paleoclimate, paleomagnetism, and continental drift: American Association of Petroleum Geologists Studies is Geology: v. 9, 31 p.

Hadizadeh, J., and Johnson, W.K., in press, Estimating local strain due to comminution in experimental cataclastic textures: Journal of Structural Geology.

Harrison, W.J. and Summa, L.L., 1991, Paleohydrology of the Gulf of Mexico Basin: American Journal of Science, v. 291, p. 109-176.

Hathon, L.A. and Houseknecht, D.W., 1991, Porosity reduction in sandstones induced by mechanical compaction: Cathodoluminescence evaluation (abs), American Association of Petroleum Geologists Annual Convention Program Abstracts, v. 75, p. 590-591.

Helset, H.M., Lander, R.H., Matthews, J.C., Reemst, P., Bonnell, L.M. and Frette, I., 2002, The role of diagenesis in the formation of fluid overpressure in clastic rocks *in* Koester, A.G. and Hunsdale, R., eds., Hydrocarbon Seal Quantification: Norwegian Petroleum Society v. 11, p. 37-50.

Henzu, Y., and Dvorkin, J., 1994, Strength of cemented grains: Geophysical Research Letters, v. 21, p. 903-906.

Hippler, S.J., 1993, Deformation Microstructures and Diagenesis in Sandstones Adjacent and Extensional Fault: Implications for fluid flow and entrapment of hydrocarbon: American Association of Petroleum Geologists Bulletin, v. 77, p. 625-637.

Hirth, G. and Tullis, J., 1989, The effects of pressure and porosity on the Micromechanics of the brittle/ductile transition in quartzite: Journal of Geophysical Research, v. 94, B, p. 17825-17838.

Hoholick, J.D., Metarko, T., and Potter, P.E., 1984, Regional variation of porosity and cement: St. Peter and Mt. Simon Sandstones in Illinois Basin: American Association of Petroleum Geologists Bulletin, v. 68, p. 753-764.

Houseknecht, D.W., 1987, Assessing the Relative Importance of Compaction Processes and Cementation to Reduction of Porosity in Sandstones: American Association of Petroleum Geologists Bulletin, v. 71, p. 633-642.

—, 1991, Use of cathodoluminescence petrography for understanding compaction, quartz cementation, and porosity in sandstones, *in* Barker, C.E., and Kopp, O.C., eds., Luminescence Microscopy and Spectroscopy: Quantitative and Qualitative Applications: SEPM, Short Course, v. 25, p. 59-75.

Hower, J.C., and Rimmer, S.M., 1991, Coal rank trends in the Central Appalachian coalfield: Virginia, West Virginia and Kentucky: Organic Geochemistry, v. 17, p. 161-173.

Jamison, W.R. and Stearn, D.W., 1982, Tectonic deformation of Wingate Sandstone, Colorado national monument: American Associate of Petroleum Geologists, v. 66, p. 2584-2608.

Johns, W.D. and Shimoyama, A.., 1972, Clay minerals and petroleum-forming reactions during burial and diagenesis: American Association of Petroleum Geologists Bulletin, v. 56, p. 2160-2167.

Johnsson, M.J., 1986, Distribution of maximum burial temperatures across northern Appalachian Basin and implications for Carboniferous sedimentation patterns: Geology, v. 14, p. 384-387.

Karner, S.L, Chester, F.M., Kronenberg, A.K. and Chester, J.S., 2003, Subcritical compaction and yielding of granular quartz sand: Tectonophysics, v. 377, p. 357-381.

Kendall, K., 1978, The impossibility of comminuting small particles: Nature, v. 272, p. 710-711.

Klein, G., and Hsui, A.T., 1987, Origin of cratonic basins: Geology, v. 15, p. 1094-1098.

Klemme, H,D., 1975, Geothermal gradients, heat flow and hydrocarbon recovery, *in* Fischer, A.G. and Judson, S., eds., Petroleum and Global Tectonics: Princeton, New Jersey, Princeton University Press p. 251-305.

Lade, P.V., Yamamuro, J.A., and Bopp, P.A., 1996, Significance of particle crushing in granular materials: Journal of Geotechnical Engineering, v. 122, p. 309-316.

Lamme, T.W. and Whitman, R.V., 1969, Soil Mechanics: New York, John Wiley and Sons, 553 p.

Land, L.S., 1984, Frio sandstone diagenesis, Texas Gulf Coast: A regional study, *in* McDonald, D.A., and Surdam, R.C., eds., Clastic Diagenesis: American Association of Petroleum Geologists Memoir, v. 37, p. 47-62.

Land, L.S., and Milliken, K.L., 2000, Regional loss of SiO2, and gain of K2O during burial diagenesis of Gulf Coast mudrocks, USA, *in* Worden, R.H., and Morad, S., eds., Quartz Cementation in Sandstones: International Association of Sedimentologists Special Publication, v. 29, p. 183-197.

Lander, R.L., Bonnell, L.M., Laubach, S.E., Larese, R.E., and Gale, J., 2004, Theory for quartz cementation in structurally deformed sandstones (abs): American Association of Petroleum Geologists Hedberg Research Conference. Structural Diagenesis: Fundamental Advances and New Applications from a Holistic View of Mechanical and Chemical Processes, Austin, TX, Feb 8-11.

Lander, R.H., and Walderhaug, O., 1997, An empirically calibrated model for sandstone reservoir prediction (abs.): American Association of Petroleum Geologists Annual Convention Program Abstracts, p. A66.

Lander, R.H., Felt, V., Bonnell, L.M, and Walderhaug, O., 1997a, Utility of sandstone diagenetic modeling for basin history assessment (abs.): American Association of Petroleum Geologists Annual Convention Program Abstracts, p. A66.

Lander, R.H., Felt, V., and Bonnell, L.M., 1997b, Sensitivity/risk assessment with basin models: approach and case example from a frontier setting (abs.): American Association of Petroleum Geologists Annual Convention Program Abstracts, p. A66.

Lander, R.H., and Walderhaug, O., 1999, Predicting porosity through simulating sandstone compaction and quartz cementation: American Association of Petroleum Geologists Bulletin, v. 83, p. 433-449.

Laubach, S.E., 1988, Subsurface fractures and their relationship to stress history in East Texas basin sandstone: Tectonophysics, v. 156, p. 37-49.

—, 1988, Subsurface fractures and their relation to stress history in East Texas Basin sandstones: Tectonophysics, v. 156, p. 495-503.

—, 1997, A method to detect natural fracture strike in sandstones: American Association of Petroleum Geologists Bulletin, v. 81, p. 604-623.

Laubach, S.E., Lander, R.H., Bonnell, L.M., Olsen, J.E., and Reed, R.M., in press, Coevolution of crack-seal textures and fracture porosity in sedimentary rocks: cathodoluminescence observations of regional fractures: Journal of Structural Geology.

Lee, K.L. and Farhoomand, I., 1967, Compressibility and crushing of granular soil in anisotropic triaxial compression: Canadian Geotechnical Journal, v. 4, p. 68-99.

Loucks, R.G., Dodge, M.M., and Galloway, W.E., 1984, Regional controls on diagenesis and reservoir quality in Lower Tertiary sandstones along the Texas Gulf Coast, *in* McDonald, D.A., and Surdam, R.C., eds., Clastic Diagenesis: American Association of Petroleum Geologists Memoir, v. 37, p. 15-45.

Lundegard, P.D., 1992, Sandstone porosity loss- A "big picture" view of the importance of compaction: Journal of Sedimentary Petrology, v. 62, p. 250-260.

Lynch, F.L., 1997, Frio shale mineralogy and the stoichiometry of the smectite-to-illite reaction; the most important reaction in clastic sedimentary diagenesis: Clays and Clay Minerals, v. 45, p. 618-631.

Mair, K., and Marone, C., 1999, Friction of simulated fault gouge for a wide range of velocities and normal stresses: Journal of Geophysical Research, v. 104, p. 28899-28914.

Makowitz, A. and Milliken, K.L., 2001, New Data on the Role of compaction in diagenesis: Frio Formation, Gulf of Mexico Basin (abs): American Association of Petroleum Geologists Annual Convention Program Abstracts, v. 85, pp. 123-124.

—, 2002, Quantitative measurement of brittle deformation in burial compaction, Frio Formation, Gulf of Mexico Basin: Gulf Coast Association of Geological Societies Transactions, v. 52, p. 695-706.

—, 2003, Quantification of brittle deformation in burial compaction, Frio and Mount Simon Formation sandstones: Journal of Sedimentary Research, v. 73, p. 999-1013.

—, 2004a, Brittle deformation during burial compaction: An elusive porosity reduction mechanism (abs): American Association of Petroleum Geologists Hedberg Research Conference. Structural Diagenesis: Fundamental Advances and New Applications from a Holistic View of Mechanical and Chemical Processes, Austin, TX, Feb 8-11.

—, 2004b, Quantifying brittle grain deformation during compaction of Mount Simon and Frio Formation sandstones. International Geological Congress Abstracts with Programs, Florence, Italy, August 20-28.

—, in preparation, Structural Diagenesis Along the Pine Mountain Overthrust: Using Scanned Cathodoluminescence to Elucidate Particle Size, Cement Distribution, and Texture of Cataclasized Sandstones.

Makowitz, A. and Sibley, D., 2001, Crystal growth mechanisms of quartz overgrowths in a Cambrian quartz arenite: Journal of Sedimentary Research, v. 71, p. 809-816.

Marone, C., and Scholtz, C.H., 1989, Particle-size distribution and microstructures within simulated fault gouge: Journal of Structural Geology, v. 11, p. 799-814.

Marrett, R., 1996, Aggregate properties of fracture populations: Journal of Structural Geology, v. 18, p. 169-178.

McBride, E.F., Diggs, T.N., and Wilson, J.C., 1991, Compaction of Wilcox and Carrizo sandstones (Paleocene- Eocene) to 4420 M, Texas Gulf Coast: Journal of Sedimentary Petrology, v. 61, p. 73-85.

McEwan, T.J., 1981, Brittle deformation in pitted pebble conglomerates: Journal of Structural Geology, v. 3, p. 25-37.

McEwan, T.J., 1981, Brittle deformation in pitted pebble conglomerates: Journal of Structural Geology, v. 3, p. 25-37.

McLaughlin, O.M., Haszeldine, R.S., and Fallick, A.E. 1996, Quartz diagenesis in layered fluids in the South Brae Oilfield, North Sea, *in* Crossey, L.J., Loucks, R., and Totten, M.W., eds., Siliciclastic diagenesis and fluid flow concepts and applications: SEPM Society for Sedimentary Geology Special Publication, v. 5, p. 103-113.

McKenna, T.E. and Sharp, J.M.Jr., 1998, Radiogenic heat production in sedimentary rocks of the Gulf of Mexico basin, South Texas: American Association of Petroleum Geologists Bulletin, v. 82, p. 484-496.

Menéndez, B., Zhu, W., and Wong, T.-F., 1996, Micromechanics of brittle faulting and cataclastic flow in Berea sandstone: Journal of Structural Geology, v. 18, p. 1-16.

Michibayashi, K., 1996, The role of intragranular fracturing in grain size reduction in feldspar during mylonitization: Journal of Structural Geology, v. 18, p. 17-25.

Milliken, K.L., 1981, History of burial diagenesis determined from isotopic geochemistry: American Association of Petroleum Geologists Bulletin, v. 65, p. 1397-1413.

—, 1994, The widespread occurrence of healed microfractures in siliciclastics rocks: Evidence from scanned cathodoluminescence imaging, *in* Nelson, P.P. and Laubach, S.E., eds., Rock Mechanics: Models and Measurements, Challenges from Industry: First North American Rock Mechanics Symposium, Rotterdam, A.A. Balkema, p. 825-823

—, 2001, Diagenetic heterogeneity in sandstone at the outcrop scale, Breathitt Formation (Pennsylvanian), eastern Kentucky: American Association of Petroleum Geologists Bulletin, v. 85, p. 795-815.

—, 2003, Microscale distribution of kaolinite in Breathitt Formation sandstone (middle Pennsylvanian): implications for mass balance: International Association of Sedimentologists Special Publication, v. 34, p. 343-360.

Milliken, K.L., and Laubach, S.E., 2000, Brittle deformation in sandstone diagenesis as revealed by scanned cathodoluminescence imaging with application to characterization of fractured reservoirs, *in* Pagel, M., Barbin, V., Blanc, P., and Ohnenstetter, D., eds., Cathodoluminescence in Geosciences: Berlin, Springer, p. 225-243.

Milliken, K.L., McBride, E.F., and Land, L.S., 1989, Numerical assessment of dissolution versus replacement in the subsurface destruction of detrital feldspars, Oligocene Frio Formation, South Texas: Journal of Sedimentary Petrology, v. 59, p. 740-757.

Milliken, K.L. and Reed, R.M., 2002, Internal structure of deformation bands as revealed by cathodoluminescence imaging, Hickory Sandstone (Cambrian): Gulf Coast Association of Geological Societies Transactions, v. 52, p. 725-736.

Milliken, K.L., Reed, R.M., and Laubach, S.E., 2004, Quantifying compaction and cementation in deformation bands in porous sandstones: American Association of Petroleum Geologists Memoir, Faults and Petroleum Traps, in press.

Mitra, S., 1988, Three-dimensional geometry and kinematic evolution of the Pine Mountain thrust system, southern Appalachians: Geological Society of America Bulletin, v. 100, p. 72-95.

—, 1988, Effects of Deformation Mechanisms on Reservoir Potential in Central Appalachian Overthrust Belt: American Association of Petroleum Geologists Bulletin, v. 72, p. 536-554.

Monzawa, N., and Otsuki, K., 2003, Comminution and fluidization of granular fault materials: implications for fault slip behavior: Tectonophysics, v. 367, p. 127-143.

Morgan, J.K., and Boettcher, M.S., 1999, Numerical simulations of granular shear zones using distinct element method 1. shear zone kinematics and micromechanics of localization: Journal of Geophysical Research, v. 104, p. 2703-2719.

Net, L.I. and Makowitz, A., 2004, Diagenetic processes and porosity evolution within deformation bands in the eolian Navajo Sandstone (Early Jurassic), southern Utah. AAPG Hedberg Conference. Structural Diagenesis: Fundamental Advances and New Applications from a Holistic View of Mechanical and Chemical Processes, Austin, TX, Feb. 8-11.

Nuccio, V.F., Wandry, C.J., Ryder, R.T., and Harris, A.G., 1997, Thermal maturity and petroleum generation of Middle Ordovician black shale source rocks, central Appalachian Basin; controls on oil and gas in Lower Silurian low-permeability sandstone reservoirs (abs), AAPG Eastern Section and the Society for Organic Petrology Joint Meeting: Lexington, Kentucky, p. 1560.

O'Hara, K., Hower, J.C., and Rimmer, S.M., 1990, Constraints on the emplacement and uplift history of the Pine Mountain thrust sheet, Eastern Kentucky: Evidence from coal rank trends: Journal of Geology, v. 98, p. 43-51.

Onasch, C.M., 1990, Microfractures and their role in deformation of a quartz arenite from the Central Appalachian foreland: Journal of Structural Geology, v. 12, p. 883-894.

Osbourne, M.J. and Swarbrick, R.E., 1997, Mechanisms for generating overpressure in sedimentary basins: A reevaluation: American Association of Petroleum Geologists Bulletin, v. 81, p. 1023-1041.

Ostrom, M.E., 1987, The Mount Simon Formation at Eau Claire, Wisconsin, *in* Biggs, D.L., ed., North-central section of the Geological Society of America, Centennial Field Guide: Geological Society of America, v. 3, p. 79-182.

Ozkan, G., and Ortoleva, P.J., 2000, Evolution of the gouge particle size distribution: A Markov model: Pure and Applied Geophysics, v. 157, p. 449-468.

Pate, C.R., 1989, Assessing the Relative Importance of Compaction Processes and Cementation to Reduction of Porosity in Sandstones: Discussion: American Association of Petroleum Geologists, v. 73, p. 1270-1273.

Paxton, S.T., Szabo, J.O., Ajdukiewicz, and Klimentidis, R.E., 2002, Construction of an intergranular volume compaction curve for evaluating and predicting compaction and porosity loss in rigid-grain sandstone reservoirs: American Association of Petroleum Geologists Bulletin, v. 86, p. 2047-2067.

Perry E.A. Jr., Hower, J, 1970, Burial diagenesis in Gulf coast politic sediments: American Association of Petroleum Geologists Bulletin, v. 56, p. 2012-2021.

Pfeiffer, D.S., 1988, Temperature variations and their relation to groundwater flow, South Texas, Gulf Coast Basin [M.A. thesis]: Austin, TX, The University of Texas at Austin.

Pittman, E.D., 1981, Effect of Fault-Related Granulation on porosity and Permeability of quartzose sandstones, Simpson Group (Ordovician), Oklahoma: The American Association of Petroleum Geologists Bulletin, v. 65, p. 2381-2387.

Pittman, E.D., and Larese, R.E., 1991, Compaction of lithic sands: Experimental results and applications: American Association of Petroleum Geologists Bulletin, v. 75, p. 1279-1299.

Prasher, C., 1987, Crushing and grinding process handbook: New York, John Wiley & Sons Limited, 474 p.

Pryor, W.A., 1973, Permeability-porosity patterns and variations in some Holocene sand bodies: American Association of Petroleum Geologists Bulletin, v. 57, p. 162-289.

Quinlan, G.M., and Beaumont, C., 1984, Appalachian thrusting, lithosphere flexure, and the Paleozoic stratigraphy of the Eastern Interior of North America: Canadian Journal of Earth Science, v. 21, p. 973-996.

Ramm, M., 1992, Porosity-depth trends in reservoir sandstones: theoretical models related to Jurassic sandstones offshore Norway: Marine and Petroleum Geology, v. 9, p. 553-567.

Rawling, G.C., and Goodwin, L.B., 2003, Cataclasis and particulate flow in faulted, poorly lithified sediments: Journal of Structural Geology, v. 25, p. 317-331.

Raynaud, S., and Carrio-Schaffhauser, E., 1992, Rock matrix structures in a zone influenced by a stylolites: Journal of Structural Geology, v. 14, p. 973-980.

Reed, R.M., and Laubach, S.E., 1996, The role of microfractures in the development of quartz overgrowth cements in sandstones: New evidence from cathodoluminescence studies: Geological Society of America Abstract, Annual Meeting, p. A-280.

Rittenhouse, G., 1971, Mechanical Compaction of Sands Containing Different Percentages of Ductile Grains: a Theoretical Approach: American Association of Petroleum Geologists Bulletin, v. 55, p. 92-96.

Roden, M.K., 1990, Apatite-fission track thermochronology of the southern Appalachian basin: Maryland, West Virginia, and Virginia: Journal of Geology, v. 99, p. 41-53.

Roden, M.K., Elliot, W.C., Aronson, J.L., and Miller, D.S., 1993, A comparison of fission-track ages of apatite and zircon to the K/Ar ages of illite/smectite (I/S) from Ordovician K-Bentonites, Southern Appalachian basin: Journal of Geology, v. 101, p. 633-641.

Rowan, E.L., Goldhaber, M.B., and Hatch, J.R., 2002, Regional fluid flow as a factor in the thermal history of the Illinois basin: Constraints from fluid inclusions and the maturity of Pennsylvanian coals: American Association of Petroleum Geologists Bulletin, v. 86, p. 257-277.

Runkel, A.C., McCay, R.M., and Palmer, A.R., 1998, Origin of classic cratonic sheet sandstone: Stratigraphy across the Sauk II- Sauk III boundary in the Upper Mississippian Valley: Geological Society of America Bulletin, v. 110, p. 188-210.

Sammis, C.G., and Biegel, R.L., 1989, Fractals, fault-gouge, and friction: Pure and Applied Geophysics, v. 131, p. 255-271.

Sammis, C.G., King, G., and Biegel, R., 1987, The kinematics of gouge deformation: Pure and Applied Geophysics, v. 125, p. 777-812.

Sargant, M.L., 1991, Sauk sequence - Cambrian system through Lower Ordovician Series, *in* Leighton, M.W., Kolata, D.R., Oltz, D.F., and Eidel, J.J., eds., Interior Cratonic Basins: American Association of Petroleum Geologists Memoir, v. 51, p. 75-85.

Scherer, M., 1987, Parameters Influencing porosity in sandstones: A model for sandstone porosity prediction: American Association of Petroleum Geologists Bulletin, v. 71, p. 485-491.

Schmoker, J.W., and Gautier, D.L., 1988, Sandstone porosity as a function of thermal maturity: Geology, v. 16, p. 1007-1010.

Sharp, J.M.Jr., Fenstermaker, T.R., Simmons, C.T., McKenna, T.E., Dickonson, J.K., 2001, Potential salinity-driven free convection in a shale-rich sedimentary basin: Example from the Gulf of Mexico basin in south Texas: American Association of Petroleum Geologists Bulletin, v. 85, p. 2089-2110.

Sippel, R.F., 1968, Sandstone petrology, evidence from luminescence petrography: Journal of Sedimentary Petrology, v. 38, p. 530-554.

Souza, R.S., 2000, Integrated diagenetic modeling and reservoir quality assessment and prediction of the Água Grande sandstones, early Cretaceous, Reconcavo Basin, Northeast Brazil [Ph.D. thesis]: Austin, Texas, The University of Texas at Austin, 260 p.

Stone, W.N., and Siever, R., 1997, Quantifying compaction, pressure solution and quartz cementation in moderately and deeply buried quartzose sandstone from the greater Green River Basin, Siliciclastic Diagenesis and Fluid Flow: Concepts and Applications: SEPM Special Publication, v. 55, p. 129-150.

Swarbrick, R.E., Osborne, M.J., and Yardley, G.S., 1997, Mechanisms for generating overpressure in sedimentary basins; a reevaluation: American Association of Petroleum Geologists Bulletin, v. 81, p. 1023-1041.

Tang, C.A., Xu, X.H., Kou, S.Q., Lindquist, P.-A., and Liu, H.Y., 2001, Numerical investigation of particle breakage as applied to mechanical crushing- Part I: Single-particle breakage: International Journal of Rock Mechanics and Mining Sciences, v. 38, p. 1147-1162.

Tankard, A.J., 1986, Depositional response to foreland deformation in the Carboniferous of Eastern Kentucky: Bulletin of the American Association of Petroleum Geologists, v. 70, p. 853-868.

Turcotte, D.L., 1986, Fractals and Fragmentation: Journal of Geophysical Research, v. 91, p. 1921-1926.

Walderhaug. O., 1994, Temperatures of quartz cementation in Jurassic sandstones from the Norwegian Continental Shelf- Evidence from fluid inclusions: Journal of Sedimentary Research, v. 64A, p. 311-323.

—., 1996, Kinetic modeling of quartz cementation and porosity loss in deeply buried sandstone reservoirs: American Association of Petroleum Geologists Bulletin, v. 80, p. 731-745.

Walker, G., and Burley, S., 1991, Luminescence petrography and spectroscopic studies of diagenetic minerals, *in* Kopp, O.C., ed., Luminescence microscopy and spectroscopy; qualitative and quantitative applications: SEPM Short Course, v. 25, p. 83-96.

Wilson, J.C., and McBride, E.F., 1988, Compaction and Porosity Evolution of Pliocene Sandstones, Ventura Basin, California: The American Association of Petroleum Geologists Bulletin, v. 72, p. 664-681.

Wilson, M.D., and Stanton, P.T., 1994, Diagenetic Mechanisms of Porosity and Permeability Reduction and Enhancement, *in* Wilson, M.D., ed., Reservoir Quality assessment and Prediction in Clastic Rocks: SEPM Short Course, v. 30, p. 59-118.

Wilson, T.V., and Sibley, D., F., 1978, Pressure solution and porosity reduction in shallow buried quartz arenite: The American Association of Petroleum Geologists Bulletin, v. 62, p. 2329-2334.

Wong, T.-F., 1990, Mechanical compaction and the brittle-ductile transition in porous sandstones, *in* Knipe, R.J., and Rutter, E.H., eds., Deformation Mechanisms, Rheology and Tectonics: Geological Society Special Publication, v. 54, , p. 111-122.

Wong, T.-F., and Wu, L.-C., 1995, Tensile stress concentration and compressive failure in cemented granular material: Geophysical Research Letters, v. 22, p. 1649-1652.

Worden, R.H., Mayall, M., and Evans, I.J., 2000, The effect of ductile-lithic sand grains in quartz cement on porosity and permeability in Oligocene and Lower Miocene clastics, South China Sea: Prediction of reservoir quality: American Association of Petroleum Geologists Bulletin, v. 84, p. 345-359.

Yin, H., and Dvorkin, J., 1994, Strength of cemented grains: Geophysical Research Letters, v. 21, p. 903-906.

Zhang, J., Wong, T.-F., and Davis, D.M., 1990, Micromechanics of pressure-induced grain crushing in porous rocks: Journal of Geophysical Research, v. 95. B1, p. 341-352.

Zoback, M.D., 1975, High pressure deformation and fluid flow in sandstone, granite, and granular materials [Ph.D. thesis]: Palo Alto, California, Stanford University.

VITA

Astrid Makowitz was born in Sindelfingen, Germany, on April 28th, 1974, the daughter of Angelika Bog and Rainer Makowitz. After graduating from Alma High School in Alma, Michigan, in 1992, she entered Michigan State University in East Lansing, Michigan. She graduated with a Bachelor of Science in 1997 and began her Master's work at Michigan State University shortly thereafter. During the summer of 1998, she took a petroleum geology internship with ARCO in Dallas, TX. Astrid graduated with a Master in Science in 1999 and entered the Ph.D. program at The University of Texas that same year. During the summer of 2000, she took an internship with British Petroleum. Astrid has two significant publications in the Journal of Sedimentary Research dating from 2001 and 2003.

Permanent Address: 7102 A Treasure Cove, Austin, TX 78745

This dissertation was typed by the author.